

Improving the consistency of greenhouse gas measurements from ground-based remote sensing instruments using a portable FTIR spectrometer

Zur Erlangung des akademischen Grades eines
DOKTORS DER NATURWISSENSCHAFTEN (Dr. rer. nat.)
von der KIT-Fakultät für Physik des
Karlsruher Instituts für Technologie (KIT)

genehmigte

DISSERTATION

von

M. Sc. Benedikt Herkommer
geboren in
Mutlangen

Erstgutachter:	Prof. Dr. Peter Braesicke
Zweitgutachter:	PD Dr. Frank Hase
Tag der mündlichen Prüfung:	21. Juli 2023



This thesis is licensed under a Creative Commons Attribution 4.0 International License
(CC BY 4.0): <https://creativecommons.org/licenses/by/4.0/deed.en>

Abstract

Mitigation of climate change is one of the most important issues of the present time. Therefore, it is crucial to have a precise knowledge of the concentrations of greenhouse gas (GHG) in the atmosphere. For this task, satellites are an appropriate tool: They are providing column-averaged dry-air mole fractions (denoted as XGas in the following) on a global scale.

However, to ensure the quality of their data they need to be calibrated and validated. The Total Carbon Columns Observing Network (TCCON) is currently the de facto standard for providing reference data for satellite calibration using ground-based remote sensing FOURIER Transform Infrared (FTIR) spectrometers distributed over the globe. For providing highly precise validation data it is crucial to ensure small site-to-site biases across the network. In this work, a new method to investigate the TCCON site-to-site consistency is described. The so called Travel Standard (TS) is based on an EM27/SUN, a small, portable FTIR spectrometer which is deployed to the TCCON sites to collect side-by-side measurements. The EM27/SUN is the standard instrument of the Collaborative Carbon Column Observing Network (COCCON). As they are portable, the COCCON is designed such that all EM27/SUN spectrometers are calibrated to a common reference unit. It is operated in Karlsruhe (Germany) and tied to the Karlsruhe TCCON site. Therefore, by comparing sites to the TS and the TS to the reference unit, it is also possible to compare them to the Karlsruhe site, which hence serves as a reference for the comparisons of the TCCON sites.

For the retrieval software of both, the TCCON and COCCON, updates were released recently. Therefore, the update and reprocessing of the Karlsruhe TCCON site as well as the calibration of the COCCON retrieval software was realized in this work. The calibration showed a difference of the TCCON and COCCON in dependency of XH₂O of up to 3 ppm (0.7 %) for XCO₂, 0.01 ppm (0.55 %) for XCH₄ and 0.56 ppb (0.56 %) for XCO. The origin of this bias is still unknown and needs further investigations. The calibration corrects these differences by an empirical calibration-factor correction.

The TS was deployed to campaigns at the TCCON sites in Tsukuba (TK) in Japan, East Trout Lake (ETL) in Canada and Wollongong (WG) in Australia. In ETL, the TCCON spectrometer broke down shortly before the TS arrived. Hence, no side-by-side comparison was possible.

Between each campaign, instrumental line shape (ILS) measurements and solar side-by-side measurements with the TS next to the COCCON reference were collected. All ILS measurements were in the expected range for an EM27/SUN spectrometer. The maximum change in the XGas measurements found between the campaigns is 0.31 ppm for XCO₂, 0.0019 ppm for XCH₄ and -0.51 ppb for XCO. For all gases this is below the estimated TCCON site-to-site bias.

At each campaign the regular TCCON high-resolution (HR) as well as low-resolution (LR) measurements were collected and compared to the TS measurements. For XCO₂ and XCH₄ deviations for the LR and HR measurements are within the estimated TCCON site-to-site bias ($\pm 0.1\%$ for XCO₂ and $\pm 0.215\%$ for XCH₄) with the exception of the TK-LR XCO₂ data with a deviation of 0.113 %. For XCO the deviations of the TK-LR and the WG-HR data are within the

estimated TCCON site-to-site bias ($\pm 2.7\%$). The TK-LR data showed deviations of more than 7% and the WG-LR data a deviation of -5.6% . However, for both datasets there are known issues causing these results. In TK and WG high noise levels of the TCCON retrievals were detected, which could be traced back to a low signal-to-noise ratio (SNR) in the O_2 retrieval. Thereupon, several TCCON sites were checked for the same issue. This investigation revealed that several sites are also suffering from this. Furthermore, in TK a timing error of -44 s was detected. These findings emphasize the usefulness of the TS for the quality maintenance of the TCCON.

Zusammenfassung

Die Bekämpfung des Klimawandels ist eines der wichtigsten Aufgaben unserer Zeit. Dafür ist es unerlässlich die Treibhausgaskonzentrationen in der Atmosphäre zu kennen. Für weltweite Messungen sind Satelliten die beste Wahl. Diese messen Säulengemittelte molare Mischungsverhältnisse bezogen auf trockene Luft (im folgenden bezeichnet als XGas).

Um die Genauigkeit von Satelliten zu gewährleisten müssen diese jedoch kalibriert und validiert werden. Das Messnetzwerk „Total Carbon Column Observing Network (TCCON)“ ist derzeit der de-facto Standard, welches Referenzdaten für die Satellitenkalibrierung bereithält. Dafür nutzt es bodengestützte Fernerkundungsmessungen von Fourier-Transformations-Infrarot (FTIR) Spektrometer, welche auf dem Globus verteilt sind. Für hochpräzises Validierungsdaten ist es entscheidend, dass die Messungen der Spektrometer untereinander konsistent sind. In dieser Arbeit wird eine neue Methode präsentiert, um diese Konsistenz zu überprüfen. Der so genannte Travel Standard (TS) basiert auf einem EM27/SUN, einem kleinen, tragbaren FTIR-Spektrometer, welches in Kapagnen Vergleichsmessungen mit TCCON Spektrometern durchführt. Das EM27/SUN ist das Standardinstrument des „Collaborative Carbon Column Observing Networks (COCCON)“. Da das EM27/SUN tragbar ist, ist das COCCON so konzipiert, dass alle EM27/SUN Spektrometer mithilfe eines gemeinsamen Referenzspektrometers kalibriert werden. Dieses Referenzspektrometer misst kontinuierlich in Karlsruhe und ist wiederum auf die Karlsruher TCCON Station kalibriert. Daher dient TCCON-Karlsruhe als Referenz für die Vergleiche mit dem TS.

Sowohl für die Auswertesoftware des TCCON als auch die des COCCON wurden kürzlich neue Versionen veröffentlicht. Daher wurde die Aktualisierung und die Prozessierung der Karlsruher TCCON Daten mit dieser neuen Version in dieser Arbeit durchgeführt. Des Weiteren wurde die neue Version der COCCON Auswertesoftware kalibriert um mit der TCCON Auswertung übereinzustimmen. Die Kalibrierung zeigt einen Unterschied zwischen TCCON und COCCON in Abhängigkeit von X_{H_2O} . Dieser beträgt bis zu 3 ppm (0.7 %) für X_{CO_2} , 0.01 ppm (0.55 %) für X_{CH_4} und 0.56 ppb (0.56 %) für X_{CO} . Die Ursache dieser Abweichung ist noch unbekannt und bedarf weiterer Untersuchungen. Die Kalibrierung korrigiert diese Unterschiede durch eine empirische X_{H_2O} -abhängige Funktion.

Mit dem TS wurden Messkampagnen an den TCCON-Standorten in Tsukuba (TK) in Japan, East Trout Lake (ETL) in Kanada und Wollongong (WG) in Australien durchgeführt. In ETL fiel das TCCON-Spektrometer kurz vor der Ankunft des TS aus. Daher war kein direkter Vergleich möglich. Zwischen den einzelnen Kampagnen wurden „Instrumental Line Shape“ (ILS) Messungen im Labor und Vergleichsmessungen mit der COCCON-Referenz durchgeführt. Alle Messungen der ILS liegen im normalen Bereich eines EM27/SUN-Spektrometers. Die maximale Änderung der Vergleichsmessungen zwischen den Kampagnen beträgt 0.31 ppm für X_{CO_2} , 0.0019 ppm für X_{CH_4} und -0.51 ppb für X_{CO} . Für alle Gase liegt dies unter der von TCCON geschätzten Abweichung zwischen den TCCON Spektrometern ($\pm 0.1\%$ für X_{CO_2} , $\pm 0.215\%$ für X_{CH_4} und $\pm 2.7\%$ für X_{CO}).

Bei jeder Kampagne wurden sowohl die regulären hochauflösenden (HR) als auch die niedrigauflösenden (LR) TCCON-Messungen durchgeführt und mit den TS-Messungen verglichen. Für XCO_2 und XCH_4 liegen die Abweichungen für die LR- und HR-Messungen innerhalb der geschätzten Konsistenz der TCCON-Spektrometer, mit Ausnahme der TK-LR XCO_2 -Daten mit einer Abweichung von 0.113 %. Für XCO liegen die TK-LR und die WG-HR innerhalb der geschätzten Abweichung von TCCON. Die TK-LR-Daten zeigten Abweichungen von mehr als 7 % und die WG-LR-Daten eine Abweichung von -5.6 %. Bei der Messungen beider Datensätze lagen jedoch bekannte Probleme vor, die diese Ergebnisse verursachen. Bei TK und WG wurde zudem ein hoher Rauschpegel festgestellt, der auf ein niedriges Signal-zu-Rausch-Verhältnis im Spektralbereich von Sauerstoff zurückgeführt werden konnte. Daraufhin wurden mehrere TCCON-Spektrometer auf das gleiche Problem hin überprüft, wobei sich herausstellte, dass mehrere Standorte das gleiche Problem haben. Außerdem wurde in TK ein Fehler im Zeitstempel der Messungen von -44 s festgestellt. Diese Resultate unterstreichen wie nützlich der Travel Standard (TS) für die Qualitätssicherung innerhalb des TCCONs ist.

List of Author's Publications

Herkommer, B., Alberti, C., Castracane, P., Chen, J., Dehn, A., Dietrich, F., Deutscher, N. M., Frey, M. M., Groß, J., Gillespie, L., Hase, F., Morino, I., Pak, N. M., Walker, B., and Wunch, D. (2024). “Using a portable FTIR spectrometer to evaluate the consistency of TCCON measurements on a global scale: The COCCON Travel Standard”. In: *EGUsphere* 2024, pp. 1–46. DOI: [10.5194/egusphere-2023-3089](https://doi.org/10.5194/egusphere-2023-3089)

Feld, L., **Herkommer, B.**, Dubravica, D., Alberti, C., and Hase, F. (2023b). *PROFFASTpylot: Running PROFFAST with Python*. JOSS: The Journal of Open Source Software. Submitted

Byrne, B., Baker, D. F., Basu, S., Bertolacci, M., Bowman, K. W., Carroll, D., Chatterjee, A., Chevallier, F., Ciais, P., Cressie, N., Crisp, D., Crowell, S., Deng, F., Deng, Z., Deutscher, N. M., Dubey, M. K., Feng, S., Garcia, O. E., Griffith, D. W. T., **Herkommer, B.**, Hu, L., Jacobson, A. R., Janardanan, R., Jeong, S., Johnson, M. S., Jones, D. B. A., Kivi, R., Liu, J., Liu, Z., Maksyutov, S., Miller, J. B., Miller, S. M., Morino, I., Notholt, J., Oda, T., O'Dell, C. W., Oh, Y.-S., Ohyama, H., Patra, P. K., Peiro, H., Petri, C., Philip, S., Pollard, D. F., Poulter, B., Remaud, M., Schuh, A., Sha, M. K., Shiomi, K., Strong, K., Sweeney, C., Te, Y., Tian, H., Velasco, V. A., Vrekoussis, M., Warneke, T., Worden, J. R., Wunch, D., Yao, Y., Yun, J., Zammit-Mangion, A., and Zeng, N. (2023). “National CO₂ budgets (2015–2020) inferred from atmospheric CO₂ observations in support of the global stocktake”. In: *Earth System Science Data* 15.2, pp. 963–1004. DOI: [10.5194/essd-15-963-2023](https://doi.org/10.5194/essd-15-963-2023)

Tsuruta, A., Kivimäki, E., Lindqvist, H., Karppinen, T., Backman, L., Hakkarainen, J., Schneising, O., Buchwitz, M., Lan, X., Kivi, R., Chen, H., Buschmann, M., **Herkommer, B.**, Notholt, J., Roehl, C., Té, Y., Wunch, D., Tamminen, J., and Aalto, T. (2023). “CH₄ Fluxes Derived from Assimilation of TROPOMI XCH₄ in CarbonTracker Europe-CH₄: Evaluation of Seasonality and Spatial Distribution in the Northern High Latitudes”. In: *Remote Sensing* 15.6. ISSN: 2072-4292. DOI: [10.3390/rs15061620](https://doi.org/10.3390/rs15061620)

Someya, Y., Yoshida, Y., Ohyama, H., Nomura, S., Kamei, A., Morino, I., Mukai, H., Matsunaga, T., Laughner, J. L., Velasco, V. A., **Herkommer, B.**, Te, Y., Sha, M. K., Kivi, R., Zhou, M., Oh, Y. S., Deutscher, N. M., and Griffith, D. W. T. (2023). “Update on the GOSAT TANSO-FTS SWIR Level 2 retrieval algorithm”. In: *Atmospheric Measurement Techniques* 16.6, pp. 1477–1501. DOI: [10.5194/amt-16-1477-2023](https://doi.org/10.5194/amt-16-1477-2023)

"Two things are infinite: the universe and human stupidity;
and I'm not sure about the universe."
- ALBERT EINSTEIN

Contents

Abstract	i
Zusammenfassung	iii
List of Author's Publications	v
1. Introduction	1
2. Theoretical Background	5
2.1. The Earth's Atmosphere and Climate Change	5
2.1.1. The Earth's Atmosphere	5
2.1.2. Energy Balance and Greenhouse Effect	8
2.2. Molecular Spectroscopy	13
2.2.1. Diatomic Molecules	14
2.2.2. Polyatomic Molecules	18
2.2.3. Spectral Line Shapes	19
2.3. Fourier Transform Infrared Spectroscopy	20
2.3.1. The Fourier Transformation	20
2.3.2. The Ideal Michelson-Interferometer	23
2.3.3. From Interferograms to Spectra	24
2.3.4. Real World Spectrometers	25
2.4. Remote Sensing using Fourier Transform Infrared Spectroscopy	32
2.4.1. Basics of Radiative Transfer	33
2.4.2. Basics of Inversion Theory	34
3. Ground-based Remote Sensing Networks for Greenhouse Gases	37
3.1. The Total Carbon Column Observing Network (TCCON)	37
3.1.1. Measured Quantities	38
3.1.2. Technical Description	39
3.1.3. Calibration Procedure and Quality Assurance	40
3.1.4. The Karlsruhe TCCON Station	42
3.2. The Collaborative Carbon Column Observing Network (COCCON)	46
3.2.1. The PROFFAST Retrieval Software and the PROFFASTpylot Interface	47
3.2.2. Calibration of PROFFAST2 to the TCCON Scale	49
3.2.3. Analysis of the XH_2O Dependency	53
3.2.4. Performance Comparison of COCCON to TCCON	57
4. Travel Standard: Technical Description	59
4.1. The Enclosure	59

4.2. Characterization and Monitoring of the Travel Standard in Karlsruhe Between the Campaigns	63
4.2.1. Approach to Retrieve Bias Compensation Factors	64
4.2.2. Characterization of the Travel Standard at the KIT for Empirical Bias Monitoring	66
4.2.3. XCO-Correction	69
4.2.4. Calibration of the Pressure Sensor	70
5. Results of the Travel Standard Campaigns	73
5.1. Evaluation Procedure of the Travel Standard Campaigns	74
5.2. Tsukuba, Japan	74
5.2.1. Correction of the Timing Error	78
5.3. East Trout Lake, Canada	78
5.4. Wollongong, Australia	81
5.5. Noise Analysis	83
5.5.1. Intensity Drop in Spectra at the O ₂ Window	84
5.5.2. High vs. Low Resolution Spectra	86
5.5.3. Network-wide Data Analysis	89
5.6. Quantitative Comparison of the Station Data	96
5.6.1. Calculation of the Bias Compensation Factors	96
5.6.2. Error Analysis	98
5.6.3. Evaluation of the Time Corrected Tsukuba Data	99
5.7. Discussion of the Results	99
5.7.1. Influence of the Timing Error in Tsukuba	101
5.7.2. Pressure Analysis	101
5.8. Summary of the Chapter	102
6. Summary and Outlook	105
A. Appendix to the Technical Details of the Travel Standard	109
B. Results of the Calibration of the PROFFAST2 Algorithm	111
B.1. Airmass Dependent Correction Factors	111
B.2. Airmass Independent Calibration	111
C. Systematic Noise Analysis for XCH₄	121
Bibliography	123
List of Figures	135
List of Tables	137
Acronyms	137
Index	141
Acknowledgment	143

Chapter 1

Introduction

In 1824, JOSEPH FOURIER was the first to discover that the Earth's atmosphere serves as an important insulating layer which warms the atmosphere and proposed the name "Greenhouse Effect" (Kleber and Richter-Krautz 2022). In 1869 SVANTE ARRHENIUS discovered that the warming effect is driven by the trace gas carbon dioxide (CO₂) and could estimate the warming quantitatively (Kleber and Richter-Krautz 2022). Since at least the 1970s there has been a sophisticated understanding of the influence of CO₂ to the warming of the atmosphere and projections on the influence of CO₂ to future warming of the atmosphere could be made (Supran et al. 2023). Besides CO₂, there are other gases which contribute to the warming of the atmosphere. After CO₂ the most important examples of the so called greenhouse gases (GHGs) are Methane (CH₄) water vapor (H₂O) and Nitrous oxide (N₂O). Despite this early knowledge about the risk of emitting large amounts of of GHG in the atmosphere, their concentration has increased tremendously. Since 1850, CO₂ was raised from 280 ppm to approximately 420 ppm today, CH₄ was raised from 808 ppb to approximately 1915 ppb today (Meinshausen et al. 2017; K.W. et al. 2022). This caused a global warming of the average surface temperature. The average surface temperature of the last decade (2011 - 2020) was 1.1 °C warmer compared to the average of each year from 1850 - 1900 (Arias et al. 2021). Without a reduction of the GHG emissions the global mean surface temperature increase compared to 1850 - 1900 is expected to rise up to 3.6 °C as the best estimate with a likely range of 2.8 to 4.6 °C until 2100 (Scenario SSP3-7.0 in Arias et al. 2021).

An increase of the global mean temperature causes various effects like rising sea levels (Fox-Kemper et al. 2021), a rise in unprecedented extreme weather events (Seneviratne et al. 2021) or changes in the hydrological circle including the increased probability of droughts (Douville et al. 2021).

Meanwhile, the extremely urgent need to reduce GHGs is also acknowledged by the political decision-makers in the Paris Agreement wherein they agreed to keep global warming at well below 2 °C (United-Nations 2015). To achieve this goal, it is indispensable to have a precise knowledge of the GHG concentration and to monitor the sources and sinks of GHGs: Precise measurements enable to,

- monitor known sources (e.g.(Tu et al. 2022a; C. D. Jones et al. 2012)) and to examine if the measures taken to reduce the emissions are successful (e.g. (Karimipour et al. 2019; Baek et al. 2014; Kern and Jess 2021)),
- find sources of emissions unknown so far (e.g. (Lisboa et al. 2011; Riddick et al. 2019)),
- understand the interaction of the biosphere with the atmosphere with increasing temperatures Stocker et al. 2013; Messerschmidt et al. 2013 and
- to provide input data for climate models.

All this knowledge can help to better predict the future developments of the climate and hence to better to mitigate and to adapt to the various effects of climate change.

For monitoring GHG sources and sinks there are two approaches:

The first is the so-called bottom-up approach. This approach considers natural sinks and source (Schulze 2006; Hodson et al. 2011) as well as statistics of fossil fuel consumption to generate emission inventories. An emission inventory considering only anthropogenic emission is for example the EDGAR database (Crippa et al. 2022). However, the bottom-up approach needs accurate knowledge of both, natural sources and sinks as well as anthropogenic emissions. For example, Solazzo et al. 2021 found that in the EDGAR database the combined emissions of CO₂, CH₄ and N₂O the lower and upper limit of the 95 % confident interval –15 % and 20 %. However, considering only a single sector like e.g. agriculture, the lower and upper limit of the 95 % confident interval for CO₂, CH₄ and N₂O are –90 % and 118 %.

Therefore, top-down method as a complementary method to the bottom-up approach is used. This method is based on the direct measurements of the GHG concentrations in the atmosphere. The measurements can be collected, for example, by in-situ measurements like performed by the GLOBALVIEW-CO₂ network, led by the US-National Oceanic and Atmospheric Administration (NOAA) (Cox et al. 2022), or by the ICOS network in Europe (Bergamaschi et al. 2022). However, in-situ measurements have a low global coverage and do not consider the concentrations at different heights. Another possibility to collect measurements is the usage of satellites. Equipped with remote sensing and orbiting Earth in a sun-synchronous orbit they are able to provide column-averaged dry-air mole fractions (DMF) covering a quasi-global area. Examples for these are the Japanese Greenhouse Gases Observing Satellite (GOSAT) (Yokota et al. 2009), the US-American Orbiting Carbon Observatory - 2 (OCO-2) (Crisp 2015) or the European TROPospheric Monitoring Instrument (TROPOMI) onboard of the Sentinel-5 precursor satellite (Veefkind et al. 2012). This data can be used to retrieve the emission strength of various sources worldwide (e.g. (Tu et al. 2022a; Zhang et al. 2020; Cusworth et al. 2021)).

To validate and calibrate the satellite-data ground-based reference measurements are needed. Ground based FOURIER Transform Infrared (FTIR) spectrometers are well suited for this purpose as the same measurement principle is used and hence, provide column-averaged DMFs as well. Currently, there are three main FTIR networks:

- the infrared working group (IRWG) of the Network for Detection of Atmospheric Composition Change (NDACC) (Kurylo 1991)
- the Total Carbon Columns Observing Network (TCCON) (Wunch et al. 2011b) and
- the Collaborative Carbon Column Observing Network (COCCON) (Frey et al. 2019; Alberti et al. 2022a).

While the NDACC-IRWG is measuring in the mid-infrared (MIR) spectral region, both, the TCCON and COCCON are measuring in the near-infrared (NIR) spectral region.

The TCCON provides reference data for the validation for the measurements of several satellites (Wu et al. 2018; Dils et al. 2014; Yoshida et al. 2013). The standard instrument of the TCCON is the BRUKER IFS 125HR spectrometer. These are high-resolution FTIR spectrometers which support measurements with a maximum optical path difference of several meters. Therefore, the spectrometers are quite large and heavy. Hence, they are hard to transport. To operate such an instrument a good infrastructure providing a reliable power supply and experienced personal are necessary. Therefore, there is a sparse distribution of TCCON sites all over the world: In May 2023, there are 28 sites around the globe. However, they are not evenly distributed but

mainly concentrated in the northern hemisphere. Therefore, the TCCON cannot provide a global coverage.

To provide reliable reference data, it is important to ensure both the calibration of the network as a whole as well as a high consistency of measurements at each site to avoid station-to-station biases. For this purpose the TCCON uses several quality checks. The TCCON network as a whole is calibrated to reproduce the units defined by the World Meteorological Organization (WMO) (B. D. Hall et al. 2021) by comparing the TCCON measurements with column-averaged trace gas concentrations which are derived from collocated profile observations by aircraft or AirCore measurements (Wunch et al. 2010; Messerschmidt et al. 2011; Karion et al. 2010; Sha et al. 2020). However, collecting such a profile data set is laborious and expensive. In addition, the number of available in-situ profiles is too small to detect minor biases of individual TCCON sites.

The TCCON uses different possibilities to monitor the proper functioning of the instruments. The first is the supervision of the so-called instrumental line shape (ILS) of an instrument using a low-pressure HCl gas cell (Hase et al. 1999). This method allows to check if the FTIR instrument deviates from its nominal behavior. The second is the investigation of a technical quantity called XAIR or XLUFT, which compares the vertical column of dry-air derived from an FTIR measurement, with the column of dry air calculated from the ground pressure (assuming a hydrostatic atmosphere).

Unfortunately, none of these two methods allows for a direct validation of the retrieved column-averaged DMFs. The direct approach to compare the column-averaged DMFs would be to perform side-by-side measurements with the spectrometers. For performing side-by-side measurements a shipment of the spectrometers would be needed. However, as the 125HR instruments are very large shipping them would be very expensive and laborious. Furthermore, the shipment would misalign the spectrometer which also impedes a useful side-by-side comparison.

In 2012, at the Institute for Meteorology and Climate Research - Atmospheric Trace Gases and Remote Sensing (IMK-ASF) the EM27/SUN has been developed in cooperation with BRUKER. This is a low-resolution FTIR spectrometer which became commercially available in 2014 (Gisi et al. 2012). These instruments are used in the COCCON. As they are portable, relatively cost-effective and easy-to-use, they were disseminated to various groups world-wide. By today more than 150 EM27/SUN spectrometers are operating world-wide, either collecting measurements at a stationary location or being used for temporary campaigns. The COCCON is tied to the WMO scale by comparing the measurements of a reference EM27/SUN spectrometer which is operated continuously in Karlsruhe with the co-located TCCON spectrometer. Furthermore, the portability of the spectrometers allows for a side-by-side measuring of all COCCON spectrometers with the COCCON reference before commissioning and being calibrated accordingly. This method provides an elegant solution of the problem of the inter-network calibration which was discussed for the TCCON before.

In this thesis, a new method for the site-to-site calibration of the TCCON network is investigated. It is based on the usage of a portable EM27/SUN FTIR spectrometer as a traveling standard. The conceptual idea is to ship a dedicated EM27/SUN - the “Travel Standard” to the different TCCON sites to collect side-by-side measurements. By comparing the column-averaged DMFs of the different TCCON sites to a common reference, it is possible to check the site-to-site consistency of the network and also the instrumental health status.

This method has already been realized for a subset of TCCON sites by Hedelius et al. 2016 and Mostafavi Pak et al. 2023. In this paper, the commissioning of a dedicated TS is presented which aims to systematically check the TCCON sites, with special regard for the global scale. Up until

now, the TS visited the TCCON sites in Tsukuba (Japan), in East Trout Lake (Canada) and in Wollongong (Australia). Already scheduled are visits in Izaña (Spain) and in Paris (France).

In this introduction, Chapter 2 gives the relevant background information about the atmosphere, the climate change and remote sensing using FTIR spectroscopy.

In Chapter 3, the TCCON and the COCCON are introduced. Furthermore, the results of the reprocessing of the TCCON data collected in Karlsruhe with the latest retrieval software of the TCCON is presented. In addition, the calibration of the latest retrieval software of the COCCON network to the Karlsruhe TCCON site is shown.

In Chapter 4, the technical realization of the TS is given. This comprises the hardware, as well as the monitoring of the instrument at its home base in Karlsruhe between the campaigns. In Chapter 5, the results of the campaigns in Tsukuba, East Trout Lake and Wollongong are presented and discussed. Finally, Chapter 6 summarizes the thesis and provides an outlook as well as a discussion of the results.

Chapter 2

Theoretical Background

In this section, the theoretical background of this thesis is given.

The FOURIER Transform Infrared (FTIR) spectrometers used in this thesis are measuring concentrations of mainly greenhouse gases (GHGs) in the Earth atmosphere. Therefore, the first section introduces the Earth's atmosphere as well as the Earth's energy balance including the green house effect and climate change in which the GHGs play a crucial role. After this, the knowledge to understand the measurement principle of an FTIR is explained. The second section gives a physical background of the absorption of radiation by different molecules. The third section covers the FTIR spectroscopy which in this thesis is used for the analysis of the atmospheric composition. The fourth section provides an overview of the principles of remote sensing using FTIR spectroscopy.

2.1. The Earth's Atmosphere and Climate Change

The Earth's atmosphere is necessary for life on earth. Among others, it provides oxygen and carbon dioxide for the metabolism of living beings, it absorbs harmful ultraviolet (UV) radiation and heats up the surface temperature making it possible for humans to survive. Following, the key features of the atmosphere are roughly explained. First, the composition and vertical structure of the atmosphere is explained. Next, the radiation balance of the Earth, including the green house effect and climate change, is discussed.

2.1.1. The Earth's Atmosphere

First, its composition will be explained. Next, the stratification of the pressure and the temperature are discussed.

Composition of the Atmosphere In the following, all concentrations given, if not stated otherwise, always refer to dry-air (i.e. free from water vapor). The constituents of the atmosphere can be separated into two types. The first type includes gases with very little variation in space and time which hence can be assumed as constant. These are listed in Table 2.1 together with their molar masses. The three most prominent gases, N_2 , O_2 and Ar make up 99.9% of the total atmosphere. The concentrations of the second type are variable in their spatial and temporal distribution and are called the trace gases. Furthermore, there are small particles called aerosols which also contribute to the atmosphere.

Table 2.1.: The composition of the seven biggest constituents of the Earth’s atmosphere. The mixing ratios are given without taking water vapor into account. For mixing ratios with a suffix of 10^{-4} the more common unit is [ppm]. Taken from (Roedel and Wagner 2017).

Component	molar mass M (g mol^{-1})	volume mixing ratio (%)
Nitrogen, N_2	28.02	78.09
Oxygen, O_2	32.00	20.95
Argon, Ar	39.94	0.93
Neon, Ne	20.18	$18.21 \cdot 10^{-4}$
Helium, He	4.003	$5.24 \cdot 10^{-4}$
Krypton, Kr	83.8	$1.14 \cdot 10^{-4}$
Xenon, Xe	131.3	$0.087 \cdot 10^{-4}$
Air	28.97	

With respect to their contributions to the climate, the most important trace gases are H_2O (water vapor), CO_2 (418 ppm), CH_4 (1900 ppb) and N_2O (337 ppm). The numbers given in brackets are volume mixing ratios in parts per million (**ppm**) or parts per billion (**ppb**). For CO_2 , CH_4 and N_2O , the values are measured at the MAUNA LOA OBSERVATORY in Hawaii in September 2022 (Lan et al. 2022; K.W. et al. 2022; Dutton and B. Hall 2022). All three gases show an annual cycle and an increase over time. At the MAUNA LOA OBSERVATORY, for CO_2 the annual growth rate averaged over the last 10 years is approximately 2.4 ppm/a but shows an increasing trend. For CH_4 the growth rate is more variable and was in average approximately 10 ppb/a in the same period. For N_2O the growth rate is approximately 1 ppb/a.

For water vapor no average concentration can be given because it strongly depends on the ambient temperature of the atmosphere and hence has a strong spatial and temporal variation. Its volume mixing ratio ranges from 1% to 4% (B. Klose and H. Klose 2016).

A further trace gas is CO. The column-averaged dry air mole fraction of CO measured in Karlsruhe in September 2022 is 83 ppb (compare with Figure 3.3. It shows a strong annual cycle with values of 70 ppb to 140 ppb. Its concentration is significantly less than the trace gases mentioned above. However, it is an important trace gas in the context of greenhouse gas measurements.

Even though the trace gases contribute less than 0.1% to the volume of the atmosphere, they represent a strong contribution to the key features of the atmosphere, due to their chemical and physical properties, like the absorption of UV-radiation (Möller 2019) or the heating of the atmosphere due to the greenhouse effect (see section 2.1.2.2).

In terms of volume mixing ratios, the atmosphere can be divided into the homosphere and the heterosphere. The homosphere extends up to approximately 100 km. Up to there, because of the collective, turbulent mixing of the air, the volume mixing ratio is almost constant. In the heterosphere, the different molar masses of the molecules in the atmosphere lead to a separation of the different molecules.

Pressure Profile For approximating the pressure of the atmosphere at a certain height, an air parcel of volume V can, in good approximation, be described by the ideal gas law:

$$p \cdot V = Nk_B T \Leftrightarrow \frac{p}{k_B T} = \frac{N}{V} = \rho. \quad (2.1)$$

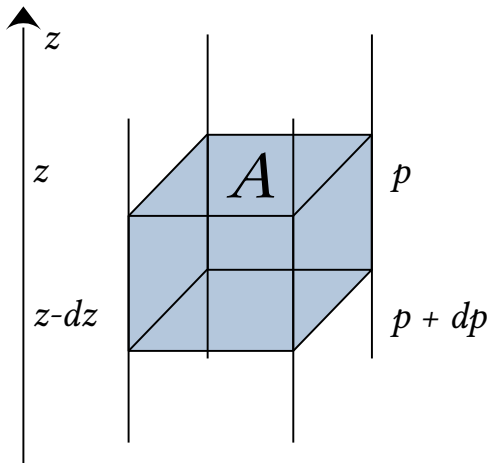


Figure 2.1: Illustration of an air parcel in a hydrostatic atmosphere. The pressure at $z + dz$ is lower by $-dp$ than p at height z . I.e. the air parcel increases the pressure by dp at height z . Taken with adaptations from (Roedel and Wagner 2017).

With p the pressure, N the number of molecules in the parcel, ρ its number density, V its volume and T its temperature. k_B is BOLTZMANN'S constant. For deriving the pressure profile of the atmosphere, a hydrostatic balanced atmosphere is assumed. This allows to divide the atmosphere in small air parcels as depicted in Figure 2.1. It demonstrates that an air parcel of volume $V = A \cdot dz$ increases the pressure at height $z - dz$ by the amount dp . Here, A describes an arbitrary area. This increase of pressure is due to the force $F = -m_{\text{parcel}} \cdot g$, created by the gravity accelerating the air within the parcel downwards with the acceleration g :

$$dp = -\frac{F}{A} = -\frac{m_{\text{parcel}} \cdot g}{A}. \quad (2.2)$$

The minus sign is needed here, since the force is directed towards the $-z$ direction. The mass of the air parcel can be expressed by the number density ρ , the molar mass of dry air $M = 0.02897 \text{ kg mol}^{-1}$:

$$m_{\text{parcel}} = M \cdot \frac{\rho V}{N_A} = M \cdot \frac{\rho A dz}{N_A}. \quad (2.3)$$

The AVOGADRO constant N_A is needed here to convert the molar mass to a mass per total number of particles. Using (2.1) to substitute ρ in (2.3) and inserting it in (2.2) yields the differential equation:

$$\frac{dp}{dz} p = -\frac{g(z)M}{N_A k_B T(z)}, \quad (2.4)$$

which can be solved to:

$$p(z) = p_0 \cdot \exp \left(- \int_0^z \underbrace{\frac{g(z')M}{N_A k_B T(z')}}_{1/H(z')} dz' \right). \quad (2.5)$$

Here, p_0 is the ground pressure at sea level. In general, the gravitational acceleration g as well as the temperature of the atmosphere T depend on the height z . $H(z)$ is known as the scaling height. Assuming a constant temperature and acceleration, the integral can be solved easily. This assumption is valid for small height differences. Assuming a temperature of 290 K (16.85 °C) and an acceleration of $g = 9.81 \text{ m/s}^2$ representing the average conditions at sea level, gives a scaling height of approximately 8.5 km.

Temperature Profile The explanation given in the upcoming section strongly follows Efremenko and Kokhanovsky 2021 and B. Klose and H. Klose 2016. In the atmosphere, five different layers can be identified: the lowermost is the troposphere, followed by the stratosphere, the mesosphere, the thermosphere and, finally the exosphere. After each layer there is a change in the sign of the temperature gradient. At the turning points between the layers there is a small area where the temperature stays approximately constant which is called “pause”.

The troposphere is ~ 6 km (in the polar region) to ~ 18 km (in the tropical regions) thick. Assuming a standard atmosphere, starting from 15°C at the ground the temperature decreases by approximately 6.5°C per kilometer until reaching approximately -70 to -80°C (in the tropical region) and -50°C (in the polar region) at the top of the troposphere. In reality, the temperature in the troposphere strongly varies in dependence of the season, the latitude and the weather. The troposphere includes up to 90% of the total mass of the atmosphere. Hence, it is the layer where most of the weather phenomena take place. Its temperature profile mainly depends on convective uplift of warm air which, due to the decrease of pressure, cools down when rising to a higher altitude (compare with equation (2.1)). The troposphere ends with the tropopause.

The stratosphere extends from the end of the troposphere up to about 50 km. The temperature increases until approximately 0°C at the stratopause. The reason for the heating is the absorption of UV-radiation by ozone. Because of the strong temperature decline in the troposphere and therefore the decreasing capability of the air to keep water vapor, the stratosphere contains almost no water.

In the mesosphere, the temperature decreases to approximately -90°C at a height of approx. 80 km. There, the lowest temperatures in the Earth’s atmosphere are reached.

The thermosphere and the exosphere are the two outmost layers. The thermosphere extends from 80 to 90 km up to 500 and 1000 km where the exosphere continues. The temperatures can reach up to 2000 K. However, because of the low particle density one can hardly assign a temperature in terms of gas kinetic particle movement but merely uses the radiation intensity as a measure of temperature.

2.1.2. Energy Balance and Greenhouse Effect

Life on earth is driven by the radiative power of the sun. The sunlight warms up the atmosphere and is the driving force of the weather. Without the energy of the sun, no life on earth would be possible. In the next section, the physical laws to describe the radiative energy balance on earth are presented. Therefore, the greenhouse effect and subsequent the climate change is explained.

2.1.2.1. The Physical Laws of Thermal Radiation

The following chapter is mainly based on Roedel and Wagner 2017 and Efremenko and Kokhanovsky 2021.

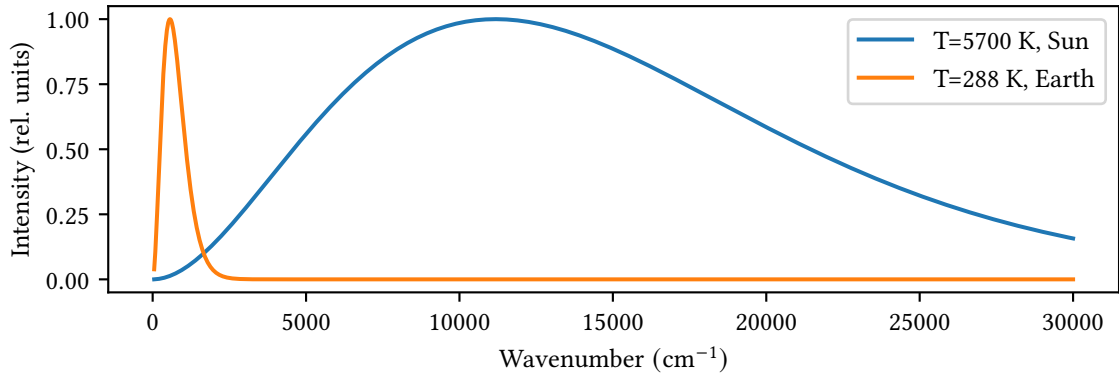


Figure 2.2.: The spectrum of two black bodies with temperatures $T = 5700$ K representing the Sun and $T = 288$ K representing the Earth. It can be seen that the maximum for bodies with higher temperatures is at higher wavenumbers (and also higher frequencies). Both curves have been normalized to unity. The maximum of the Sun divided by the Earth maximum is 7752.6.

All matter permanently absorbs and emits electromagnetic radiation. The spectral distribution of the emitted radiation is described by PLANCKS law, in the following given in dependency of the frequency ν and the wavenumber $\tilde{\nu}$ (Kramm and Mölders 2009):

$$B(\nu, T) = \frac{2h\nu^3}{c^2} \frac{1}{\exp\left(\frac{h\nu}{k_B T}\right) - 1}, \quad (2.6)$$

$$B(\tilde{\nu}, T) = 2hc^2\tilde{\nu}^3 \frac{1}{\exp(hc\tilde{\nu}/(k_B T)) - 1}. \quad (2.7)$$

B describes the spectral emitted power per unit area and unit solid angle. h is PLANCKS constant, c the speed of light in vacuum, k_B BOLTZMANN'S constant and T the temperature. The Formulas (2.6) and (2.7) assume a idealized body, which absorbs all incident electromagnetic radiation, independent of the frequency or the angle of incidence of the radiation.

The wavenumber $\tilde{\nu}$ is a quantity often used in spectroscopy. It has a dimension of cm^{-1} and is defined as $\tilde{\nu} = 1/(100 \cdot \lambda)$, with λ being the wavelength in meters. The factor 100 is needed to convert the wavelength from meter to centimeter, which is the unit of the wavenumber. An example spectrum of a blackbody with temperature $T = 5700$ K (the approximate surface temperature of the Sun) and a blackbody with $T = 288$ K (the approximate surface temperature of the Earth) is shown in Figure 2.2.

For the calculation of the Earth's energy balance, the total power P emitted by a body is needed. To get this, (2.7) is integrated over all frequencies and a hemisphere the body radiates to:

$$F = \int_0^{2\pi} \int_0^{\pi/2} \int_0^{\infty} B(\nu, T) d\nu \cos(\theta) \sin(\theta) d\theta d\phi \quad (2.8)$$

$$= \pi \int_0^{\infty} \frac{2h\nu^3}{c^2} \frac{1}{\exp\left(\frac{h\nu}{k_B T}\right) - 1} d\nu \quad (2.9)$$

$$= \frac{2\pi k_B^3 T^3}{h^2 c^2} \int_0^{\infty} \frac{h^3 \nu^3}{k_B^3 T^3} \frac{1}{\exp\left(\frac{h\nu}{k_B T}\right) - 1} dx \quad (2.10)$$

The $\cos(\theta)$ in (2.8) is a result of the application of LAMBERT'S COSINE LAW (Asimellis 2020). Substituting $x = \frac{h\nu}{k_B T}$ leads to the differential $dx = \frac{h}{k_B T} d\nu$ which gives:

$$F = \frac{2\pi k_B^4 T^4}{h^3 c^2} \int_0^\infty \frac{x^3 e^{-x}}{1 - e^{-x}} dx \quad \text{with} \quad \frac{e^{-x}}{1 - e^{-x}} = \sum_{n=1}^\infty e^{-nx}$$

$$= \frac{2\pi k_B^4 T^4}{h^3 c^2} \sum_{n=1}^\infty \int_0^\infty x^3 e^{-nx} dx \quad (2.11)$$

$$= \frac{2\pi k_B^4 T^4}{h^3 c^2} \sum_{n=1}^\infty \frac{6}{n^4} = \frac{2\pi k_B^4 T^4}{h^3 c^2} \frac{\pi^4}{15} \quad (2.12)$$

$$= \underbrace{\frac{2\pi^5 k_B^4}{15 h^3 c^2}}_{\sigma} T^4 = \sigma T^4 . \quad (2.13)$$

The integration in (2.11) is done by integration by parts. The sum in (2.12) can be evaluated using RIEMANN'S Zeta-function (Kerner and Wahl 2013).

Equation (2.13) is known as the STEFAN-BOLTZMANN-law. It describes the total power a body is emitting per unit area. The constant σ has a numerical value of $\sigma \approx 5.67 \times 10^{-8} \text{ W/m}^2\text{K}^4$ and is known as the STEFAN-BOLTZMANN-constant.

Equation (2.13) is only applicable for a black body. This means a body which is able to absorb all the radiation hitting it. The materials observed in the real-world deviate from the perfect black body. This is considered by introducing the emissivity ϵ which is in the range $0 \leq \epsilon \leq 1$. In other words, the emissivity can be described as the radiation efficiency of the real-world body divided by the radiation efficiency of an ideal black body as described by PLANK'S law.

For the upcoming consideration, it is important to note that these equations are also valid for gases. Furthermore, the emissivity in general depends on the wavelength, which will be indicated by the subscript in ϵ_λ .

To summarize this section, a body in thermal equilibrium emits and absorbs the same energy amount of electromagnetic radiation. The spectral dependency of this absorbance and emittance is described by the PLANK-law ((2.6)). Integration over all angles and wavelength leads to the STEFAN-BOLTZMANN-law (2.13) which gives the total power of the absorbed and emitted radiation in dependency of the temperature.

2.1.2.2. The Earth as a Black Body: Energy Balance and the Greenhouse Effect

In a first approximation, the earth can be assumed to be a black body in thermal equilibrium. Subsequently under this assumption the expected temperature of Earth's surface is calculated.

For this it is necessary to know the power flux density of the Sun at the Earth's orbit around the Sun. This is called the solar constant $S_0 \approx 1360 \text{ W m}^{-2}$. It is determined by e.g. satellite measurement outside of the Earth's atmosphere (Crommelynck et al. 1996; Fröhlich and Lean 2004). It is important that this is not a physical constant like e.g. BOLTZMANN'S constant k_B . The Earth has a cross-section of a disc with the Earth's radius R_E . The radiating surface, however, is a sphere. Thus, the average power flux S per square meter is:

$$S = S_0 \frac{\pi R_E^2}{4\pi R_E^2} = \frac{S_0}{4} \approx 340 \text{ W m}^{-2} . \quad (2.14)$$

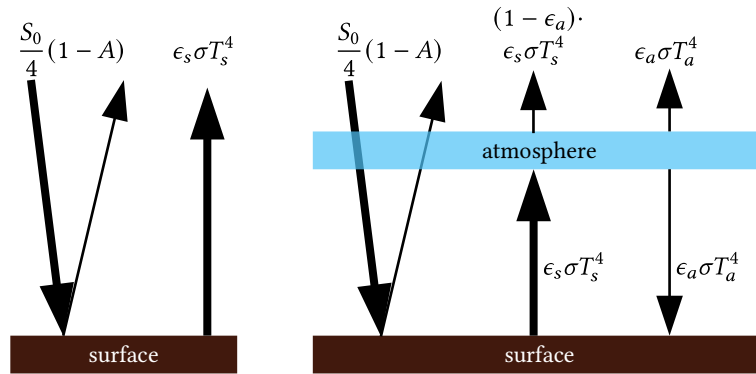


Figure 2.3.: A simplified model of the Earth's energy balance. At the left-hand side panel, no atmosphere is assumed. The incident sunlight is partly reflected and partly absorbed. The amount of the reflected light is described by the albedo A . (the two arrows on the very left). The surface emits the radiation determined by the STEFAN-BOLTZMANN-law with the equilibrium surface temperature T_s .

At the right-hand panel an atmosphere is considered. The atmosphere and the surface both are at their equilibrium temperature T_s and T_a , respectively. The shortwave radiation coming from the sun and reflected at the surface can pass the atmosphere without interaction. The radiation emitted by the surface is partly absorbed by the atmosphere (described by the emissivity ϵ_a), which heats up the atmosphere. The atmosphere emits the same amount of radiation back to space and back to earth.

Not all of the radiation hitting the Earth's surface is absorbed but some of it is reflected back. This is considered by a quantity called the albedo A . It is a measure of the reflectance of the surface and is defined by a value ranging from 0 (no reflection) to 1 (complete reflection). Different surfaces on Earth have different albedos. For example, snow and ice have an albedo close to unity, whereas forests and the ocean have a lower albedo (Efremenko and Kokhanovsky 2021). Averaged over the whole surface, the Earth's albedo is $A \approx 0.3$.

The power of the absorbed and the emitted radiation must be equal: Now, by treating the Earth as a thermal emitter with $A = 0.3$ and $\epsilon_s = 0.95$ the Earth's surface temperature T_s can be calculated because the power of the absorbed and emitted radiation must be equal (Compare with Figure 2.3, left panel):

$$\frac{S_0}{4}(1-A) = \sigma \epsilon_s T_s^4 . \quad (2.15)$$

This results in a surface temperature of $T_s = 258 \text{ K} = -15^\circ \text{C}$. The observed mean surface temperature on Earth, however is 15°C . The reason of the temperature difference is the atmosphere, which was not considered in this model.

In a more advanced model, the atmosphere is considered to be a thermal infrared emitter surrounding the earth as a second layer on top of the surface. See right-hand side in Figure 2.3. Assuming that both the surface and the atmosphere are in thermal equilibrium, they have the temperature T_s and T_a , respectively. The long wave radiation emitted by the sun and reflected by the surface can pass the atmosphere without interaction. The radiation emitted by the surface is partly absorbed by the atmosphere (described by the emissivity ϵ_a) and thus heats up the atmosphere. The atmosphere emits the same amount of radiation back to space as it emits back to Earth. The atmosphere has the equilibrium temperature of T_a , the emissivity of ϵ_a and an albedo of $A = 0$. This model can be described by the two following equations:

$$\epsilon_s \sigma T_s^4 = (1-A) \frac{S_0}{4} + \epsilon_a \sigma T_a^4 \quad (2.16)$$

$$\epsilon_s \sigma T_s^4 = (1-\epsilon_a) \epsilon_s \sigma T_s^4 + 2\epsilon_a \sigma T_a^4 \quad (2.17)$$

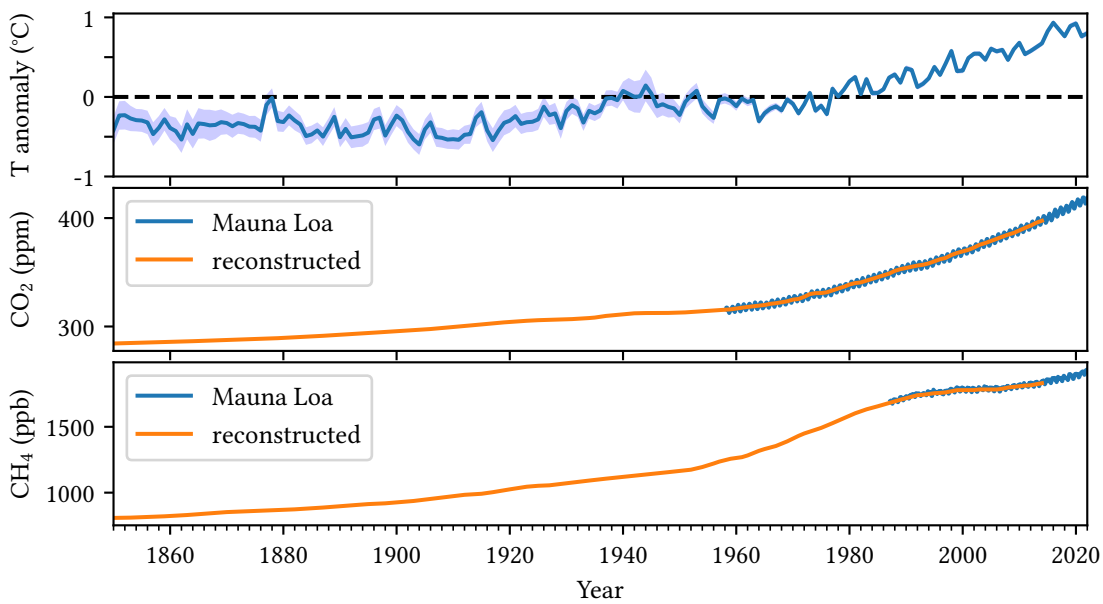


Figure 2.4.: The Earth’s surface anomaly and GHG concentrations from 1850 until now. The top panel shows the temperature anomaly of the average surface temperature on Earth relative to the period 1961 - 1990. The blue shaded area is the 95% confidence interval. The data is taken from (Morice et al. 2021). The middle and lower panel show the dry-air mole fraction of CO_2 and CH_4 . The blue curves are both in situ values measured at the Mauna Loa observatory in Hawaii ((K.W. et al. 2022) and (Lan et al. 2022)). In orange, reconstructed data from several sources are plotted (Meinshausen et al. 2017).

Equation (2.16) describes the condition for thermal equilibrium of the surface. Equation (2.17) describes the condition for thermal equilibrium at the atmosphere. The two equations can be solved for the two unknown values T_a and T_s . Using $\epsilon_a = 0.75$, $\epsilon_s = 0.95$, $A = 0.3$, the obtained surface temperature is $T_s \approx 287 \text{ K} = 13.85^\circ \text{C}$. This is in good agreement with observed temperatures (P. D. Jones et al. 1999).

The effect depicted by the model above is called the greenhouse effect. The shortwave radiation coming from the sun is mostly penetrating the atmosphere. Whereas the long wave radiation emitted by the earth is absorbed into the atmosphere by the so-called greenhouse gases (mostly H_2O , CO_2 , N_2O and CH_4) causing the Earth’s surface temperature to rise. The simple calculation with and without taking the atmosphere into account, shows that life on Earth would not be possible without the warming that can be traced back to the natural greenhouse effect.

2.1.2.3. Climate Change

Since the beginning of the industrial era in the 18th century, the concentrations of GHG in the atmosphere increased significantly due to the burning of fossil fuels. CO_2 incremented from around 280 ppm in 1850 to approximately 420 ppm in 2022 (Meinshausen et al. 2017; K.W. et al. 2022). This is an increase of 50%, which means that the CO_2 concentration is now 150% of the value back in 1850. Similar CH_4 incremented by 137% from 808 ppb in 1850 to 1915 ppb in 2022. This is visualized in Figure 2.4.

The increase of GHGs in the atmosphere causes a warming in the atmosphere due to the greenhouse effect. Since the temperature increase is due to the anthropogenic emission of GHGs this is also called the anthropogenic greenhouse effect. The temperature increase is visualized in

the upper panel in Figure 2.4. The two lower panels show the concentration of CO₂ and CH₄ in the atmosphere. The data labeled with “reconstructed” is taken from Meinshausen et al. 2017 which is reconstructed using historical GHG concentrations including many different sources.

The mechanism of the temperature increase is explained schematically by the model described in Section 2.1.2.2. There, an increase in GHGs is represented by an increase of the emissivity ϵ_a of the atmosphere. This causes a smaller fraction of the long wave radiation emitted by the Earth surface to be transmitted to space and more radiation being reflected back towards the surface.

The Intergovernmental Panel for Climate Change (IPCC) is an intergovernmental, scientific body of the United Nations with the purpose of increasing the scientific knowledge about climate change and its consequences. The changing climate causes a lot of different phenomena, among others rising of the sea level, an increased frequency and strength of extreme weather events and melting polar ice shields (Pörtner et al. 2022). The mechanisms connecting the increase of GHGs, the increase of the global mean temperature and the phenomena described above are very complex and interconnected which each other (Arias et al. 2021). Hence, they are not described in further detail. Further details can be found in Arias et al. 2021.

An important part in fighting and monitoring climate change is to monitor the amount of GHGs in the atmosphere. This thesis will contribute to this attempt by increasing the consistency of remote sensing measurements of CH₄ and CO₂ in the framework of the Total Carbon Columns Observing Network and the Collaborative Carbon Column Observing Network (compare with section 3).

Asides from the direct GHGs, another important gas is CO because of the following reason: CO is a product of the incomplete combustion of fossil fuels, of industrial processes and biomass burning. Hence, it can be used to detect wildfires and also inefficient burning processes of fossil fuels. Furthermore, CO reacts with other gases which represents that it has an indirect influence on the concentration of GHGs in the atmosphere (Daniel and Solomon 1998). The two main reactions are going to be described in the following. The reaction with OH is acting as a sink for CO is (Spivakovsky et al. 2000):



On the other hand, OH reacts with CH₄ and hence it is a major sink for CH₄:



Equation (2.18) leads to an increase in CO₂ and prevents the depletion of CH₄. Hence, CO has an indirect influence on the climate change.

2.2. Molecular Spectroscopy

In order to understand the physical background of the absorption of radiation in the atmosphere, the interaction of molecules with electromagnetic radiation is investigated in this section. The absorption and emission of radiation by molecules must be treated taking into account quantum mechanics. By doing so, it is found that the energy of a quantum mechanical system can only be at discrete levels (Demtröder 2018; Wolf and Haken 2006). By absorbing radiation, the molecule is excited to a higher discrete energy level. The emission of radiation is vice versa the

de-excitation of the molecule to a lower state. Since energy is correlated with frequency, only frequencies matching the difference of two levels can be absorbed or emitted.

The effects shaping the energy levels are described in this section. First, the general principles are derived. For simplicity, only diatomic molecules are considered here. Next, it is briefly explained what needs to be taken into account for polyatomic molecules. Lastly, the line shapes of the spectral lines are discussed. This section is based on Demtröder 2018 and Wolf and Haken 2006.

2.2.1. Diatomic Molecules

Molecules are made of two or more atoms being bound together by different type of bonds: chemical bonds like the covalence bond, the ionic bonds, VAN-DER-WAALS bonds and hydrogen bonds. In this section, only molecules consisting of two atoms are considered for deriving general principles.

In quantum mechanics the state of a molecule is described by the current total energy E_{tot} of the molecule. It can be divided into the energy of the electrons E_{el} , the energy of the rotation of the molecule E_{rot} and the energy of the vibration of the molecule E_{vib} . In an accurate treatment, the energy of the electrons and the rotational and vibrational motion of the atoms are coupled. In good approximation, known as the BORN-OPPENHEIMER-APPROXIMATION, this coupling can be neglected and the energies can be summed up and treated independently:

$$E_{\text{tot}} = E_{\text{el}} + E_{\text{rot}} + E_{\text{vib}}. \quad (2.20)$$

The energies of the vibrational and rotational states are mostly in the infrared (IR)-range of the electromagnetic spectrum (wavelength $\lambda = 1 \text{ mm}$ to $\lambda = 690 \text{ nm}$). For the energies of the electronic excitation there are a few in the IR but most of them in the visible-range ($\lambda = 690 \text{ nm}$ to $\lambda = 380 \text{ nm}$) and the UV-range ($\lambda = 380 \text{ nm}$ to $\lambda = 10 \text{ nm}$) of the light. In this thesis the focus is put on the IR spectrum of the light. Therefore, electronic transitions are not considered further here.

2.2.1.1. Vibrational spectra

Following, the vibrational states of a two atomic molecules are derived. First a harmonic potential of the bond energy is assumed. In a second step, this is extended to a more general description.

Harmonic oscillations In a first approximation, the vibration of the molecules is described by using a harmonic potential, i.e. the restoring force of the molecular bond is proportional to the elongation. For a harmonic oscillator the SCHRÖDINGER equation can be solved analytically. Its energy levels are:

$$E_{\text{vib}} = \hbar\omega \left(\nu + \frac{1}{2} \right) \quad \text{with } \omega = \sqrt{\frac{k}{\mu}}. \quad (2.21)$$

Here, \hbar is the reduced PLANCK constant, $\nu = 0, 1, 2, \dots$ the quantum number numbering the oscillation states and ω the vibration frequency determined by the force constant k and the

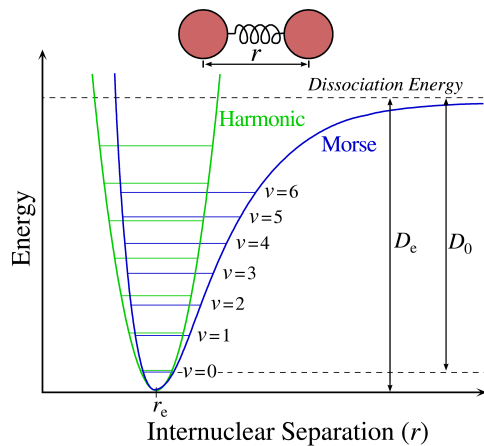


Figure 2.5: Schematic plot of the Morse-potential and the harmonic potential. For low quantum numbers ν ($\nu = 0, 1$) there is a good agreement of the energy levels. For larger quantum numbers, the energy levels of the MORSE-potential are lower compared to the ones of the harmonic oscillator. Furthermore, they are not equidistant anymore. Image is taken from <https://commons.wikimedia.org/w/index.php?curid=660816>, last access 2023-05-11

reduced mass $\mu = \frac{m_1 m_2}{m_1 + m_2}$. The energy difference of two energy levels is $\Delta E = \hbar\omega$. Since the selection rules for the harmonic oscillator are $\Delta\nu = \pm 1$, the vibrational spectra only have a single absorption line at the energy ΔE . To connect the values directly to wavenumbers the symbol $F = \frac{1}{\lambda} = \frac{\nu}{c} = \frac{E}{hc}$ is used:

$$\Delta F_{\text{vib}} = \frac{\hbar\omega}{hc} . \quad (2.22)$$

Anharmonic oscillations For the lower energy state, the harmonic oscillator is a good approximation. For higher energies however, it cannot reproduce energy levels correctly. For example, this theory does not allow a molecule to dissociate which however, is observed in reality. An often-used empirical approximation for a real potential is the so-called MORSE-potential:

$$V_{\text{morse}}(x) = D_e \left[1 - e^{-a(r-r_e)} \right]^2 . \quad (2.23)$$

Here, D_e is the dissociation energy, r the distance between the nuclei, r_e the equilibrium distance and $a = \frac{\hbar\omega}{hc} (\mu/2D_e)^{1/2}$. It is depicted in Figure 2.5 together with the harmonic potential. Solving the SCHRÖDINGER equation with (2.23) provides the energy levels which are in good approximation:

$$E_{\text{vib}} = \hbar\omega \left(\nu + \frac{1}{2} \right) \left[1 - x_e \left(\nu + \frac{1}{2} \right) \right] \quad \text{with } x_e = \frac{\hbar\omega}{4D_e} . \quad (2.24)$$

The first part is equal to the energy levels of the harmonic oscillator. The second part is due to the inharmonicity of the potential. As a consequence, the energy levels are no longer equidistant. Furthermore, the selection rules are extended to be $\Delta\nu = \pm 1, \pm 2, \pm 3, \dots$. However, the probability to excite a transition with $|\Delta\nu| > 1$ however, is small. For the spectrum of the vibrations, this represents not only a single line but more lines which are converging for larger ν and due to the decreasing probability are lower in their intensity.

2.2.1.2. Rotational spectra

Rotation is a further degree of freedom of molecules. Here, the energy states of molecular rotation are derived. First, a rigid rotator is assumed which is extended afterwards to a more realistic non-rigid rotor model.

Rigid rotator In a first approximation, the distance r between the two atoms is assumed to be constant. Using this approximation and a semiclassical approach, it is possible to derive the energy levels of the rotation. The rotational energy in classical mechanics, E_{rot} is:

$$E_{\text{rot}} = \frac{1}{2}I\omega^2 = \frac{\mathbf{L}^2}{2I} , \quad (2.25)$$

with I the moment of inertia, and ω the angular velocity. Using the classical definition of the angular momentum $|\mathbf{L}| = I\omega$ to replace ω the right-hand term in (2.25) is derived. The moment of inertia of a two atomic molecule with distance r_e between the atoms is:

$$I = \mu r^2 . \quad (2.26)$$

Here, $\mu = \frac{m_1 m_2}{m_1 + m_2}$ is the reduced mass. Using the absolute square of the quantum mechanical angular momentum:

$$|\mathbf{L}|^2 = \hbar^2 J(J+1), \quad (2.27)$$

with the quantum number $J = 0, 1, 2, 3, \dots$ and inserting (2.27) in (2.25) gives the energy levels of the rigid rotator:

$$E_{\text{rot}} = \frac{\hbar^2}{2\mu r_e} \cdot J(J+1) . \quad (2.28)$$

The selection rules for J are $\Delta J = \pm 1$. With this, the transition energies hence become:

$$\Delta E_{\text{rot}} = E_{\text{rot}}(J+1) - E_{\text{rot}}(J) = \frac{\hbar^2}{\mu r_e} (J+1) . \quad (2.29)$$

In terms of wavenumbers this can be expressed by:

$$\Delta F_{\text{rot}} = 2B_e(J+1), \quad (2.30)$$

with $B_e = \hbar^2/2\mu r_e^2 hc$ which is known as the rotational constant. This means that the rotational spectrum of diatomic molecules is a series of equidistant lines with a distance of $2B_e$.

Non-rigid rotator In experiments, it was found that the absorption lines of rotational spectra are not equidistant, but their distance is decreasing with increasing quantum number J . This is because the approximation of the rigid rotator neglected the centrifugal force, which results in a widening of the equilibrium distance r_e between the atoms. For taking this into account, it is further assumed that the force of the bond between the atoms is a result of a quadratic potential $\varphi(r) = 1/2 \cdot k \cdot (r - r_e)^2$ with a constant k and the distance r between the atoms. The restoring force of the bond must be equal to the centrifugal force:

$$\mu r \omega^2 = k(r - r_e) . \quad (2.31)$$

With $\omega^2 = \frac{\mathbf{L}^2}{I^2} = \frac{\hbar^2 J(J+1)}{\mu^2 r^4}$ it is possible to write:

$$r - r_e = \frac{\hbar^2 J(J+1)}{\mu k r^3} . \quad (2.32)$$

Here again, the correspondence principle to replace the angular momentum by its quantum mechanical version is used. Consequently, the total energy in the rotation molecule is:

$$E_{\text{rot}} = \frac{\hbar^2}{2\mu r_e} \cdot J(J+1) + \frac{1}{2}k(r - r_e)^2 . \quad (2.33)$$

Since $r \approx r_e$, it is possible to replace r by r_e in (2.32). Inserting this in (2.33) gives:

$$E_{\text{rot}} = \frac{\hbar^2}{2\mu r_e} \cdot J(J+1) - \frac{\hbar^4}{2\mu^2 k r_e^6} J^2(J+1)^2 . \quad (2.34)$$

Expressing it in terms of wavenumbers gives:

$$F_{\text{rot}} = B_2 J(J+1) - D_e J^2(J+1)^2 . \quad (2.35)$$

Here, the so-called distortion constant $D_e = \hbar^4/2\mu^2 k r_e^6 hc$ is introduced. Using the selection rule $\Delta J = \pm 1$ the energy difference between two levels can be calculated by:

$$\Delta F_{\text{rot}} = 2B_e(J+1) - 4D_e(J+1)^3 . \quad (2.36)$$

Compared to the rigid rotator, the energy levels are decreased by the second term.

2.2.1.3. Rovibrational spectra

Through experiments a combination of the vibrational and the rotational spectrum is observed. These are called the rovibrational spectra. Neglecting coupling between the vibrational and the rotational states it is possible to write the energy of the rovibrational states as the sum of both:

$$E_{\text{rovib}} = E_{\text{rot}}(J) + E_{\text{vib}}(\nu) . \quad (2.37)$$

A more detailed description which considers the coupling of both is given in (Demtröder 2018; Wolf and Haken 2006). The energy difference of the vibrational states is significantly larger than for the rotational states. A typical energy level scheme is shown in Figure 2.6. The rotational states with a single dash (J') are added to the vibrational state with $\nu' = 1$. The rotational states with a double dash (J'') are added to the vibrational state with $\nu'' = 0$. In blue, the transitions with $\Delta\nu = +1$ and $\Delta J = -1$ are drawn. These transitions result in the lines of the P-branch. In red, the transitions with $\Delta\nu = +1$ and $\Delta J = +1$ are drawn. These transitions result in the lines from the R-branch. With dashed green, the transitions with $\Delta\nu = 1$ and $\Delta J = 0$ are drawn. These transitions are only allowed for molecules with their angular momentum being parallel to their symmetry axis. If B_e and D_e are equal for both rotational levels of the transition, then the Q-branch is a single line. Otherwise, it consists of several tightly spaced lines.

The intensity distribution within the single branches is mainly determined by the number N_J of the population of the single rotational energy levels. It can be described by using the BOLTZMANN statistics. For simplicity, only the energy levels of the rigid rotator are used:

$$N_J \propto (2J+1)e^{\frac{E_J - E_0}{k_B T}} \propto (2J+1)e^{-\frac{hcB_e J(J+1)}{k_B T}} . \quad (2.38)$$

For small J , the factor $2J+1$ dominates. Hence, the line intensities are increasing. For larger J , the exponential function is dominating and the intensity is decreasing. The maximum between the two states can be calculated by taking the derivative of (2.38):

$$J_{\text{max}} = \sqrt{\frac{k_B T}{2B_e hc}} - \frac{1}{2} . \quad (2.39)$$

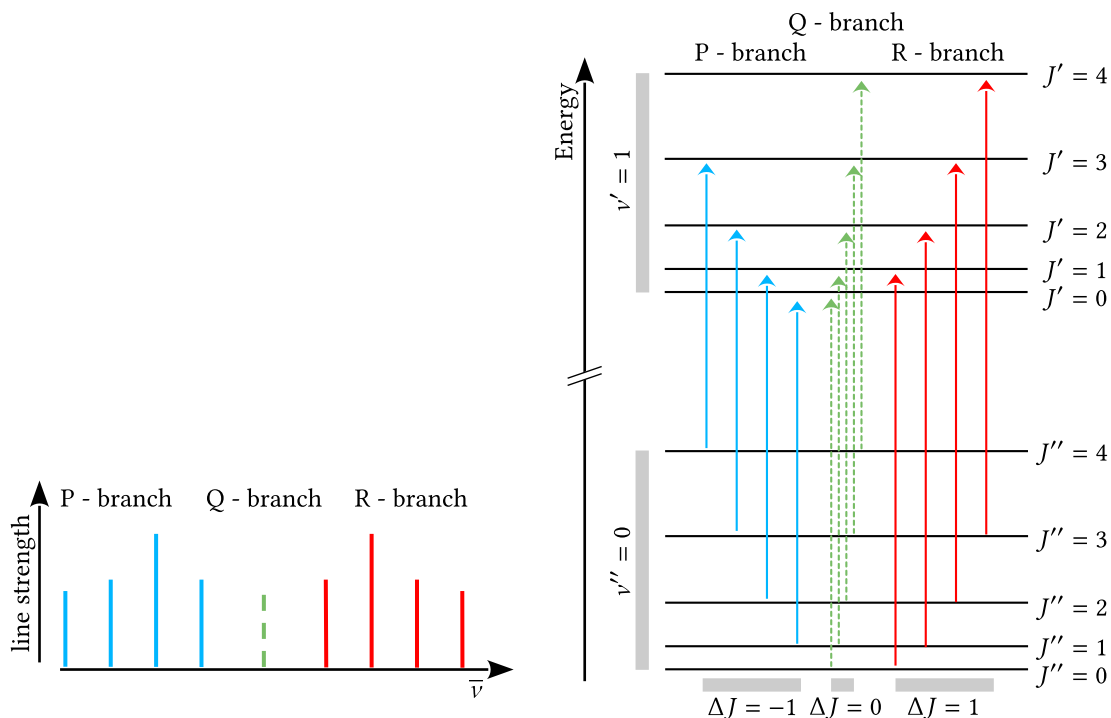


Figure 2.6.: A schematic drawing of a rovibrational spectrum in the left panel and the corresponding level scheme in the right panel. All rotational states with the one and two-dashed J values are split up on top of the energy levels of the vibrational state. In blue, the transitions with $\Delta\nu = +1$ and $\Delta J = -1$ are drawn. These transitions result in the lines of the P-branch. In red, the transitions with $\Delta\nu = +1$ and $\Delta J = +1$ are drawn. These transitions result in the lines from the R-branch. With dashed green, the transitions with $\Delta\nu = 1$ and $\Delta J = 0$ are drawn. These transitions are only allowed for molecules with their angular momentum being parallel to their symmetry axis. If B_e and D_e are equal for both rotational levels of the transition, the Q-branch is only a single line. Otherwise, it consists of several tightly spaced lines. The figure is adapted from (Wolf and Haken 2006).

2.2.2. Polyatomic Molecules

In the section above, only diatomic molecules were discussed. For polyatomic molecules the description is more complex, since more than one vibrational and rotational direction is possible. In general, an N atomic molecule has $3N$ degrees of freedom (DOF). To describe translational movements, 3 dimensions are needed. A non-linear molecule can rotate around three main axes of inertia. Hence, 3 DOFs are needed to describe the rotation. For linear molecules however, only 2 possible rotational modes have to be considered. This is because a rotation around the axis of the molecule is not connected with a rotation of the nuclear skeleton but with the rotation of the electronic shell and is accounted for when considering the electronic movements. Hence, only 2 DOFs are needed for the rotation of linear molecules. This gives $f = 3N - 6/5$ different vibrational modes for linear/non-linear molecules. To describe these different modes, it can become necessary to introduce further quantum numbers.

It is not possible to give a general formulation of the energy levels of polyatomic molecules. Their derivation and even the energy level structure can become quite complex. Therefore, this is not developed further here. For more details see, (Demtröder 2018; Wolf and Haken 2006).

2.2.3. Spectral Line Shapes

In the previous sections for the absorption and emission of spectral lines it was assumed that they are δ -shaped, i.e. they are only emitting and absorbing at a monochromatic frequency. Measured spectra, however, show that the lines have a certain width and shape, the so-called spectral line shape. In the following, three contributions are discussed: The natural line shape, the DOPPLER-broadening and the pressure broadening. These three contributions are explained and subsequently the VOIGT-profile is explained, an approach to combine the described effects.

2.2.3.1. The Natural Line Shape

The natural line shape applies to all observed lines. It is a result of the finite lifetime Δt of the excited states in every system. Due to the energy-time uncertainty relationship of quantum mechanics, the finite lifetime results in an uncertainty ΔE of the energy levels. This causes a Lorentzian line shape. The typical full width at half maximum is in the order of $\delta\nu = 8 \times 10^{-8} \text{ cm}^{-1}$ (see (Hase 2000)). In the field of atmospheric remote sensing, the contributions of pressure and DOPPLER-broadening, are dominant. Hence, the natural Line shape can be neglected.

2.2.3.2. Doppler Broadening

The DOPPLER broadening is induced by thermal motion of molecules in a gas. Since the individual molecules in a gas are moving with different velocities, the sum of the shift induced by each molecule results in a broadening of the absorption lines. Assuming a molecule is moving with the velocity v , the wavenumber $\tilde{\nu}$ of the observed absorption or emission is changed relative to the wavenumber of a molecule in rest $\tilde{\nu}_0$ by (Haken and Wolf 1987):

$$\tilde{\nu} = \tilde{\nu}_0 \left(1 \pm \frac{v}{c} \right) . \quad (2.40)$$

For a gas in thermal equilibrium, the number of molecules n in the interval $[v, v + dv]$, which are moving in the same direction as the radiation wave under consideration, is given by a GAUSSIAN distribution:

$$n(v)dv = N \sqrt{\frac{m}{2\pi k_B T}} \exp \left[-\frac{mv^2}{2k_B T} \right] dv . \quad (2.41)$$

Here, N is the total number of molecules and m their mass. This results in the line shape:

$$P_D(\tilde{\nu}) \propto \exp \left[\frac{mc^2(\tilde{\nu}_0 - \tilde{\nu})^2}{2k_B T \tilde{\nu}_0} \right] . \quad (2.42)$$

The line width $\tilde{\nu}_D$ is defined as the full width at half maximum (FWHM) and is given by:

$$\Delta\tilde{\nu}_D = \tilde{\nu}_0 \sqrt{\frac{8k_B T \ln(2)}{mc^2}} . \quad (2.43)$$

2.2.3.3. Pressure Broadening

Pressure broadening is also known as collision induced broadening, since it originates in the collision of molecules with each other. This results in a shortened lifetime of the excited states. Considering the energy-time uncertainty relation, this leads to an increased line width. The line shape is described by a LORENTZIAN function:

$$P_p(\nu) = \frac{1}{\pi} \frac{\gamma}{\nu^2 + \gamma^2} . \quad (2.44)$$

Here, γ is the scale parameter, describing the half width at half maximum of the function. The values for γ can be estimated by the mean time between two collisions τ_{coll} :

$$\gamma = \frac{1}{2\pi c \tau_{coll}} \quad \text{with} \quad \tau_{coll} \propto \frac{\sqrt{T}}{p} . \quad (2.45)$$

2.2.3.4. The Voigt Profile

For the conditions in the atmosphere the pressure and the DOPPLER broadening are of the same order of magnitude, both effects contribute to the final line shape. This can be modeled by the so-called Voigt profile which is a convolution of the pressure and the DOPPLER broadening:

$$P_V(\tilde{\nu}) = (P_p \otimes P_D)(\tilde{\nu}) = \int_{-\infty}^{\infty} P_p(\tilde{\nu}') P_D(\tilde{\nu} - \tilde{\nu}') d\tilde{\nu}' . \quad (2.46)$$

It is not possible to solve this equation analytically. To solve it numerically in an efficient way, there are several approximations in use, see e.g. (Liu et al. 2001).

2.3. Fourier Transform Infrared Spectroscopy

FTIR spectroscopy is a well established spectroscopic tool in many fields of science. It is used to obtain the infrared spectrum of a probe. It is based on a two-beam interferometer and the FOURIER transformation. In this thesis it is used to measure the concentration of GHG in the atmosphere. First, the FOURIER transformation is introduced. Next, the MICHELSON interferometer is presented and the theory of FTIR spectroscopy is derived. Finally, the most relevant deviations of a real-world spectrometer compared to an ideal spectrometer are described. The content of this chapter is based on (Griffiths et al. 2007; Davis et al. 2001).

2.3.1. The Fourier Transformation

This section gives an introduction to the analytical FOURIER transformation as well as some important theorems. Furthermore, the numerical implementation, including important features of the numerical implementation, are presented.

2.3.1.1. The Continuous Fourier Transformation

The FOURIER transformation is a mathematical tool to decompose a continuous signal $I(x)$ into a spectrum $S(\tilde{\nu})$

The transformation \mathcal{F} and the inverse transformation \mathcal{F}^{-1} are defined as:

$$S(\tilde{\nu}) = \mathcal{F}(I(x))(\tilde{\nu}) = \int_{-\infty}^{\infty} I(x) e^{-i2\pi\tilde{\nu}x} dx , \quad (2.47)$$

$$I(x) = \mathcal{F}^{-1}(S(\tilde{\nu}))(x) = \int_{-\infty}^{\infty} S(\tilde{\nu}) e^{i2\pi\tilde{\nu}x} d\tilde{\nu} . \quad (2.48)$$

In the following, an important characteristic of the FOURIER-transformation is derived. Using EULERS identity the complex exponential can be rewritten as:

$$\begin{aligned} \mathcal{F}(I(x))(\tilde{\nu}) &= \int_{-\infty}^{\infty} I(x) [\cos(2\pi\tilde{\nu}x) - i \sin(2\pi\tilde{\nu}x)] dx \\ &= \int_{-\infty}^{\infty} I(x) \cos(2\pi\tilde{\nu}x) dx - i \int_{-\infty}^{\infty} I(x) \sin(2\pi\tilde{\nu}x) dx . \end{aligned} \quad (2.49)$$

This allows to split the FOURIER transformation into a real and an imaginary part. From this form an important feature can be derived.

If the function $I(x)$ which is to be transformed is an even function (i.e. $I(x) = I(-x)$), the imaginary part in (2.49) becomes zero, because $\sin(2\pi\tilde{\nu}x) \cdot I(x)$ is odd and is integrated over symmetrical limits, which results in 0. In contrast, if $I(x)$ is odd, the integration becomes non-zero. This causes both, the real and the imaginary part in (2.49) to be non-zero. This means, the FOURIER-transform of an even function results in a purely real function.

The Rayleigh Theorem The RAYLEIGH theorem states that the integral from $-\infty$ to ∞ of the absolute square of a function $I(x)$ is equal to the integral of the absolute square from $-\infty$ to ∞ of its FOURIER-transform,

$$\int_{-\infty}^{\infty} |I(x)|^2 dx = \int_{-\infty}^{\infty} |S(\tilde{\nu})|^2 d\tilde{\nu} . \quad (2.50)$$

Zerth Moment Theorem The zeroth moment theorem states that the integral of a function from $-\infty$ to ∞ is equal to the central ordinate of its FOURIER-transform. This can be seen easily when substituting $x = 0$ and $\tilde{\nu} = 0$ in Equations (2.47) and (2.48) which gives,

$$S(0) = \int_{-\infty}^{\infty} I(x) dx \quad (2.51)$$

$$I(0) = \int_{-\infty}^{\infty} S(\tilde{\nu}) d\tilde{\nu} \quad (2.52)$$

2.3.1.2. The Discrete Fourier Transformation

The Equations (2.47) and (2.48) can only be applied to continuous functions. Every measured signal, however, is only available at discrete measurement points. Therefore, a method to apply the FOURIER to discrete functions is needed.

The Nyquist Theorem Before the discrete FOURIER-transformation is given, the NYQUIST-theorem is introduced first, which is very important to consider, when dealing with discrete functions. The NYQUIST-theorem provides a limit to the minimum sampling rate which is necessary to correctly reproduce a continuous signal with frequency $\tilde{\nu}$ at equidistant discrete support points. In a formula it reads:

$$\tilde{\nu}_N = \frac{1}{2\delta x} \Leftrightarrow \delta x = \frac{1}{2\tilde{\nu}_N} . \quad (2.53)$$

This means that all frequencies that are larger than $\frac{1}{2\delta x}$ cannot be sampled correctly by a discrete signal with sampling rate δx . Frequencies larger than this threshold are folded back to the sampled range. This effect is known as aliasing.

The Discrete Fourier Transformation A method to apply a FOURIER transformation to discrete functions is the so-called discrete FOURIER transformation (DFT). Let I be a discrete signal, sampled at an equidistant grid $x_n = x_0 + n\delta x$ with $n = 0, \dots, N - 1$. Hence, there are N sampling points with the distance δx and the total length $L = N \cdot \delta x$. Then, the discrete Fourier transformation and its inverse are given by:

$$\mathcal{F}_{\text{DFT}}(I(\tilde{\nu}_j)) = \frac{1}{\sqrt{N}} \sum_{n=0}^{N-1} I(x_n) \cdot \exp \left[-\frac{2\pi i}{N} nj \right] \quad (2.54)$$

$$\mathcal{F}_{\text{DFT}}^{-1}(S(x_n)) = \frac{1}{\sqrt{N}} \sum_{j=0}^{N-1} S(\tilde{\nu}_j) \cdot \exp \left[\frac{2\pi i}{N} jn \right] \quad (2.55)$$

The spectral grid spacing is given by:

$$\delta\tilde{\nu} = \frac{1}{N\delta x} = \frac{1}{L} \quad (2.56)$$

This means the resolution of the transformed signal does *not* depend on the spacing δx but only on the total sample length L .

An important issue to be considered when implementing a DFT is the following: At $N/2$, the frequency of the $\tilde{\nu}$ grid is equal to the NYQUIST frequency. Hence, the coefficients with an index larger than $N/2$ are wrapped to the negative frequencies. This is illustrated using an example of a 8-point transformation. Let the result of the transformation be $[0, 1, 2, 3, -4, -3, -2, -1]$. To deal with this in practice, often a function called DFTshift is used. It shifts the entries with the index $[N/2, N - 1]$ of an array with index $[0, \dots, N/2, \dots, N - 1]$ in front of the other entries. This results in an array with the entries shifted as follows: $[N/2, N/2 + 1, \dots, N - 1, 0, 1, \dots, N/2 - 1]$.

For the example, this results in an array like $[-4, -3, -2, -1, 0, 1, 2, 3]$.

The Symmetrical Discrete Fourier Transformation In the DFT as given here, the start value x_0 of the sample grid was not considered. This means that the DFT assumes its input function I to start at $x_0 = 0$. Often (also in the case of FTIR-spectroscopy) the input function I is sampled symmetrically around 0. That is, for a signal of length $X = \delta x \cdot N$ and x is in the range $-\frac{X}{2} \leq x < \frac{X}{2}$. To take this into account, the grids have to be shifted as follows:

$$x_n = \left(n - \frac{N}{2} \right) \delta x , \quad (2.57)$$

$$\tilde{\nu}_j = \left(j - \frac{N}{2} \right) \delta\tilde{\nu} . \quad (2.58)$$

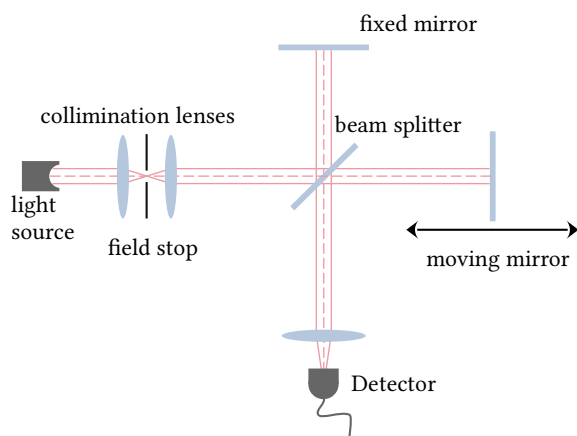


Figure 2.7: A schematic drawing of the Michelson-interferometer. The light may originate in any light source. It is collimated and hits a beam splitter. One of the beams is directed to a fixed mirror and then reflected. The other is reflected at a second mirror whose position can be changed. The reflected beams are recombined at the beam splitter and fall into the detector. There, the intensity in dependency of the position of the mirror, also known as optical path difference, is measured.

Accordingly, in equations (2.54) and (2.55) in the exponential function, n and j have to be replaced by $n - N/2$ and $k - N/2$, respectively. This results in the following equations:

$$\mathcal{F}_{\text{DFT,sym}}(I(\tilde{\nu}_j)) = \frac{1}{\sqrt{N}} \sum_{n=0}^{N-1} I(x_n) \cdot \exp \left[-\frac{2\pi i}{N} nj - i \frac{\pi N}{2} \right] (-1)^n (-1)^j \quad (2.59)$$

$$\mathcal{F}_{\text{DFT,sym}}^{-1}(S(x_n)) = \frac{1}{\sqrt{N}} \sum_{j=0}^{N-1} S(\tilde{\nu}_j) \cdot \exp \left[\frac{2\pi i}{N} nj + i \frac{\pi N}{2} \right] (-1)^n (-1)^j \quad (2.60)$$

This implementation, however, is not very efficient. A fast variation of the DFT implementation is the Fast FOURIER transformation (FFT) implementation by Cooley and Tukey (Cooley and Tukey 1965). In this implementation, it is not possible to introduce the shifted indices. Therefore, there is an alternative method which makes it possible to use the standard implementation. Therefore, the input data and the one of the resulting function are shifted before and after the transformation. For this, the function DFTshift which is introduced above, is used. In addition, the reverse function, iDFTshift is needed which reverses the operation of DFTshift. This allows for a use of standard implementations as follows:

$$\mathcal{F}_{\text{DFT,sym}}(S(\tilde{\nu}_j)) = \text{DFTshift} [\mathcal{F}_{\text{DFT}}(I\{\text{iDFTshift}(x_n)\})] \quad (2.61)$$

$$\mathcal{F}_{\text{DFT,sym}}^{-1}(I(x_n)) = \text{DFTshift} [\mathcal{F}_{\text{DFT}}^{-1}(S\{\text{iDFTshift}(\tilde{\nu}_j)\})] \quad (2.62)$$

2.3.2. The Ideal Michelson-Interferometer

The classical interferometer used for FTIR-spectroscopy is the MICHELSON-interferometer. Its working principle is to split the incident light into two parts using a beam splitter. The principle is depicted in figure 2.7. The two parts of the beams are reflected at mirrors and recombined again before hitting the detector. By moving one of the mirrors by a distance $x/2$ a path difference is introduced which causes variable interference of the two beams at the detector. The distance x is also known as optical path difference (OPD).

In the following, the basic mathematical description of an ideal two beam interferometer is derived. At the detector, the superposition of the two waves, being reflected from mirror 1 and mirror 2 is measured. They are denoted by E_1 , E_2 , respectively. The intensity measured by the detector is a superposition of both signals:

$$I_D \propto |E_1 + E_2|^2 = |E_1|^2 + |E_2|^2 + E_1^* E_2 + E_1 E_2^*. \quad (2.63)$$

Assuming monochromatic waves, E_1 and E_2 can be described by:

$$E_1 = |E_1|e^{i2\pi\tilde{\nu}l+i2\pi c\tilde{\nu}t}, \quad (2.64)$$

$$E_2 = |E_2|e^{i2\pi\tilde{\nu}(l+x)+i2\pi c\tilde{\nu}t} \quad (2.65)$$

here, $\tilde{\nu}$ is the wavenumber $\tilde{\nu} = \frac{1}{\lambda}$, with λ the wavelength, l is the length of the arms of the interferometer and x the path difference which is introduced by moving the second mirror. Hence, the measured intensity as a function of x is stated:

$$I(x) \propto |E_1|^2 + |E_2|^2 + 2|E_1||E_2| \cos(2\pi\tilde{\nu}x). \quad (2.66)$$

Note that the time dependency cancels out when taking the absolute square. In case of a perfect 50:50 beam splitter it is $|E_1| = |E_2| = |E_0|$. With this the equation simplifies to:

$$I(x) \propto 2|E_0|^2(1 + \cos(2\pi\tilde{\nu}x)). \quad (2.67)$$

In a more general case with a polychromatic signal instead of a monochromatic signal, equation (2.67) has to be integrated over all frequencies. Furthermore, $|E_0(\tilde{\nu})|$ now depends on $\tilde{\nu}$:

$$\begin{aligned} I(x) &\propto \int_0^\infty 2|E_0(\tilde{\nu})|^2(1 + \cos(2\pi\tilde{\nu}x))d\tilde{\nu} \\ &= \int_0^\infty 2|E_0(\tilde{\nu})|^2d\tilde{\nu} + \int_0^\infty 2|E_0(\tilde{\nu})|^2 \cos(2\pi\tilde{\nu}x)d\tilde{\nu}. \end{aligned} \quad (2.68)$$

The first part of equation (2.68) becomes constant with respect to the optical path difference x . The second term describes the variation of the intensity in dependency of the path difference. This term is called the interferogram and will be denoted by $I(x)$ in the following:

$$I(x) = \int_0^\infty 2|E_0(\tilde{\nu})|^2 \cos(2\pi\tilde{\nu}x)d\tilde{\nu}. \quad (2.69)$$

Here the proportional factor has been chosen to be unity. The classical Michelson interferometer is the simplest spectrometer which can be used for FTIR spectroscopy. Even though there exist spectrometers for the infrared regime with more complicated beam geometries, they are all based on the introduction of path difference between two parts of a split beam. Hence, Equations (2.67) and (2.69) are valid for them as well.

2.3.3. From Interferograms to Spectra

Equation (2.69) describes an interferogram measured by a FTIR-instrument for a polychromatic signal. The desired term however, is $|E_0(\tilde{\nu})|^2$ which is proportional to the intensity in dependency of the wavelength. In the following, $|E_0(\tilde{\nu})|^2$ will be renamed as $S(\tilde{\nu})$. Let us for now assume $S(\tilde{\nu})$ is known. Since it contains intensities in dependency of the wavenumber it is only defined for $\tilde{\nu} > 0$, since negative wavenumbers are nonphysical. $S(\tilde{\nu})$ is now extended to a new function $\hat{S}(\tilde{\nu})$:

$$\hat{S}(\tilde{\nu}) = \begin{cases} S(\tilde{\nu}) & \tilde{\nu} > 0 \\ 0 & \tilde{\nu} = 0 \\ S(|\tilde{\nu}|) & \tilde{\nu} < 0 \end{cases}. \quad (2.70)$$

Replacing $S(\tilde{\nu})$ with (2.70) in (2.69) and extending the integration limits, yields:

$$I(x) = \frac{1}{2} \int_{-\infty}^{\infty} 2\hat{S}(\tilde{\nu}) \cos(2\pi\tilde{\nu}x) d\tilde{\nu} . \quad (2.71)$$

Because $\cos(\tilde{\nu}x)$ and $\hat{S}(\tilde{\nu})$ are both even, everything in the integral is counted twice. To ensure that this does not change the result, the double count gets annihilated by the multiplication of $1/2$.

In Section 2.3.1.1, it is shown that the FOURIER transform of an even function is purely real. Therefore, it is possible to add a second part that equals to 0:

$$I(x) = \int_{-\infty}^{\infty} \hat{S}(\tilde{\nu}) \cos(2\pi\tilde{\nu}x) d\tilde{\nu} - i \int_{-\infty}^{\infty} \hat{S}(\tilde{\nu}) \sin(2\pi\tilde{\nu}x) d\tilde{\nu} = \int_{-\infty}^{\infty} \hat{S}(\tilde{\nu}) \exp [i2\pi\tilde{\nu}x] d\tilde{\nu} . \quad (2.72)$$

This is exactly the inverse FOURIER transformation as given in (2.47). This shows that the complex FOURIER transformation can be used to convert the measured interferogram $I(x)$ to the spectrum $S(x)$ and vice versa:

$$S(\tilde{\nu}) = \mathcal{F}(I(x))(\tilde{\nu}), \quad (2.73)$$

$$I(x) = \mathcal{F}^{-1}(S(\tilde{\nu}))(x) . \quad (2.74)$$

Since for an ideal instrument the interferogram is an even function, the FOURIER transformation gives a purely real spectrum, containing positive and negative frequencies. The negative frequencies are neglected since they are nonphysical.

Some Examples For getting a better understanding of the transformation between the recorded interferogram and the spectrum, Figure 2.8 gives some examples. The examples in this figure are simulated assuming a perfect instrument. In the left column, the spectra and in the right column, the corresponding interferograms are shown. The units for the optical path difference and the wavenumber domain are not given since in principle they can be chosen arbitrarily.

In the top panel a monochromatic frequency is assumed. This results in a cosine interferogram. This is the simplest case and can be understood directly by Equation 2.69.

In the middle panel two nearby frequencies with the wavenumbers $\tilde{\nu}_1 = 1.5$ and $\tilde{\nu}_2 = 1.8$ are shown. This leads to a beat frequency phenomenon. The envelope has a frequency of $\Delta\tilde{\nu} = \tilde{\nu}_2 - \tilde{\nu}_1 = 0.3$ corresponding to a path difference of 3.33. The carrier frequency is $(\tilde{\nu}_1 + \tilde{\nu}_2)/2 = 1.65$ corresponding to a path difference of $\frac{1}{1.65} \approx 0.606$.

In the lowermost panel, a Lorentzian shaped spectrum is given. The corresponding interferogram is a superposition of a lot of nearby frequencies and an exponential decaying envelope. The high peak at zero path difference (ZPD) is called the center burst. This is a result of the FOURIER transform of the white background. Mathematically speaking, this is because the FOURIER transform of a constant value is the δ -function.

2.3.4. Real World Spectrometers

In the previous sections, idealized spectrometers were assumed. In the real world, however, there are some very important deviations from the perfect spectrometer. Here, some of the most important are summed up. For more details see (Griffiths et al. 2007; Davis et al. 2001).

Real-world interferometers are affected by various error sources. The following gives a short overview of some of the typical issues of a real-world spectrometer.

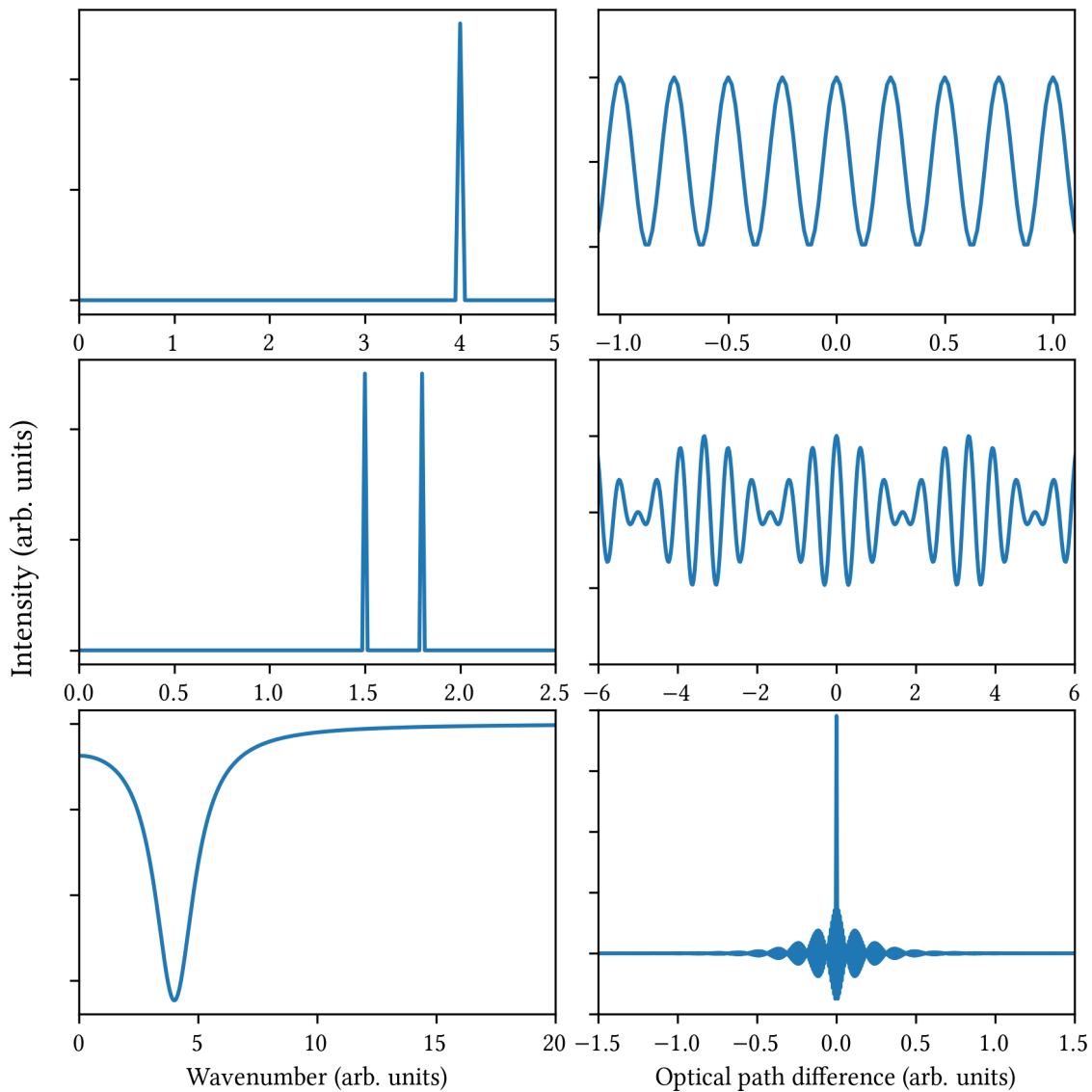


Figure 2.8.: Simulated pairs of spectra (left column) and the corresponding interferograms (right column) for an ideal FTIR interferometer. In the top panels a monochromatic frequency is assumed. In the middle panel two nearby frequencies are assumed. In the last panel a Lorentzian shaped absorption from a white spectrum is assumed. This is the case observed for remote sensing in the atmosphere. There, the interferogram shows the typical center burst which is the result of the FOURIER transform of the unity shaped background.

1. *Finite OPD:* An important limitation is the finite OPD, since it limits the resolution in the spectral domain.
2. *Channeling:* Coarsely described, channeling occurs if an optical element acting as a thin resonator is placed somewhere in the line of sight of the beam, leading to fast oscillations in the spectrum.
3. *Phase Errors:* For the derivation of Equation (2.72) a perfect symmetrical interferogram is assumed. In reality, however, this is not the case which results in a real and a complex part of the spectra. This is a direct consequence of the mathematical properties of the FOURIER described in 2.3.1.1.

4. *Self-Apodization*: The self-apodization is a consequence of the finite field of view (FOV). The FOV is twice the maximum angle from which radiation enters the spectrometer. This causes rays in the spectrometer with an angle up to $\alpha_{\max} = \text{FOV}/2$ off the ray axis. For those rays, the path difference x is then shortened by $x(\alpha_{\max}) = \cos(\alpha_{\max}) \cdot x$. This causes that a real world interferogram for a wavenumber $\tilde{\nu}_0$ is multiplied with a sinc-function:

$$M_{\text{self}}(x) = \text{sinc}(\pi\delta\tilde{\nu}x) \quad \text{with} \quad \delta\tilde{\nu} = \frac{1}{2}\tilde{\nu}_0\alpha_{\max}^2. \quad (2.75)$$

5. *Noise*: Every measured signal is affected by noise. The noise in the spectrum is connected to other properties like the maximal OPD.
6. *Detector Non-linearity*: The dynamical range of a highly resolved interferogram can become quite large which can cause a non-linear response of the used detector element. For a monochromatic line, the interferogram is $I(x) = \cos(2\pi\tilde{\nu}x)$. A non-linear response $\tilde{I}(x)$ of the detector can be described by $\tilde{I}(x) = I(x) + a \cdot I^2(x) + b \cdot I^3(x) + \dots$. Therefore, the interferogram becomes (considering only terms up to the power of three):

$$\tilde{I}(x) = \frac{1}{2}a + \left(1 + \frac{3}{4}b\right) \cos(2\pi\nu x) + \frac{1}{2} \cos(2\pi(2\nu)x) + \frac{1}{4}b \cos(2\pi(3\nu)x). \quad (2.76)$$

This causes artifacts in the spectrum at a wavenumber of zero as well as at wavenumbers twice or three times the incident wavenumber. For more details see Hase 2000.

7. *Sampling Errors*: The interferograms have to be sampled at equidistant points. This is realized by using a HeNe laser which coupled into the actual interferometer. At every zero-crossing of the lasers interferograms a data point is sampled. Sampling error occur when the zero crossing are not defined or detected correctly (e.g. du to a problem in the signal processing of the electronics). This causes the intensity of the true spectral lines to be decreased and the occurrence of spectral artifacts, the so-called “ghosts”. For more details see Messerschmidt et al. 2010.

Item 1, 2, 3 and 5 are explained in more detail in the following.

2.3.4.1. Finite Optical Path Difference

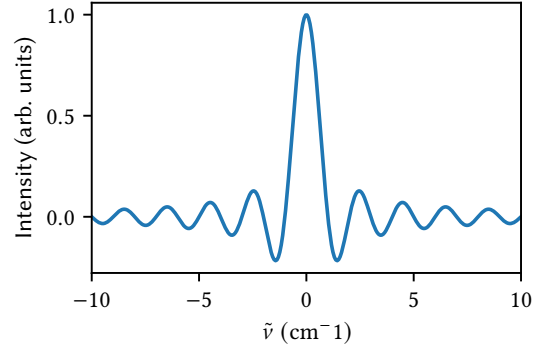
For a real-world spectrometer, the maximum OPD is finite, which is the limiting factor for the resolution in the spectral domain.

First, it is derived using an argumentative way: Let us assume a spectrum consisting of two different frequencies spaced with the distance $\Delta\tilde{\nu}$. As depicted in the middle panel of Figure 2.8, this results in a beating pattern in the interferogram domain. The frequency of the envelope of the pattern is $\tilde{\nu}_{\text{beat}} = 2\pi\Delta\tilde{\nu}$ which means that it repeats after $\frac{1}{\Delta\tilde{\nu}}$ cm in the interferogram domain. Hence, a OPD of at least $\frac{1}{\Delta\tilde{\nu}}$ cm is needed to resolve the whole information in the spectrum. Consequently, for a spectrometer with a maximal OPD of OPD_{\max} , the nearest distance of two frequencies that can be resolved completely, is $\Delta\tilde{\nu} = \frac{1}{\text{OPD}_{\max}}$.

In the following, a more mathematical way is used to describe the finite OPD. It is described by multiplying the interferogram $I(x)$ with a boxcar function $B(x)$, where:

$$B(x) = \begin{cases} 1, & \text{if } -\text{OPD}_{\max} \leq x \leq \text{OPD}_{\max} \\ 0, & \text{else} \end{cases}. \quad (2.77)$$

Figure 2.9: The sinc function. It is the FOURIER transform of the Boxcar function. It is centered symmetrical at $\tilde{\nu} = 0$ and intersects the x -axis at $\tilde{\nu}_0^n = \frac{n}{2\text{OPD}_{\text{max}}}$



The spectrum $S(\tilde{\nu})$ is calculated by the FOURIER transformation:

$$\begin{aligned} S(\tilde{\nu}) &= \int_{-\infty}^{\infty} B(x) \cdot I(x) e^{-2\pi i \tilde{\nu} x} dx \\ &= \int_{-\infty}^{\infty} B(x) e^{-2\pi i \tilde{\nu} x} dx \star \int_{-\infty}^{\infty} I(x) e^{-2\pi i \tilde{\nu} x} dx \\ &= \mathcal{F}(B(x))(\tilde{\nu}) \star \mathcal{F}(I(x))(\tilde{\nu}). \end{aligned} \quad (2.78)$$

For this description the convolution theorem has been used which states that a multiplication of two functions evolves into a convolution after performing a FOURIER transformation. Here, it is depicted using the \star symbol. The FOURIER transform of a boxcar function reads:

$$\begin{aligned} \mathcal{F}(B(x))(\tilde{\nu}) &= 2\text{OPD}_{\text{max}} \cdot \frac{\sin(2\pi \tilde{\nu} \text{OPD}_{\text{max}})}{2\pi \tilde{\nu} \text{OPD}_{\text{max}}} \\ &= 2\text{OPD}_{\text{max}} \cdot \text{sinc}(2\pi \tilde{\nu} \text{OPD}_{\text{max}}). \end{aligned} \quad (2.79)$$

This function is plotted in Figure 2.9. It is centered symmetrical at $\tilde{\nu} = 0$ and intersects the x -axis at $\tilde{\nu}_0^n = \frac{n}{2\text{OPD}_{\text{max}}}$. Assuming a spectrum which is composed of two different frequencies $\tilde{\nu}_1$ and $\tilde{\nu}_2$, the convolution with $\mathcal{F}(B(x))(\tilde{\nu})$ becomes:

$$\begin{aligned} S(\tilde{\nu}) &= \mathcal{F}(B(x))(\tilde{\nu}) \star \mathcal{F}(I(x))(\tilde{\nu}) \\ &= \int_{-\infty}^{\infty} 2\text{OPD}_{\text{max}} \cdot \text{sinc}(2\pi(\tilde{\nu} - \tilde{\nu}')\text{OPD}_{\text{max}}) \cdot (\delta(\tilde{\nu}_1) + \tilde{\nu}_2) d\tilde{\nu}' \\ &= 2\text{OPD}_{\text{max}} \cdot [\text{sinc}(2\pi(\tilde{\nu} - \tilde{\nu}_1)\text{OPD}_{\text{max}}) + \text{sinc}(2\pi(\tilde{\nu} - \tilde{\nu}_2)\text{OPD}_{\text{max}})], \end{aligned} \quad (2.80)$$

where $\delta(\tilde{\nu})$ is the δ -distribution. The result are two sinc-functions with their maxima at $\tilde{\nu}_1$ and $\tilde{\nu}_2$, respectively. Considering the first intersection of x -axis as the width of the sinc functions, they are both fully resolved for a distance of:

$$\Delta\tilde{\nu} = \frac{1}{\text{OPD}_{\text{max}}}. \quad (2.81)$$

This produces the same result as the argumentative way. It is important to note that this formula says that the two peaks are both *fully* resolved. However, in reality the peaks of two sinc functions can still be distinguished when their distance is less than $\frac{1}{\text{OPD}_{\text{max}}}$. Consequently, in reality, the maximum resolution often is given with a number less than one for the nominator, like $\Delta\tilde{\nu} = \frac{0.9}{\text{OPD}_{\text{max}}}$.

2.3.4.2. Channeling

Channeling occurs when an optical element passed by the beam and works as a FABRY-PEROT resonator of low finesse. This causes a fast oscillating modulation in the spectra. The frequency in units of wavenumbers, $\Delta\tilde{\nu}$ of the oscillations can be calculated by:

$$\Delta\tilde{\nu} = \frac{1}{2nd} . \quad (2.82)$$

Here d is the thickness and n the refractive index of the material of the resonator. The effect can be quite small. Hence, it is hard to identify it on measured spectra. However, when using the FTIR-measurements for retrieving atmospheric gases, this can have a large effect on the retrieved concentrations of species with weak absorptions, like XCO. For more details see Frey 2018.

2.3.4.3. Phase Correction

We made in the derivation of Equation (2.72) use of the fact that the general complex FOURIER transformation simplifies into a cosine FOURIER transformation. In reality, however, the interferograms are not symmetric. Reasons for this can be for example, imperfections in measuring the OPD x when sampling the interferogram or a phase introduced by the beam splitter. As a consequence of the non-even interferogram, the spectrum becomes complex. To correct for this asymmetric shape of the interferograms (the phase error) several mechanisms have been developed in the past years (Mertz 1967; Codding and Horlick 1973; L. et al. 1966; Artsang et al. 2018; Mertz 1965).

Here, the method described by MERTZ (Mertz 1965; Mertz 1967) is presented briefly. As a first step, the original interferogram is truncated and FOURIER transformed. Because of the truncation, the resolution of the resulting spectrum is reduced (compare Section 2.3.4.1) giving a smoothed version $S_{\text{lr}}(\tilde{\nu})$ of the original spectrum $S(\tilde{\nu})$. In the next step, this smoothed spectrum is used to calculate a smoothed phase $\theta_{\text{lr}}(\tilde{\nu})$:

$$\theta_{\text{lr}}(\tilde{\nu}) = \arctan \left(\frac{\text{Im}(S_{\text{lr}}(\tilde{\nu}))}{\text{Re}(S_{\text{lr}}(\tilde{\nu}))} \right) . \quad (2.83)$$

The interferogram with the full resolution $S(\tilde{\nu})$ can be written as follows:

$$S(\tilde{\nu}) = |S(\tilde{\nu})| \cdot e^{i\theta(\tilde{\nu})} . \quad (2.84)$$

Here, $|S(\tilde{\nu})|$ is the absolute value of the complex spectrum and $\theta(\tilde{\nu})$ the corresponding phase. The actual phase correction is done by subtracting the smoothed phase of the low-res spectrum θ_{lr} from the phase of the high-res spectrum. Since $\theta(\tilde{\nu}) \neq \theta_{\text{lr}}(\tilde{\nu})$, the quantity after the phase correction is still complex. Hence, the phase corrected spectrum $\hat{S}(\tilde{\nu})$ becomes the real part of this quantity:

$$\begin{aligned} \hat{S}(\tilde{\nu}) &= \text{Re} \left[|S(\tilde{\nu})| \cdot e^{i\theta(\tilde{\nu})} \cdot e^{-i\theta_{\text{lr}}(\tilde{\nu})} \right] \\ &= \text{Re} [S(\tilde{\nu})] \cdot \cos(\theta_{\text{lr}}(\tilde{\nu})) + \text{Im} [S(\tilde{\nu})] \cdot \sin(\theta_{\text{lr}}(\tilde{\nu})) . \end{aligned} \quad (2.85)$$

2.3.4.4. The Instrumental Line Shape

The instrumental line shape (ILS) describes the deviation of a measurement of a real-world instrument compared to a theoretical, ideal instrument. As described in 2.3.4.1 for an instrument with finite resolution, which measures a monochromatic signal, the theoretical δ -peak in the spectrum is convoluted with a sinc-function. This sinc-function is then the ILS of a perfectly aligned instrument with a infinitesimally small field of view.

A real-world spectrometer deviates from the ideal instrument not only in the resolution but also in e.g. the misalignment, non-perfect beam splitter and others. These effects cause the ILS to change from its ideal behavior.

For a correct interpretation of the results, it is necessary to quantify these deviations. In this thesis, the ILS is described by two parameters, the modulation efficiency (ME) and the phase error (PE) as used in Hase et al. 1999 which are explained below.

Modulation Efficiency The modulation efficiency can be described best in the interferogram domain and assuming the cosine pattern of a monochromatic signal. For an ideal instrument, the amplitude of the cosine should be constant for all OPDs x . The ME is the deviation from this ideal behavior. This implies that in general, the ME depends on the OPD.

Phase Error The PE can be explained illustratively in the interferogram domain assuming a monochromatic input signal. In this case, the interferogram is a harmonic function multiplied upon a decreasing envelope due to the self-apodization. For a real-world instrument this harmonic function might be phase shifted in comparison to a theoretical one. This phase shift depends on the OPD and defines the PE.

For the EM27/SUN spectrometer used in this scientific research, both, the ME and the PE are described by a single number. For the ME, it is the amplitude at the maximum optical path difference (OPD_{max}), assuming a amplitude of 1 at zero OPD. All amplitudes between $OPD = 0$ and the OPD_{max} are linearly interpolated. The PE is assumed to be constant for all OPDs

2.3.4.5. Noise Analysis

The following part is mainly taken from Davis et al. 2001. Next, an equation to describe the noise in a spectrum is derived. However, as a starting point, we look at the interferogram $I(x)$ as measured by the detector. The interferogram can be described by the “true”, noise-free signal $I_t(x)$ and a noise ϵ_x ,

$$I(x) = I_t(x) + \epsilon_x . \quad (2.86)$$

Here, it is assumed that the noise ϵ_x is independent of the path difference x . The subscript x indicates the noise in the interferogram domain. The assumption of ϵ_x being independent of x can be justified as several error sources as e.g. noise of the detector or a jitter of one of the mirrors are independent of x . For a detailed justification for this see Davis et al. 2001, page 120. With this, the signal-to-noise ratio (SNR) can be described as:

$$SNR_x = \frac{I(0)}{\epsilon} . \quad (2.87)$$

This definition has the advantage that it is easy to be accessed in experimental data.

To derive a mathematical relationship between the noise in the interferogram domain and in the spectral domain, it is assumed further that noise is white, i.e. it is equally distributed at all frequencies. Let $\epsilon_{\tilde{\nu}}$ be the noise in the spectral domain. The FOURIER-transformation of white noise is also white noise which means that the noise in the spectrum domain does not depend on the wavenumber either. Since ϵ_x is uneven, $\epsilon_{\tilde{\nu}}$ becomes a complex quantity:

$$\epsilon_{\tilde{\nu}} = \epsilon_{\tilde{\nu}}^{\text{Re}} + i\epsilon_{\tilde{\nu}}^{\text{Im}} . \quad (2.88)$$

To connect the two domains the RAYLEIGH-theorem is used:

$$\int_{-\infty}^{\infty} |\epsilon_x|^2 dx = \int_{-\infty}^{\infty} |\epsilon_{\tilde{\nu}}|^2 d\tilde{\nu} \quad (2.89)$$

$$\iff \int_{-\text{OPD}_{\text{max}}}^{\text{OPD}_{\text{max}}} |\epsilon_x|^2 dx = \int_{-\tilde{\nu}_{\text{max}}}^{\tilde{\nu}_{\text{max}}} |\epsilon_{\tilde{\nu}}|^2 d\tilde{\nu} \quad (2.90)$$

$$\iff 2\text{OPD}_{\text{max}} \cdot (\epsilon_x)^2 = 2\tilde{\nu}_{\text{max}} [(\epsilon_{\tilde{\nu}}^{\text{Re}})^2 + (\epsilon_{\tilde{\nu}}^{\text{Im}})^2] . \quad (2.91)$$

As the noise is independent from x and $\tilde{\nu}$ respectively, the integral becomes equal to the difference of its limits. The white noise is equally distributed between the real and imaginary part, i.e. $\epsilon_{\tilde{\nu}}^{\text{Re}} = \epsilon_{\tilde{\nu}}^{\text{Im}}$. With this, it is possible to transform (2.91) to,

$$\epsilon_{\tilde{\nu}}^{\text{Re}} = \sqrt{\frac{\text{OPD}_{\text{max}}}{2\tilde{\nu}_{\text{max}}}} \epsilon_x . \quad (2.92)$$

To enhance readability, the Re superscript will be omitted from here on. With this, the noise of the two domains is connected successfully.

To find a relation between the two signals, Equation (2.52) is used. However, it must be rewritten for discrete functions which gives,

$$I(0) = \sum_{n=0}^{N-1} S(\tilde{\nu}_n) \cdot \delta\tilde{\nu} = \delta\tilde{\nu} \cdot N\bar{S} . \quad (2.93)$$

Here, N is the number of sampling points, $\delta\tilde{\nu}$ the spacing of the wavenumber grid and \bar{S} is the mean of the signal in the spectral domain over all grid-points. According to (2.56) $\delta\tilde{\nu} = 1/(2 \cdot \text{OPD}_{\text{max}})$. Here, we use that the total recording length $L = 2 \cdot \text{OPD}_{\text{max}}$ as OPD_{max} describes the length of only one arm of the double sided interferogram. Similarly, $\tilde{\nu}_{\text{max}} = 1/2 \cdot N \cdot \delta\tilde{\nu}$. The factor $1/2$ is needed because the $\tilde{\nu}$ grid ranges from the negative to the positive. Combining both gives $\tilde{\nu}_{\text{max}} = 1/2 \cdot N \cdot \delta\tilde{\nu} = N/(4 \cdot \text{OPD}_{\text{max}})$.

Inserting this and (2.92) and (2.93) in (2.87) yields,

$$\begin{aligned} \text{SNR}_x &= \frac{I(0)}{\epsilon_x} = \frac{\delta\tilde{\nu} N \bar{S} \sqrt{\text{OPD}_{\text{max}}}}{2\tilde{\nu}_{\text{max}} \epsilon_{\tilde{\nu}}} \\ &= \sqrt{\frac{N}{2}} \cdot \frac{\bar{S}}{\epsilon_{\tilde{\nu}}} . \end{aligned} \quad (2.94)$$

Finally, the SNR in the spectrum in dependency of SNR_x can be calculated by,

$$\text{SNR}_{\tilde{\nu}} = \frac{S(\tilde{\nu})}{\epsilon_{\tilde{\nu}}} = \sqrt{\frac{2}{N}} \frac{S(\tilde{\nu})}{\bar{S}} \cdot \text{SNR}_x . \quad (2.95)$$

Note that $SNR_{\bar{\nu}}$ depends on the wavenumber whereas SNR_x is independent of the path difference.

This shows that for an equal SNR in the interferogram, the SNR in the spectrum decreases with higher resolution. Furthermore, the ratio of the signal strength at a certain wavenumber to the average signal strength over all wavenumbers is crucial for the local SNR.

Note that the derivation of Equation (2.95) assumes that the noise in the interferogram ϵx is independent of the chosen OPD_{\max} . This assumption is only true if scan velocity is maintained regardless of OPD_{\max} . If the scan velocity would be increased to keep the scan duration constant ϵx would increase as well. The evaluation as presented implies that the duration for measuring a spectrum increases proportional to OPD_{\max} .

2.4. Remote Sensing using Fourier Transform Infrared Spectroscopy

In 2.1, 2.2 and 2.3, the Earth's atmosphere, including its composition, the interaction of electromagnetic radiation with the molecules of the atmosphere and the FTIR spectroscopy to measure the spectra of molecules have been introduced. In this section, it will be explained how FTIR spectroscopy can be used to measure the concentration of GHG in the atmosphere using the knowledge of the interaction of electromagnetic radiation with the molecules in the atmosphere. This is called remote sensing because the sensor and the air parcel in which the GHG concentration is to be measured are not co-located.

The main idea of atmospheric remote sensing is laid out subsequently. Radiation which can originate from a various sources of electromagnetic radiation interacts with the atoms and molecules in the target to be measured. The interaction with the target changes the spectral signature of the radiation which finally is measured by a detector. In this thesis solar absorption remote sensing using FTIR spectrometers is applied. In this case, the Sun is used as the source of radiation. On its way to the Earth's surface, the radiation of the Sun is absorbed by various different gases. Hence, the spectrum of the radiation of the Sun hitting the Earth's surface, contains the signature of all the molecules the radiation is interacting with on its way through the atmosphere which is finally measured by a FTIR spectrometer. To retrieve the number of molecules causing the measured signatures, the following steps are performed.

First, the spectrum is measured using an FTIR-spectrometer. Second, a model including the absorption in the atmosphere the characteristics of the measuring instrument is needed. This is the so-called forward model. Finally, the prediction of the forward model is compared to the measured spectrum. The concentration of the gases is retrieved by iteratively minimizing the difference between the model and the measurement.

The whole procedure is complex and a lot of factors have to be considered. In the next two sections two key elements are presented. The first section introduces the transport of radiation through the atmosphere. The second section gives an overview of the inversion theory which serves as the theoretical background for the minimization of residuals.

These sections are based on Rodgers 2000, Efremenko and Kokhanovsky 2021 and Burrows et al. 2011.

2.4.1. Basics of Radiative Transfer

The radiative transport is the most important part of the forward model. The forward model itself is the heart of atmospheric retrieval work. If the forward model performs poorly there is no possibility to obtain satisfying results.

The formula that describes the transport of radiation through the atmosphere is called the radiative transfer equation (RTE). It describes the change of the radiant flux L when it travels the distance dz through the atmosphere. In its general form it reads (Burrows et al. 2011):

$$\begin{aligned} dL(z, \tilde{\nu}, T) = & - [\epsilon_a(z, \tilde{\nu}, T) + \epsilon_s(z, \tilde{\nu}, T)] L(z, \tilde{\nu}, T) dz \\ & + \epsilon_a(z, \tilde{\nu}) \cdot B(\tilde{\nu}, T) \\ & + \epsilon_s(z, \tilde{\nu}) \int_0^{2\pi} \int_0^\pi L(z, \tilde{\nu}, \theta, \varphi) \frac{S(\theta, \varphi)}{4\pi} d\varphi \sin(\theta) d\theta . \end{aligned} \quad (2.96)$$

In the first part of the sum, ϵ_a is the so-called absorption coefficient and ϵ_s the so-called scattering coefficient. They describe the amount of absorbed and scattered radiation, respectively. Hence, these are the losses in the RTE.

In the next part of the sum, $B(\tilde{\nu}, T)$ is the PLANCK-function (2.7). This contributes to the thermal emissions of the gases in the atmosphere.

The last part contributes to the increase of the radiation flux due to the scattering into the line of sight. S is a function which includes a description of the directional characteristics of the scattering, which will not be treated in greater detail. The φ and θ as arguments for the radiant flux L indicates that for scattering the angle of the incoming and outgoing scattered radiation must be considered. In general, the RTE cannot be solved analytically.

For the purpose of solar absorption measurements in the infrared region, the scattering part can be neglected. Furthermore, the thermal radiation can be neglected because of the largely different temperatures of the Sun as background source and the lower temperatures of the atmosphere. This becomes obvious using a short estimate of the different magnitudes: For the Sun, a temperature of approximately 5700 K is assumed. The maximum temperature in the line of sight is estimated with 370 K. At a wavenumber of 7000 cm^{-1} (approximately the center of the spectral range used in this thesis), the relation of a PLANCK-function at 370 K and 5700 K is $1 : 1.367 \times 10^{11}$ (compare with Equation (2.7) and Figure 2.2).

With these simplifications the RTE reduces to:

$$dL(z, \tilde{\nu}, T) = -\epsilon_a(z, \tilde{\nu})L(z, \tilde{\nu}, T)dz . \quad (2.97)$$

This differential equation can be solved to:

$$L(s_2, \tilde{\nu}, T) = L(s_1, \tilde{\nu}, T) \exp \left[- \underbrace{\int_{s_1}^{s_2} \epsilon_a(s, \tilde{\nu}, T) ds}_{\tau(s_1, s_2, \tilde{\nu}, T)} \right] . \quad (2.98)$$

$\tau(s_1, s_2, \tilde{\nu}, T)$ is also known as the optical depth. Equation (2.98) is also known as the LAMBERT-BEER equation. The absorption indices for the different wavelengths and conditions in the atmosphere can be retrieved by using the High-resolution Transmission Molecular Absorption Database (HITRAN) (I. Gordon et al. 2022) which provides line-by-line parameters to model the transmission of light in the atmosphere for various molecular species at different temperatures and pressures.

2.4.2. Basics of Inversion Theory

In general, the inversion theory is a method to retrieve information about quantities which cannot be directly measured. A simple example is an electrical circuit with a single consumer. To measure the resistance R of the consumer, we need to measure the voltage V and the current I . The the measurements can be inverted using the formula $U = R \cdot I$.

Using FTIR spectroscopy, inversion theory is used to retrieve the concentration of trace gases in the atmosphere. In contrast to the simple example above, the atmosphere is much more complex with multiple variables to be determined from a single measurement. In this case, the inversion is often ill-posed. This means that there are several possible solutions. However, to get the correct one, it is necessary to use external constraints. This is explained later in more detail.

To start with, the so-called forward model \mathbf{F} is introduced:

$$\mathbf{y} = \mathbf{F}(\mathbf{x}) + \epsilon_{\mathbf{y}}. \quad (2.99)$$

Here, \mathbf{x} is called the state vector. Its entries describe the state of the atmosphere. This comprises for example the pressure, the temperature and the amount of the trace gases in the atmosphere. \mathbf{y} represents the measurement. In case of solar absorption measurements, this is the interferogram or the spectrum respectively, measured by the spectrometers. $\epsilon_{\mathbf{y}}$ describes the error of the measurement.

The forward model contains a complete description of the whole measurement process. This includes for example the physical processes of absorption in the atmosphere (described by the RTE) and the characteristics of the measurement instrument. However, the spectrum of the solar radiation also has to be considered (**Hase_AceSolarSpectrum_2010**).

To solve such a problem numerically, it is necessary to linearize it:

$$\mathbf{y} \approx \mathbf{F}(\mathbf{x}_0) + \frac{\partial \mathbf{F}(\mathbf{x})}{\partial \mathbf{x}} (\mathbf{x} - \mathbf{x}_0) + \epsilon_{\mathbf{y}} \quad (2.100)$$

$$= \mathbf{F}(\mathbf{x}_0) + \mathbf{K}(\mathbf{x} - \mathbf{x}_0) + \epsilon_{\mathbf{y}}. \quad (2.101)$$

The linearization is only a valid approximation locally around \mathbf{x}_0 . Therefore, the inversion must be performed iteratively. \mathbf{K} is a $m \times n$ matrix which is called the JACOBIAN matrix. The elements are determined by $K_{ij} = \frac{\partial F_i(\mathbf{x})}{\partial x_j}$. In general, $m \neq n$ and hence, \mathbf{K} is not invertible.

For deriving a general method to solve for \mathbf{x} in Equation (2.101), the so called least-square method is used. It assumes that the probability to measure the value \mathbf{y} is described by a GAUSSIAN probability description. For a single entry y_i of the vector \mathbf{y} , it reads:

$$P_i = \frac{1}{\sqrt{2\pi}\sigma_i} \exp \left[-\frac{(y_i - \bar{y}_i)^2}{2\sigma_i^2} \right]. \quad (2.102)$$

Here, \bar{y}_i is the expected value and σ_i the standard deviation. For the complete vector, the probability P is the product over all P_i values (assuming that the y_i are uncorrelated):

$$P = \exp \left[-\frac{1}{2} \sum_{i=1}^n \frac{(y_i - \bar{y}_i)^2}{\sigma_i^2} \right] \prod_{i=1}^n \frac{1}{\sqrt{2\pi}\sigma_i}. \quad (2.103)$$

The idea of the least-squares method is that the most probable solution shall be found. Since the factor of the exponential function does not depend on \mathbf{y} , it is sufficient to minimize the

exponent. For this, the expected value is replaced by the forward model $\mathbf{F}(\mathbf{x})$. This is directly written in matrix-notation:

$$\text{minimal} = (\mathbf{y} - \mathbf{F}(\mathbf{x})) \mathbf{S}_y^{-1} (\mathbf{y} - \mathbf{F}(\mathbf{x}_0)) . \quad (2.104)$$

Here, \mathbf{S}_y^{-1} is the covariance matrix. Its diagonal elements are the variance ($S_{y,ii} = \sigma_i$) and the off-diagonal elements, the covariances ($S_{y,ij} = \sigma_{ij}$). To minimize it, the derivative with respect to \mathbf{x} is calculated and set to zero. After some mathematical transformations, this can be solved for \mathbf{x} :

$$\mathbf{x} = \mathbf{x}_0 + \left(\mathbf{K}^T \mathbf{S}_y^{-1} \mathbf{K} \right)^{-1} \mathbf{K}^T \mathbf{S}_y^{-1} (\mathbf{y} - \mathbf{F}(\mathbf{x})) . \quad (2.105)$$

Note that $\mathbf{K}^T \mathbf{S}_y^{-1} \mathbf{K}$ becomes a square matrix in this case. Due to the linearization in (2.101) this solution is not exact, but has to be iterated several times:

$$\mathbf{x}_{i+1} = \mathbf{x}_i + \left(\mathbf{K}_i^T \mathbf{S}_y^{-1} \mathbf{K}_i \right)^{-1} \mathbf{K}_i^T \mathbf{S}_y^{-1} (\mathbf{y} - \mathbf{F}(\mathbf{x}_i)) . \quad (2.106)$$

Please note that the JACOBIAN matrix \mathbf{K} needs to be calculated for each iteration step. The iterations are finished as soon as the difference $\mathbf{x}_i - \mathbf{x}_{i+1}$ is below an arbitrary threshold.

If this method is used to solve problems which have a strong non-linearity, the approximation in (2.101) can be too coarse. In this case, it can happen, that when going from one to the other iteration step, the solution is bypassed. To avoid this, with increasing number of iterations the step size is reduced. This is known as the LEVENBERG-MARQUARDT method. This method introduces a regularization parameter λ :

$$\mathbf{x}_{i+1} = \mathbf{x}_i + \left(\mathbf{K}_i^T \mathbf{S}_y^{-1} \mathbf{K}_i + \lambda \mathbf{I} \right)^{-1} \mathbf{K}_i^T \mathbf{S}_y^{-1} (\mathbf{y} - \mathbf{F}(\mathbf{x}_i)) . \quad (2.107)$$

Here, \mathbf{I} is the $n \times n$ unity-matrix.

For retrievals of remote sensing problems, Equation (2.107) is not sufficient to get a proper solution. Because the information obtained from the measurements is insufficient, there is an additional source of information needed which provides side constraints. For this, the so called a priori information is used. In case of FTIR based remote sensing, these are height resolved profiles of the trace gases to be retrieved, which are calculated by atmospheric simulations. This results in the following iterative solution:

$$\mathbf{x}_{i+1} = \mathbf{x}_i + \left(\mathbf{K}_i^T \mathbf{S}_y^{-1} \mathbf{K}_i + \gamma \mathbf{B}^T \mathbf{B} \right)^{-1} \left[\mathbf{K}_i^T \mathbf{S}_y^{-1} (\mathbf{y} - \mathbf{F}(\mathbf{x}_i)) + \gamma \mathbf{B}^T \mathbf{B} (\mathbf{x}_a - \mathbf{x}_i) \right] . \quad (2.108)$$

Here, \mathbf{B} usually is the discrete first order derivative operator and γ a regularization parameter. The larger γ , the larger is the influence of the a priori to the measurement.

An important product from the retrieval is the so-called averaging kernel \mathbf{A} :

$$\mathbf{A} = \left(\mathbf{K}^T \mathbf{S}_y^{-1} \mathbf{K} + \gamma \mathbf{B}^T \mathbf{B} \right)^{-1} \mathbf{K}^T \mathbf{S}_y^{-1} \mathbf{K} . \quad (2.109)$$

The columns of \mathbf{A} describe the influence of a change on the retrieved concentration in a certain level. In other words, it provides information about how the column averaged value changes if the concentration at level i is changed. It is important to note that \mathbf{A} depends on the resolution of the measurement instrument.

Chapter 3

Ground-based Remote Sensing Networks for Greenhouse Gases

Within this work, the data collected by two different ground-based remote sensing networks for GHGs are used and compared. The two networks are the Total Carbon Columns Observing Network (TCCON) and the Collaborative Carbon Column Observing Network (COCCON). Both networks are based on sets of FOURIER Transform Infrared (FTIR) spectrometers, while they use different instruments. The TCCON was launched in 2004 with the objective to provide validation data for satellites. The COCCON is based on the EM27/SUN by BRUKER, a low-resolution small and transportable FTIR instrument. Due to its transportability, the instrument can be used either for stationary measurements or for campaign based measurements.

Further on, the TCCON and the COCCON are described in detail.

First, the quantities measured and the subsequent conversion to column-averaged dry-air mole fraction, which is the final product of the networks, are described. Next, a technical description is given, followed by the quality assurance and the calibration methods of the TCCON. At the campus of the KARLSRUHE INSTITUTE OF TECHNOLOGY (KIT), a TCCON site is located. This site is described, and the collected data is presented.

After this, the COCCON is presented. A general overview of the network is given and the retrieval software is introduced. Next, the calibration of the COCCON network is presented.

Finally, a performance analysis of the COCCON compared to the TCCON is described.

3.1. The Total Carbon Column Observing Network (TCCON)

The TCCON is a network of high-resolution FTIR spectrometers around the globe. It was founded 2004 with the first spectrometer located in Park Falls, Wisconsin, USA with the objective to support the validation of the OCO-2 satellite which is operated by the National Aeronautic and Space Administration (NASA).

It senses the most relevant GHGs, such as CO₂, CH₄, N₂O, H₂O, HDO as well as CO. In 2023, there were 28 active TCCON stations around the world, as shown in Figure 3.1.

The data of the network was successfully used for satellite validation (Sha et al. 2021; Hong et al. 2022; Wu et al. 2018; Wunch et al. 2017; Yoshida et al. 2013; Wunch et al. 2011a; Dils et al. 2014; Someya et al. 2023) and other scientific studies like the correlation of the forest temperatures in the Northern Hemisphere and the atmospheric CO₂ concentration (Wunch et al. 2013), the evaluation of the exchange of GHG between the bio- and the atmosphere (Messerschmidt et al.

Figure 3.1: The current status of the TCCON network. In 2023, there were 28 active TCCON stations all over the world. The image is taken from https://tccodata.org/img/tccon_map.jpg, last access 2023-05-11



2013; Tsuruta et al. 2023), studies of the carbon cycle for CO_2 and CH_4 (Deutscher et al. 2014; Sussmann et al. 2012), to derive the Earth's carbon budget (Byrne et al. 2023) or improving spectroscopic models and line lists (Tran et al. 2010; I. E. Gordon et al. 2011).

3.1.1. Measured Quantities

In this section, a short definition of the values measured by both the TCCON and the COCCON is described.

Both remote sensing networks retrieve the total number of molecules of the considered gases in the air column between the instrument and the sun. These so-called total column values of the gases are denoted as VC_{gas} and defined as:

$$VC_{\text{gas}} = \int_{z_s}^{\infty} f_{\text{gas}}(z) \cdot n(z) dz . \quad (3.1)$$

Here, $f_{\text{gas}}(z)$ and is the mole fraction of the gas and $n(z)$ the total number density. The output quantities of the evaluation are the column-averaged dry-air mole fractions (DMF). These are defined as:

$$X_{\text{Gas}} = \frac{VC_{\text{gas}}}{VC_{\text{dry-air}}} . \quad (3.2)$$

Here, $VC_{\text{dry-air}}$ is the total column of all molecules in a dry-air column. Hence, X_{Gas} describes the fraction of the number of molecules of a certain gas relative to the total number of molecules, averaged over the whole air-column. However, the total column of dry-air cannot be measured directly. To calculate the X_{Gas} values, the dry-air mole fraction of O_2 is used, which is known and approximately constant in height:

$$X_{\text{O}_2} = \frac{VC_{\text{O}_2}}{VC_{\text{dry-air}}} \approx 0.2095 . \quad (3.3)$$

Inserting (3.3) in (3.2) gives:

$$X_{\text{Gas}} = \frac{VC_{\text{Gas}}}{VC_{\text{O}_2}} \cdot 0.2095 . \quad (3.4)$$

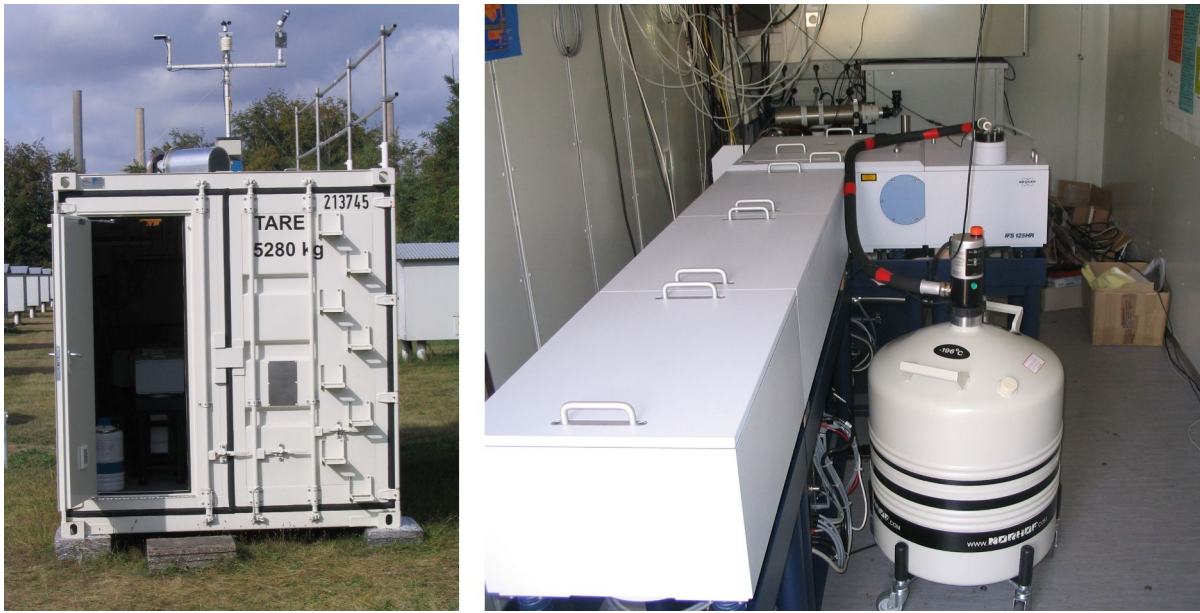


Figure 3.2.: The Karlsruhe IFS125 HR spectrometer (right panel) and the container it is housed in (left panel). As one can see the shipping container is heavy, and a crane is needed to move it. The IFS125 HR is a classical MICHELSON interferometer. Its movable mirror is housed inside the long case at the left-hand side of the right image. The white bottle in the foreground contains liquid nitrogen which is used to cool the Indium Antimonide (InSb) sensor.

This is an easy-to-use formula for calculating the XGas values because VC_{O_2} can be measured directly using FTIR spectroscopy. This formula has the advantage that systematic errors occurring in VC_{O_2} and VC_{gas} are mitigated strongly, which facilitates the experimental calculation. Note, that the latest retrieval software (also used in this work) substitute the constant dry-air mole fraction of O_2 by a variable mole fraction decreasing slowly over time considering the increasing trend in the CO_2 concentrations of approximately 1.99 ppm per year.

3.1.2. Technical Description

The FTIR spectrometers used by the TCCON are the BRUKER 125HR and the upgraded BRUKER 120/5HR instruments. Both instruments are based on a classical MICHELSON interferometer, and both record single sided interferograms. This means that the movable mirror of the interferometer moves only a short distance in one direction but a long distance in the other direction. This design allows to have a large OPD_{max} with a relatively compact physical design. The OPD_{max} used for TCCON is 45 cm resulting in a resolution of approximately 0.02 cm^{-1} (Wunch et al. 2011b).

The instruments are large which is why they are mostly operated in laboratories or, as in Karlsruhe, in a shipping container. In Figure 3.2, the Karlsruhe TCCON spectrometer is shown.

The retrieval software used by the TCCON is called GGG, it is developed and maintained by the CALIFORNIA INSTITUTE OF TECHNOLOGY (Caltech). It comprises the preprocessing software INTERFEROGRAMS TO SPECTRA (I2S) to convert interferograms to spectra, a least-square fitting algorithm called GFIT, a post processing suite which performs airmass independent and airmass dependent corrections, and several helper programs. The latest software version is GGG2020

which was released in 2021, replacing the previous GGG2014.

The GGG2014 suite furthermore contains a program to generate the a prioris for the retrieval. In GGG2020, this was replaced by a centralized program running on a server at Caltech. The reprocessing of the Karlsruhe TCCON data with the latest GGG version is presented in Section 3.1.4.

For the GGG2014 data, the error budget is assumed to be 0.25 % (~ 1 ppm) for XCO_2 , 0.5 % (~ 5 ppb) for XCH_4 and 4 % (~ 4 ppb) for XCO (Wunch et al. 2015).

For GGG2020, there is no official released error budget yet. In a publication released in early 2023 (Mostafavi Pak et al. 2023), the error budget for GGG2020 was given as 0.16 % (~ 0.64 ppm) for XCO_2 , 0.34 % (~ 6.1 ppb) for XCH_4 and 1.4 % (~ 1.4 ppb) for XCO. These numbers in Mostafavi Pak et al. 2023 are based on a private communication with J. Laughner, the deputy chair of the TCCON algorithm board.

According to Laughner 2023, these number were updated in May 2023 to 0.12 % (0.47 ppm) for XCO_2 , 0.22 % (3.90 ppb) for XCH_4 , 1.7 % (1.70 ppb) for XCO. Over the course of this thesis the updated numbers will be used. The absolute concentrations used to convert between an absolute and a relative error are 400 ppm for XCO_2 , 1800 ppb for XCH_4 and 100 ppb for XCO.

As for the error-budget, there is no official estimation of the site-to-site biases, yet. However, a preliminary estimate is obtained from Laughner 2023. This estimate is calculated from the spread of the TCCON versus in-situ airplane profiles. It is important to note that the numbers are preliminary, and are provided with the caveat that they implicitly include uncertainties from the in-situ airplane profiles as well. The biases are 0.20 % (0.81 ppm) for XCO_2 , 0.43 % (7.80 ppb) for XCH_4 and 5.40 % (5.40 ppb) for XCO. These numbers will be used as an official reference. They are in a similar order as the maximal biases found by Mostafavi Pak et al. 2023 which are 0.53 ppm, 4.3 ppb and 6.1 ppb for XCO_2 , XCH_4 and XCO, respectively.

3.1.3. Calibration Procedure and Quality Assurance

In order to use the data of the TCCON as reference data, it is of utmost importance to ensure consistency of data collected by different sites as well as to calibrate the network as a whole to the units realized by the in-situ measurements collected by the World Meteorological Organization (WMO). The relevant methods used by the TCCON to achieve the absolute calibration and for ensuring the site-to-site consistency are described next.

Airplane Overflights/Air Cores To calibrate the network to the WMO scale (B. D. Hall et al. 2021), in-situ measurements are used. These measurements are either collected by airplanes (Wunch et al. 2010; Messerschmidt et al. 2011; Inoue et al. 2016) or by a system called AirCore (Karion et al. 2010; Sha et al. 2020; Mostafavi Pak et al. 2023).

The airplane measurements are taken in-flight during a spiral-like trajectory of the plane carrying the in-situ sensor, near the TCCON site. As a result, height-resolved in-situ measurements are obtained.

The AirCores are sampled by using a long, coiled tube, which is open at one end and closed at the other. When ascending (mostly with the help of a balloon), the tube evacuates due to the reduced pressure at high altitude. When descending again, it is filled with the ambient air. After landing, the collected air is analyzed in the lab. Using the AirCore method, height-resolved profiles of the gas concentrations in the air are obtained as well.

However, both methods also have some disadvantages: The collection of data by airplane overflights is tedious and expensive. Balloon based air-core measurements are less expensive, but, in areas with high air traffic, as it is the case for most of the rural areas, this sampling method is difficult to realize. Furthermore, the height resolution and vertical coverage is limited for both methods. The lowermost part of the measurement has to be extrapolated by using model data or by using tall tower in situ measurements. This problem can increase the uncertainty of the calibration significantly (Messerschmidt et al. 2011).

ILS Monitoring using Cell Measurements A common method to monitor the performance of an FTIR spectrometer is the measurement of the ILS. This method was already implemented by Hase et al. 1999 and was improved later for the TCCON (Hase et al. 2013).

For this purpose, the TCCON uses validated, low-pressure HCl cells. The cells are filled with a known amount of gas. With the measured temperature and the known volume of the gas it is possible to calculate the pressure inside the tube (compare (2.1)) and hence, to simulate the spectrum precisely. The ILS is then determined by comparing the measured and the simulated spectrum and adapting the ILS parameter using a least-squares fit.

An ILS measurement allows checking for instrumental errors like misalignment, problems with the detectors or similar. The gas used for this method only offers a limited spectral range and therefore a limited number of absorption lines. Hence, with this method, issues outside the spectral range may not be detected.

Furthermore, the method offers little sensitivity to errors which are associated with spectrally low-resolved artifacts as generated by non-linearity or associated with spectral ghosts due to periodic sampling errors. In addition, this method cannot detect any errors in the retrieval algorithm, nor is it able to compare the retrieved concentrations of the GHGs.

XAIR as a Measure of Consistency A measure which is used to check for consistency in the retrieval process is an artificial quantity called XAIR or XLUFT (the latter is the naming used in GGG2020). In GGG, it is calculated using the following formula (Wunch et al. 2015):

$$\text{XAIR} = \underbrace{\frac{VC_{\text{air}}}{VC_{\text{O}_2}} \cdot 0.2095}_{\text{XAIR}_{\text{GGG1}}} - \underbrace{XH_2\text{O} \cdot \frac{m_{\text{H}_2\text{O}}}{m_{\text{dry-air}}}}_{\text{XAIR}_{\text{GGG2}}}, \quad (3.5)$$

$$VC_{\text{air}} = \frac{p_s}{\bar{g}} \cdot \frac{m_{\text{dry-air}}}{N_A}. \quad (3.6)$$

Here, VC_{O_2} is the total number of O_2 molecules in the air-column, $XH_2\text{O}$ the column-averaged, dry air mole fraction of H_2O , $m_{\text{H}_2\text{O}}$ and $m_{\text{dry-air}}$ are the mean molar masses of H_2O and dry air, respectively, N_A is AVOGADRO's constant and \bar{g} the column-averaged gravitational constant. The first part in (3.5) compares the total column of dry air ($VC_{\text{dry-air}} = VC_{\text{O}_2}/0.2095$, Equation (3.3)) to the amount of air molecules calculated by using the surface pressure and assuming a hydrostatic balanced atmosphere. The surface pressure however, depends on the amount of water vapor in the atmosphere. This is considered in the second term. The naming of the two parts into $\text{XAIR}_{\text{GGG1/2}}$ is needed for a later comparison with the implementation of XAIR by PROFFAST (see Section 3.2.1).

XAIR is designed to become unity for a perfectly aligned and working spectrometer. Any deviations from unity indicate an error either in the used ground pressure, some misalignment

in the instrument itself or other problems. Common reasons for a XAIR deviation include an out-of-center solar disk on the detector or wrong internal clock settings of the recording computer leading to wrong solar positions in the forward model. Unfortunately, there are also several sources of errors which do not have any impact on XAIR and hence, cannot be detected by this method. This occurs because the calculation considers the spectral range covering the windows of O_2 and H_2O . Issues in other spectral ranges could remain undiscovered. In addition, like the ILS measurement XAIR cannot be used for comparing the final DMF since its values are distributed around unity for all instruments.

3.1.4. The Karlsruhe TCCON Station

The Karlsruhe TCCON-site is located 49.103° North and 8.436° East at 130 masl at the Campus North of the KIT. It operates a BRUKER IFS 125HR spectrometer which is housed in a 20 ft shipping container. The spectrometer in its container is shown in Figure 3.2. The container is air-conditioned to provide a constant ambient temperature. The optical setup differs from the standard TCCON setting, as explained in the following. The spectral range needed to measure the gases of interest of the TCCON is 3800 cm^{-1} to $11\,000\text{ cm}^{-1}$. The majority of the TCCON instruments operates an extended Indium Gallium Arsenide (InGaAs) detector covering a spectral range from 3800 cm^{-1} to about $12\,000\text{ cm}^{-1}$. The Karlsruhe site operates a non-extended InGaAs and an InSb detector in combination with a dichroic filter allowing to measure with both detectors simultaneously. The spectral range from 5250 cm^{-1} to $11\,000\text{ cm}^{-1}$ is covered by the InGaAs detector. The spectral range from 3800 cm^{-1} to 5250 cm^{-1} is covered by the InSb detector (Kiel 2016). This setup allows to simultaneously measure in the mid-infrared (MIR) and near-infrared (NIR) range of the solar spectrum. It is chosen like this to measure the TCCON gases as well as parts of the Network for Detection of Atmospheric Composition Change (NDACC) (Kiel 2016). Furthermore, the Karlsruhe site is the prototype site for the CamTracker system developed by Gisi et al. 2011 which enables very accurate tracking of the Sun.

In this section, the reprocessing of the data using GGG2020 and the subsequent continuous evaluation is described. For the GGG2020 software suite, a PYTHON-wrapper for automating the retrieval was implemented and the complete dataset of the Karlsruhe (KA) TCCON site was reprocessed. The time series of XCO_2 , XCH_4 , XCO and XAIR are plotted in Figure 3.3.

Issues in the Karlsruhe Data During the operation time of the spectrometer, some issues occurred. These are listed in the following and discussed in this section.

1. **Laser Error, (2021-01-01 - 2021-07-01):** In the given date range, the laser used to determine the position of the sledge carrying the movable mirror, was erroneous. This leads to a high noise level. Therefore, the data is flagged manually and is not included in the public data. It is not clear what caused the error. The beam expander, the InGaAs preamplifier of the detector and some integrated circuits on the laser board were changed, which finally solved the problem.
2. **Bad alignment (~2022-03 - 2022-08):** The sun tracker was not aligned properly causing a changing position of the solar disk in the course of the day. This results in a higher noise level than usual.

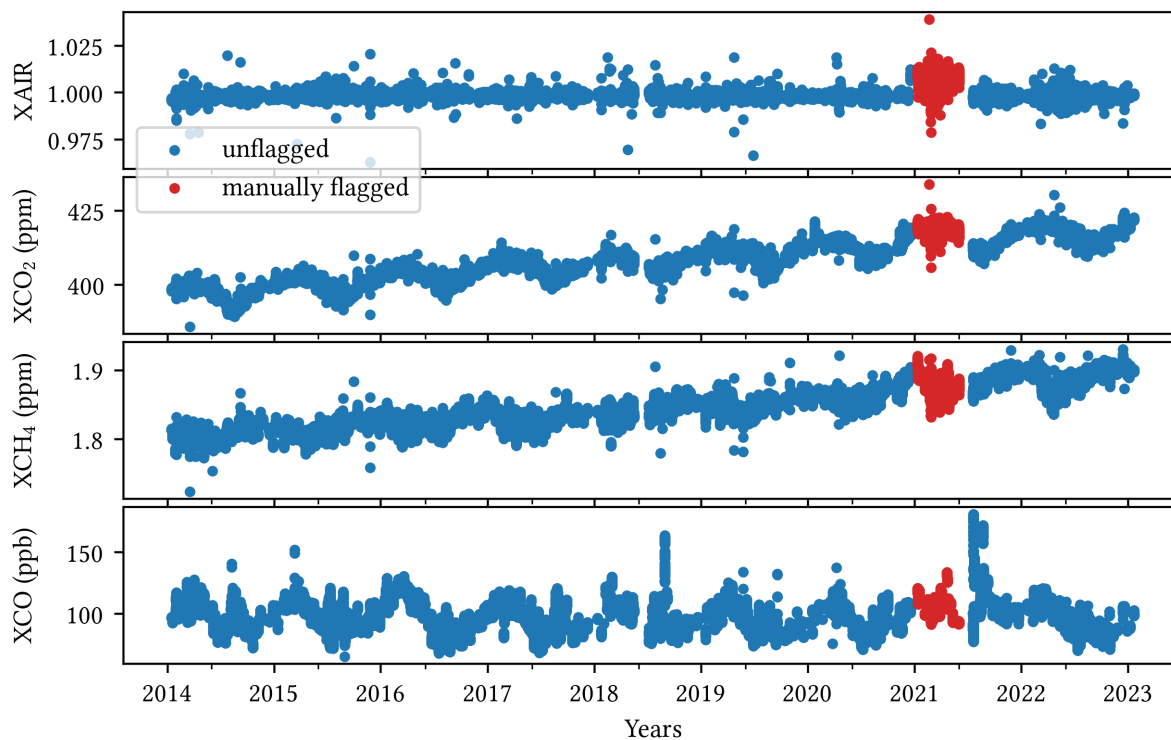


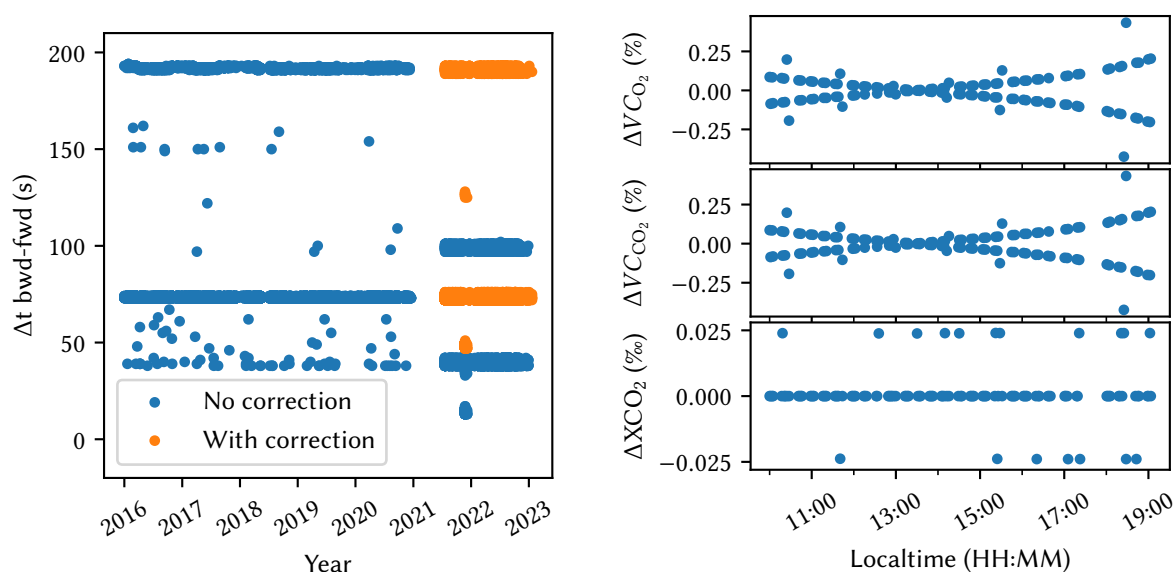
Figure 3.3.: The time series of the TCCON Karlsruhe site. The data in red is flagged manually due to a Laser error. Furthermore, from approximately May 2022 until August 2022, the noise of the data is higher due to a misalignment. Both issues are described in 3.1.4. The data flagged automatically is not shown here.

3. **Laser failure, 2022-09-19:** At the given date, the Laser broke. It was replaced within a day. The new laser also resolved the problem with the out-of-band artifacts mentioned above.
4. **Timing error of the forward and backward measurements (since ~2021-07-01):** The XAIR product shows a bifurcation dependent on the Solar Zenith Angle (SZA). The two branches can be assigned to spectra recorded when the sledge is moving forward (fwd) and backward (bwd), respectively. Presumably, the origin of this is the update of the OPUS software causing a wrong processing of the data in the program I2S which converts the interferograms to spectra. This was resolved using a software-sided correction in the GGG processing. More details on this are given in the following.

The fwd-bwd timing error gives interesting insights into various properties of FTIR spectroscopy. Therefore, it is discussed in more detail in the following paragraphs. The two branches of the bifurcation can be assigned to spectra recorded when the mirror is moving forwards (fwd-spectra) and backwards (bwd-spectra). This is plotted in the two left panels in Figure 3.5.

The reason for this difference is assumed to be an update of the software OPUS by BRUKER which is used to collect the measurements with the instrument: When converting the interferograms to spectra, I2S reads the files produced by OPUS and calculates the measurement time of the fwd and bwd spectra. After the update these values were no longer calculated correctly.

This is illustrated in Figure 3.4a. There, the difference of the calculated timestamp of the fwd and bwd spectra is plotted. The different accumulation of data points at 73 s and 192 s is due to the two different resolutions used in Karlsruhe because the larger the OPD_{max} , the larger the time difference as the mirror moves with constant velocity. The line at ~73 s refers to a



(a) The time difference between fwd and bwd spectra as calculated by i2S over the measurement time. (b) The relative difference of the corrected to the uncorrected data (from the top to the bottom panel) of VC_{O_2} , VC_{CO_2} and XCO_2 at 2022-06-10.

Figure 3.4.: Visualization and assessment of the timing error at the Karlsruhe TCCON site. In (a) the time difference between bwd and fwd spectra as calculated by i2S is plotted. Starting from July 2021, there is an error in calculating the times. This error is corrected resulting in the orange colored data. The reason for the two outliers in late 2021 as well as for the outliers before the correction is unknown. The influence of this error to the different products is plotted in (b) for an exemplary day.

resolution of 0.02 cm^{-1} , the line at $\sim 192 \text{ s}$ to a resolution of 0.0075 cm^{-1} . After the update of OPUS in July 2021, the time difference for a resolution of 0.0075 cm^{-1} is reduced to $\sim 100 \text{ s}$ and for 0.02 cm^{-1} to $\sim 40 \text{ s}$. This issue was fixed by manually adding and subtracting a time offset to the fwd- and bwd-spectra in the GGG processing chain at the stage of the “sunrun” product¹.

The timing error leads to an error of the calculated the solar position in the forward model which in turn distorts the retrieved XGas products. The larger the SZA, the larger the influence on the retrieved values. This is because the change in the airmas is larger with a varying the SZA by ΔSZA , for larger absolute values of the SZA. This influences directly the retrieved vertical columns, as can be seen at the upper two panels in Figure 3.4b. The relative difference of the corrected and the uncorrected data is plotted for the total columns of O_2 and CO_2 . For large SZA, i.e. in the morning and in the late afternoon, this introduces an error of up to $\sim 0.25\%$. It is interesting to see that the influence on the DMF product of CO_2 , which is plotted in the lowermost panel, is rather small with a maximum of 0.025% .

There are two very interesting aspects to this error and its solution. First, it demonstrates the advantage of the way the DMFs are calculated (using Equation (3.2)) which cancels out the error occurring on both the VC_{O_2} and the VC_{CO_2} data almost completely. This becomes clear by comparing the two top panels with the lower panel of Figure 3.4b.

Second, the diagnostic capabilities of XAIR can also be demonstrated nicely. In Figure 3.5, XAIR is plotted in dependency on the SZA. The panels at the left-hand side shows the uncorrected data. On the regular quality control (QC) of the data, the SZA dependency of XAIR is checked. A dependency of XAIR on the SZA occurring there leads to a further investigation. Only by

¹ see <https://tcccon-wiki.caltech.edu/Main/SunRun>, last access 2023-05-30

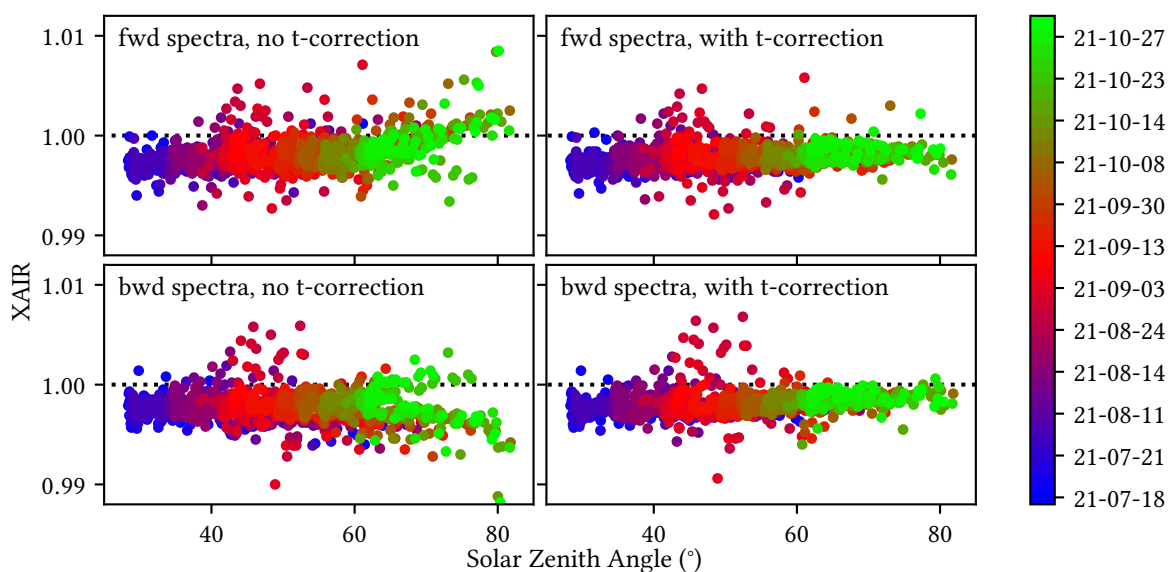


Figure 3.5.: All panels show the SZA dependency of XAIR with and without the time correction. All panels show XAIR plotted over the SZA. The two top panels show the forward-spectra, the two lower panels show the backward-spectra. For the data shown in the left column no correction of the fwd/bwd measurements times is applied, whereas it is applied for the data in the right-hand panels. The correction is able to remove the dependency almost completely.

splitting the forward and backward spectra, different spectral patterns can be observed, enabling the detection of the timing error.

XAIR Analysis As XAIR is a quantity to check the consistency of the data and for a coarse misalignment spectrometer, it will be used in Chapter 5 to check the data of the sites visited with the Travel Standard. In Chapter 5, the KA-TCCON site will be used as a reference. Hence, to have a reference in which range a XAIR value can be considered as “valid” here, the XAIR value of the Karlsruhe site is analyzed. For this, the mean value and the standard-deviation over the whole time period is determined. Flagged data is not taken into account. The result is $\text{XAIR} = 0.99833 \pm 0.00105$.

However, the XAIR values slightly vary from instrument to instrument. Therefore, here the XAIR values of the Sodankylä TCCON site also are evaluated. This site is chosen, as it was extensively tested against an EM27/SUN in the framework of the Fiducial Reference Measurements for Ground-Based Infrared Greenhouse Gas Observations (FRM4GHG) project supported by the European Space Agency (ESA) (Sha et al. 2020) and is also used in Section 3.2.2 as a reference station. For Sodankylä the result is $\text{XAIR} = 1.00120 \pm 0.00138$.

The average of both sites is $\text{XAIR} = 0.99977 \pm 0.00122$. The 1σ interval $\text{mean} \pm 1\sigma$ becomes $[0.999855, 1.00099]$ and the 2σ interval $[0.99733, 1.00221]$.

As one can see, the mean XAIR values of Sodankylä and Karlsruhe are different by 0.0287 which is larger than the calculated standard-deviations. Hence, the calculated intervals are not able to provide a hard limit to classify the XAIR values as “good” or “bad”, but are rather intended to provide a rough indication which values can be expected by a correctly operating spectrometer.

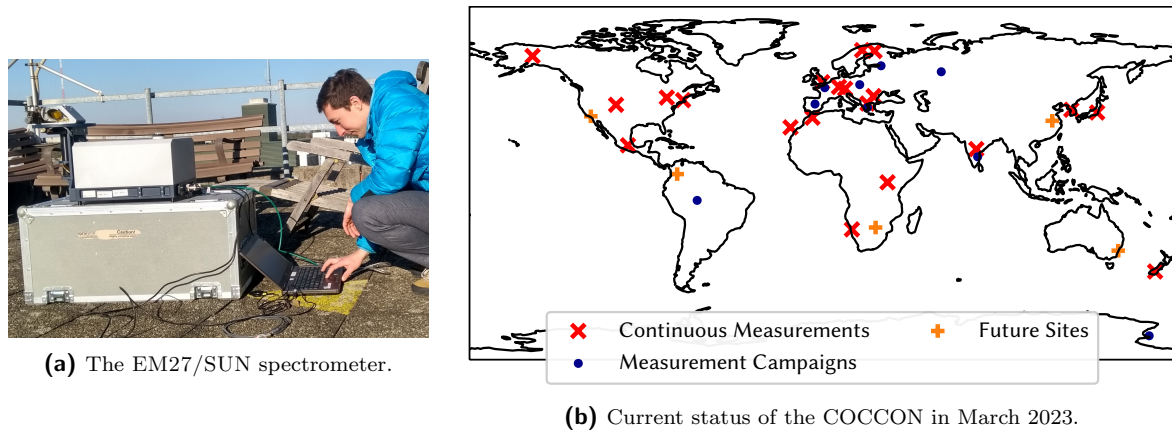


Figure 3.6.: In (a) a photograph of the EM27/SUN is shown. It is small and light enough to be carried by one person. In (b) the current status of active and continuous FTIR measurements using the EM27/SUN spectrometer as well as campaign measurements are shown.

3.2. The Collaborative Carbon Column Observing Network (COCCON)

The COCCON is a network for measuring GHGs using FTIR spectroscopy based on the BRUKER EM27/SUN spectrometer. The measured values (VC_{gas} converted to X_{Gas} using VC_{CO_2}) by this network are the same as described in 3.1.1 for the TCCON. The EM27/SUN is a small, portable, low-resolution FTIR spectrometer, which was developed by the KIT in cooperation with BRUKER starting in 2011 (Gisi et al. 2012). In 2014, it became commercially available. This leads to a strong increase in the number of spectrometers and a large dissemination worldwide. In 2015, a second measurement channel was added covering the spectral range as used by the Tropospheric Monitoring Instrument (TROPOMI) (Hase et al. 2016).

The EM27/SUN spectrometer features a compact design with a total weight of 30 kg, allowing for its handling by a single person (see Figure 3.6a). Furthermore, it is simple to use because it only needs a power supply and a laptop for controlling the instrument and reading the data. Due to its low power consumption (approx. 50 W), it can even be battery powered, enabling mobile operation during field campaigns.

Studies proved the long-term and ensemble stability of the EM27/SUN (Frey et al. 2019; Alberti et al. 2022a). As a measure of the stability, the given studies use the ILS of each spectrometer and the comparison of the X_{Gas} values. Combined with its high flexibility, the EM27/SUN allowed to perform several urban measurement campaigns to be conducted all over the world during the last decade (Tu et al. 2022b; Alberti et al. 2022b; Hase et al. 2015). In addition to city campaigns, also permanent monitoring stations are currently established in large cities (Dietrich et al. 2021) using several EM27/SUN spectrometers distributed around the city to derive GHG emissions. Moreover, installations on mobile platforms such as ships (Klappenbach et al. 2015; Butz et al. 2022; Knapp et al. 2021; Butz et al. 2017) or trucks (Luther et al. 2019; Butz et al. 2017) have been successfully demonstrated.

In addition, several sites collecting continuous measurements are established worldwide to provide reference data for satellite validation. A graphical summary of all COCCON activities is given in Figure 3.6b).

The high instrument stability allows for meaningful side-by-side comparisons of the EM27/SUN spectrometers. This allows to quantify residual instrument specific imperfection in the framework of campaign deployments (compare with Section 4.2).

The COCCON takes advantage of the stability of the EM27/SUN by performing a side-by-side characterization of the individual spectrometers at KIT including ILS measurements. In this way, all spectrometers used for COCCON are calibrated with respect to a common reference (Alberti et al. 2022a; Frey et al. 2015; Frey et al. 2019).

Due to their high stability and mobility several EM27/SUN were also used for the comparison of subsets of TCCON sites (Mostafavi Pak et al. 2023; Hedelius et al. 2016). In the framework of this thesis, it is also aimed at comparing subsets of TCCON sites. However, a systematic worldwide approach is used as in contrast to the previous studies.

The standard retrieval algorithm used within the COCCON is the PROFFAST² retrieval algorithm. In 2022, PROFFAST version 2 was developed by Hase, F.

In the framework of this thesis, a novel interface, called the PROFFASTPYLOT, for the existing PROFFAST2 package was developed by the author in collaboration with Feld, L. (Feld et al. 2023b). The PYLOT is easy to use and hence, allows for easy data processing for any researcher involved in the COCCON. PROFFAST and its interface are discussed in Section 3.2.1.

To tie the COCCON as a whole to the WMO scale (B. D. Hall et al. 2021), the PROFFAST software is calibrated in a way that its XGas result matches with the Karlsruhe TCCON site. The TCCON is calibrated to the WMO scale by an airplane overpass as explained in Section 3.1.3 (Messerschmidt et al. 2011). The calibration of the COCCON as a whole to the TCCON is presented in Section 3.2.2.

3.2.1. The PROFFAST Retrieval Software and the PROFFASTpylot Interface

In this section the PROFFAST retrieval software and the PROFFASTPYLOT (in the following abbreviated as PYLOT) are introduced. The processing chain is depicted in Figure 3.7. The steps inside the blue-shaded area refer to the PROFFAST algorithm. Steps in the orange-shaded area belong to the PYLOT. PROFFAST contains three different programs: PREPROCESS, PCXS and INVERS. The PREPROCESS-program is used to convert the interferograms to spectra. Here, the paths of the interferograms has to be added to the “PREPROCESS input file”, which is indicated by the dashed line.

The atmospheric simulation, which is part of the forward-model, is generated by PCXS. The path of the a prioris must be added to the “PCXS configuration file”, again indicated by the dashed line. The last step is the actual retrieval performed by “INVERS”. In the “INVERS configuration file”, the path to the spectra and the atmospheric simulation data must be given. Furthermore, the ground pressure at the site must be included. For each day, several output files are generated by INVERS.

² <https://www.imk-asf.kit.edu/english/3225.php>, last access 2023-05-31

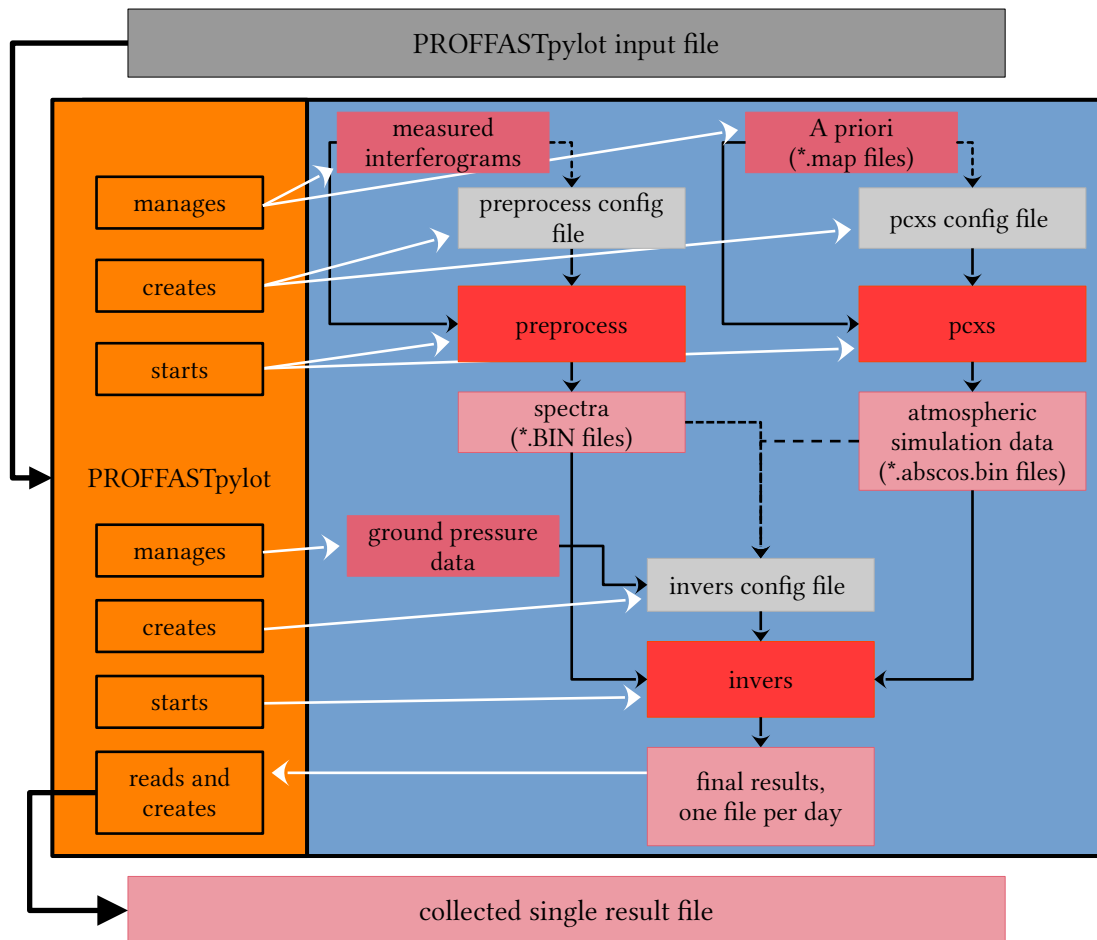


Figure 3.7.: Processing chain of PROFFAST (blue area) including the PROFFASTpylot (orange area and white arrows). Input files are drawn in gray colors, data files with external data are drawn in red, data files produced by PROFFAST are drawn in pink. Solid black arrows indicate that the files are read in by a program. Dashed black arrows mean that only information about the files (e.g. the path or the filename) are read. The PROFFASTPYLOT provides an easy-to-use interface for the processing chain. It manages the external data, creates the input files and calls and monitors the programs of PROFFAST. The functions of the PROFFASTPYLOT are indicated by the white arrows. All necessary settings for the PROFFASTPYLOT are given by a single input file (PROFFASTPYLOT input file). The daily results generated by INVERS are collected by the PROFFASTPYLOT to a single result file.

PROFFASTpylot The PYLOT was developed by the author of this thesis as an interface to simplify the usability of the PROFFAST software. It takes care of managing all the files, creates the input files, and starts and monitors the programs of PROFFAST. It also collects the final results of each day and combines them into a single results file. The settings of the PYLOT are given in a single input file. As a result, instead of running several programs one after another and creating the necessary input files manually, the PYLOT provides a user-friendly program that further automates the data evaluation. The simple usage allows for efficient big-data processing and therefore is an important contribution to the COCCON community and a future up-scaling of the network. Currently, it is used by research groups worldwide as the standard tool for data processing with PROFFAST.

The PYLOT is licensed under GPLv3 and hosted on a GITLAB server: <https://gitlab.eudat.eu/cocon-kit/proffastpylot>.

XAIR definition An important difference of the PROFFAST software compared to the GGG software is the definition of XAIR. This is important to know for the correct interpretation and comparison of the data processed with GGG and PROFFAST:

$$\text{XAIR}_{\text{PROFFAST}} = \frac{VC_{\text{O}_2}}{0.2095} \cdot \frac{\bar{g} \cdot m_{\text{dry-air}}}{N_A \cdot p_s} + VC_{\text{H}_2\text{O}} \cdot \frac{m_{\text{H}_2\text{O}} \cdot \bar{g}}{N_A \cdot p_s} . \quad (3.7)$$

Here, VC_{O_2} and $VC_{\text{H}_2\text{O}}$ are the total column values of O_2 and H_2O molecules, respectively. $m_{\text{H}_2\text{O}}$ and $m_{\text{dry-air}}$ are the mean molar masses of H_2O and dry air, respectively, N_A is AVOGADRO's constant and \bar{g} is the column-averaged gravitational constant. Using the abbreviation $\text{XAIR}_{\text{GGG1}}$ and $\text{XAIR}_{\text{GGG2}}$ defined in Equation (3.5) and Equation (3.6), it is possible to rewrite Equation (3.7) as:

$$\text{XAIR}_{\text{PROFFAST}}' = \frac{1}{\text{XAIR}_{\text{GGG1}}} + \text{XAIR}_{\text{GGG2}} \frac{1}{0.2095 \cdot VC_{\text{air}}} . \quad (3.8)$$

As the first part of the equation is dominant, the inverse values of GGG or PROFFAST must be considered when comparing the results.

3.2.2. Calibration of PROFFAST2 to the TCCON Scale

In this section, the calibration of the PROFFAST2 gas products code to the TCCON scale is presented. The TCCON network is chosen to serve as a reference because it is tied to the WMO scale by airplane overflights (Wunch et al. 2010; Messerschmidt et al. 2011; Inoue et al. 2016) or by ballon based air-core measurements (Karion et al. 2010; Sha et al. 2020; Mostafavi Pak et al. 2023). The calibration of FTIR based remote-sensing measurements usually consists of two different correction types. The first type are the so called Airmass Independent Correction Factor (AICF) and the second type the Airmass Dependend Correction Factor (ADCF). The ADCFs correct for errors emerging from different airmasses and hence, depend on the SZA. The AICFs are used to correct for a constant bias in the data. In 2022, a first, preliminary version of the calibration was published together with the PYLOT using the tag 1.1 in GITLAB³. They are denoted as the “old” calibration factors in the following.

For the PROFFAST2 calibration, a third type of correction factor is introduced. The comparison of the XGas values of the COCCON and the TCCON XGas shows a deviation in dependence of the water vapor concentration in the atmosphere. To correct for this, a XH_2O correction is introduced. This is explained in more detail in Section 3.2.2.1.

For the calibration, data measured by three different instruments (SN037, SN039 and SN122) is used. The instrument SN037 is measuring continuously in Karlsruhe and serves as the COCCON reference device. The data recorded in the time period of 2018 to 2022 is used for the calibration.

The instruments SN039 and SN122 measured data in Sodankylä, Finland and hence are compared to the Sodankylä TCCON site. This site is chosen as it was extensively compared against an EM27/SUN in the framework of the FRM4GHG project funded by ESA (Sha et al. 2020). For the SN039 instrument, the data recorded in the 2017 and 2018 is used and for the SN122 instrument the data recorded from the beginning of 2020 until end of March 2021 is used.

³ https://gitlab.eudat.eu/coccon-kit/proffastpylot/-/tree/v1.1?ref_type=tags

The “new” calibration factors are given in the following. They are released together with version 1.2 of the PROFFASTPYLOT⁴.

3.2.2.1. Airmass Dependent Correction Factors

The ADCFs are necessary since for larger airmasses (which occur at larger SZA, i.e. in the morning and the evening) spectroscopic inaccuracies introduce errors to the measurements. As a result, measurements taken during a day with large SZA values at the beginning and at the end of the day typically have a parabolic shape.

To calculate the ADCF it is necessary to isolate this effect within the data. For this, it is assumed that the SZA dependency is low in an interval of $20^\circ \leq 50^\circ$. Therefore, for each day, the data points of each species are divided by the average of the species measured in the SZA interval from 20° to 50° . The resulting data for the instrument SN037 (the COCCON reference), is plotted in Figure 3.8 in the dependency of the SZA. In blue, the data processed without SZA corrections are shown. The data in orange are processed using the final correction factors as released with version 1.2 of the PROFFASTPYLOT (Feld et al. 2023a). A strong airmass dependency results in a deviation of the gas contents from unity for larger SZA. To correct for the airmass dependency, the *total column* (and not the XGas products as one might expect) values of each gas VC_{Gas} are corrected by the function $c(x)$:

$$c(x) = \frac{1 + \text{ADCF}_1 \cdot x^4 + \text{ADCF}_2 \cdot x^{12} + \text{ADCF}_3 \cdot x^{24}}{1 + \text{ADCF}_1 \cdot x_{\text{ref}}^4 + \text{ADCF}_2 \cdot x_{\text{ref}}^{12} + \text{ADCF}_3 \cdot x_{\text{ref}}^{24}}. \quad (3.9)$$

Here, $x = 0.63661977 \cdot \text{SZA}$ with the SZA in radiant and $x_{\text{ref}} = 0.66666666$. The value of x_{ref} is the angle where the correction polynomial equals to unity. In degrees, the value of x_{ref} corresponds to 38.20° . The factor $2/\pi$ used to calculate x from the SZA is chosen in a way that x becomes unity at $\text{SZA} = 90^\circ$. Hence, due to Equation 3.2 all XGas values are influenced by the ADCFs of the gas itself as well as of XAIR.

As a measure of the airmass dependency a quadratic function $f(sza) = 1 + a \cdot sza^2$ is fitted to the data. The closer the fit parameter a , the better the correction.

The ADCF are determined using an iterative approach taking into account the results of all three instruments. The resulting ADCFs are summed up in Table 3.1.

The ADCF₃ implements a strong correction for large SZA. Since the airmass dependency of a single species is not this strong, ADCF₃ is not used. However, it is implemented already for a potential future use case. The reason why for some gases (e.g. XCH₄) there is still a residual airmass dependency is that the ADCFs are determined in a way that the average performance of the three different instruments is optimal. Therefore, the airmass dependency for the instrument SN39 shown here, still has a low bias for some gases, whereas the airmass dependency of the other instruments show a small high bias. Hence, considering the instrument ensemble, the average of the correction is satisfactory. (Compare with Figures B.1 and B.2).

⁴ https://gitlab.eudat.eu/coccon-kit/proffastpylot/-/tree/v1.2?ref_type=tags

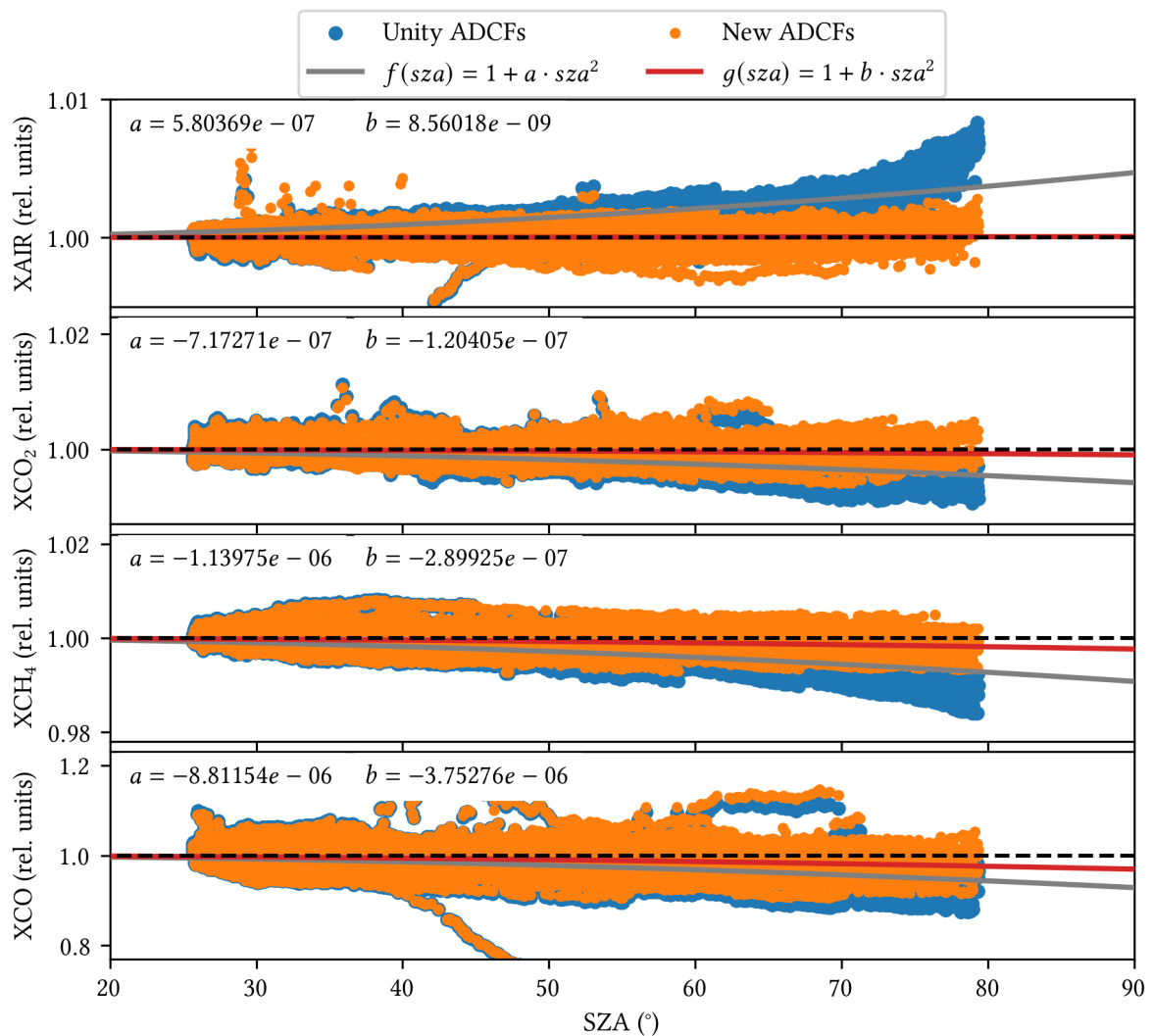


Figure 3.8.: A comparison of the the airmass dependency of XGas values retrieved by PROFFAST2 with unity and the “new” ADCFs. The data plotted here, is calculated by dividing the data of each day by an average of that day. For the calculation of the average only data in a SZA interval from 20° to 50° is used. The data in blue is retrieved using unity correction factors. By an iterative procedure the ADCFs are determined so to minimize the airmass dependency (i.e. the bending of the data). This results in the data in orange. As a measure of the airmass dependency, a quadratic function $f/g(sza) = 1 + a/b \cdot sza^2$ is fitted to the uncorrected data and the data processed using the final ADCFs, respectively. The reason for the data in orange not being aligned perfectly is, that the ADCFs are chosen such that the overall data measured by three different instruments (SN037, SN039 and SN122) is optimized. The plots of the other instruments can be found in the appendix.

3.2.2.2. Airmass Independent Correction Factors

To determine the AICFs, the time series recorded by the three EM27/SUN are compared with the time series of the TCCON sites in Karlsruhe and Sodankylä. For this, the time series of the XGas values are binned into intervals of $l = 10$ min. The temporally corresponding bins of the time series are compared by dividing values of the TCCON spectrometer by the values of the EM27/SUN spectrometer. The average of the quotient over all bins gives the AICF of an instrument. The approach is described in detail in Section 4.2.1.

For the instruments SN39 and SN122, bias correction factors to align them with the COCCON reference (SN37) instrument are applied before deriving the AICFs. For both instruments, the bias correction factors are determined by side-by-side measurements with the reference SN037 in Karlsruhe in 2015-04-14 and 2015-04-15 for the SN39 device and in 2019-11-24 and 2019-11-30 for the SN122 device. The data is processed using PROFFAST2 with the calibration published with the PYLOT version 1.1.

When comparing the “old” calibration with the TCCON sites, the PROFFAST2 data shows systematically higher values during summer and lower values during winter compared to the TCCON sites. This is illustrated in Figure 3.9 for XCO₂ as an example. For other gases, the plots look similar and are shown in the appendix. Panel a) shows the XCO₂ time series of the Karlsruhe TCCON data and the SN037 data processed with the old calibration factors. In panel b) the difference $\Delta\text{XCO}_2 = \text{TCCON-KA} - \text{SN37}$ is plotted. The deviation of the data processed with the old calibration from the data processed with the “new” calibration can be seen from the raw data (panel a) and more clearly from the differences (panel b).

To find the reasons for the deviations, ΔXCO_2 is checked for dependencies on the SZA, the ground temperature and the DMF of H₂O. The results are plotted in the panels c) to e) in Figure 3.9. A dependency of ΔXCO_2 on all three parameters is visible. This is not surprising since the parameters are influenced by each other (high SZA are often measured in the winter, when cold temperatures are causing low XH₂O values). With this information, an empirical correction for XH₂O can be deduced, and is included in the new calibration of PROFFAST2. The reasons for choosing XH₂O as a correction are the following:

- A correction for the SZA is not very reasonable since the PROFFAST2 already is corrected for the SZA as described in the previous section.
- Comparing the “compactness” of the correlation of the ground temperature and the XH₂O amount, the XH₂O amount shows the clearest correlation. There, the relation is about to be linear, which is not detectable as clearly for the ground temperature.

Empirical H₂O correction The empirical H₂O detection is applied to the XGas values. Therefore, the correction is applied on top of the SZA correction. It is applied to all retrieved species except for XAIR and XH₂O itself. The correction is implemented using the following formula:

$$\text{XGas}_{\text{corr}} = \text{XGas} \cdot \left[1 + CF_{\text{XH}_2\text{O}} (\text{XH}_2\text{O} - 2500) \right] . \quad (3.10)$$

Here, $CF_{\text{XH}_2\text{O}}$ is the new additional correction factor. By subtracting 2500, the correction is designed to pivot at 2500 ppm.

The application of the corrections is illustrated for the example of XCO₂ and the instrument SN037 in Figure 3.10. In orange, the same data as in Figure 3.9 is plotted. In green, the results of new calibration including the XH₂O correction is plotted. The reason causing the dependency on XH₂O is still unclear and a topic of current research. Also, it is not clear, if it is an error in the GGG retrieval software or if it is an error in the PROFFAST2 algorithm or due to the use of different spectroscopic data. A more thorough investigation of this issue can be found in Section 3.2.3

For the remaining gases and the other instruments, the structure looks similar. They are not described in the main part but can be found in the appendix B.

The final ADCFs and AICF for all species are listed in Table 3.1.

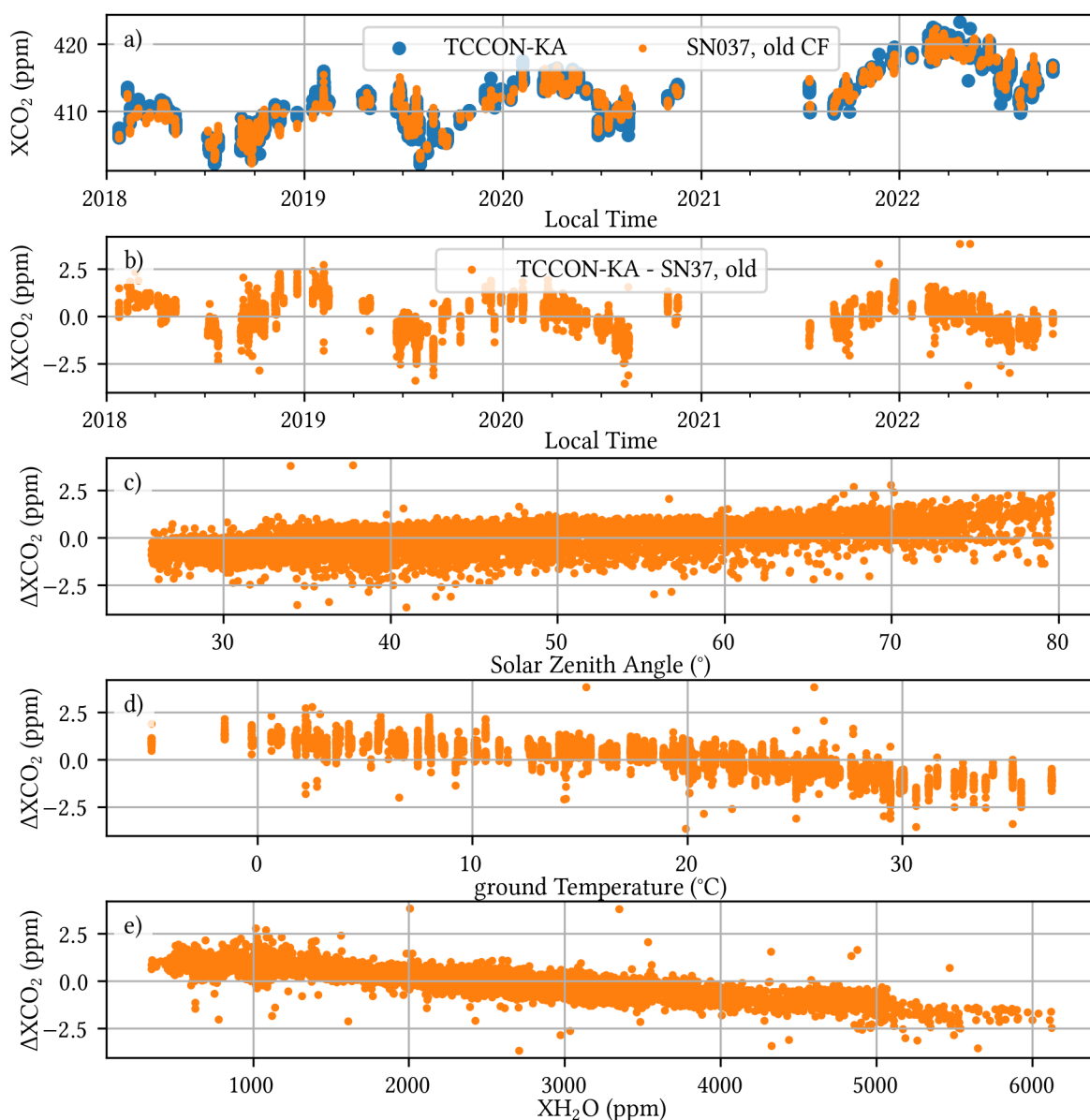


Figure 3.9.: Comparing the old calibration of PROFFAST2 with the Karlsruhe TCCON site for the example of XCO₂. The used COCCON data is measured with the COCCON reference instrument SN37. In panel b) a large seasonal variation is visible. The dependency of the SZA, the ground temperature and XH₂O are shown in panel c), d) and e). For all of them a dependency is visible. However, the most compact correlation can be seen for XH₂O. Based on this observation, an additional correction for XH₂O is introduced. For more details, see in the main text.

3.2.3. Analysis of the XH₂O Dependency

With the application of the empirical XH₂O correction in the calibration, it is possible to reproduce the results of the TCCON with good agreement. However, such an ad-hoc correction is only covering up some unknown source of miscalibration in the retrieval. The fact that the correction is in a similar order for XCH₄ and XCO₂ indicates an systematic reason. Furthermore, the comparison with the TCCON data only allows for relative comparisons but cannot tell if the results of the PROFFAST retrieval are causing the deviation or if there is an XH₂O dependency

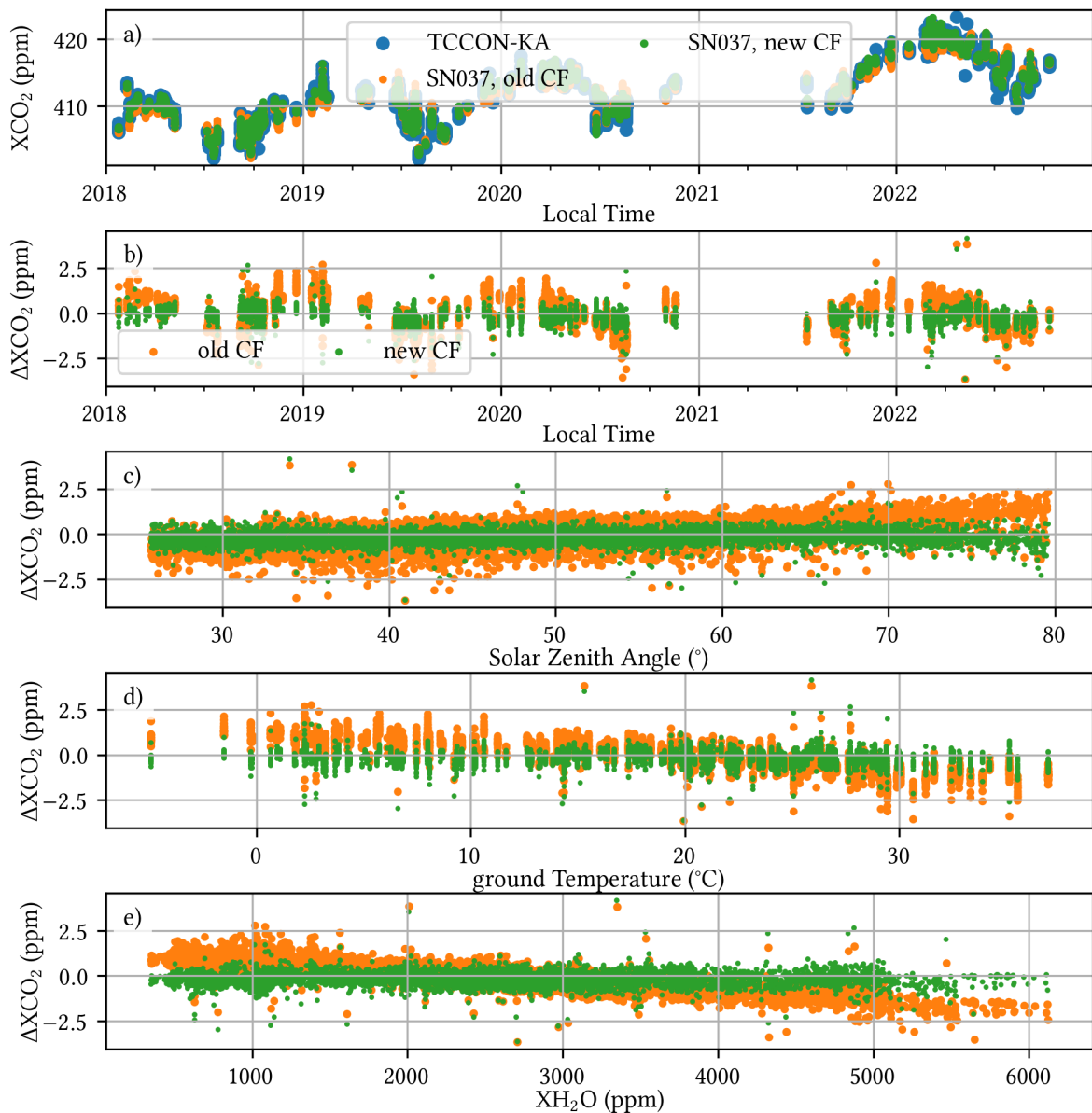


Figure 3.10.: The result of the XH_2O correction for the example of XCO_2 . In orange the same data as in Figure 3.9 is plotted. For the data in green the XH_2O correction is applied. Panel e) shows the direct influence of the correction, which corrects the slope in the XH_2O dependency of XCO_2 . Consequently, the seasonal variation visible in panel b) for non-corrected data in orange is decreased significantly. As a measure of consistency, the dependency of the SZA and the ground temperature is plotted in panel c) and d) respectively. For both the dependency is reduced as well.

in the TCCON data, as well. Hence, here the reason for the XH_2O dependency is investigated in more detail.

As a first step, the retrieval code and the handling of the a priori in the PROFFAST and PROFFASTPYLOT is carefully checked for obvious errors. However, nothing obvious could be found.

With the update from PROFFAST1 to PROFFAST2 the H_2O line list was also updated. To check if the dependency results from this update, the Karlsruhe data is reprocessed by using the

Table 3.1.: The ADCFs and AICFs for the PROFFAST2 retrieval algorithm. The ADCF₃ parameter is added in the code for a potential later correction, however, it is not used currently.

XGas	ADCF ₁	ADCF ₂	ADCF ₃	AICF	CF _{XH₂O}
XH ₂ O	0.00000	0.0000	0.0000	1.0000	–
XAIR	–0.0075	–0.0072	0.0000	0.9910	0.00
XCO ₂	0.00040	0.0020	0.0000	0.9975	–1.50
XCH ₄	0.00275	0.0100	0.0000	0.9884	–0.72
XCH ₄ ^{S5P}	–0.0008	0.0025	0.0000	0.9950	–0.72
XCO	0.07150	0.0060	0.0000	1.0000	–0.30

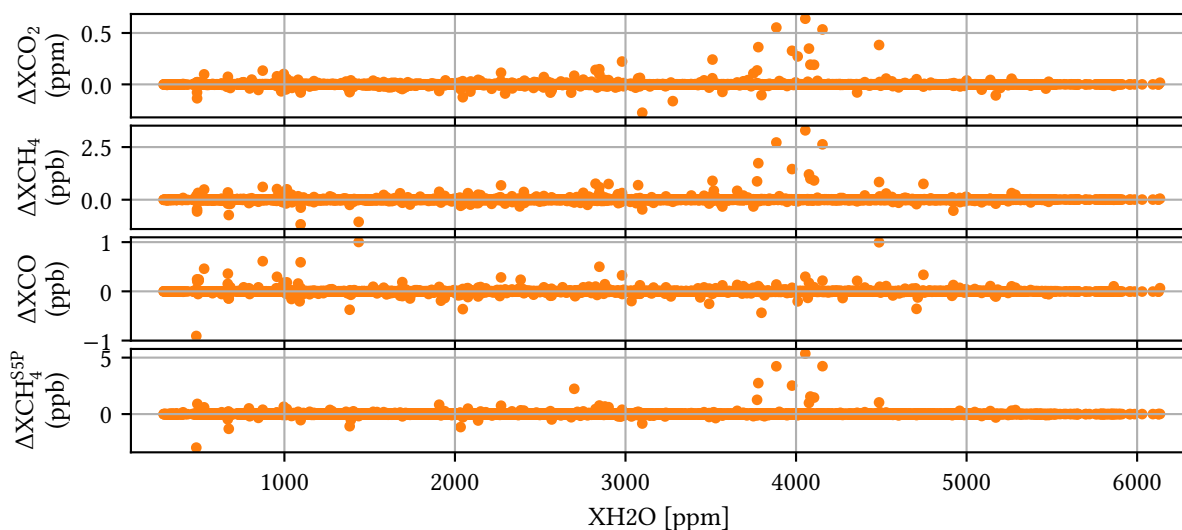


Figure 3.11.: Difference of the retrievals using the new and the old line list of H₂O in PROFFAST2. The plots show the differences of the XGas values of the Karlsruhe data retrieved with PROFFAST2 and the old line list and with the new line list. The old line list is the one used by PROFFAST1 and the new line list the one used by PROFFAST2. For none of the differences a dependency on the XH₂O value can be seen. This indicates clearly, that the XH₂O dependency was not introduced by the new H₂O line list.

H₂O line list of PROFFAST1 in the PROFFAST2 version. The differences of this retrieval and a standard retrieval for the different XGas values in dependency of XH₂O are plotted in Figure 3.11. From this figure it can be seen clearly that for none of the gases an XH₂O dependency can be found. This implies that the improved line list is not causing the problem.

As a next step, the results of the Karlsruhe dataset but processed with previous versions (i.e. GGG2014 and PROFFAST1) are compared to each other. This allows to check, if the dependency only occurs for the comparison with the current versions or maybe is detectable also for previous versions. If it is detectable also for the new versions, this would help to narrow down the sources of the dependency. The difference of GGG2020 and PROFFAST1 in dependency of XH₂O is shown in Figure 3.12. The Figure also contains the difference to PROFFAST2 as a comparison. To increase the visibility of the trend in the data, a linear function $f(\text{XH}_2\text{O}) = a + b \cdot \text{XH}_2\text{O}$ is fitted to the data. For XCO₂ and XCH₄^{S5P}, the same trend for the PROFFAST1 and PROFFAST2 data is found. For XCH₄, the data of PROFFAST1 shows the inverse trend as for PROFFAST2. This result also excludes a programming error which occurred when updating from PROFFAST2 to PROFFAST1.

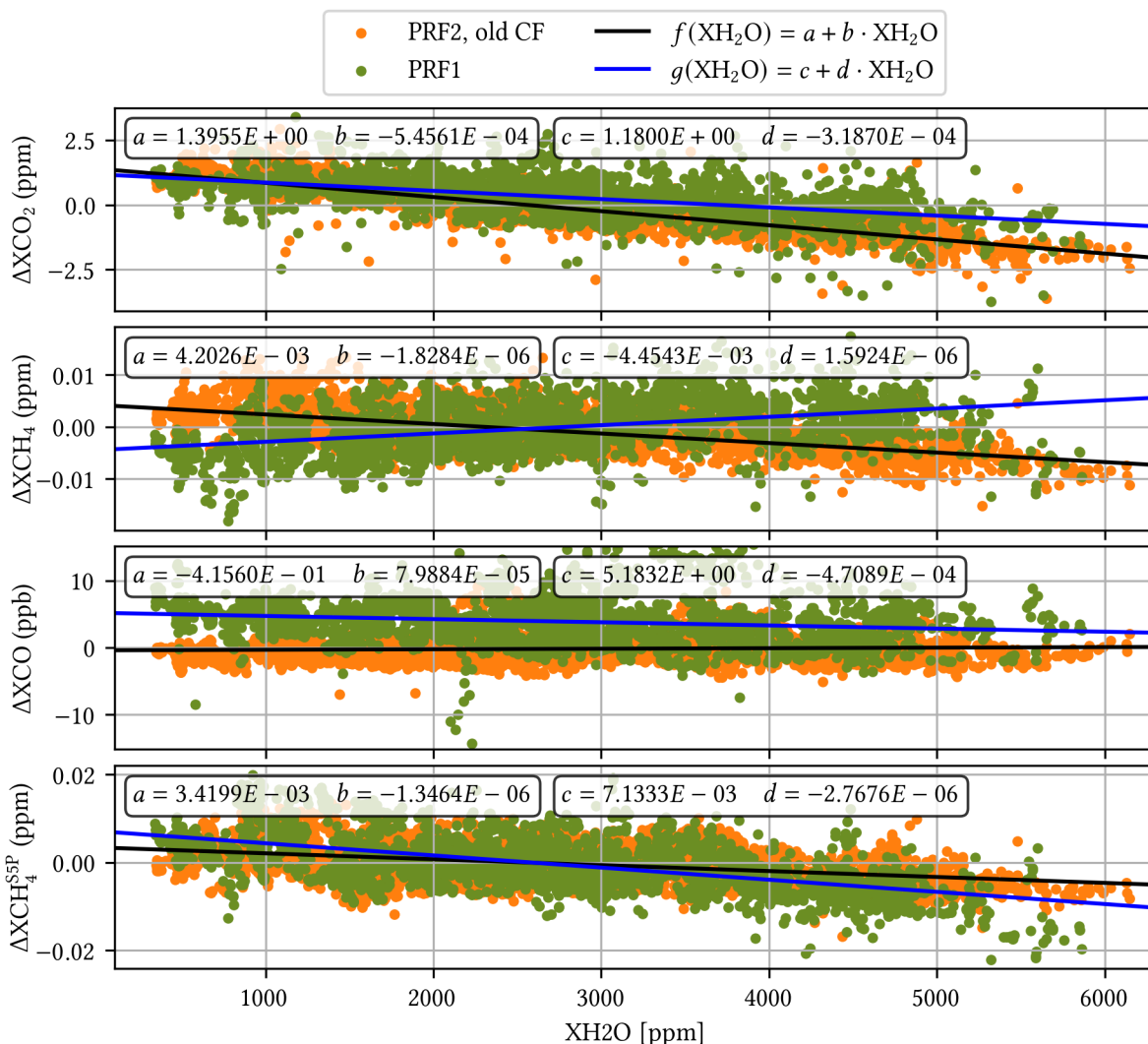


Figure 3.12.: Comparison of the XH_2O dependency of the difference of PROFFAST1 and PROFFAST2 with GGG2020. In orange, the differences of GGG2020 - PROFFAST2 and in green, the difference of GGG2020 - PROFFAST1 are plotted. To increase the visibility of the trend in the data the linear functions f and g are fitted to the differences. For XCO_2 and XCH_4^{SP} the same dependency can be found for the PROFFAST1 data, but with different strength. For XCH_4 it is interesting to see that the dependency of PROFFAST1 is the inverse of the dependency of PROFFAST2 and have a similar strength.

As a further analysis, the difference of GGG2020 - GGG2014 is examined and plotted in Figure 3.13. There, no XH_2O dependency is apparent for XCO_2 and XCO . However, the XCH_4 difference shows a clear dependence on XH_2O . The fit indicates that for a water vapor difference of 5500 ppm (6000 - 500 ppm), the XCH_4 difference is approximately 0.007 ppm. This is a little less than for the difference of PROFFAST2 - GGG2020 which is 0.01 ppm but still significant.

These findings are very valuable since they allow one to draw the following conclusions:

1. The fact that the difference of PROFFAST1 - GGG2020 also shows dependencies in XH_2O shows clearly that this is not an issue of PROFFAST2 alone.
2. The update of the XH_2O line list is not the reason for the behavior.

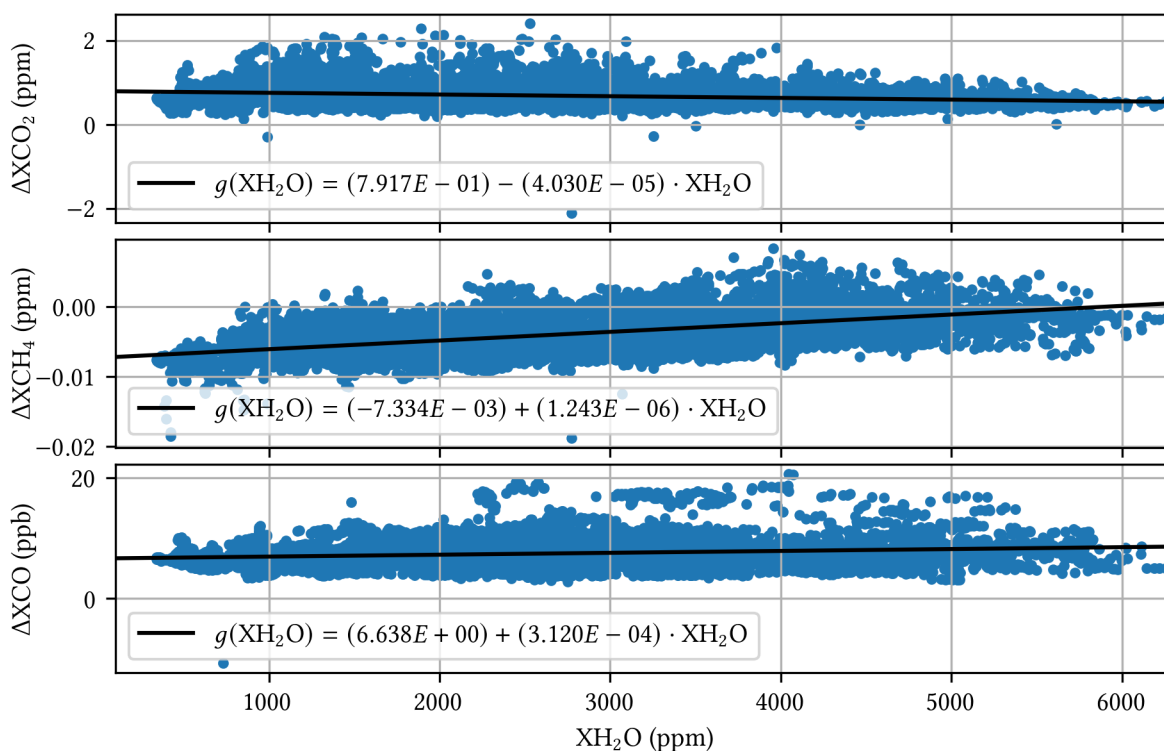


Figure 3.13.: The difference GGG2020 - GGG2014 of different species plotted over the X_{H_2O} value of GGG2020. For X_{CO_2} and X_{CO} , there is no apparent dependency visible. For X_{CH_4} , the dependency is clearly visible. The increase is approximately 0.007 ppb from low to high water vapor concentration.

3. As the comparison of the X_{CH_4} differences of GGG2020 and GGG2014 also shows a X_{H_2O} dependency, this indicates, that this is not only an issue of PROFFAST but also of GGG.
4. The question arises as to which of the programs is closer to the true value, since there is an X_{H_2O} dependency in some gases in both PROFFAST and GGG.

In general, the worst case would be that these differences are the upper limit of a potential bias of the remote sensing data product. For X_{CO_2} , the difference is up to 3 ppm (0.7%), 0.01 ppm (0.55%) for X_{CH_4} and 0.56 ppb (0.56%) for X_{CO} (they are calculated using the slope of the fit in Figure 3.12 and a difference of X_{H_2O} of 5500 ppm). For both X_{CO_2} and X_{CH_4} , the deviations are larger than the TCCON error budget of GGG2014 and GGG2020.

It is of great importance to investigate the reasons for the deviation more closely and to verify the X_{H_2O} dependency of PROFFAST and GGG. For this a wide-ranging comparisons of PROFFAST and GGG with XGas values retrieved from AirCores or airplane in-situ measurements at days with different X_{H_2O} amounts are planned for clarifying this issue.

3.2.4. Performance Comparison of COCCON to TCCON

The calibrated data is used for a systematical analysis of the performance of the COCCON relative to the TCCON data.

For this, the COCCON data is restricted to a maximum SZA value of 78° . The XGas values of both TCCON and COCCON are binned into 10 min intervals. The i -th bin of the TCCON

and COCCON data is denoted as $\overline{\text{XGas}}_i^{\text{TC/CC}}$, where TC and CC are used as abbreviations for TCCON and COCCON respectively. For each timely corresponding bin, the difference $\Delta\text{XGas}_i = \overline{\text{XGas}}_i^{\text{TC}} - \overline{\text{XGas}}_i^{\text{CC}}$ is calculated. Using these differences, the mean value,

$$\overline{\Delta\text{XGas}} = \frac{1}{N} \sum_{i=1}^N \Delta\text{XGas}_i \quad (3.11)$$

and the standard deviation,

$$\sigma_{\Delta\text{XGas}} = \sqrt{\frac{1}{N-1} \sum_{i=1}^N (\Delta\text{XGas}_i - \overline{\Delta\text{XGas}})^2} \quad (3.12)$$

are calculated. Both values are divided by the temporal mean value $\overline{\text{XGas}}_{\text{TCCON}}$ of the XGas value of the TCCON data to get relative values $\widehat{\Delta\text{XGas}} \pm \widehat{\sigma_{\Delta\text{XGas}}}$:

$$\widehat{\Delta\text{XGas}} \pm \widehat{\sigma_{\Delta\text{XGas}}} = \frac{\overline{\Delta\text{XGas}}}{\overline{\text{XGas}}_{\text{TCCON}}} \pm \frac{\sigma_{\Delta\text{XGas}}}{\overline{\text{XGas}}_{\text{TCCON}}}. \quad (3.13)$$

The results are summarized in Table 3.2. By construction the AICF align the mean values of

Table 3.2.: Comparison of the performance of the single instruments compared to the TCCON data. In each column the values of $\widehat{\Delta\text{XGas}} \pm \widehat{\sigma_{\Delta\text{XGas}}}$ in percentage are given. The last column shows the average over the values of the three instruments. For a discussion of the values see in the main text.

Species	SN37 (%)	SN39 (%)	SN122 (%)	Average of (SN37, SN39, SN122) (%)
XCO ₂	-0.0429 ± 0.0949	0.0464 ± 0.0861	0.0817 ± 0.1591	0.02840 ± 0.11337
XCH ₄	0.0006 ± 0.1596	0.0184 ± 0.1536	-0.0583 ± 0.2575	-0.01310 ± 0.19023
XCH ₄ ^{S5P}	0.0342 ± 0.2403	0.0110 ± 0.2252	-0.1628 ± 0.3371	-0.03920 ± 0.26753
XCO	0.9157 ± 2.3268	-0.8551 ± 1.1736	-0.8832 ± 1.3094	-0.27420 ± 1.60327
XH ₂ O	-1.5683 ± 2.5825	-1.1757 ± 1.6904	-0.8717 ± 1.3903	-1.20523 ± 1.88773
XAIR	-0.1759 ± 0.1410	0.0823 ± 0.3581	0.0942 ± 0.2633	0.00020 ± 0.25413

the compared datasets. Therefore, it is not surprising that the $\widehat{\Delta\text{XGas}}$ values are low. The more significant number is the relative standard deviation $\widehat{\sigma_{\Delta\text{XGas}}}$, which describes the scattering of the COCCON values over the TCCON measurements. Comparing the relative standard deviation with the errors-budget for GGG2020, for XCO₂, XCH₄, XCH₄^{S5P} and XCO they are all within the error-bars, which is an excellent agreement.

Chapter 4

Travel Standard: Technical Description

This chapter is mainly based on the following publication:

Herkommer, B., Alberti, C., Castracane, P., Chen, J., Dehn, A., Dietrich, F., Deutscher, N. M., Frey, M. M., Groß, J., Gillespie, L., Hase, F., Morino, I., Pak, N. M., Walker, B., and Wunch, D. (2024). “Using a portable FTIR spectrometer to evaluate the consistency of TCCON measurements on a global scale: The COCCON Travel Standard”. In: *EGUsphere* 2024, pp. 1–46. DOI: [10.5194/egusphere-2023-3089](https://doi.org/10.5194/egusphere-2023-3089)

It is published under the CREATIVE COMMONS ATTRIBUTION 4.0 license, which allows copying, redistributing and adapting its content. For the contributions of the individual authors to the cited work, see the “Author Contribution” section in the publication.

In the previous chapter, the TCCON and the COCCON were presented, which give the background for the introduction of the Travel Standard (TS) in this chapter. The TS is an EM27/SUN FTIR spectrometer operated to meet COCCON requirements which is deployed to TCCON stations to perform side-by-side measurements and hence, serves as a common reference the TCCON sites can be compared to. This chapter focuses on the technical description and realization. The scientific discussion and results are given in Section 5.

The chapter starts with a technical description of the enclosure used to realize the TS. Next, the instrumental characteristics of the EM27/SUN used as the TS unit are investigated and presented. This is done by performing and evaluating side-by-side measurements with the COCCON reference device to derive the instrument specific biases. To compensate those biases and to tie the TS to the COCCON reference unit, for each species a bias compensation factor is derived from those measurements. Furthermore, an error calculation for the bias compensation factors is carried out. Finally, the pressure sensor included within the enclosure is characterized.

4.1. The Enclosure

For the technical realization of the enclosure, two key demands are identified. First, there is a need for some kind of enclosure which facilitates the deployment to the various sites by enabling remote control of the spectrometer and the enclosure. This enables the TS to be shipped to a site without the need of a person accompanying the device and therefore, helps to visit TCCON sites in a high frequency.

Figure 4.1: The enclosure of the Travel Standard. The EM27/SUN used as Travel Standard inside of the enclosure used at the rooftop of the institute building in Karlsruhe, performing side-by-side measurements with the COCCON reference unit. The enclosure is at the right-hand side. The rotatable dome has a cut-out which enables the Sun to illuminate the spectrometer. The person at the picture is 1.8 m tall, giving a reference for the size of the enclosure and the EM27/SUNs.



As a second key demand, it is desirable to have comparable ambient conditions when operating the spectrometer at various sites. This helps to avoid systematic errors caused by extreme cold or hot temperatures. Hence, the enclosure should provide a rain cover, a heater, and a cooling mechanism.

These demands are solved by using an enclosure which is developed and build by the Technical University Munich (TUM) (Dietrich et al. 2021; Heinle and Chen 2018) and purchased by the Institute for Meteorology and Climate Research - Atmospheric Trace Gases and Remote Sensing (IMK-ASF). Figure 4.1 shows it alongside the COCCON reference unit and a further EM27/SUN spectrometer collecting side-by-side measurements at the rooftop of the IMK-ASF building in Karlsruhe.

The enclosure is equipped with a simple and reliable software running on a programmable logic controller (PLC) for controlling the dome. An industrial computer is included to control the EM27/SUN and for collecting the measurements. By a router which is able to connect to the internet using LAN, WiFi or mobile data, the whole enclosure is connected to the internet enabling remote access and control. At the top of the cover, a rain sensor is mounted to close the dome immediately as soon as rain is detected. A small uninterruptible power supply (UPS) is included to power the enclosure long enough to close the dome and protect the interior in case of a blackout.

For using the enclosure in the context of the Travel Standard, several modifications have been made when compared to its original status as assembled by Heinle and Chen 2018.

Power Supply In its original design by TUM, the enclosure is built to be used in Europe. Hence, various electrical components inside the box were not able to deal with voltages and frequencies other than the European power grid. To solve this problem, the electronics are adapted to cope with a large range of voltages and power grid frequencies.

Temperature Management The enclosure is equipped with a fan and a heater for controlling the temperature inside the enclosure. The task of the temperature management is to keep the temperature in a range which is uncritical for the electronics inside the enclosure. Low temperatures can become critical as soon as wet air starts to condensate. The water can cause corrosion and also damage electrical circuits. Therefore, the temperatures should always be high enough to prevent condensation. To ensure this, the heater is set to keep 25 °C as the lowest temperature. On the other hand, the electronics produce heat inside the enclosure. Furthermore, the enclosure is irradiated directly by the Sun and hence, the temperature inside of the enclosure

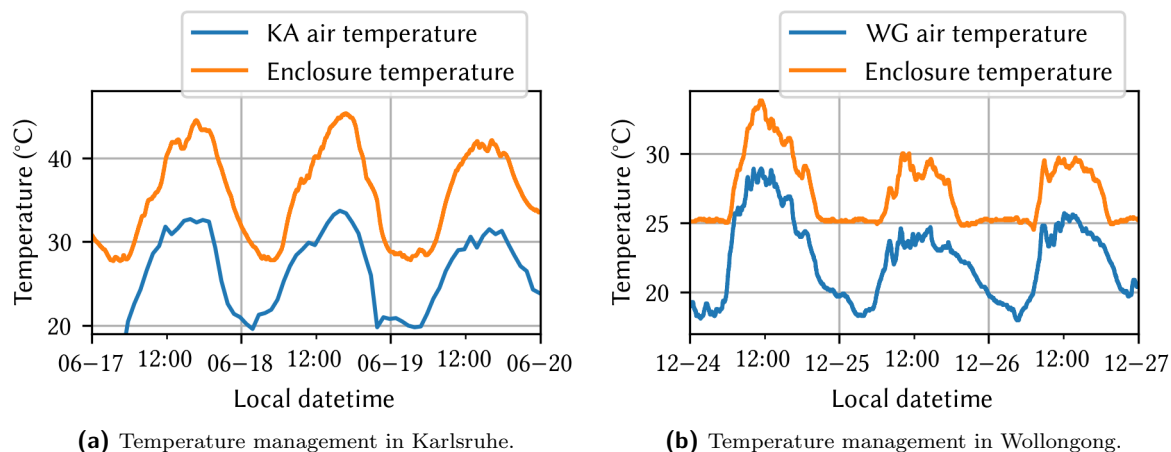


Figure 4.2.: Temperature records inside and outside of the enclosure in Karlsruhe (a) and Wollongong (b). The inside temperature is plotted in orange and the ambient air temperature as measured by the TCCON station plotted in blue. The data in (a) was recorded in summer 2020 in Karlsruhe. The data in (b) was recorded during the campaign in Wollongong, Australia. In (b) it is noticeable that the target temperature of 25 °C is kept even though the outside temperature falls to a lower temperature. When the temperature starts to rise, the fan starts venting in order to cool down the enclosure. The reason the temperature inside the enclosure rises to higher values than the ambient temperature is that a) the electric components inside the enclosure produce heat and b) the radiation hitting the enclosure directly additionally heats up the enclosure. The cooling does not work efficiently. However, even during hot summer days like shown in (a) the measurements worked fine.

is warmer than the ambient temperature. To cool the enclosure, a fan is used to transport the hot air to the outside of the enclosure.

Figure 4.2 presents the ambient temperature and the temperature measured inside the enclosure in summer 2020 in Karlsruhe and during the Wollongong campaign. The target temperature inside the enclosure is set to be 25 °C. The heating works well which is apparent as the temperature never dropped below that level. However, the fan cannot circulate enough air to compensate the heating caused by the electronics and the irradiating Sun. In Wollongong, the inside temperature was up to 5 °C warmer than the ambient temperature. The problem also occurred in Heinle and Chen 2018 who used an improved cooling by using an thermoelectric cooling. However, even when operating the enclosure on warmer days (tested to a maximum ambient temperature of up to 33 °C, and a measured enclosure temperature of 45 °C in summer 2021 in Karlsruhe) the electronics as well as the measurement works fine. Hence, no further improvement of the cooling was necessary.

Pressure Sensor An important auxiliary quantity for the retrieval of XGas values is the ground pressure. According to a study by Tu 2019, conducted for low resolution spectra and using the PROFFIT algorithm, for CO₂ a change of 1 hPa results in an error of 0.035 ppm. To have reliable pressure measurements available for all measurements, the enclosure is equipped with a VAISALA PTB330 meteorological pressure sensor. Furthermore, this enables to use the TS to compare the pressure measurements of the visited TCCON sites to a common reference.

Guided by the data collected at the first campaign in Tsukuba an issue that has not been considered was addressed: The pressure data of the first campaign in Tsukuba shows some abrupt changes which are not recorded by co-located pressure sensors (as the sensor used for the Tsukuba TCCON site). Figure 4.3 shows this phenomenon for 2021-04-10 as an example using green color. For comparison, the pressure as recorded by the TCCON site is shown in

Figure 4.3: Example of the dynamic pressure created by the fan inside of the enclosure. The figure shows pressure and temperature measurements collected in Tsukuba, Japan. In green is plotted the pressure data as recorded by the VAISALA PTB330 inside the enclosure. In blue is plotted the pressure data recorded by the sensor of the TCCON station. In orange the same data is plotted but corrected for height and an offset (compare section 5.2) to match the pressure level of the Travel Standard sensor. In red the temperature inside the enclosure is plotted. It refers to the axis at the right-hand side of the figure. The fan within the enclosure starts venting a approximately 08:00 and stops at 18:00 causing the TS pressures sensor measuring significantly higher values due to the dynamic pressure.

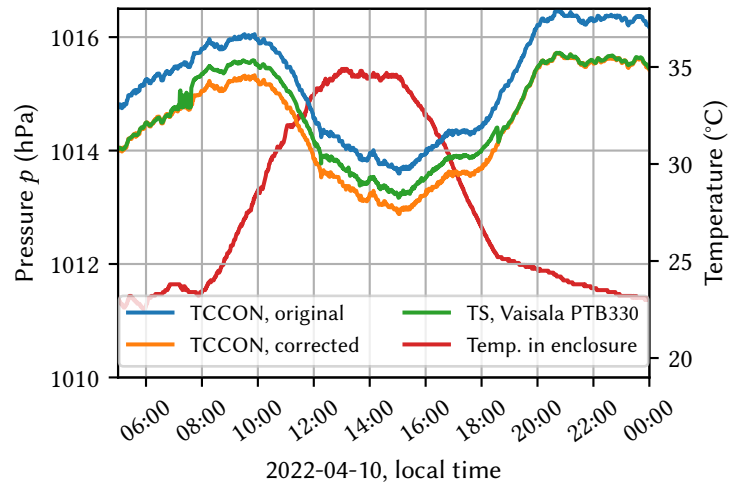
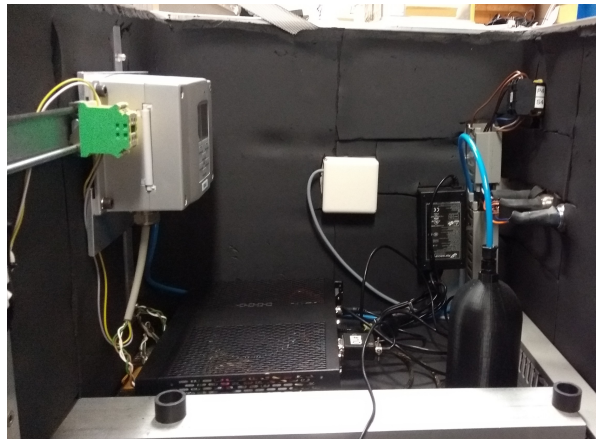


Figure 4.4: The pressure sensor inside of the TS enclosure. The VAISALA PTB330 sensor can be seen at the left-hand side of the enclosure. It is connected to the plastic cup mounted at the bottom of the enclosure via the blue tube. The bottom under the cup is cut in a way that the tube is directly sensing the outside pressure. The tube is sealed with a pressure-permeable cover to prevent insects or other dust particles to enter the tube and the sensor. This solution enables the measurement of the ambient pressure without being affected by the dynamic pressure created by the venting fan inside the enclosure.



blue. The data corrected for height and an offset between the two sensors (see Section 5.2) is given in orange. In Figure 4.3, the abrupt changes in the pressure data recorded by the TS at approximately 08:00 and 18:00 can be seen clearly. The reason for these jumps is a dynamic pressure created by the venting fan which is used to control the temperature inside of the enclosure. Since there is no log data giving an information when the fan starts to vent, the temperature inside the enclosure is used as a proxy: As soon as the temperature starts to rise, the fan starts venting, trying to keep the temperature in the enclosure below 35 °C. In the evening, it stops again. The stopping point is perfectly visible since the decrease rate suddenly slows down at approximately 18:00. At this point, the pressure offset stops as well and both sensors measure the same pressure.

To solve this problem, after the Japan campaign, a pipe is used which connects the pressure sensor to the outside of the enclosure. It ends in a 3D-printed cup mounted at the bottom of the enclosure. Figure 4.4 shows the pipe and the cup inside the box.

Transport Logger When transporting goods on roads, ships or airplanes, mechanical shocks can happen to the goods due to potholes, swells or turbulences. To avoid damages to the TS, it is packed properly in foam. Even though the EM27/SUN has proven to be quite resistant to

Table 4.1.: Records of the transport data-logger attached directly to the EM27/SUN. For the shock recording, it is necessary to set up thresholds for the acceleration $a_{\min;\max}$ (as a multiple of the earth acceleration $g = 9.81 \text{ m s}^{-1}$), the duration of the shock T_{dur} , and the frequency rate f_{rate} with which the data is recorded. The temperature and humidity records are both in a non-critical range. The maximal acceleration recorded by the logger is 16 g. Hence, it is not clear if the actual acceleration was larger. However, no misalignment or any other errors could be found when checking the instrument.

Site	Temperature	Humidity	Shock thresholds	Shock records
Tsukuba, Japan	$T_{\max} = 44.1 \text{ }^\circ\text{C}$ $T_{\min} = 11.0 \text{ }^\circ\text{C}$	$H_{\max} = 25 \%$	$a_{\min;\max} = [-3.0; 3.0]\text{g}$ $T_{\text{dur}} = 30 \text{ ms}$ $f_{\text{rate}} = 1600 \text{ Hz}$	No events recorded
ETL, Canada	$T_{\max} = 46.4 \text{ }^\circ\text{C}$ $T_{\min} = 24.0 \text{ }^\circ\text{C}$	$H_{\max} = 63 \%$	$a_{\min;\max} = [-3.6; 3.6]\text{g}$ $T_{\text{dur}} = 20 \text{ ms}$ $f_{\text{rate}} = 1600 \text{ Hz}$	No events recorded
Wollongong Australia	$T_{\max} = 31.2 \text{ }^\circ\text{C}$ $T_{\min} = 13.1 \text{ }^\circ\text{C}$	$H_{\max} = 63.3 \%$	$a_{\min;\max} = [-3.6; 3.6]\text{g}$ $T_{\text{dur}} = 15 \text{ ms}$ $f_{\text{rate}} = 400 \text{ Hz}$	EM27: 3 events $a_{\max} = 16 \text{ g}$ $T_{\text{dur}}^{\max} = 35 \text{ ms}$

mechanical shocks, it is desirable to know about any impacts which happen when transporting. In case of strong impacts, this is an indicator to check for misalignment.

Furthermore, very high temperatures or very low temperatures also can affect the alignment due to thermal expansion. In addition, low temperatures combined with a high humidity of the air can cause condensation of water and hence, may damage the electronics and the mirrors.

Especially for a Traveling Standard it is of utmost importance to keep track of shocks and check for potential issues arising from this. For this purpose, the Travel Standard is equipped with two ASPION G-LOG2 transport-data logger. One is mounted at the inside of the enclosure, the other one is mounted directly to the EM27/SUN which is transported in a separate box. The loggers record mechanical shocks, the temperature, and the humidity over the entire transportation period. The data recorded by the logger directly attached to the EM27/SUN is summarized in Table 4.1. The data recorded by the logger mounted at the inside of the enclosure is given in the appendix in Table A.1. The temperature and the relative humidity were both in a non-critical range for all transports. During the transportation to Tsukuba and East Trout Lake (ETL) no shock events were recorded. The shocks recorded during the transportation for the Wollongong campaign lead to an intensive check of the EM27/SUN and the enclosure. For the EM27/SUN no misalignment or other errors could be determined. However, the changes in the side-by-side measurements with the COCCON reference unit are larger than the changes found before and after of the other campaigns. This might be an impact of those shocks. In the enclosure, several screws mounting the internal computer to the enclosure bottom were loose or had even completely fallen off. Beside the mentioned damage, no other damages could be detected.

4.2. Characterization and Monitoring of the Travel Standard in Karlsruhe Between the Campaigns

To monitor the instrument between the campaigns, side-by-side measurements with the COCCON reference spectrometer (SN37) are collected. The deviation to the COCCON reference unit is

described by multiplicative factors K which are called bias compensation factors in this thesis. In the first part of this section, the approach to derive these factors is explained and applied. A further tool to monitor the stability of the TS unit is the measurement of the ILS, compare with Section 2.3.4.4. Hence, between the campaigns, the ILS is measured and the results are presented. Finally, the pressure sensor mounted in the Travel Standard enclosure is characterized and compared to the data of a nearby weather station of the German weather service (Deutscher Wetterdienst (DWD)).

4.2.1. Approach to Retrieve Bias Compensation Factors

For the comparison of different XGas data measured with two different instruments, empirical bias compensation factors are established (Frey et al. 2015; Alberti et al. 2022a). In good approximation, they are assumed to be airmass independent. This approach is used several times within this thesis, therefore it is presented here in detail. The following notation will be used:

To correct the bias of the species XGas of instrument xx to match with the reference instrument yy, the bias compensation factor is denoted as $K_{xx}^{yy}(\text{XGas})$ such that:

$$\text{XGas}_{yy} = K_{xx}^{yy}(\text{XGas}) \cdot \text{XGas}_{xx} . \quad (4.1)$$

The derivation is described in detail below.

Before calculating the bias compensation factors, the following criteria are used to filter the data:

1. As a first step, measurements with a large baseline variation are filtered out. The baseline variation indicates clouds or a bad tracking of the sun. This is done automatically by the preprocessor of PROFFAST2. The sensitivity of the filter is set to the default settings as delivered with the PROFFASTPYLOT 1.2.
2. All measurements recorded at a SZA larger than 80° are deleted. This is done since with larger SZAs, the airmass increases with approximately $1/\cos(\text{SZA})$ (assuming a plane parallel atmosphere). Hence, the measurement uncertainties increase faster due to the fact that the airmass varies faster with the SZA. In addition, empirical airmass-dependent corrections and the assumption of hydrostatic balance become less reliable.
3. Obvious outliers in XAIR are deleted. To detect them, the data for each day are smoothed and the original data is subtracted by the smoothed version. The result of this division scatters around zero. This is used to calculate the standard deviation σ_{XAIR} of XAIR for each day. All data points outside of $\pm 2\sigma_{\text{XAIR}}$ are assumed to be outliers and thus deleted.
4. In case the XAIR filter was not able to detect an outlier, for each XGas, all remaining obvious outliers are deleted. The upper-lower limits used for this are 1.6 - 1.95 ppm for XCH₄, 350 - 450 ppm for XCO₂, and 40 to 200 ppb for XCO. This happens mostly for data recorded with the second channel since the data used to calculate XAIR is only recorded by the first channel. If e.g. the second channel is over-saturated this leads to bad XCO and XCH₄^{S5P} values which are then removed from the evaluation.

To calculate the bias compensation factors the XGas values of both instruments, xx and yy, are binned in intervals of l minutes, denoted as $\overline{\text{XGas}}_{xx/yy}^i$, here i enumerates the bins. Next, the

bias compensation factors are calculated by dividing the coincident bins of instrument yy by the ones of instrument xx and taking the average of it:

$$K_{xx}^{yy} = \frac{1}{N} \sum_{i=\text{coincident bins}}^N \frac{\overline{\text{XGas}}_{yy}^{t_i}}{\overline{\text{XGas}}_{xx}^{t_i}} \quad (4.2)$$

$$= \frac{1}{N} \sum_{i=\text{coincident bins}}^N (q_{xx}^{yy})^i. \quad (4.3)$$

Here, $(q_{xx}^{yy})^i = \frac{\overline{\text{XGas}}_{yy}^{t_i}}{\overline{\text{XGas}}_{xx}^{t_i}}$.

4.2.1.1. Error Analysis of the Bias Compensation Factors

For any measurement, the error can be split into a systematic and a random error. Assuming constant conditions, a systematic error falsifies repeated measurements all by the same amount. The known bias between the instruments is a systematic error and is described using the bias compensation factors. For the TS instrument, a further systematic error for the XCO product is detected and discussed in Section 4.2.3. Apart from this no other systematic errors are known. The error of interest therefore is the random error, which randomly influences the results.

The random error is described by the standard error:

$$s_i^{\text{ID}} = \frac{\sigma_i^{\text{ID}}}{\sqrt{n_i}} \quad (4.4)$$

of the data. Here σ_i^{ID} is the estimated standard deviation of the data of one instrument in the i^{th} bin and n_i the number of measurements in the bin. Note that for each bin of each instrument the standard error is calculated.

To calculate the error of the quotient $(q_{xx}^{yy})^i$ of each bin, GAUSSIAN error propagation is used. In the following, an error of a quantity x will be denoted as $\epsilon(x)$. This notation is used to indicate that the error is not a standard deviation and also to avoid confusion with the difference between two values which is denoted with Δ . For a product $x = x_1 \cdot x_2$ or for an quotient $x = x_1/x_2$, the formula for the propagation of the relative error $\epsilon(x)/x$ is the same (see e.g. Kaloyerou 2018):

$$\frac{\epsilon(x)}{x} = \left[\left(\frac{\epsilon(x_1)}{x_1} \right)^2 + \left(\frac{\epsilon(x_2)}{x_2} \right)^2 \right]^{\frac{1}{2}}. \quad (4.5)$$

Using Equation 4.5, the relative error for the quotient of the i^{th} bin is calculated by:

$$\frac{\epsilon(q_{xx}^{yy})_i}{(q_{xx}^{yy})_i} = \left[\left(\frac{s_i^{\text{xx}}}{\overline{\text{XGas}}_{xx}^{t_i}} \right)^2 + \left(\frac{s_i^{\text{yy}}}{\overline{\text{XGas}}_{yy}^{t_i}} \right)^2 \right]^{\frac{1}{2}}. \quad (4.6)$$

Using GAUSSIAN error propagation applied to Equation (4.3), the error of the final bias compensation factor is calculated by:

$$\epsilon(K_{xx}^{yy}) = \left[\frac{1}{N^2} \sum_{i=1}^N (\epsilon(q_{xx}^{yy})_i)^2 \right]^{\frac{1}{2}}. \quad (4.7)$$

Note that because Equation (4.3) is a sum, the absolute errors $\epsilon(q_{xx}^{yy})_i$ and not the relative errors $\frac{\epsilon(q_{xx}^{yy})_i}{(q_{xx}^{yy})_i}$ need to be used. They can be calculated by multiplying Equation (4.6) with $(q_{xx}^{yy})^i$. The relative error of K can be calculated by $\frac{\epsilon(K_{xx}^{yy})}{K_{xx}^{yy}}$.

4.2.2. Characterization of the Travel Standard at the KIT for Empirical Bias Monitoring

For the purpose of monitoring and characterizing the TS-spectrometer (serial number SN39), before and after each campaign, side-by-side measurements with the COCCON reference instrument (serial number SN37) are collected. Using these measurements, the instrument-specific bias compensation factors $K_{SN39}^{SN37}(XGas)$ for XCO_2 , XCH_4 and XCO are calculated. As a complementary tool to monitor the Travel Standard instrument, open path measurements in the laboratory are collected to retrieve the ILS of the spectrometer.

In Figure 4.5, the results of the side-by-side measurements are plotted. For the retrievals with PROFFAST2, the calibration presented in Section 3.2.2 is used. It is released with the PROFFASTpylot¹ version 1.2.

Table 4.2.: The bias compensation factors K_{SN39}^{SN37} for the TS spectrometer relative to the COCCON reference unit. They are calculated using the data shown in Figure 4.5. For XCO , the correction described in 4.2.3 is applied. ΔK_{SN39}^{SN37} (%) denotes the deviation to the correction factor in the row above and $\overline{\Delta XGas}$ the difference of the temporal mean over each measurement period. $\Delta(\overline{\Delta XGas})$ gives the change of the difference to the previous encounter. The values of ΔK_{SN39}^{SN37} and $\Delta(\overline{\Delta XGas})$ are used to measure the stability of the instrument. The smaller, the more stable are the instruments against each other. For all measurement periods (December 2021/January 2022; June 2022; October 2022; March 2023), the drift between two characterization measurements is less than the TCCON error budget given in Section 3.1.2.

Species	Date	K_{SN39}^{SN37}	ΔK_{SN39}^{SN37} (%)	$\overline{\Delta XGas}$	$\Delta(\overline{\Delta XGas})$
XCO ₂	January 2022	0.99887 ± 0.00004	–	–0.4684 ppm	–
	June 2022	0.99942 ± 0.00007	0.063 13 %	–0.2575 ppm	0.210 96 ppm
	October 2022	0.99960 ± 0.00003	0.012 28 %	–0.1626 ppm	0.094 84 ppm
	March 2023	1.00036 ± 0.00005	0.070 60 %	0.1444 ppm	0.307 00 ppm
XCH ₄	January 2022	1.00036 ± 0.00004	–	0.0007 ppm	–
	June 2022	0.99962 ± 0.00006	–0.066 84 %	–0.0006 ppm	–0.001 29 ppm
	October 2022	1.00066 ± 0.00002	0.098 62 %	0.0013 ppm	0.001 88 ppm
	March 2023	1.00004 ± 0.00005	–0.070 77 %	–0.0001 ppm	–0.001 35 ppm
XCO	January 2022	1.00159 ± 0.00029	–	0.1608 ppb	–
	June 2022	1.00071 ± 0.00075	–0.053 60 %	0.0831 ppb	–0.077 67 ppb
	October 2022	1.00052 ± 0.00022	–0.047 68 %	0.0403 ppb	–0.042 82 ppb
	March 2023	0.96076 ± 0.00054	–0.587 17 %	–0.4636 ppb	–0.503 94 ppb
XCH ₄ ^{S5P}	January 2022	1.00036 ± 0.00003	–	0.0006 ppm	–
	June 2022	0.99834 ± 0.00007	–0.198 34 %	–0.0032 ppm	–0.003 84 ppm
	October 2022	0.99962 ± 0.00002	0.125 25 %	–0.0008 ppm	0.002 46 ppm
	March 2023	0.99872 ± 0.00011	–0.095 63 %	–0.0023 ppm	–0.001 54 ppm

¹ <https://gitlab.eudat.eu/coccon-kit/proffastpylot>

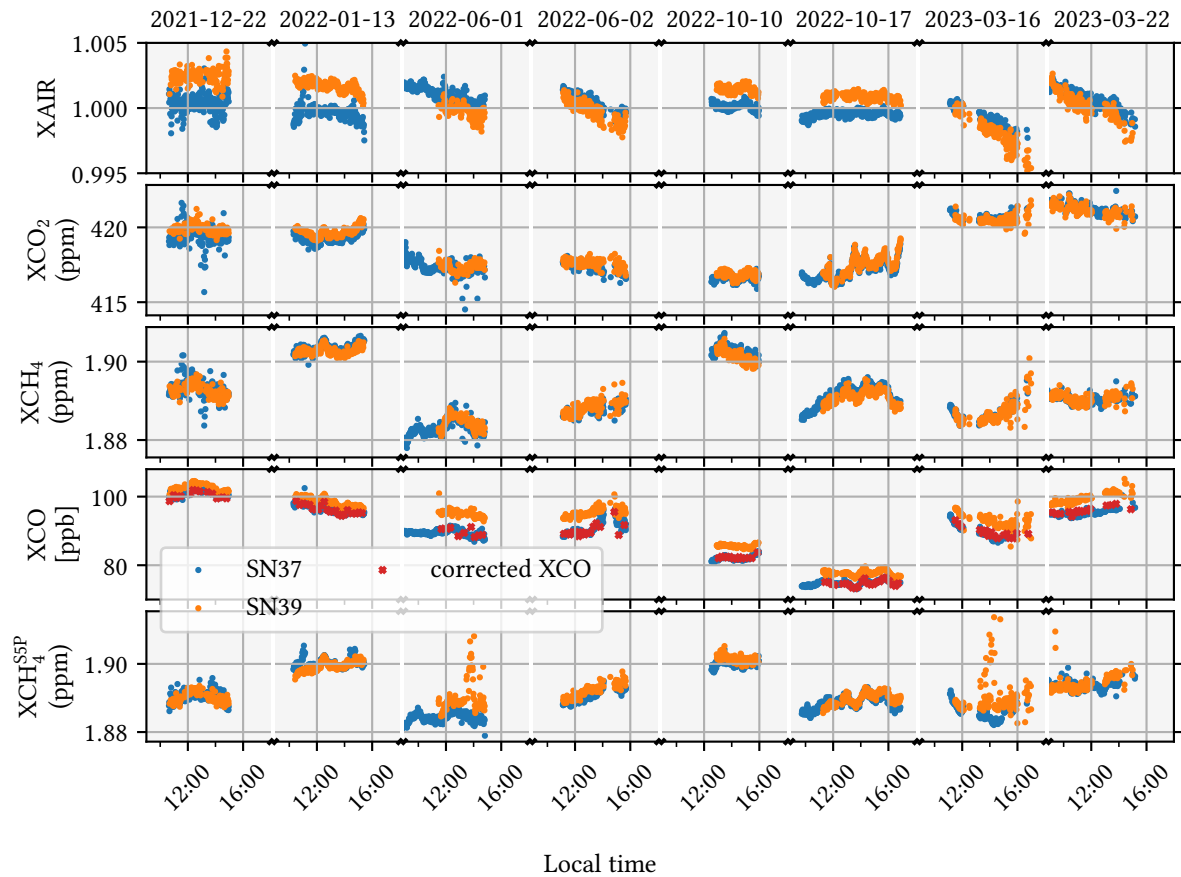


Figure 4.5.: The results of the side-by-side measurements of the COCCON reference unit (SN37) and the TS (SN39). The data of the reference unit is plotted in blue and the Travel Standard in orange. In the top panel, XAIR is plotted, next XCO₂, XCH₄, XCO and in the lowest panel XCH₄^{SSP}, which is the column averaged DMF of CH₄ derived from a window covered by the second channel of the EM27/SUN. For each of species, empirical bias compensation factors are calculated and summed up in Table 4.2. For XCO₂ and XCH₄, the difference of the two instruments shows minor variability over time. However, for XCO, a significant variability is visible. To correct this variability, an empirical SZA dependent function is used. The corrected data is plotted using the red “x”-shaped markers. From the corrected XCO data, only every 12th marker is plotted to provide a clearer figure.

The measurements were collected on two days before and after each campaign. Before the Japan campaign in December 2021 and January 2022, before the Canada campaign in June 2022, before the Australia campaign in October 2022, and after the Australia campaign in March 2023.

A visual analysis reveals a good agreement for XAIR, XCO₂ and XCH₄ during all measurement periods. The higher noise level on 2021-12-22 and 2022-06-01 and at the end of 2022-06-02 are most probably due to cloudy conditions on that day causing a higher DC variation of the interferogram and reducing the accuracy of solar tracking. For XCO, there are larger differences between the measurement campaigns. This is corrected using an empirical approach resulting in the red crosses and investigated closer in Section 4.2.3.

Using the data given in the plot, the bias compensation factors K_{SN39}^{SN37} are calculated using the approach explained in Section 4.2.1. They are given in Table 4.2, together with the errors calculated as described in Section 4.2.1.1. Furthermore, the table shows the relative deviation of each bias compensation factor to its precursor in the row above ΔK_{SN39}^{SN37} in percentage. In

addition, $\overline{\Delta X_{\text{Gas}}}$ gives the difference of the temporal mean values of both instruments, considering all values in a comparison period. To monitor the change of the instruments, the difference to the previous value is given as $\Delta(\overline{\Delta X_{\text{Gas}}})$.

For all gases, the changes of the differences ($\Delta(\overline{\Delta X_{\text{Gas}}})$) are smaller than the estimated TCCON site-to-site biases, given in Section 3.1.2. This shows that the EM27/SUN spectrometer unit used as a Travel Standard is stable enough to serve as a common reference between the TCCON stations.

However, for XCO, there is a larger deviation before and after the Australia Campaign (October 2022 and March 2023). The reason for this could be the high mechanical shocks of up to 16g recorded during the shipments to Australia and back, compare with Table 4.1. Due to these shocks, the spectrometer was checked for loose screws and an obvious misalignment. However, both tests were negative. Furthermore, the ILS measurement did not reveal a misalignment (compare with Figure 4.6). However, the ILS measurements consider only the first channel of the EM27/SUN, whereas the XCO window is measured with the second channel and hence can not detect a misalignment in the second channel. Furthermore, the $\text{XCH}_4^{\text{SSP}}$ does not show a large deviation during this period which also indicates that the second channel was not misaligned.

The changes of the differences $\Delta(\overline{\Delta X_{\text{Gas}}})$ will be used later as an uncertainty when comparing the different TCCON sites in Section 5.

XAIR Analysis XAIR is a quantity designed to check the consistency of the data and whether there is any coarse misalignment of the spectrometer. This feature will be used in Chapter 5 to verify that the TS works correctly.

The data used for the calibration of the COCCON (see Section 3.2.2) is collected with the same EM27/SUN instrument as it is used now for the Travel Standard (Serial Number SN039). Therefore, the datasets collected in Sodankylä in 2017 and 2018 are used to determine an expected range for the XAIR value for the Travel Standard. Furthermore, the data measured in 2021 in Karlsruhe (plotted in Figure A.1) is used. For both data-sets, the temporal mean value and the standard deviation are calculated. As given in Section 3.2.1 the definitions of XAIR are different in PROFFAST and GGG. Therefore, when comparing data processed with PROFFAST2 and GGG2020, in the following for all PROFFAST2 products $1/\text{XAIR}$ is plotted. Hence, here as well $1/\text{XAIR}$ is used.

This gives values of $\text{XAIR} = 0.99981 \pm 0.00094$ and $\text{XAIR} = 0.99907 \pm 0.00078$ for the data measured in Sodankylä and Karlsruhe, respectively. The average of both is $\text{XAIR} = 0.99944 \pm 0.00086$. With this, the 1σ interval (mean $\pm 1\sigma$) becomes [1.00030, 0.99858] and the 2σ interval [0.99772, 1.00116]. All values within the 1σ range will be denoted as an excellent agreement and all values within the 2σ range are still within the expected range.

ILS Measurements As described in Section 2.3.4.4, the ILS is an excellent tool to monitor the performance of an FTIR spectrometer. Therefore, the ILS of the Travel Standard instrument is measured before and after each campaign. The measured ILS values are plotted in Figure 4.6. The measurements prior to 2020 are of no relevance to the TS. However, they are listed in the figure to provide a comparison of the new measure values to the previously collected ILS values.

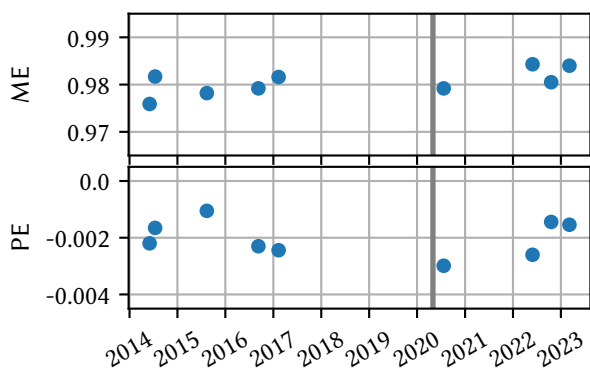


Figure 4.6: The instrumental line shape parameters of the EM27/SUN spectrometer SN39 used as the Travel Standard measured at different dates. It is described by the Modulation Efficiency (ME) and the Phase Error (PE) (compare with Section 2.3.4.4). The gray line indicates the date after which the measurements is relevant for this paper. The data before are plotted to show the values in the context of the history of the instrument. The measurement in summer 2020 was recorded before the Tsukuba campaign. The three measurements in 2022 - 2023 were performed after the Tsukuba, ETL and Wollongong campaign.

As a measure of the stability, the mean and the standard deviation of the ME and the PE are calculated over all available ILS measurements. For the ME and PE, the result are:

$$\begin{aligned} \text{ME} &= 0.98051 \pm 0.00272 , \\ \text{PE} &= -0.00202 \pm 0.00063 . \end{aligned}$$

To provide a comparison, the values for ME and PE of the COCCON reference instrument SN037 as published in (Alberti et al. 2022a) are:

$$\begin{aligned} \text{ME} &= 0.98361 \pm 0.00267 , \\ \text{PE} &= 0.00145 \pm 0.00122 . \end{aligned}$$

These values are in the same order of magnitude, indicating that the TS instrument operates within the normal range of an EM27/SUN spectrometer. For the evaluation of the measurements of the TS data, always the latest available ILS measurement is used.

4.2.3. XCO-Correction

In Figure 4.5, the XCO product of the Travel Standard unit (SN39) and the COCCON reference unit show seasonal variable differences. The reason for this is investigated in the following.

A known issue for the measurement of XCO is the so-called channeling at one of the optical elements, as demonstrated by Frey 2018. Channeling describes the phenomenon of an optical element in the optical path accidentally acting as a cavity, compare with Section 2.3.4.2. As a consequence of this finding, all new EM27/SUN spectrometers are improved by adding an anti-reflection coating of the long-pass filter causing the channeling. However, the instrument SN039 used as Travel Standard is the prototype version of the implementation of the second channel (Hase et al. 2016). Therefore, this instrument is not coated with the anti-reflection layer. To recheck this, laboratory measurements as described by Frey 2018 are collected. However, they seem to be free of channeling which does not support the hypothesis of channeling being the source of the deviation.

Another possible error source is a misalignment of the second channel. A direct way to test for this is a second XCH₄ product, called XCH₄^{S5P}, which is retrieved from an alternative window within the range of the second channel. In case of a misalignment, one would expect XCH₄^{S5P} to show the same or a similar deviation as well. It is plotted in Figure 4.5. As it does not show the same behavior as XCO, this result does not support the misalignment hypothesis.

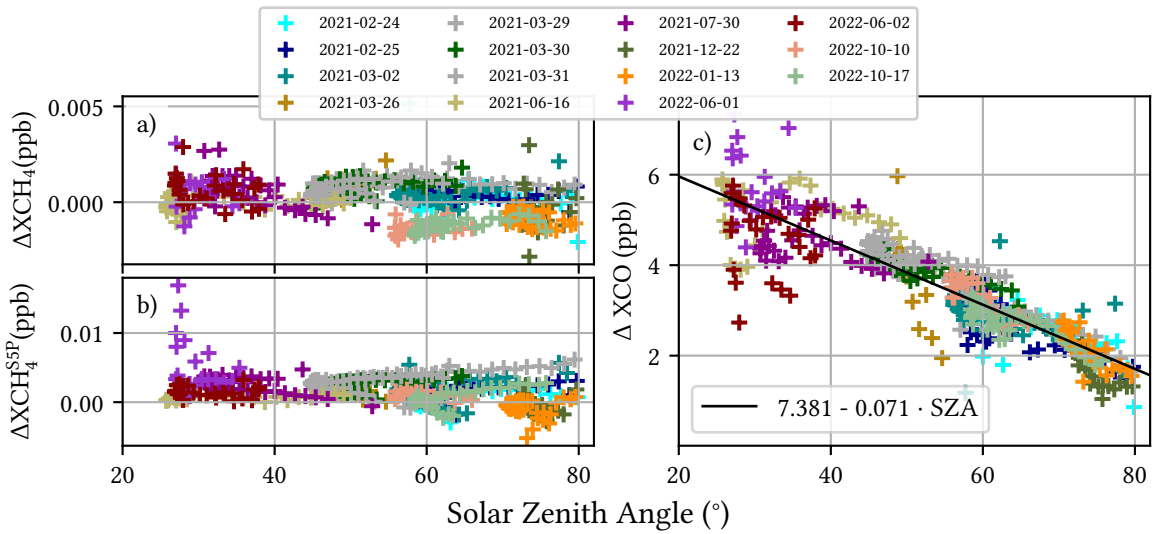


Figure 4.7.: The SZA dependency of the differences of XCH_4 , XCH_4^{55P} and XCO between the COCCON reference unit and the TS spectrometer. In Panels a) and b), the ΔXCH_4 and ΔXCH_4^{55P} values are plotted respectively. In panel c), the ΔXCO . In a) and b), no dependency of the SZA is visible. In contrast, ΔXCO shows a clear SZA dependency. The reason for this is still under investigation. However, this dependency is used to derive an empirical linear correction of the XCO values. The correction is applied to all measured data in this paper. In Figure 4.5, the corrected XCO values are plotted using red "x"-shaped markers.

In 2021, a larger dataset of side-by-side measurements is recorded from 2021-02-24 until 2022-10-17. The time series of this is plotted in Appendix A.1. From this dataset, it is possible to see a dependency on the XCO difference at the solar zenith angle. In Figure 4.7 panel c), the difference ΔXCO between the reference instrument and the TS instrument is plotted in dependency of the solar zenith angle. The data shows a clear dependency on the SZA. Therefore, the data is used to derive an empirical correction by fitting a linear regression line to the data. The resulting correction function is:

$$k_{XCO}(SZA) = 7.36682 - 0.07077 \cdot SZA . \quad (4.8)$$

It is applied to all XCO measurements collected with the Travel Standard in this work. The only exception is the data plotted in Figure 4.5 with the orange color to compare the non-corrected XCO data to the corrected XCO. The corrected data is plotted using the red "x"-shaped markers.

The reason for this behavior is still unclear and part of ongoing investigations. To exclude a systematic issue of the second channel (for example a broken detector or over-saturation) of the SN39 spectrometer as a reason, the SZA dependency of XCH_4 and XCH_4^{55P} are investigated. They are plotted in the panels a) and b) in Figure 4.7. In case the second channel is misaligned, XCH_4^{55P} would show a similar behavior as XCO. However, this is not the case. Hence, these results indicate that the Travel Standard instrument is aligned correctly.

4.2.4. Calibration of the Pressure Sensor

The Travel Standard is equipped with a Vaisala PTB330 pressure sensor acquired in April 2021 which is also compared at KIT against the pressure data used for the Karlsruhe TCCON retrieval.

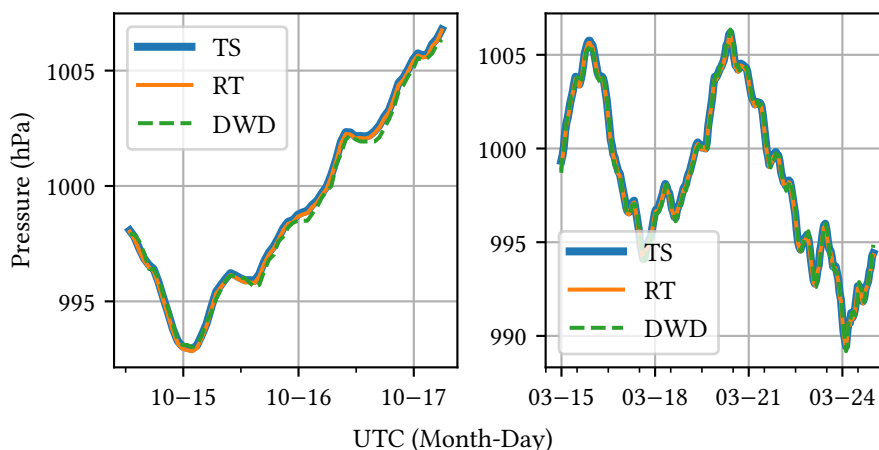


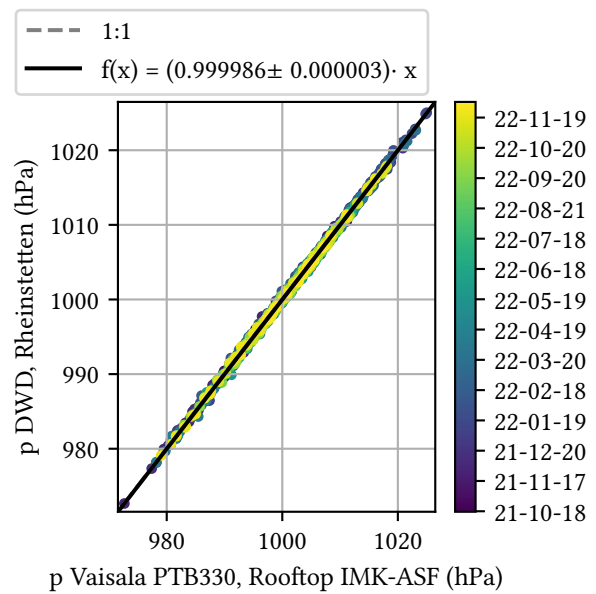
Figure 4.8.: Comparison of the Vaisala PTB330 sensor deployed with the TS with the data of a co-located weather station of the German weather service DWD. A further sensor is a second Vaisala PTB330 mounted permanently on the institutes rooftop which is denoted as RT in the figure. The measurements in the left and right panels are taken in October 2022 (between Canada and Australia) and March 2023 (after Australia), respectively. For the two periods, bias compensation factors of $K_{TS}^{DWD}(\text{Can}) = 0.9998129$ and $K_{TS}^{DWD}(\text{Aus}) = 0.9999243$ are found. The pressure data of the Rheinstetten DWD station is corrected for altitude.

The data is retrieved at a nearby weather station (Rheinstetten, 15 km south-south-west of the TCCON station) of the German weather service (DWD) .

Unfortunately, there was an undetected problem with the software collecting the pressure measurements of the TS sensor before the Tsukuba and ETL campaigns, so there is no side-by-side data for these periods. The only measurements available were taken after the Canada and Australia campaigns. These measurements are plotted in Figure 4.8. The data shows a very good agreement with the height-corrected data from the DWD-Rheinstetten site, resulting in the bias compensation factors of $K_{TS}^{DWD}(\text{Can}) = 0.9998129$ and $K_{TS}^{DWD}(\text{Aus}) = 0.9999243$ for the measurements before and after the Wollongong campaign. This gives a change of only -0.1% . Due to this stability, for further calculations the average of both values is used, which is $K_{TS_p}^{DWD} = 0.9998686$. Assuming an pressure of 1000 hPa, the average deviation is 0.131 hPa. Figure 4.8 also shows the data of a further sensor which is mounted permanently at the rooftop of the IMK-ASF building and is collecting data continuously. This sensor is denoted as ‘‘Rooftop (RT) sensor’’. This sensor also agrees very well with the TS sensor.

To investigate the stability of the Vaisala PTB330 sensors, the RT sensor is compared to the DWD data. Figure 4.9 shows a scatter plot of the comparison. There, an excellent agreement is found. A linear function $p_{RT}(p_{DWD}) = c \cdot p_{DWD}$ fitted to the data gives $c = 0.999986 \pm 3.061845 \cdot 10^{-6}$. The average deviation over the whole period is 0.0138 hPa. This shows the high stability of the PTB 330 sensors. Hence, it is justified to use it as a reference sensor for the TS.

Figure 4.9: Results of the comparison of a Vaisala PTB330 mounted on the rooftop of the IMK-ASF at the 7th floor and the DWD weather station in Rheinstetten in 16 km distance to the institute. The data shows an very good agreement and does not show drift over time. A linear function $p_{RT}(p_{DWD}) = c \cdot p_{RT}$ is fitted to the data. The fit parameter is $c = 0.999986 \pm 3.061845 \cdot 10^{-6}$. The average deviation over the whole comparison period is 0.0138 hPa.



Chapter 5

Results of the Travel Standard Campaigns

This chapter is mainly based on the following publication:

Herkommer, B., Alberti, C., Castracane, P., Chen, J., Dehn, A., Dietrich, F., Deutscher, N. M., Frey, M. M., Groß, J., Gillespie, L., Hase, F., Morino, I., Pak, N. M., Walker, B., and Wunch, D. (2024). “Using a portable FTIR spectrometer to evaluate the consistency of TCCON measurements on a global scale: The COCCON Travel Standard”. In: *EGUsphere* 2024, pp. 1–46. DOI: [10.5194/egusphere-2023-3089](https://doi.org/10.5194/egusphere-2023-3089)

It is published under the CREATIVE COMMONS ATTRIBUTION 4.0 license, which allows copying, redistributing and adapting its content. For the contributions of the individual authors to the cited work, see the “Author Contribution” section in the publication.

In the previous chapters, the COCCON and the TCCON were presented as the framework the TS is embedded in. After the technical description in Chapter 4, in this chapter the scientific results achieved the application of the TS are presented. In the framework of this thesis, the Travel Standard visited three TCCON sites: Tsukuba (TK) in Japan, ETL in Canada and Wollongong (WG) in Australia. Further, the results of each campaign are presented.

For the visits of the TS at the TCCON sites, three goals are identified.

1. The thorough comparison of the collected data with the TCCON and the TS spectrometer are used to search for instrumental issues in the TCCON sites.
2. The comparison of the XGas measurements are used to compare the XGas values retrieved by the TCCON sites to a common reference.
3. The comparison of the pressure measurement as an important auxiliary value of the retrievals.

To realize these goals, it is important that the measurements at each site are comparable and hence systematic biases are avoided. Therefore, the same measurement procedure is applied at all stations. This procedure is described in 5.1.

Next, the data collected at each site is presented and analyzed in Sections 5.2 to 5.4. Two of the sites show a high noise level in the XGas results. Therefore, the origin of the noise is discussed in Section 5.5. The main idea of the TS is to compare the XGas results to the TS as a common reference. This analysis is covered by Section 5.6. Finally, in Section 5.7 the results of the comparison are discussed.

5.1. Evaluation Procedure of the Travel Standard Campaigns

At each of the TCCON sites visited, the same measurement procedure is performed to enable comparable conditions across all sites. The TCCON instrument performs two different measurements in an alternating manner: High-resolution standard TCCON measurements and low-resolution measurements. With the TCCON standard setting, single-sided interferograms with a $OPD_{max} = 45$ cm are collected. The low-resolution measurements are double-sided interferograms with a $OPD_{max} = 1.8$ cm and hence, mimic the spectral characteristics of the EM27/SUN spectrometer. The low-resolution data is recorded for several reasons. First, it is known that the resolution can affect the retrieved XGas values (Petri et al. 2012). This is mainly due to different column sensitivities of the retrieval caused by the different resolutions which triggers different XGas results if the a-priori deviates from the actual profile shape. When comparing the low-resolution measurements with the TS measurements, this effect can be excluded. Furthermore, the TCCON low resolution data can be processed using PROFFAST2, avoiding any bias introduced by a different evaluation software.

The high-resolution data is supposed to be the same as the official TCCON data and therefore, retrieved using GGG2020 by the PI of each station. Following, the low-resolution data of a site will be denoted as ID-LR. Here, ID is the two-letter identification of the TCCON site. The high-resolution data will be denoted as ID-HR.

In addition to the FTIR measurements, at each site the pressure is recorded using the sensor included in the TS-enclosure and it is compared with the pressure measurements used for the official TCCON evaluation.

The analysis of the data for each site comprises an analysis of the pressure data, of the XAIR and of the XGas values. For the XAIR analysis, the data is compared with XAIR values derived from reference intervals collected with the TS instrument in Sodankylä and Karlsruhe. Compare with Section 4.2.2. For the TCCON measurements a reference interval is determined by using the Karlsruhe and Sodankylä TCCON data. This is carried out in Section 3.1.4).

Finally, for all sites a quantitative comparison to the Karlsruhe TCCON site is conducted by using bias compensation factors.

5.2. Tsukuba, Japan

In this section, the data collected in Tsukuba, Japan is analyzed. The Tsukuba TCCON station is located 22 meters above sea level (**masl**), the TS at an altitude of 30 masl. The latitude and longitude of both, the TS and the TCCON site are 36.0513 north, 140.1215 east. The TS stayed in Tsukuba from 2022-03-24 until 2022-04-25. In this period, measurements at 8 days were collected. The TCCON spectrometer collected high- and low-resolution data. The data will be denoted as Tsukuba high-resolution (TK-HR) and Tsukuba low-resolution (TK-LR).

Pressure Analysis: For the Tsukuba campaign, the pressure sensor was installed in a way that the pressure inlet was within the enclosure. Therefore, the data shows an offset when the cooling fan was venting. Compare with Section 4.1 and Figure 4.3.

Fortunately, a side-by-side measurement with the Tsukuba TCCON site pressure sensor was collected, with the fan turned off. From this data, a factor could be computed to relate the data

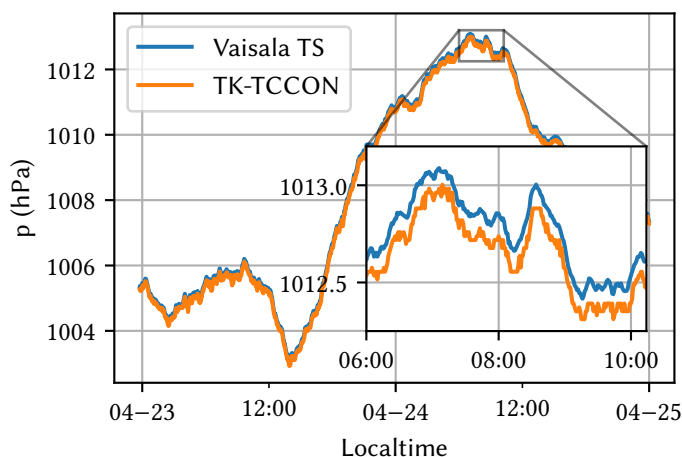


Figure 5.1: Side-by-side pressure recordings in Tsukuba, Japan. The results are consistent. From the inset axis, it can be seen that there is small difference of -0.105 hPa on average (TK-TCCON relative to Vaisala TS). The fan was turned off for these measurements.

obtained with the pressure sensor at the Tsukuba site to the pressure sensor of the TS. Thus, the pressure data from the official TCCON evaluation is used, though including a correction for altitude and a second correction to match the pressure sensor of the TS. The data of the side-by-side comparison is plotted in Figure 5.1. The overall mean difference is -0.105 hPa. This gives an bias compensation factor of $K_{TK_p}^{TS_p} = 1.0001042$.

The pressure offset is small enough that the effect on XGas retrieval is expected to be negligible.

To convert TCCON pressure data in order to be used for the evaluation of the TS data, it is necessary to use in addition to the $K_{TK_p}^{TS_p}$ correction a height correction factor, considering the different heights of the Tsukuba TCCON pressure sensor and the location of the TS when calculating solar measurements. The height correction is calculated using Equation 2.5 with a constant gravitational acceleration of $g = 9.81 \text{ m s}^{-2}$ and the ambient air temperature as measured by TCCON station for each data point. This gives a height correction factor of 0.9991497.

XAIR Analysis: Figure 5.2 shows the retrieved data of XAIR, XCO₂, XCH₄, and XCO. The TS data is shown in blue, the TK-LR data in orange, and the TK-HR data in green.

There is a clear airmass dependence on XAIR in the TK-LR and TK-HR data. Such an airmass dependence is an indicator for an error in the recorded time stamp of the interferogram, which leads to a wrong calculation of the solar position. Empirically, it has been found that correcting the measurement times by -44 s removes the airmass dependence. For further analysis, the uncorrected data will be used. This is because the purpose of this scientific research is to analyze the current status of the TCCON stations as it is and not the result of possible corrections. However, in Section 5.2.1, the influence of the correction is investigated. The reason for this offset is still under investigation by the principal investigator (PI) of the Tsukuba TCCON site.

It is important to note that the airmass dependencies of TK-LR and TK-HR have the same shape, although it is expected different due to the inverse definitions in GGG and PROFFAST, as discussed in Section 3.2.1. This is because for the TK-LR and the TS data, the inverse of the data as calculated by PROFFAST is plotted and used for all further analyzes.

The XAIR values of the TS are distributed around unity. They have a small dependence on the solar zenith angle for almost all days. The exceptions are April 8th, when XAIR shows fast oscillations early in the day and March 25th, as well as April 12th when XAIR started low and

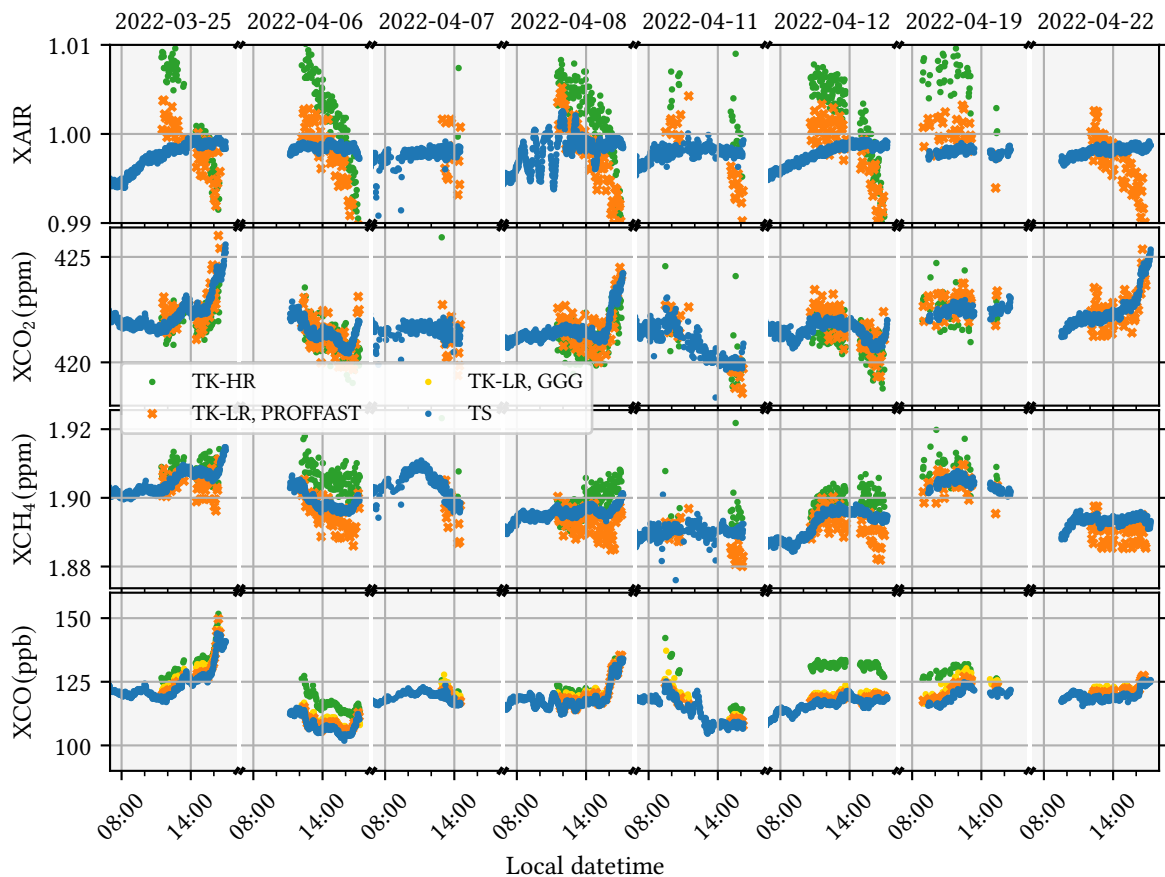


Figure 5.2.: The XGas results for XCO_2 , XCH_4 and XCO of the side-by-side measurements in Tsukuba, Japan. The results of the TS measurements are plotted in blue, in orange the TK-LR measurements and in green the TK-HR measurements. Overall the values are in good agreement for all species. The TCCON results are noisier than the TS. The cause of this is the signal drop for higher wavenumbers in the interferogram. For XCO there are significant day-to-day variations of the TK-HR relative to the TK-LR and TS data. To check if this is caused by an issue with PROFFAST2, the TK-LR data is also processed with the GGG software suite and plotted in yellow. The fast oscillation of XAIR in the morning of 2022-04-08 occurs due to pressure oscillations measured independently of the weather station of the Japan Meteorological Agency in Tsukuba, too.

raised during the course of the day. Such an increase normally indicates an timing error or an issue with the tracker. However, apparently in the afternoon when the comparison starts, the XAIR values stabilize close to unity. Therefore, the comparison is not influenced by this. Since the phenomenon only occurred on those two days, it is not investigated further.

The reason for the oscillations on April 8th can be traced back to the pressure record which also shows the same oscillations and directly affects XAIR (compare with Equation (3.7)).

The oscillations are also detected by a pressure station operated by the Japanese Meteorological Agency in Tsukuba, Japan (Tateno)¹, link in Japanese).

These rapid, quasi-periodic pressure variations may be the effect of mountain waves generated by the surrounding peaks. The wave activity in this area can be extreme, as shown by the crash

¹ https://www.data.jma.go.jp/obd/stats/etrn/view/10min_s1.php?prec_no=40&block_no=47646&year=2022&month=4&day=8&view, last access 2023-05-12

of flight BOAC911². The heavy pressure oscillation ends before the TCCON measurements start. Consequently, it does not affect the side-by-side evaluation.

As a quantified measure of the XAIR analysis, the following metric will be used: XAIR is designed to be unity for a perfectly aligned instrument. Therefore, the mean and standard deviation are calculated based on the time series of XAIR. The closer the first value is to unity, and the second to zero, the better is the quality of the XAIR. For the TS data this is 0.99778 ± 0.00130 , 1.00224 ± 0.00482 for the TK-HR, and 0.99774 ± 0.00355 for the TK-LR data.

The mean value of the TK-HR XAIR value is slightly outside of the 2σ interval derived from the Karlsruhe and Sodankylä TCCON data (see Section 3.1.4). The standard deviation is larger than for each, the Sodankylä and Karlsruhe data. This indicates the high noise level.

The mean XAIR value of the TS is little below the $1\text{-}\sigma$ interval defined in Section 4.2.2. The reason for this might be the usage of the height corrected pressure value of the TCCON site instead of the usage of the pressure data recorded by the TS. As the height used for the conversion could only be estimated, this might result in slightly wrong pressure values for the TS. However, the XAIR values are still within a non-critical range. The standard deviation is larger than for the reference period discussed in Section 4.2.2. This is mainly due to the oscillations on 2022-04-08 and the low XAIR values in the morning of 2022-03-25. Excluding these two days from the analysis changes the values of the TS to 0.99786 ± 0.00091 . This reduces the standard deviation by a factor of 0.7.

XGas Analysis: A first visual analysis of the data in Figure 5.2 shows a high noise level for XAIR, XCO₂ and XCH₄ of the TK-LR and the TK-HR data. This can be explained by an intensity drop in the spectra towards higher wavenumbers. This phenomenon is discussed in detail in Section 5.5.1.

The comparison with the TS data shows a good absolute agreement for XCO₂ and XCH₄ for both, the TK-HR and the TK-LR data. As a quick quantitative comparison, the average difference of the TS data to the TK-HR and TK-LR data over all measurement days are calculated. A detailed quantitative analysis is given in Section 5.6. The differences are summarized in Table 5.1. For each, XCO₂ and XCH₄, the average biases are within the error budget of the TCCON

Table 5.1.: The average bias of the TS and the TK TCCON data.

Species	TK-LR	TK-HR
XCO ₂	0.257 70 ppm	-0.016 26 ppm
XCH ₄	-0.004 70 ppm	0.002 77 ppm
XCO	-1.566 07 ppb	-8.635 95 ppb

(given in Section 3.1.2) and hence, each are in good agreement. For XCO, the absolute agreement for TK-LR data is good whereas a variable day to day offset can be found for the TK-HR data. For example on 2022-04-08, the agreement is well, whereas it is worse for 2022-04-12. This results in a much better agreement of the TK-LR data compared to the TK-HR data.

The reason for this is most probably an effect arising from the different resolution, combined with a known issue of the CO a priori: The column sensitivity describes the change of the

² (https://en.wikipedia.org/wiki/BOAC_Flight_911, last access 2023-05-12)

retrieved vertical column if x molecules are inserted at height h . Furthermore, it depends on the resolution of the measurement. For both GGG and PROFFAST, the same a priori are used. They are generated using model data provided by Goddard Earth Observing System - Forward Processing for Instrument Teams (GEOS-FPIT). It is known that this model uses outdated CO emission inventories from 2008, causing an over-, or an underestimation (depending on the area) of the CO a priori in urban or energy intensive areas (Laughner et al. 2023; Laughner 2023). By the end of 2023, the GEOS-FPIT model will be updated. This might solve this issue.

To ensure that the variable bias is no issue resulting from the PROFFAST retrieval software, the TK-LR data is also processed using GGG2020. The result of this analysis is plotted with yellow "x" shaped markers. The day-to-day variability is similar to that of the PROFFAST TK-LR data processing. This indicates that it is not a problem with the PROFFAST code but supports the aforementioned hypothesis.

5.2.1. Correction of the Timing Error

To test the influence of the timing error to the Tsukuba data, the TK-LR data is reprocessed with an offset of -44 s. To keep consistency, the high-resolution data is processed by the PI of each TCCON site. Unfortunately, for the TK-HR data, a time-corrected dataset was not available yet when finishing this thesis. The reprocessed XGas values are plotted in Figure 5.3. The time correction removes the airmass dependency in XAIR almost completely. This gives a mean value and a standard deviation of 1.00048 ± 0.00186 for the XAIR values. Compared to the uncorrected values, this is a significant improvement. The differences averaged over all measurement days are -0.02700 ppm for XCO₂, 0.00272 ppm for XCH₄ and -1.57713 ppb for XCO. Interestingly, the changes in these values are less significant than for the change in XAIR. The reason for this is that a timing error influences the total column amounts of O₂ and of each species in a very similar manner. Hence, when calculating the XGas value using Equation (3.4) the error is mitigated almost completely. This can be seen nicely in Figure 5.9 where both the total column values of O₂ and CO₂ show the same steep increase after approximately 14:00 local time. A quantitative evaluation using bias compensation factors is given in Section 5.7.1.

5.3. East Trout Lake, Canada

The ETL TCCON site is located at 54.353 north, 104.987 west at an altitude of 502 masl. The Travel Standard visited the ETL TCCON site from 2022-08-16 until 2022-08-21. Unfortunately, shortly before the TS arrived, the reference laser which is needed to operate the IFS 125HR TCCON spectrometer, broke down. Hence, no side-by-side measurements were possible. However, there are several days of measurements with high-, and low-resolution (denoted as East Trout Lake high-resolution (ETL-HR) and East Trout Lake low-resolution (ETL-LR)) measurements recorded before the TS arrived. These measurements are used to perform an analysis of XAIR and of the noise of the individual gases. Furthermore, it was possible to record pressure data for a comparison.

Pressure Analysis: In the temporal interval from 2022-08-16 at 8:00 to 2022-08-17 at 20:00 local time, the side-by-side pressure measurements are collected. The data is plotted in Figure 5.4. The ETL pressure data has a high noise level. It is recorded with a frequency of 1 Hz. Hence to reduce the noise, a rolling mean over 60 s is calculated and plotted in orange. To make

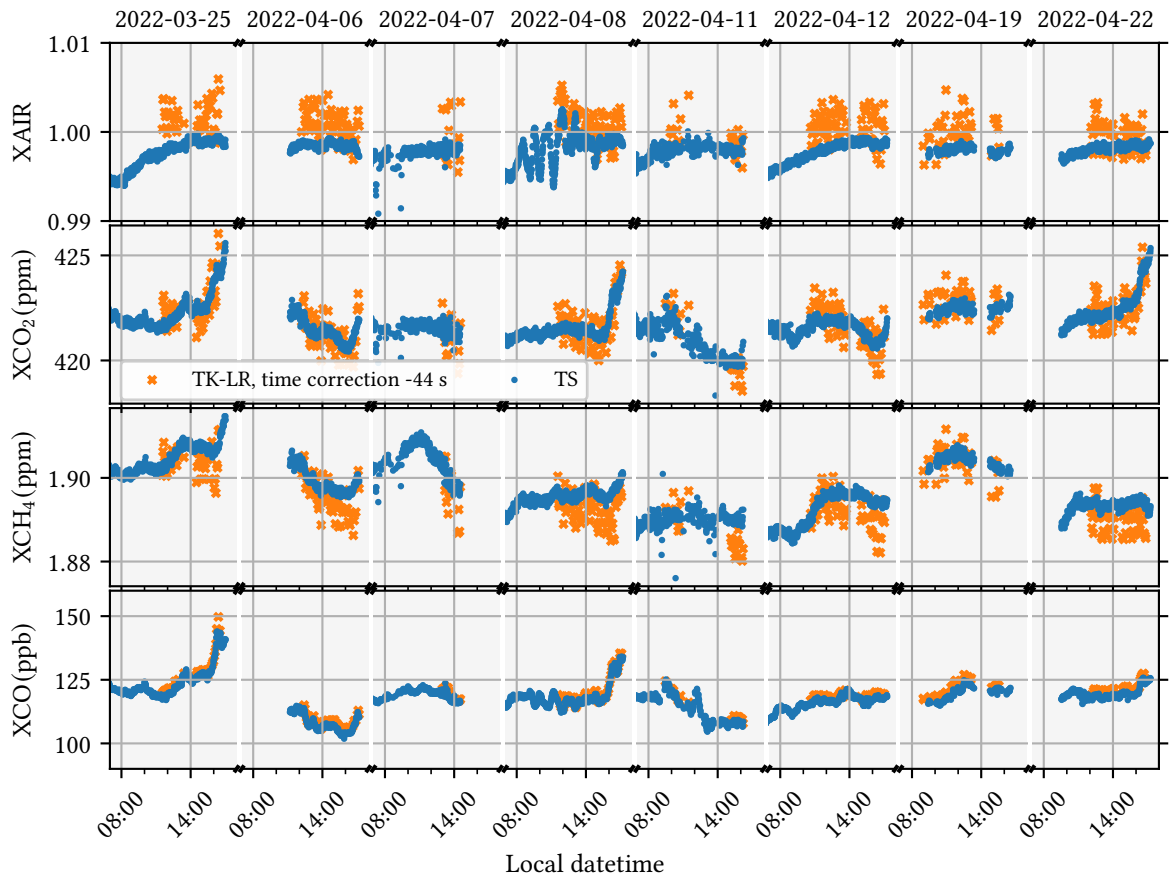


Figure 5.3.: XGas results of the Tsukuba data with -44 s time correction. The correction removes the airmass dependency of XAIR almost completely. For a more detailed evaluation see in the main text.

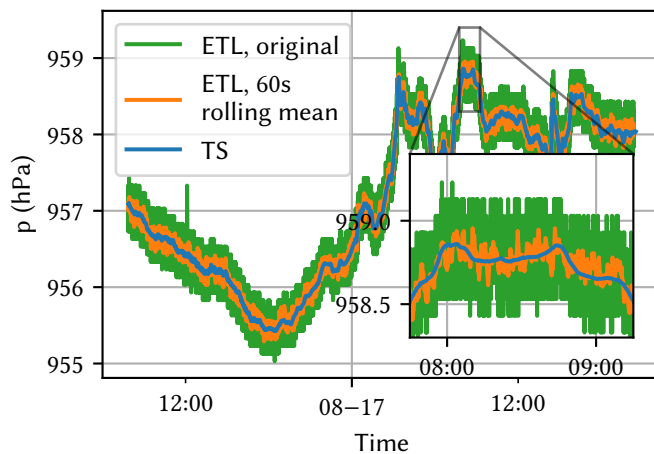


Figure 5.4: Side-by-side comparison of pressure data in ETL. The data is collected by the pressure sensors of the ETL TCCON and the TS. The TCCON pressure data shows a high noise level. Therefore, it is smoothed by calculating a rolling mean with a window size of 60 s, plotted in orange. To compare measurements with those of the TS data, both, the TS and the rolling mean data are resampled to 60 s bins. The deviation in average is -0.00419 hPa giving a bias compensation factor of $K_{TS_p}^{ETL} = 0.9999956$

them comparable, both, the running average and the TS data are resampled to 60 s bins. The average deviation is -0.00419 hPa giving a bias compensation factor of $K_{TS_p}^{ETL} = 0.9999956$. This indicates an excellent agreement between the pressure sensors. For the TCCON evaluation, the pressure values are smoothed. Therefore, no deviations to the XGas values are expected from the pressure record.

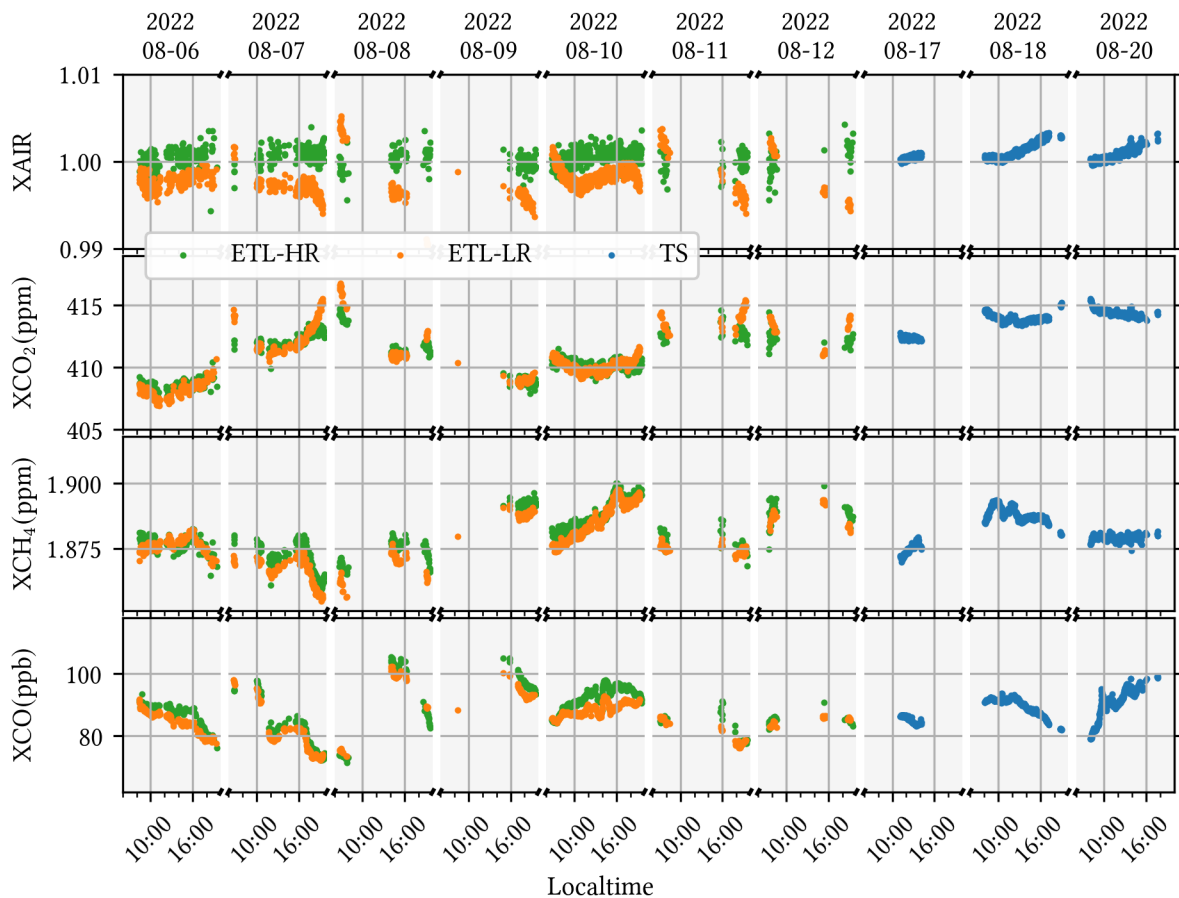


Figure 5.5.: XGas measurements in ETL, Canada. In blue the data of the TS, in green and orange the high- and low-resolution data is plotted, respectively. The laser of the ETL TCCON side broke down shortly before the TS arrived. Therefore, no side-by-side measurements are available. However, the data allows to analyze the noise level and XAIR. For the analysis, see the main text.

XAIR Analysis In Figure 5.5, the XAIR and XGas values measured in ETL by the TCCON and subsequently the TS are plotted. The visual analysis does not reveal any anomalies in the measured data. For the XAIR data, the mean and the standard deviation of the time series of XAIR is calculated for the TS and the ETL-HR and ETL-LR. This is 1.00043 ± 0.00131 for the ETL-HR data, 0.99976 ± 0.00163 for the ETL-LR data, and 1.00095 ± 0.00082 for the TS data. The TS mean is within the expectations for the instrument (compare with Section 4.2.2). The ETL-HR and ETL-LR are both within the 1σ interval of the Karlsruhe and Sodankylä data, compare with Section 3.1.4. Therefore, no instrumental problems are detectable from this. This is remarkable as one might expect artifacts or a bad quality of data resulting from the dying laser.

Noise Analysis: The ETL-HR and ETL-LR data can also be used to check for the noise level. From a visual inspection, it is already apparent that the noise level is lower than it is for the Tsukuba data. A quantitative analysis is provided in Section 5.5.

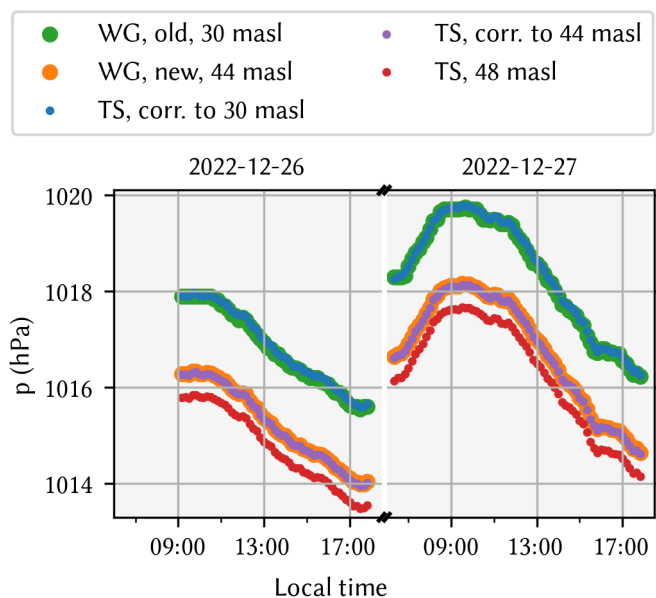


Figure 5.6: Comparison of the pressure records in Wollongong. In Wollongong both, the old and the new TCCON sites are equipped with pressure sensors. The old is at 30 masl, the new at 44 masl altitude. The data of the new sensor is plotted in green and of the old ones in orange. The TS was located at 48 masl hence it is height corrected for an altitude of -4 m (purple dots) and -18 m (blue dots). Both, the pressure data of the old and the new TCCON site are in good agreement with the height corrected TS pressure data. The new pressure sensor is -0.025 17 hPa higher than the TS data. On average, the data of the old TCCON sensor is 0.037 70 hPa lower than the TS data corrected to 30 masl. This gives a bias compensation factor of $K_{WG_p}^{TS_p} = 1.0000373$. The pressure data of the new WG-TCCON site, is not used in this evaluation. The shown days are chosen randomly, for the calculation of the bias compensation factor and the offset, all days in the measurement period are used.

5.4. Wollongong, Australia

The Travel Standard visited Wollongong from 2022-12-06 until 2023-01-26. In this period 15, days of side-by-side measurements could be collected. Currently a new TCCON station is set up in Wollongong. The new one is still in a test phase and does not yet measure continuously. The official TCCON data is still provided by the old instrument. The old TCCON site is located at 34.406 south, 150.879 east at an altitude of 35 masl. The new TCCON site is located in a building nearby at 34.406 south, 150.880 east. The tracker altitude is at 49 masl. The TS was located at the rooftop next to the new TCCON instrument but one meter below at an altitude of 48 masl. The new TCCON instrument is still in the testing phase and therefore, not collecting measurements regularly. Very little data is available during the period of the TS campaign. Therefore, the following evaluation will only consider the data of the old instrument. The only exception to this is the pressure analysis, as the pressure sensor is already measuring continuously. The high-resolution data collected with the old TCCON spectrometer will be denoted as Wollongong high-resolution (WG-HR), the low-resolution data as Wollongong low-resolution (WG-LR).

Pressure Analysis: Both, the old and the new TCCON sites are equipped with separate pressure sensors. The one at the new site is located at 44 masl, the pressure sensor of the old site is located at 30 masl. To compare the pressure data of both sites with the TS measurements, the TS records are corrected for an height difference of -4 m and -19 m, respectively, using equation 2.5 with an average temperature of $T = 22$ °C and $g = 9.81$ m s $^{-2}$. The data is compared over the whole time range the TS collected measurements in Wollongong. In Figure 5.6, two exemplary days of the pressure comparison are plotted. The data of the new TCCON site and the corrected TS data (orange dots and purple crosses) agree well, with a small high bias of the WG sensor of 0.025 17 hPa.

The pressure data of the old TCCON and the corrected TS data to 30 masl are also in good agreement. In average, the measurements of the old TCCON sensor is 0.037 70 hPa lower than the TS data corrected to 30 masl. This gives a bias compensation factor of $K_{WG_p}^{TS_p} = 1.0000373$.

It is important to note, that when writing this thesis the altitudes of the sensors and the trackers are only known with a remaining uncertainty of around 1 m. This is because due to the visit of the TS an error in the altitude of the sensors and the trackers assumed so far was detected. The now used altitudes are determined by pressure measurements of a smartphone.

Furthermore, since the tracker of the old TCCON site is at a height of 35 masl, the pressure data of the old TCCON site should be corrected for the pressure difference resulting from the 5 m height difference. This accounts for an approximate pressure difference of ~ 0.58 hPa that is significant for the retrieval. In the course of the data analysis of the TS, it was found that this correction was not applied to the complete GGG2020 dataset. Luckily, this dataset is not published yet and can be corrected now before publishing it. Furthermore, this error is also present in the GGG2014 dataset. However, no reprocessing is planned, since the GGG2020 data will be the official data product.

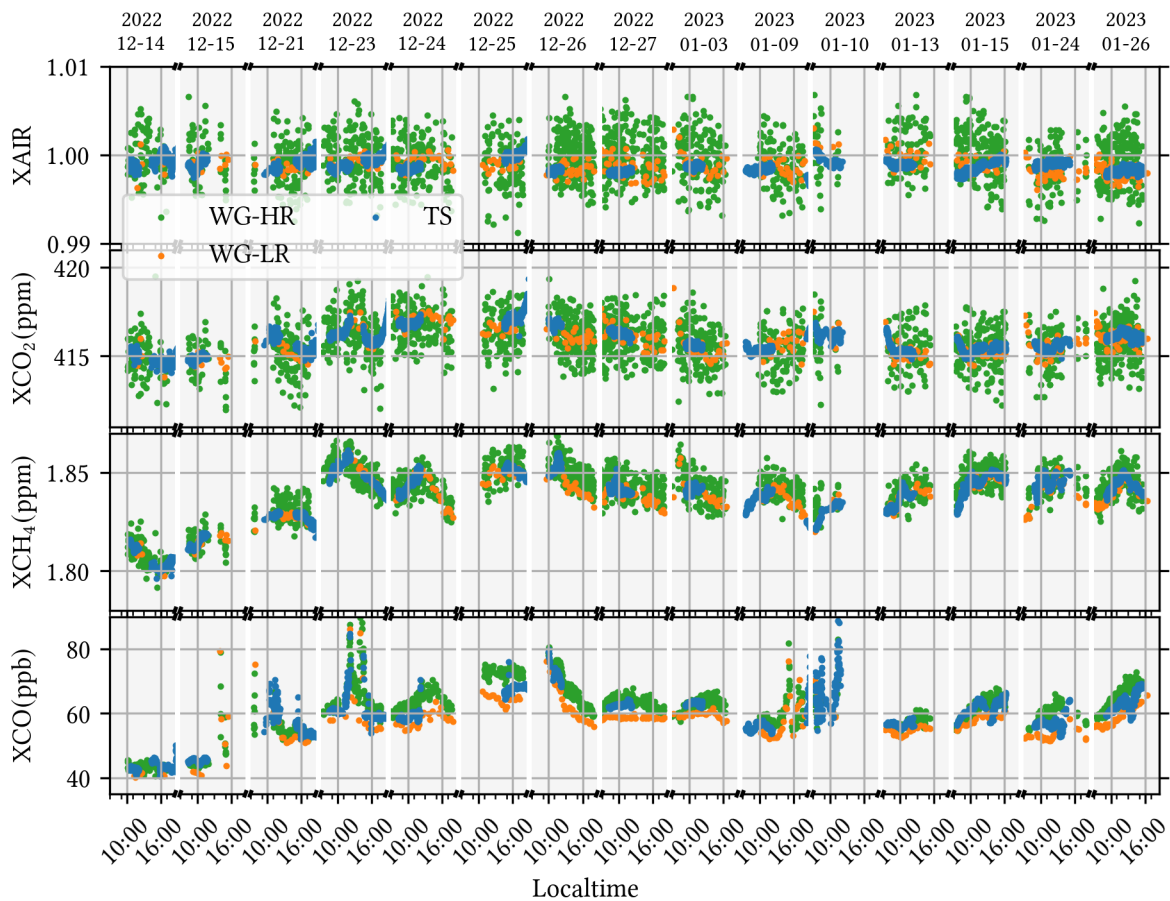


Figure 5.7.: XGas measurements in Wollongong. The WG-HR data processed by the PI of the site is plotted in green, the WG-LR data in orange and the TS data in blue. The overall agreement for all gases is good. Both the WG-HR and WG-LR show a high noise level. This probably results from an intensity drop of the spectra at the O_2 window. It is remarkable that the WG-LR data has a significant lower noise level than the WG-HR data. Furthermore, it is interesting to see that the XCO data does not show a day-to-day variability as the Tsukuba data does. For a discussion of these phenomena, see main text.

XAIR Analysis: The WG-LR data was processed using the pressure data recorded at the old WG-TCCON site with a correction of 5 m to match with the tracker height of the old TCCON site.

The XAIR values measured in Wollongong are plotted in the uppermost panel of Figure 5.7. For the XAIR values of the WG-LR and the TS, the inverse of the retrieved data is plotted to consider the different definitions in GGG and PROFFAST (compare with Section 3.2.1).

For all three, the WG-LR, the WG-HR and the TS data, no severe airmass dependency can be detected. A visual analysis of the WG-HR data reveals a high noise level but the values are distributed evenly around unity. To quantify the XAIR measurements, the mean and the standard deviation of XAIR are calculated. For the WG-HR data, this is 0.99957 ± 0.00253 , 0.99881 ± 0.00105 for the WG-LR data, and 0.99885 ± 0.00078 for the TS data. The data for the TS is in excellent agreement with the expectations defined in Section 4.2.2.

The mean value of both the WG-HR and the WG-LR data is within the 2σ interval of the Karlsruhe and Sodankylä reference data (see Section 3.1.4). The standard deviation for the WG-HR data is 3.2 times larger than for the TS data and 2.4 times larger than the WG-LR data which confirms the visual impression of the high noise level. Except for this, no instrumental issues are detected with the XAIR values of the TCCON site.

XGas Analysis: It is interesting to see that the noise of the WG-HR data is significantly higher than for the WG-LR data. In theory, it is expected that the low-resolution data has less noise than the high-resolution data. However, for the Wollongong data the difference is more apparent than for the other sites. This phenomenon is discussed in more detail in Section 5.5.

The overall agreement is good for all gases. The average difference of the (TS - TCCON) are summarized in Table 5.2. For XCO₂ and XCH₄, the average biases are within the error budget

Table 5.2.: The average bias of the TS and the TK TCCON data.

Species	WG-LR	WG-HR
XCO ₂	0.131 631 ppm	0.137 408 ppm
XCH ₄	0.000 575 ppm	-0.002 489 ppm
XCO	3.190 191 ppb	-1.248 275 ppb

(given in Section 3.1.2). For XCO, the visual analysis of Figure 5.7 does not show a distinct day-to-day difference as it could be seen for the TK data. This is probably because Wollongong is a less urban area than Tsukuba, which is located nearby the Tokyo mega city. Therefore, it is expected that the CO a priori are closer to reality for Wollongong than for Tsukuba.

However, it is interesting to see that the average bias is larger for the XCO WG-LR data than for the WG-HR data. A reason for this is most probably an issue which can hardly be seen from the Figure: The measurement frequency of the WG-LR data is much lower than for the WG-HR or even the TS data. The temporal distance between two measurements is between 10 to 15 min. Hence, sharp peaks like in XCO on 2022-12-23 are not sampled very well and consequently, when comparing the data this can contribute to larger differences.

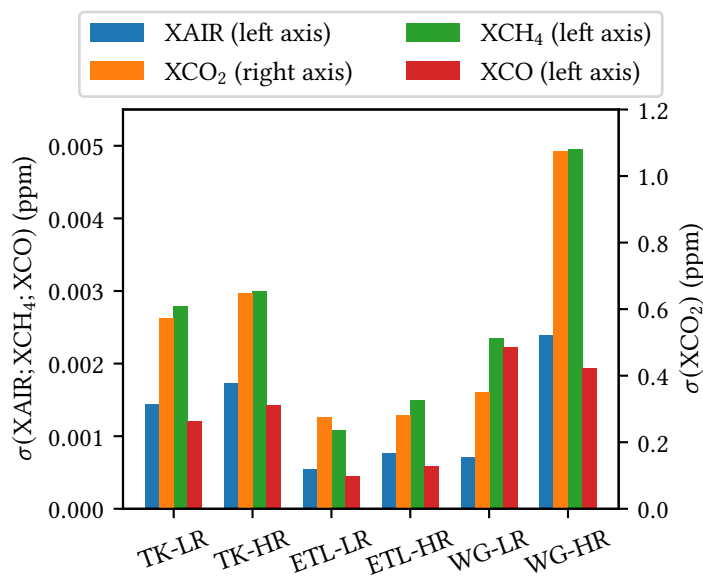
5.5. Noise Analysis

The visual analysis of the Tsukuba and the Wollongong data reveals for both datasets a significantly higher noise level than for the ETL data. To quantify this, the noise is determined by calculating the standard deviation of the de-trended data. The de-trended data is calculated

Table 5.3.: The noise of the different species at the different sites visited with the TS. The data is calculated by first taking rolling mean of 15 data points and subtracting the smoothed data from the original values. The standard deviation of the resulting data is used as a measure of the noise. The data is visualized in Figure 5.8. For XAIR no unit is available, the numbers given here are the standard deviation of the actual measurements.

Species	TK-LR	TK-HR	ETL-LR	ETL-HR	WG-LR	WG-HR
XAIR	0.00145	0.00172	0.00054	0.00077	0.00072	0.00239
XCO ₂ (ppm)	0.57111	0.64637	0.27585	0.28125	0.35094	1.07527
XCH ₄ (ppm)	0.00279	0.00300	0.00108	0.00149	0.00235	0.00495
XCO (ppb)	1.21170	1.42212	0.44576	0.58671	2.22172	1.92952

Figure 5.8: The noise analysis of the XGas values of the three TCCON sites visited with the TS. Note that XCO₂ scale is on the y-axis to the right and the scale of all other gases refer is on the y-axis to the left. XCO is plotted in ppm to increase its visibility. For XAIR no unit is available, the numbers given here are the standard deviation of the actual measurements. The data confirms the visual analysis that the Tsukuba and Wollongong datasets is much noisier than the ETL data. Furthermore, for all sites and almost all species (except XCO), the high-resolution (HR) data has a higher noise level than the low-resolution (LR) data. The numbers are also given in Table 5.3.



for each day by calculating the rolling mean of 15 data points and subtracting the smoothed curve from the original values. Based on these values, the standard deviation is calculated as a measure of the noise. The data is given in Table 5.3 and visualized in Figure 5.8. There, two interesting features can be observed. First, the visual impression of a higher noise level of the Tsukuba and Wollongong data is confirmed. Especially the high noise of the WG-HR data is clearly visible. Second, for all instruments and all species, except XCO, the low-resolution data is less noisy than the high-resolution data. This can be explained by the signal-to-noise ratios of the interferograms. This is discussed in more detail in the following sections.

5.5.1. Intensity Drop in Spectra at the O₂ Window

According to Equation (3.4), the XGas products are calculated using the total column number of O₂ (VC_{O_2}) and the respective species. In order to track down the source of the noise it is necessary to check these two values. For both, Tsukuba and Wollongong, they are plotted in Figure 5.9. These figures show clearly that for the TCCON data, the noise level of the O₂ columns are significantly higher than for the CO₂ columns. For the TS data, the noise levels are comparable. Furthermore, it can be seen clearly that the noise level of the high-resolution data is higher than for the low-resolution data (compare with Section 5.5.2).

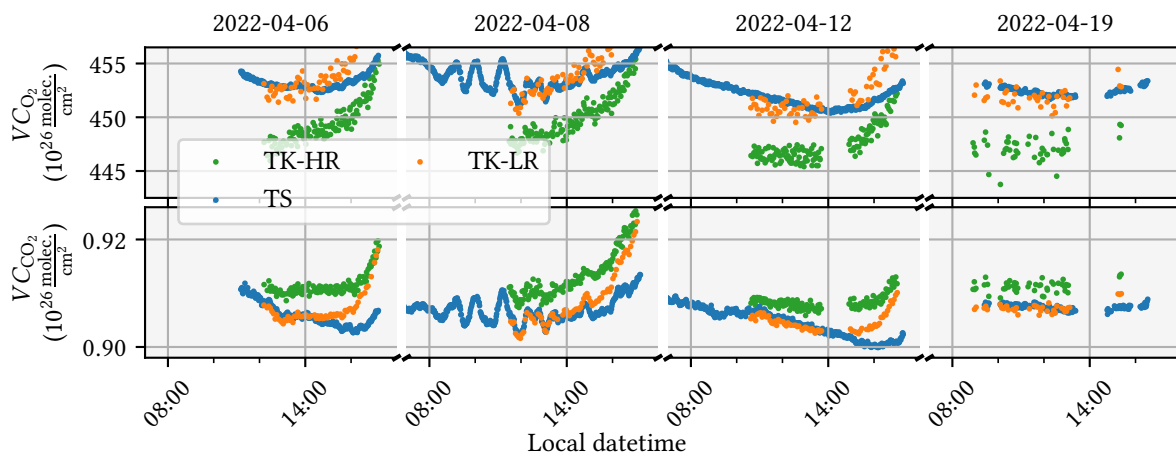


Figure 5.9.: Total columns of O_2 (top panel) and CO_2 (lower panel) measured in Tsukuba by the TS and the TCCON site. The TS data are plotted in blue, the TK-LR data in green and the TK-HR data in orange. The dates are selected because these days the absolute values are similar such that the plots have to cover a limited y-range and can show more details. Both dataset show clearly that for VC_{O_2} the noise level of the TCCON data is much higher than for the TS data. Furthermore, it can be seen that the noise level of the low-resolution data is less than for the high resolution data. For VC_{CO_2} the noise level of the TCCON data is significantly smaller than for the VC_{O_2} data. The TS data are comparable in noise for both gases.

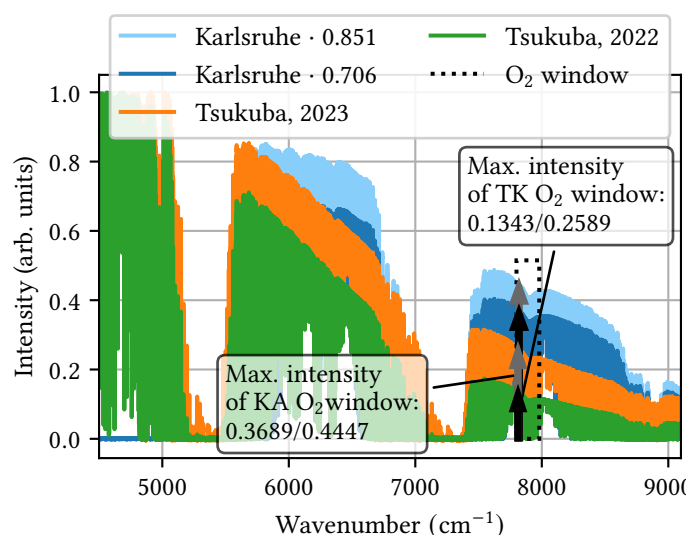
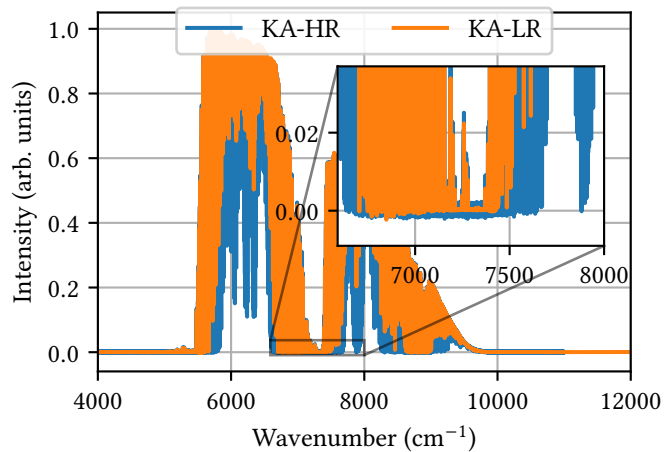


Figure 5.10.: Comparison of the spectra as recorded by TCCON spectrometer in Karlsruhe (blue and light blue) and in Tsukuba (green and orange). The green spectrum is recorded in 2022, the orange in 2023. The Karlsruhe data shows the same spectrum twice, recorded in 2022 but multiplied with different factors. The Tsukuba spectra are normed to unity, the Karlsruhe spectra are normed to the intensity of the Tsukuba spectrum at 5680 cm^{-1} . The Karlsruhe spectrum in light blue is normed to the 2023 Tsukuba spectrum and the spectrum in dark blue is normed to match with the 2022 Tsukuba spectrum. The reason for the Karlsruhe spectrum drops to zero at 5450 cm^{-1} is the non-standard TCCON setup in Karlsruhe (compare with section 3.1.4). The spectral window used to retrieve the O_2 column is marked using the dashed black rectangle. The strong intensity decrease towards higher wavenumbers is the reason for the high signal to noise level in the Tsukuba XGas values. After a realignment of the Tsukuba spectrometer in early 2023 the intensity drop is less significant.

The reason for the higher noise level in the VC_{O_2} values can be found in the shape of the spectra. In Figure 5.10, example spectra of Tsukuba and Karlsruhe are compared. The Tsukuba spectrum is plotted in green and the Karlsruhe spectrum in dark blue. The TK spectrum is normed to unity. Due to the different setup of the Karlsruhe TCCON site, the KA spectrum does not cover

Figure 5.11: Comparison of the low-, and high-resolution spectra of the Karlsruhe TCCON spectrometer. Both spectra are normed to unity. The SNR of the Karlsruhe low-resolution (KA-LR) spectrum is significantly higher than for the Karlsruhe high-resolution (KA-HR) spectrum. Furthermore, it can be seen that the absorption lines of the LR spectrum are less pronounced than for the HR spectrum. Both effects are in agreement with theory.



the same range as the TK spectrum. Therefore, the KA spectrum is multiplied with a factor such that the intensities of the TK and the KA spectra at 5450 cm^{-1} are equal. This makes the spectra comparable at the O_2 window. The intensity of the TK spectrum drops fast towards higher wavenumbers. Relative to the highest value in the TK spectrum, the intensity in the spectral window used for the O_2 retrieval (marked by the dashed black rectangle) is only 13.43%, whereas it is 36.89% for the KA spectrum. After a realignment of the Tsukuba instrument in early 2023, the intensity drop became less severe. This is plotted using orange color for the TK spectrum and light blue color for the KA spectrum. The KA spectrum is plotted again to serve as a reference. It is multiplied with a different factor since it needs to be adapted to the maximum intensity at 5450 cm^{-1} of the Tsukuba spectrum to be comparable. The realignment improved the shape of the spectrum so that the maximum intensity in the O_2 window increased by more than 90%. However, it is still worse than for the Karlsruhe spectrum. From this, one still would expect a significant larger noise level in the TCCON data. The remaining issue is probably due to the beam splitter or the detector element.

This is an important discovery because it is probably an issue several TCCON stations are having and it influences the precision of the TCCON data. Therefore, this is examined systematically in Section 5.5.3.2.

5.5.2. High vs. Low Resolution Spectra

The previous sections showed that for XCO_2 and XCH_4 , the low-resolution measurements are less noisy compared to the high-resolution measurements. For XCO , this behavior is not as pronounced.

While there are several parameters that can influence the precision of the retrieval of a XGas value, here two key criteria are identified and put into focus:

1. The resolution of the spectrum must be high enough to resolve the absorption lines properly. In general, for higher resolved spectra, the absorption lines are more pronounced than for low-resolution spectra. This is because reducing the resolution has the same effect as smoothing the spectrum using a sinc-kernel (compare with Section 2.3.4.1).
2. The SNR in the spectra should be high. Since the noise is a statistical quantity, it cannot be reproduced by the forward model and is therefore causing higher fit residuals.

To increase the resolution of a spectrum, the OPD_{\max} must be increased. However, according to theory, the SNR decreases with increased OPD_{\max} (compare with Equation (2.95) in Section 2.3.4.5). This can be seen in Figure 5.11 which shows the Karlsruhe LR and HR spectra. The high-resolution spectrum has a clearly higher noise level than the low-resolution measurement (compare especially with the inset in the figure). Furthermore, it can be seen clearly that the absorption lines in the low-resolution spectrum are less pronounced than in the high-resolution spectrum.

Both CO_2 and CH_4 are strong absorbers in the NIR. Therefore, the criterion 1 given above is less dominant. Consequently, the low SNR for the high-resolution spectra is dominant and thus, the noise in the retrieved products is increased, too.

In contrast, CO is a weak absorber in the NIR. Therefore, the advantage of more pronounced lines of the higher resolution is more dominant. Therefore, the noise level in the XCO retrieval is similar for both, the HR and LR measurements or even larger for the low-resolution measurements. Both effects, the lower noise for the LR spectra and the more pronounced lines for the HR spectra can be seen in Figure 5.8.

The noise level of XCO_2 and XCH_4 is significantly larger for the WG data than for the TK and KA data. The reason for this is investigated in the following.

When recording spectra with a FTIR-spectrometer it is possible to average several fwd and bwd measurements to a single interferogram and to select different scan speeds. Sampling time per interferogram point and resulting statistical noise level depends on these choices. Therefore, as a first step the selected scan speed and the number of averaged fwd and bwd interferograms for the measurements at the different sites are looked up and are summarized in Table 5.4. From

Table 5.4.: The number of fwd (n_{fwd}) and bwd (n_{bwd}) scans averaged for the HR and LR measurements at different sites as well as the scan speed. The scan speed are the number of iterferogram points sampled per seconds.

Site	n_{fwd}	n_{bwd}	scan speed (kHz)
KA-LR	2	2	10
KA-HR	2	2	10
TK-LR	2	2	10
TK-HR	1	1	7.5
WG-LR	8	8	10
WG-HR	1	1	10

theory it is known, that the averaging of n samples reduces the random noise and therefore also the SNR by a factor of \sqrt{n} . This indicates that the reason for the larger difference of noise levels in the WG-HR and WG-LR XGas time series are caused by the different amount of averaged interferograms.

It would be desirable to have a way to test if the above assumption is true. That is, we want to test if the large difference in noise level between the WG-HR and WG-LR XGas time series is caused only by the different number of averaged interferograms, or if there are some other cause as well. However, there is no unique law to propagate the noise level in the interferograms to the noise level in the XGas time series. (Compare with Section 5.5.3.2, in which it is tried to empirically derive a relationship between the local SNR in the spectrum and the XGas time series.)

Alternatively, the noise level of the spectra can be checked instead. Therefore, here a consistency test is developed in the following which tests if the noise levels of HR and LR spectra are comparable. This allows to check if e.g. for the HR measurement problems arise at larger OPDs or for some unknown other issues. For this, the SNR of low-resolution spectra recorded with the TCCON spectrometer are compared to the SNR of truncated high-resolution spectra recorded with the same spectrometer. Truncated means that the interferograms of the spectra are truncated at the OPD_{\max} of the low-resolution interferograms.

Assuming that the HR and LR spectra are recorded using the same parameters (besides the resolution), both, the truncated and the natively LR spectra should have a very similar SNR. If this is not the case, this is a strong indicator that there is an undetected issue with the instrument. The result of this comparison are summed up in Table 5.5. The spectra used for this comparison are created from the interferograms and truncated using OPUS and are all apodized with the OPUS build-in “Norton-Beer-Medium” function and used the OPUS build-in phase correction method “Mertz”. OPUS automatically averages all fwd and bwd spectra. To take this into account, the SNR listed in Table 5.5 are divided by $\sqrt{n_{\text{bwd}} + n_{\text{fwd}}}$ to make them comparable. The method to calculate the SNR is the following: All of the examined spectra contain fully

Table 5.5.: Comparison of the SNR of LR and truncated HR spectra. The HR spectra are converted to the same resolution as the LR spectra using OPUS. The maximum value O_2 window is the maximum value found in the spectral window from 7800 cm^{-1} to 7980 cm^{-1} of a spectrum normed to unity. The SNR is determined by dividing the maximum value within the O_2 window by the noise. The noise is determined by taking the standard deviation of the spectra in the range larger than 15000 cm^{-1} and smaller than 3800 cm^{-1} in which no signal is present. The relative deviation of the SNRs of the LR and truncated HR spectra are calculated using the SNR corrected for the number of averaged fwd and bwd spectra.

Site	max. val. O_2 window	SNR	$\frac{\text{SNR}}{\sqrt{n_{\text{bwd}} + n_{\text{fwd}}}}$	Deviation (%)
KA-HR	0.5558	2622.43	1311.22	2.29 %
KA-LR, truncated	0.5543	2562.00	938.00	
TK-LR	0.1487	1876.00	938.00	7.03 %
TK-HR, truncated	0.1488	1234.02	872.59	
WG-LR	0.1478	1618.85	404.35	3.47 %
WG-HR, truncated	0.1481	591.50	418.26	

opaque regions beyond 15000 cm^{-1} and below 3800 cm^{-1} . The noise is then calculated by taking the standard deviation of all data-points within these regions. As a measure of the signal strength the maximal value within the O_2 window ($7800 \leq \tilde{\nu} \leq 7980$) is used.

When considering the averaged forward and backward measurements the maximal relative deviation of the LR and truncated HR spectra is 7.03 % for the TK data. For KA and WG the deviation is only 2.29 % and 3.47 % which is very small. The reason for the larger deviation of the TK measurements is probably the different scan speed of the HR (7.5 kHz) and LR (10 kHz) measurements.

This results does not indicate any undetected problems and hence, underlines the assumption that the high noise difference in the XGas WG-HR and WG-LR spectra are due to the different number of averaged interferograms.

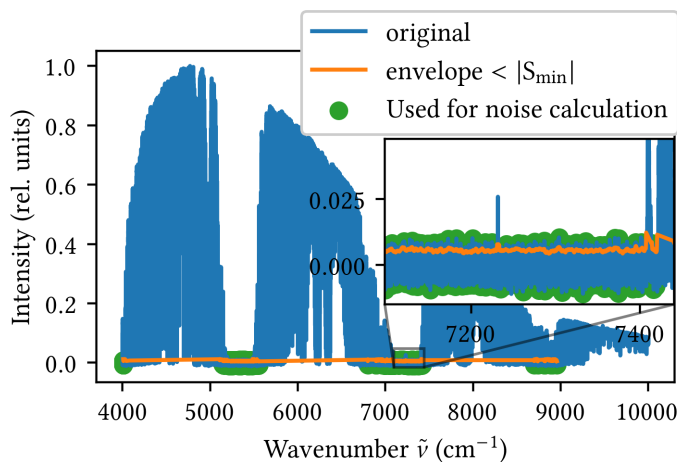


Figure 5.12: Calculation of the SNR for the O₂ window. The spectrum is measured at the Ny-Ålesund TCCON site. As the spectrum does not have a “tail” outside of the spectral signal which can be used to determine the noise, self-written algorithm is used to calculate the SNR. This algorithm identifies spectral ranges which contain no signal (marked with the green dots). The noise is calculated by taking the standard deviation of these data-points. The signal is calculated by taking the local maximum in the O₂ window (7800 cm⁻¹ - 7980 cm⁻¹). The algorithm to find the spectral ranges without signal coarsely works as follows: First, it calculates the envelope of the spectrum. Second, all values larger than the absolute of the global minimum $|S_{\min}|$ (which is negative) are deleted. The result of this step is marked with the orange line. Lastly, outliers from the remaining data are removed. A detailed description is given in the main text.

The analysis of comparing natively LR and truncated HR spectra may be a helpful method for future investigation of TCCON sites. Especially, because it can be done without any other equipment like gas-cells for ILS measurements or even the TS as an external reference.

5.5.3. Network-wide Data Analysis

Since the high noise level in WG and TK are both caused by an intensity drop in the spectra towards higher wave numbers, it is reasonable to assume that the problem also occurs with other stations in the network. This is investigated in this section. First by a direct approach which analyzes spectra of different TCCON sites directly and second, by an indirect method which uses the evaluated GGG data.

5.5.3.1. Direct Spectra Analysis

For the direct analysis, the PIs of the TCCON network were asked to send spectra of a clear, sunny day at around local noon. Unfortunately, not all of the spectra sent by the PIs have enough data points before and after the spectrum which can be used to determine the noise, as it is done in the previous section. This can be seen in Figure 5.12, which shows the spectra from Ny-Ålesund. There, no “tails” are available which can be used to determine the noise. Instead, these spectra are analyzed by a self-written algorithm which determines the SNR ratio in the O₂ window. The main idea of the algorithm is simple. It detects the spectral ranges in the spectrum which do not contain any signal even though when no “tails” are available. These data-points are used to calculate the standard-deviation which is used as a measure of the noise. The signal strength is calculated by taking the global maximum within the O₂ window (7800 cm⁻¹ - 7980 cm⁻¹).

The working-principle of the algorithm is illustrated in Figure 5.12. It performs four steps:

1. Calculate the global minimum S_{\min} of the spectrum. Since the noise scatters around zero, this is a negative value.

2. Calculate the envelope and delete all data points of the envelope which are larger than $|S_{\min}|$ (orange line in Figure 5.12).
3. This line describes already approximately the wavenumber ranges without signal. However, there it can still include some data-points with signal. To detect these, a further step is needed. The remaining data-points which describe the envelope are clustered. All data-points of the original spectrum which lie within such a cluster are used for the further analysis: The mean m and the standard deviation σ of these data-points is calculated. All points outside of $m \pm \sigma$ are assumed to contain a signal and are deleted.
4. The remaining points are used to calculate the standard deviation which is used as a measure of the noise. These points are highlighted with green color in the figure.

As one can see in Figure 5.12, the method reliably detects the correct wavenumbers which contain no signal. As a measure of the signal strength, the maximal value in the O₂ window (7800 cm⁻¹ - 7980 cm⁻¹) is taken.

In Table 5.6 a comparison of the SNRs calculated by the presented algorithm and the “tail” method used in Section 5.5.2 using the same spectra as in 5.5.2. It can be seen that the deviation

Table 5.6.: Comparison of different methods to calculate the SNR. The SNRs calculated by the algorithm presented in Section 5.5.3.1 are compared to ones calculated with the “tail” method in Section 5.5.2. The used spectra are the same as used in Section 5.5.2. The difference can be up to 25%. It is assumed that the “tail” method is superior, however, not usable for all type of spectra.

Site	max. val. O ₂ window	SNR by using algorithm	SNR by using “tails”	Deviation (%)
KA-LR	0.5558	3031.81	2622.43	15.6
KA-HR	0.5543	2766.22	2562.00	8.0
TK-LR	0.1487	1397.46	1876.00	25.5
TK-HR	0.1488	1080.04	1234.02	12.5
WG-LR	0.1478	1265.32	1618.85	21.81
WG-HR	0.1481	567.38	591.50	4.0

can be up to 25.5% which is a quite large deviation. However, when writing this work, it is the best available option to determine the SNR of all spectra provided across the TCCON and therefore still used.

The results of the analysis with this algorithm are given in Table 5.7. The results vary clearly for the different sites. The high noise levels found for the TK and WG with the TS analysis can also be found in this table. The sites which have recently installed a new spectrometer show, that for the newer ones, the SNR is better. After a realignment of the Tsukuba instrument in 2023, the SNR and the maximal O₂ level increased significantly.

This analysis, however, shows clearly that there are other stations which suffer from a low SNR, like Ny-Ålesund, Zugspitze or Anmyeondo. As the example of Tsukuba shows, a realignment of the spectrometers at those stations might already improve the SNR. As an interesting side note, one can see that the Karlsruhe TCCON spectrometer by far has the highest SNR ratio. The main reason for this is the different setting of the site as described in Section 3.1.4: The spectral range needed for TCCON measurements is covered by two detectors instead of one. Here, we are considering two effects contributing to this observation.

Table 5.7.: SNR analysis of the O₂ window for various TCCON sites. All the spectra were recorded at around noon on a clear, sunny day. The method to determine the SNR values is explained in the main text. It is clearly visible that the SNRs vary strongly across the network. Furthermore, the sites in Tsukuba and Wollongong have some of the lowest SNRs which is also found by the analysis of the TS. In Tsukuba, the instrument is realigned in 2023 which significantly increased the SNR.

Site	max. value within O ₂ window	SNRs for spectral O ₂ window
Rikubetsu	0.3075	271.2298
Burgos	0.3395	392.7592
Izaña	0.3052	212.2268
Wollongong, new	0.5692	274.7110
Wollongong, old	0.1510	49.8372
Lauder, old	0.3097	272.7060
Lauder, new	0.6145	306.8384
Ny-Ålesund	0.2775	101.6041
Anmyeondo	0.2968	163.7335
Karlsruhe	0.5212	901.7539
Tsukuba	0.1348	95.6686
Tsukuba, realigned	0.2585	220.1736
East Trout Lake	0.2881	197.2654
Garmisch	0.5086	223.6055
Zugspitze	0.0963	63.1467

The first is that each detector has a maximum intensity it can measure without showing unacceptable non-linearity effects (i.e. the measured voltage is not linearly correlated to the number of incident photons). This means, the maximum amount of photon flux a detector can measure is limited. Therefore, a smaller spectral bandwidth allows to reach a higher spectral signal to noise ratio as more photons per spectral range can be collected. In Karlsruhe, the spectral range a single sensor has to cover is less than for the standard TCCON setting. Therefore, the amount of photons the detector can handle needs to be distributed to a smaller spectral range. This allows to increase the diameter of the shutter of a FTIR-instrument such that a higher amount of photons are falling onto the detector, hence there are more photons wavenumber-interval. This increases the signal and hence, causes a higher SNR.

The second is caused by the so-called photon-noise. Due to the particle character of light, there are statistical fluctuations in the number of photons per time interval (i.e. intensity). Let n be the number of photons which are collected in the sampling time interval, then the noise scales with \sqrt{n} (Davis et al. 2001). Hence, by reducing the spectral range using e.g. an filter, the number of photons is decreased and hence, also the noise level is decreased. When choosing the filter such, that only the region of interest is covered, this reduced the noise in the interferogram but not the signal strength in the desired interval. Therefore, the SNR increases as well.

5.5.3.2. Systematic Analysis Using Internal TCCON Engineering Data

The analysis of the SNR in the spectra as described above is an interesting tool for a quick analysis of the spectrum quality. However, it has some disadvantages: First, it is based on a single interferogram which may not be representative for the instrument since it can be affected by e.g. cloudy conditions, a bad tracking or similar incidents. Furthermore, the spectra files are

provided as OPUS files, a proprietary program by BRUKER. Therefore, it was not possible to ensure that for all spectra the same settings (phase correction or apodization) were used for the generation from the interferograms. In addition, it only can assess the SNR in the spectra, but not the noise level in the final XGas product. Lastly, the organizational effort to get and manage the spectra from the individual PIs is high.

Therefore, an alternative approach for investigating this is presented in this section. It uses the TCCON-internal engineering files of the GGG2020 evaluation. These files contain more diagnostic information than the public available TCCON results.

However, this data does not contain a direct measure of the SNR. Therefore, another quantity is used, which can be used to approximate the SNR. This quantity is called the “root-mean-square-over-continuum-level” (rmsocl). It is the root-mean-square of the residuum of the retrieval divided by the continuum level of the window.

The residuum is the difference between the simulated and the measured spectrum. The deviation of the simulated and measured data origins from systematic errors like inaccuracies in the spectroscopic data or an inaccurate description of the FTIR-spectrometer. But also the measured noise contributes to the residual. Here, it is assumed that the systematic contributions are small and therefore, the residuum can be used as a measure of the noise level in the spectra. The continuum level is a parameter which describes the envelope of the spectrum in the spectral window used to retrieve a parameter. I.e. it describes the maximal signal which is measured at wavenumbers at which no absorption lines are located and hence is a direct measure of the signal strength. Therefore, the inverse of the rmsocl is assumed to be similar to the SNR.

To indicate that $1/\text{rmsocl}$ is only similar to the SNR it is denoted as “spectral signal quality” (SSQ) in the following:

$$\text{SSQ}_{\text{wn-gas}} = \frac{1}{\text{gas_wn_rmsocl}} .$$

`gas_wn_rmsocl` is the notation used in the engineering files, where `gas` is the chemical formula of the species and `wn` is the central wavenumber of the spectral window.

Some gases like CO_2 or CH_4 are measured by the TCCON in several spectral windows. Hence, the TCCON-engineering files contain rmsocl-values for each window. For those species the SSQ is calculated by first taking the average of the rmsocl of all spectral windows and then calculating the inverse of this average:

$$\text{SSQ}_{\text{gas}} = \frac{1}{1/N \sum_{\text{wn}} \text{gas_wn_rmsocl}} .$$

Here, N is the number of spectral windows.

Comparison of the SSQ and the SNR To assess if it is valid to use the SSQ as a proxy for the SNR, the SSQ and the SNR values are compared in this section. For the comparison the SNR values given in Table 5.7 are used. For the calculation of the SSQ, the TCCON-engineering data after 2021-01-01 are used. Unfortunately, the overlap of sites which provided a spectrum and which uploaded the GGG2020 data is only 10. The data is plotted in Figure 5.13. The figure shows a clear correlation between the SNR and the SSQ. Interestingly, the data split up in two groups: For the TCCON sites in Burgos, Rikubetsu and Karlsruhe (“bu”, “rj”, “ka”) the SNR/SSQ ratio is around 240 (orange fit line at the right panel in Figure 5.13). The remaining sites have a SNR/SSQ ratio of around 90. The reason why the data splits into two groups is still under

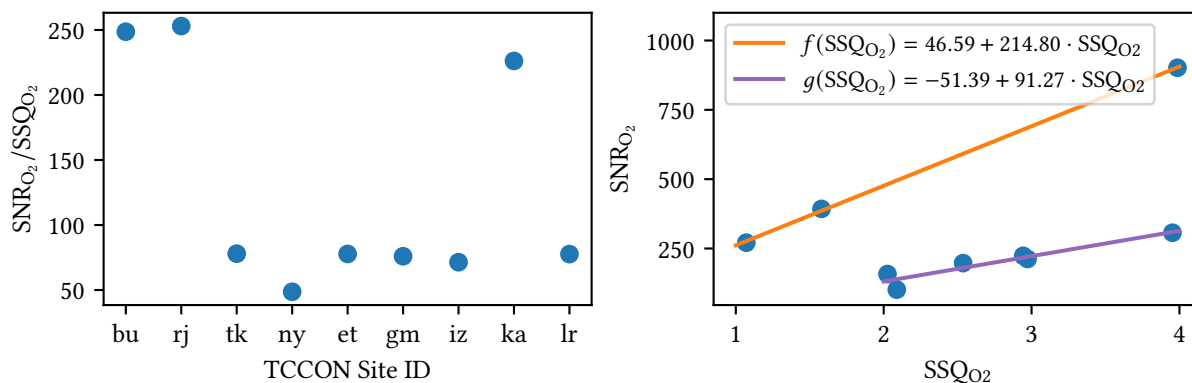


Figure 5.13.: Comparison of the SSQ value derived from the engineering files and the SNR values given in Table 5.7. The left panel shows the ratio of the SNR over the SSQ for the O₂ window. The right panel shows a scatter plot of the SNR data over the SSQ data. The data show a clear correlation between the SSQ and the SNR values of the sites. Interestingly, the sites can be divided into two groups: The first with a SNR/SSQ ratio of averaged 214 (sites “bu”, “rj” and “ka”) at the left panel correspond to the orange fit at the right panel. The second sites with a SNR/SSQ ratio of around 90 at the left panel correspond to the purple fit at the right panel. The reason for the two groups is still under investigation.

investigation. This shows that due to the clear correlation the SSQ value can be used as a proxy for the SNR.

Note that for Tsukuba the average of the SNR values in 2022 and 2023 is used. This is because the SSQ value is an average of the data since 2021 and it is assumed that the alignment deteriorated over time. Hence, by using the average it is attempt to generate a value which is similar to the timely average of the deterioration.

Correlate SSQ With the Noise of XGas A major advantage of the analysis using the internal TCCON engineering files is the following. It allows to not only have a measure of the SNR in the spectrum but also to retrieve the noise level of the final XGas time series.

The noise levels of the XGas time series are derived in three steps: First, the time dependent data is smoothed by an running average. Second, the original time series is divided by the smoothed series. Third, the standard deviation of this data is calculated as a measure of the noise of the XGas values. The so calculated noise will be denoted as σ_{XGas} .

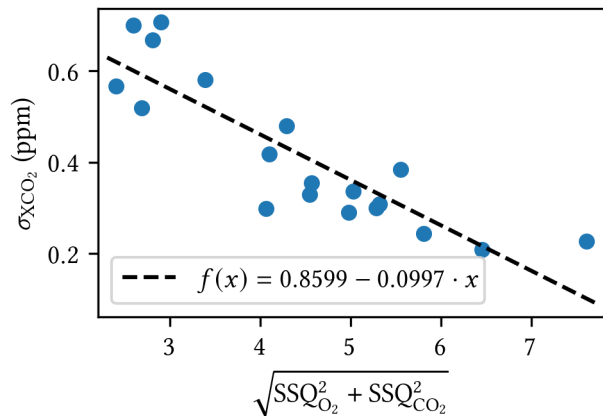
Therefore, this method allows to check if there is a correlation between the SSQ (or the SNR, respectively) in the spectra and the noise level in the XGas time series. From theory one would expect that *high* SSQ values cause *low* noise levels in the XGas time series.

For the upcoming analysis the TCCON-engineering data beyond 2021-01-01 is used. Here, only the correlation for CO₂ is examined. The examination for CH₄ is given in Appendix C.

According to Equation (3.4), for the calculation of XCO₂ the retrieved values from the O₂ window and from the CO₂ windows are used. Therefore, the SSQ values of both, CO₂ and O₂ have to be considered. It is assumed that the SSQ (and hence, the SNR) are mostly caused by a random error. Therefore, the SSQ values are added quadratically before and the square-root is taken: $\sqrt{\text{SSQ}_{\text{CO}_2}^2 + \text{SSQ}_{\text{O}_2}^2}$. To verify the presumed correlation, the added SSQ values are plotted against the noise level of the XCO₂ time series (σ_{XCO_2}) in Figure 5.14.

This figure clearly shows that the XCO₂ noise level are related to the SSQs (and hence the

Figure 5.14: The figure shows the correlation between the quadratically added SSQs and the XCO₂ noise level σ_{XCO_2} . The calculated values are based on the internal TCCON-engineering files starting from 2021-01-01. Not all TCCON sites have uploaded data after this date. Therefore, some sites are missing. The SSQ values are added quadratically because it is assumed that they are mostly caused by a random error. The plot indicates that both values are correlated.



SNRs) in the spectra. However, the correlation is not very clear, indicating that there are other quantities that influence the noise level σ_{XCO_2} of the XCO₂ time series.

In order to be able to assign the points in the plot to the individual stations, σ_{XCO_2} the SSQ values are shown as a bar chart in Figure 5.15. A list of the site abbreviations is given in Appendix C.

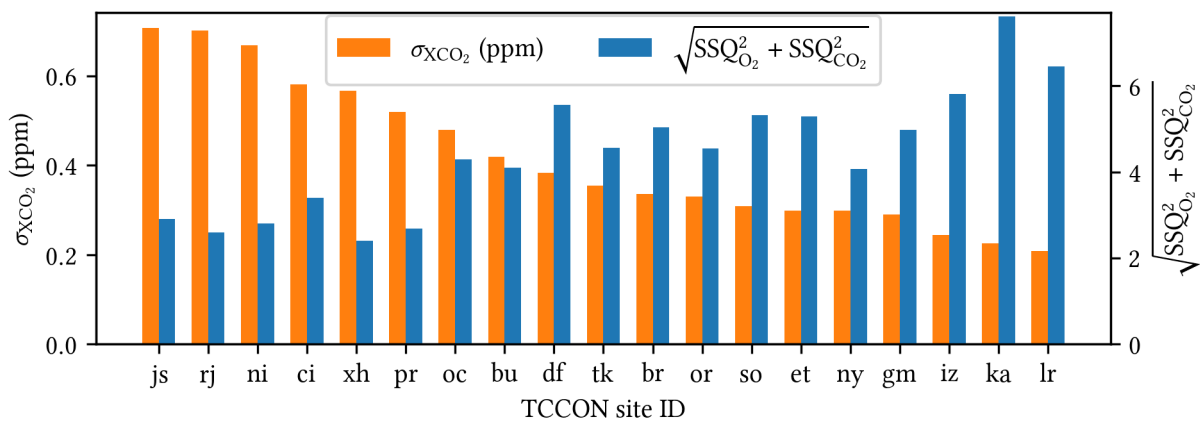


Figure 5.15.: A bar chart of the noise levels of the XCO₂ time series (σ_{XCO_2}) and the SSQs for various TCCON sites. The data is the same as given in Figure 5.14. The $\sigma_{\Delta\text{XCO}_2}$ values refers to the scale on the left ordinate, the quadratically summed SSQs to the scale at the right ordinate. It can be seen that in general a higher SNR gives a lower noise level. However, there are also some exceptions as e.g. “df”. The sites are sorted in descending order of the σ_{XCO_2} values from left to right. A list of the TCCON site abbreviations (ID) is given in Appendix C.

It can be seen that all sites with a low noise level (below 0.3 ppm) in the XCO₂ time series also show high SSQ values. This suggests that a high SSQ value is a prerequisite for a small noise level σ_{XCO_2} in the XCO₂ time series.

However, the other way round no suggestion can be made. An example of this is the site in Edwards, USA (“df”) which has the ninth highest XCO₂ noise level but also the fourth highest SSQs. This indicates that at this site the reason for the high σ_{XCO_2} value are not the low SSQs but something else which needs further investigations.

For the sites with the six highest σ_{XCO_2} values (“js” to “pr”) the low SSQ level is apparent. This indicates that the low SSQs are the reason for the high noise level in XCO₂ time series. Hence, it is worth to check these sites thoroughly. As indicated by the TK site, a realignment might help to increase the SSQs.

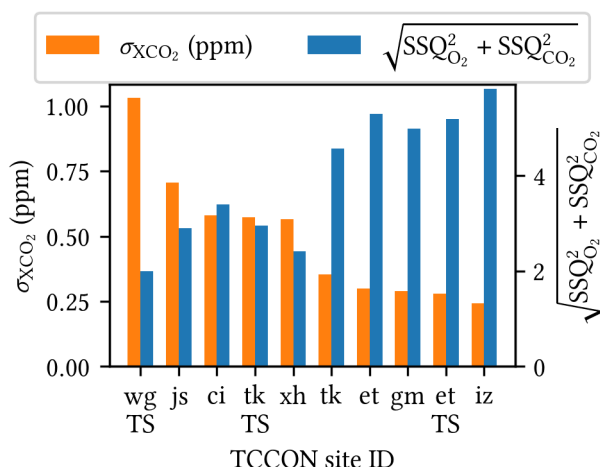


Figure 5.16: The plot shows the systematic noise analysis presented in Section 5.5.3.2 applied to the TCCON data measured during the TS campaigns. The campaign data is marked by a “TS” annotation. The results of the other sites not visited by the TS are the same as in Figure 5.15. They are shown here to place the campaign data in the context of Figure 5.15. The results of the campaign data in this plot are in very good agreement with the spectra analysis in Section 5.5.3.1 and the other results of the TS campaigns: The WG data is expected to show the lowest SSQs in the network due to the low SNR in Table 5.7. For WG no GGG2020 data was published at the time writing the thesis. Therefore, only the campaign data can be shown. The spectrometer in TK was poorly aligned during the campaign causing the low SSQ values and high σ_{XCO_2} values. For ETL, no major difference is expected between the campaign and non-campaign data, as no instrumental problems were found for the ETL spectrometer.

For XCH_4 the analysis is carried out in Appendix C. It shows the same qualitatively behavior.

Application of the Method to the Travel Standard Data Figure 5.16 shows the results of the noise analysis presented in this section applied to the TCCON data recorded during the TS campaigns. The results of this analysis are in very good agreement with the results of the SNR calculations in Section 5.5.3.1 and the results obtained from the time series recorded during the TS campaigns:

- In Table 5.7, the WG spectrum had the lowest SNR ratio of all the spectra analyzed. Therefore, the finding of the lowest network-wide SSQ values is consistent with the low SNR. It is also interesting to note that the σ_{XCO_2} is the highest of all TCCON sites analyzed. Note that for WG not GGG2020 data was published at the time writing this work. Hence, only the campaign data can be shown.
- The analysis of the SNRs in the TK spectra from 2022 (during the TS campaign) and from 2023 (after the realignment) clearly showed that the spectrometer was badly aligned in early 2022. This is in agreement with the SSQ analysis of the TK campaign data in Figure 5.16. The non-campaign data of TK shows higher SSQs and lower σ_{XCO_2} than the campaign data. As the correlation between SNR and SSQ could be shown in this section, it can be expected that the data measured after the realignment in 2023 will again show a much lower noise level in the XGas time series. noise level in the XGas time series.
- The XAIR analysis of the ETL data showed no instrumental problems. Therefore, for the ETL data, similar values for SSQ and σ_{XCO_2} are expected for the campaign and the previous data. This is confirmed in Figure 5.16.

Summary of the Method The method presented in this section successfully reproduces the results obtained with other methods (see the analysis of the TS campaign data). Furthermore, it clearly shows that only sites with a high SSQ have a low noise level in the XGas time series. Moreover, it can detect sites with high noise levels in the XGas products and simultaneously allows to check if a low SSQ (and hence low SNR) is the reason for this. Thus, the analysis

could be a valuable addition to the routine QA/QC procedure of the TCCON. There it can help to improve the detection of high XGas noise levels and low SNRs in the spectra caused by instrumental problems.

5.6. Quantitative Comparison of the Station Data

A main part of the TS analysis is to compare the XGas values of the TCCON sites against the Karlsruhe TCCON site as a common reference. The choice of Karlsruhe as a reference was made because the COCCON reference unit is regularly compared with the Karlsruhe TCCON station. This does not mean that Karlsruhe TCCON is the absolute reference for the network. However, it is an obvious choice to use it as a reference for relative comparisons.

To assess the quality of the compared data it is necessary to know the errors of the comparison. Considering this, an error calculation is carried out for the results. Finally, the data will be summed up and discussed.

5.6.1. Calculation of the Bias Compensation Factors

For each campaign, bias compensation factors between the TS and the TCCON spectrometer are calculated using the method described in Section 4.2.1. These factors are denoted as $K_{\text{TC-ID}}^{\text{TS}}$ and are summed up in Table 5.8 including their random relative error.

Table 5.8.: The bias compensation factors of the TCCON site relative to the TS. They are denoted as $K_{\text{XX-LR}}^{\text{TS}}$ and $K_{\text{XX-HR}}^{\text{TS}}$ for the TCCON-LR, and HR data of the various sites to the Travel Standard including the random relative errors as described in 4.2.1.1. The XX stands for the two letter TCCON ID.

Site	Species	$K_{\text{XX-LR}}^{\text{SN39}}$	$K_{\text{XX-HR}}^{\text{SN39}}$
TK	XCO ₂	1.00000 ± 0.00007	1.00085 ± 0.00007
	XCH ₄	1.00153 ± 0.00008	0.99767 ± 0.00008
	XCO	0.98674 ± 0.00036	0.93233 ± 0.00031
WG	XCO ₂	1.00026 ± 0.00007	1.00037 ± 0.00010
	XCH ₄	1.00026 ± 0.00008	0.99872 ± 0.00009
	XCO	1.05846 ± 0.00258	0.98153 ± 0.00105

Following, it is assumed that the bias compensation factors fully describe the systematic bias between two instruments. Hence, in this ideal assumption the temporal mean $\overline{\text{XGas}}_{\text{YY}}$ of an instrument YY multiplied with a bias compensation factor is equal to the temporal mean $\overline{\text{XGas}}_{\text{XX}}$ of an instrument XX which are both measuring side-by-side:

$$\overline{\text{XGas}}_{\text{XX}} = \overline{\text{XGas}}_{\text{YY}} \cdot K_{\text{YY}}^{\text{XX}}. \quad (5.1)$$

Multiplying the bias compensation factors of different spectrometers allows calculating a resulting factor which allows to compare the data of a remote station to the Karlsruhe TCCON-station:

$$K_{\text{TC-ID}}^{\text{TC-KA}} = K_{\text{TC-ID}}^{\text{TS}} \cdot K_{\text{TS}}^{\text{SN37}} \cdot K_{\text{SN37}}^{\text{TC-KA}} \quad (5.2)$$

This scheme is illustrated in Figure 5.17. Note that $K_{\text{SN37}}^{\text{TC-KA}}$ is unity per definition because the COCCON network as a whole is calibrated such that it matches with the Karlsruhe TCCON station, compare with Section 3.2.2.

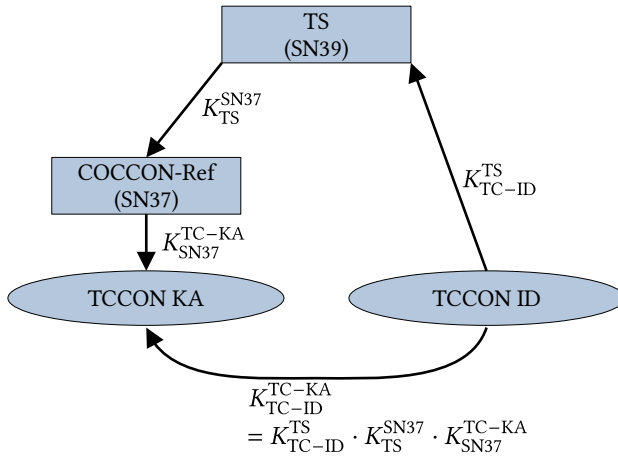


Figure 5.17: A graphical illustration on how to calculate resulting bias compensation factors. The individual factors of each site are used to compare the measurements of a visited TCCON site to the Karlsruhe TCCON site. Note that the K_{SN37}^{TC-KA} is unity due to the calibration of the COCCON network to the Karlsruhe TCCON site as described in 3.2.2.

Table 5.9.: The bias compensation factors between the visited TCCON sites and the KA reference (SN37). All values are given with a random error followed by a systematic error. The errors are described in Section 5.6.2. Since the COCCON network as a whole is calibrated in a way that the reference spectrometer matches with the TCCON Karlsruhe data, a comparison with the reference unit is equal to a comparison of the TCCON-Karlsruhe site.

Site	Species	K_{XX-LR}^{SN37}	K_{XX-HR}^{SN37}
TK	XCO ₂	0.99886 ± 0.00008 + 0.00063	0.99970 ± 0.00008 + 0.00063
	XCH ₄	1.00188 ± 0.00009 - 0.00067	0.99802 ± 0.00009 - 0.00067
	XCO	0.98833 ± 0.00047 - 0.00053	0.93383 ± 0.00043 - 0.00050
WG	XCO ₂	0.99987 ± 0.00007 + 0.00071	0.99998 ± 0.00010 + 0.00071
	XCH ₄	1.00093 ± 0.00008 - 0.00071	0.99939 ± 0.00010 - 0.00071
	XCO	1.05909 ± 0.00259 - 0.00622	0.98212 ± 0.00108 - 0.00577

Table 5.10.: The deviations in percentage of the individual TCCON sites visited with the TS to the COCCON reference unit. The first error given is the random error emerging from the noise of the measurements. The second error is a calibration error which is calculated by considering a potential drift of the TS device relative to the COCCON. A visualization of the data is given in Figure 5.18.

Site	Species	Δ_{XX-LR}^{SN37} [%]	Δ_{XX-HR}^{SN37} [%]
TK	XCO ₂	0.11368 ± 0.00829 - 0.06314	0.02956 ± 0.00839 - 0.06309
	XCH ₄	-0.18738 ± 0.00871 + 0.06685	0.19875 ± 0.00906 + 0.06711
	XCO	1.18111 ± 0.04798 + 0.05455	7.08623 ± 0.04909 + 0.05773
WG	XCO ₂	0.01264 ± 0.00744 - 0.07104	0.00163 ± 0.01023 - 0.07103
	XCH ₄	-0.09253 ± 0.00840 + 0.07089	0.06115 ± 0.00956 + 0.07100
	XCO	-5.57937 ± 0.23080 + 0.55486	1.82105 ± 0.11168 + 0.59835

The bias compensation factors are given in Table 5.9, together with a random error and a calibration error. The errors are described in detail in Section 5.6.2.

These bias compensation factors contain already all the relevant information. However, to make the comparison more intuitive, they are converted to a deviation in percentage. First, an offset in units of a volume mixing ratio from a bias compensation factor is calculated. This is done by multiplying the bias compensation factors with $\overline{XGas_{XX}}$, the temporal average of the XGas over the comparison period:

$$\Delta XGas_{YY}^{XX} = \overline{XGas_{YY}}(1 - K_{YY}^{XX}) . \quad (5.3)$$

Using Equation (5.3) a deviation in percentage relative to the site XX can be calculated using,

$$\Delta_{\%}XGas_{XX}^{YY} = \frac{\Delta XGas_{XX}^{YY}}{\overline{XGas}_{YY}} \cdot 100 \quad (5.4)$$

$$= \frac{1 - K_{XX}^{YY}}{K_{XX}^{YY}} \cdot 100 . \quad (5.5)$$

To deduce Equation (5.5), it is used that \overline{XGas}_{YY} can be replaced by (5.1) causing \overline{XGas}_{YY} to cancel out. The calculated values in percentage are given in Table 5.10.

5.6.2. Error Analysis

To assess the quality of the comparison of the TCCON sites, it is crucial to estimate the potential error which is determined by two different contributions: A random error which is calculated by considering the noise of the individual measurements as well as a calibration error which is calculated by considering a potential drift of the TS instrument relative to the COCCON reference spectrometer.

Random Error: The random error describes the uncertainty arising from the precision of the individual instruments. It is calculated by using the relative random errors of the individual bias compensation factors as described in Section 4.2.1.1. When taking the product of two correction factors, the random error of the resulting product is calculated by using the GAUSSIAN error propagation, as described in Equation (4.5):

$$\frac{\epsilon_{\text{rand}}(K_{\text{TC-ID}}^{\text{SN37}})}{K_{\text{TC-ID}}^{\text{SN37}}} = \left[\left(\frac{\epsilon(K_{\text{TC-ID}}^{\text{TS}})}{K_{\text{TC-ID}}^{\text{TS}}} \right)^2 + \left(\frac{\epsilon(K_{\text{TS}}^{\text{SN37}})}{K_{\text{TS}}^{\text{SN37}}} \right)^2 \right]^{\frac{1}{2}} . \quad (5.6)$$

The errors described by Equation (5.6) are given in Table 5.9.

For the deviation in percentage, as given in Table 5.10, the relative error is also calculated by the GAUSSIAN error propagation of Equation (5.5):

$$\frac{\epsilon_{\text{rand}}(\Delta_{\%}XGas)}{\Delta_{\%}XGas} = \sqrt{\left[\frac{\partial}{\partial K_{\text{TC-ID}}^{\text{SN37}}} (\Delta_{\%}XGas_{\text{TC-ID}}^{\text{SN37}}) \cdot \frac{\epsilon_{\text{rand}}(K_{\text{TC-ID}}^{\text{SN37}})}{K_{\text{TC-ID}}^{\text{SN37}}} \right]^2} \quad (5.7)$$

$$= \frac{1}{(K_{\text{TC-ID}}^{\text{SN37}})^2} \cdot \frac{\epsilon_{\text{rand}}(K_{\text{TC-ID}}^{\text{SN37}})}{K_{\text{TC-ID}}^{\text{SN37}}} . \quad (5.8)$$

Calibration Uncertainty: The second part is an uncertainty introduced by a potential drift of the Travel Standard instrument relative to the COCCON reference. Its upper limit is estimated by the change of the bias compensation factors $\Delta K_{\text{SN39}}^{\text{SN37}}$ before and after each campaign as given in Table 4.2. The uncertainty $\Delta K_{\text{SN39}}^{\text{SN37}}$ is given in percentage. Hence, the calibration uncertainties of $K_{\text{ID-LR/HR}}^{\text{SN37}}$ are calculated by:

$$\epsilon_{\text{cal}}(K_{\text{ID-LR/HR}}^{\text{SN37}}) = \Delta K_{\text{SN39}}^{\text{SN37}} \cdot \frac{1}{100} \cdot K_{\text{ID-LR/HR}}^{\text{SN37}} . \quad (5.9)$$

The relative errors calculated by this equation are given in Table 5.9.

For the deviation in percentage, the calibration uncertainty is calculated by applying linear error propagation to Equation (5.5):

$$\epsilon_{\text{cal}}(\Delta\%) = \frac{\partial}{\partial K_{\text{TC-ID}}^{\text{SN37}}} (\Delta\% \text{XGas}_{\text{TC-ID}}^{\text{SN37}}) \cdot \epsilon_{\text{cal}}(K_{\text{TC-ID}}^{\text{SN37}}) \quad (5.10)$$

$$= \frac{-1}{(K_{\text{TC-ID}}^{\text{SN37}})^2} \cdot \epsilon_{\text{cal}}(K_{\text{TC-ID}}^{\text{SN37}}) \cdot \quad (5.11)$$

The result of this error analysis is given in table 5.10. There, the random error is given first and the calibration uncertainty second.

5.6.3. Evaluation of the Time Corrected Tsukuba Data

In Tsukuba a timing error was detected. For the TK-LR data, the error could be corrected by adding a time difference of -44 s as described in Section 5.2.1. The corrected data is evaluated using the same procedure as for the uncorrected data. The results of the evaluation are given in Table 5.11

Table 5.11.: Bias compensation factors for the time-corrected Tsukuba data. The correction is only applied to the TK-LR data because the correction of the TK-HR data was not finished by the PI of the TK TCCON site when this thesis was submitted. The left column shows the bias compensation factors of the time corrected TK-LR data relative to the TS. The middle column shows bias compensation factor comparing the TK-LR data to the reference in Karlsruhe. The right columns shows the same comparison but with a deviation in percentage.

Species	$K_{\text{TK-LR}}^{\text{SN39}}$	$K_{\text{TK-LR}}^{\text{SN37}}$	$\Delta_{\text{TK-LR}}^{\text{SN37}}$ (%)
XCO ₂	1.00000 ± 0.00007	$0.99836 \pm 0.00008 + 0.00063$	$0.16408 \pm 0.00830 - 0.06318$
XCH ₄	1.00149 ± 0.00008	$1.00111 \pm 0.00009 - 0.00067$	$-0.11087 \pm 0.00873 + 0.06690$
XCO	0.98689 ± 0.00037	$0.98556 \pm 0.00047 - 0.00053$	$1.46475 \pm 0.04874 + 0.05470$

5.7. Discussion of the Results

For a more intuitive comparison of the results of the comparison, the data given in Table 5.10 is visualized in Figure 5.18.

In gray, the estimated site-to-site bias of the TCCON for GGG2020 as given in Section 3.1.2 is plotted. Note that the length of the bars are equal to the given bias, i.e. the 0.2% precision of XCO₂ results in a bar from -0.1% to 0.1% . Plotting the bar in a way that it starts from 0 and r at $\pm 0.2\%$ would double the error budget.

For each site, the results of the low-, and high-resolution data are given. The error of all measurements is clearly dominated by the calibration error which considers a potential drift of the TS unit compared to the COCCON reference unit SN37 (compare with Section 4.2). As the calibration errors are signed values, the error bars are asymmetrical.

For XCO₂, all of the data, except the TK-LR is within the estimated TCCON site-to-site error.

For XCH₄ all data is withing the estimated TCCON site-to-site bias. However, considering the calibration error, there is a uncertainty that the TK-HR data is outside of the estimated

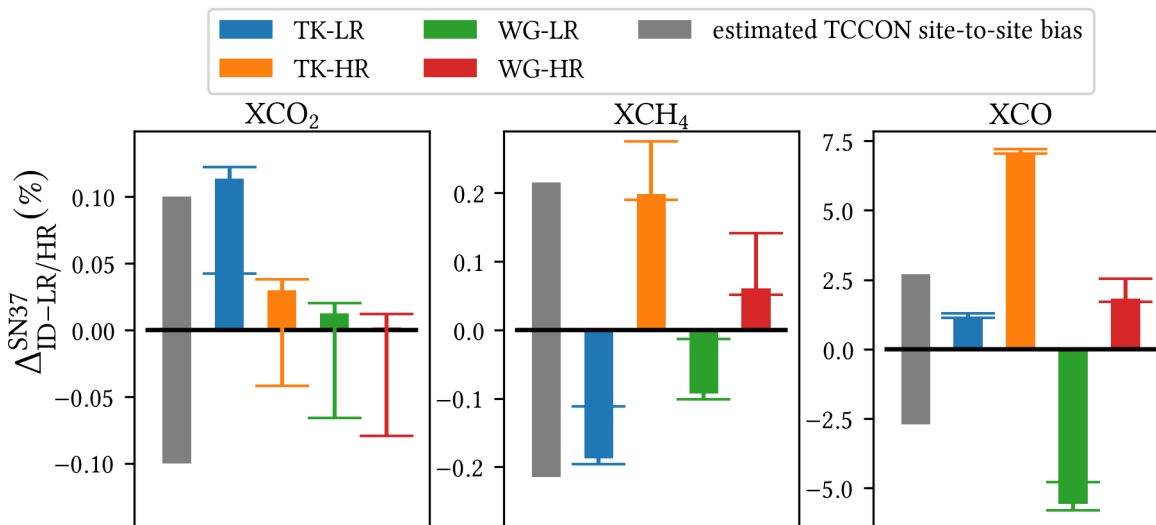


Figure 5.18.: Visualization of the deviations in percentage of the TCCON sites to the Karlsruhe reference. The data of this figure are given in Table 5.10. The gray bars are the preliminary, estimated site-to-site biases of the TCCON given in Section 3.1.2. Note that the length of the bars representing the bias is equal to the given precision, i.e. the 0.2% precision of XCO₂ results in a bar from -0.1% to 0.1%. The error markers include both the random error and the calibration error. Since the calibration errors are signed values, the error markers are asymmetric. The calibration error is clearly dominant. For XCO₂ and XCH₄, the results are in or slightly outside of the estimated TCCON bias. However, for XCO, both sides deviates clearly from each other. The main reason for the deviation of the TK-HR data is assumed to be the outdated emission inventories in the a priori. The reason for the large WG-LR data is assumed to be the much lower data sampling rate compared to the TS data.

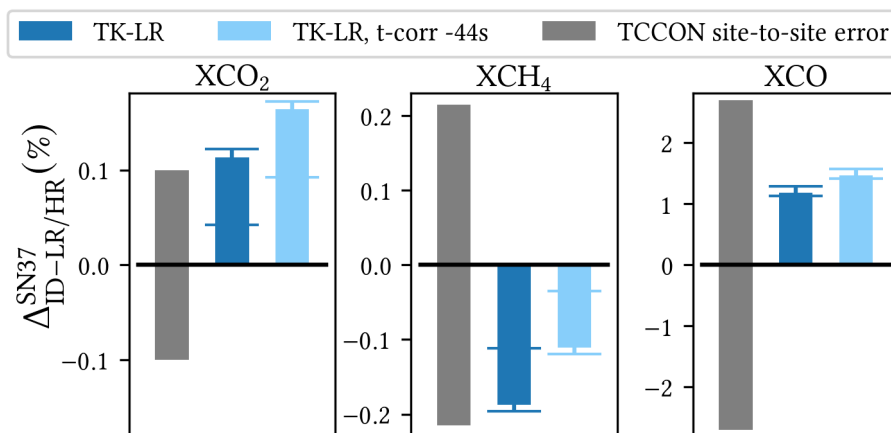


Figure 5.19.: Comparison of the time corrected and the uncorrected TK data. The data is plotted in the same way as described for Figure 5.18. It is interesting to see that for the different species the correction changes the values in different directions.

site-to-site bias. Furthermore for XCH₄, it is interesting that the deviations of the low-resolution data are negative (i.e. the measurements are higher compared to the reference) and the high-resolution data is positive. Future comparisons will show whether this is a general property of different resolutions of XCH₄ measurements.

For XCO, the deviations are significantly larger than the TCCON error. However, for XCO there are some issues which potentially can cause the large deviations. First, as already discussed, the difference between TK-HR and TK-LR data is clearly visible. This is due to the poor quality

of the a-priori, which causes a difference between the HR and TS measurements. In contrast, the TK-LR results are almost within the error budget. For Wollongong, it is surprising that the WG-LR data shows such a large deviation. However, the WG-LR data suffers from the low sampling frequency, which probably causes the difference. This can be seen well in the data recorded at 2022-12-23. There is a larger peak in the XCO data. When this data is binned into 30 minute bins, the difference in the data rate can lead to large differences.

The findings of the campaigns described in this thesis are comparable with the results presented in Mostafavi Pak et al. 2023 which used a similar comparison method. The cited publication gives absolute values, they are converted to relative values using 400 ppm for XCO₂, 1800 ppb for XCH₄ and 100 ppb for XCO.

For high-resolution TCCON data the maximal biases of Mostafavi Pak et al. 2023 are 0.13 % (0.53 ppm) for XCO₂, 0.24 % (4.30 ppb) for XCH₄ and 6.10 % (6.10 ppb) for XCO. For XCO₂ and XCH₄, the values in this work are slightly lower whereas for XCO, the result of this work is with 0.9 percentage points slightly higher, which is still very similar.

For the low-resolution measurements, the maximal biases of Mostafavi Pak et al. 2023 are 0.21 % (0.83 ppm) for XCO₂, 0.18 % (3.20 ppb) for XCH₄ and 2.10 % (2.10 ppb) for XCO. For XCO₂, the values in this work are lower. For XCH₄, it is slightly and for XCO, it is significant higher. As discussed earlier, the XCO for the LR data is dominated by the WG site which suffers from a low measurement frequency for the LR data.

It is important to note, that the study by Mostafavi Pak et al. 2023 uses GGG2020 as a retrieval software for both the TCCON and the EM27/SUN data. Furthermore, the low-resolution data in this study was truncated and not natively measured. As presented in Section 5.5.2, the truncated spectra are not necessarily comparable in terms of noise to natively recorded low-resolution spectra.

5.7.1. Influence of the Timing Error in Tsukuba

As presented in 5.2, the XAIR values indicate an timing error of -44 s. In Figure 5.19, the deviation to the Karlsruhe reference is plotted for both the uncorrected and the corrected TK-LR data. It is interesting to observe, that for the different species, the correction changes the deviations in different directions: For the TK data, the timing error increases the relative deviation to the Karlsruhe reference by 0.05 percentage points for XCO₂ and 0.28 for XCO. For XCH₄, the deviation decreased by 0.07 percentage points. For all species, the difference is significant. Even though this data only shows the TK-LR measurements, it is expected that a correction of the timing error influences the XGas values of the TK-HR data as well. Therefore, it is of great importance to find the source of the timing error, and redo the analysis with the corrected TK-HR data as soon as they are available.

5.7.2. Pressure Analysis

The pressure data collected at each site is summarized and compared to the DWD Rheinstetten data. For this, the bias compensation factors of the pressure measurements are multiplied, similar to the XGas values:

$$k_{ID_p}^{DWD_p} = k_{TS_p}^{DWD_p} \cdot k_{ID_p}^{TS_p} . \quad (5.12)$$

Table 5.12.: The summary of the bias compensation factors for the pressure and the comparison to the level of the DWD Rheinstetten weather station. The deviation in hPa is calculated by assuming a pressure of 1000 hPa.

Site (ID)	$k_{ID_T}^{TS_T}$	$k_{TS_p}^{DWD_p}$	$k_{ID_p}^{DWD_p}$	Δ_{ID}^{DWD} (hPa)
TK	1.0001042	0.9998686	0.9999728	0.02721
ETL	0.9999956	0.9998686	0.9998642	0.13580
WG	1.0000373	0.9998686	0.9999059	0.09410

In Table 5.12, the results are summarized. The absolute differences are calculated by:

$$\Delta_{ID}^{DWD} = 1000 \cdot \left(1 - k_{ID_p}^{DWD_p}\right) \quad (5.13)$$

Tu 2019 found, by using PROFFIT as a retrieval software and low-resolution spectra, that a change of 1 hPa in the measured ground pressure causes an average increase of about 0.035% in XCO₂, 0.039% in XCH₄ and 0.052% in XCO, respectively. These values can be used to estimate the effect of the pressure error to the data. Hence, for none of the sites a large influence on the XGas values due to the pressure measurements is expected.

5.8. Summary of the Chapter

In this section, the data collected with the Travel Standard during three different campaigns in Tsukuba, East Trout Lake and Wollongong is presented and successfully compared to the TCCON sites. The three goals identified at the beginning of the chapter are 1) the search for instrumental issues, 2) the comparison of the XGas values, and 3) the comparison of the pressure records. By means of these three goals, the chapter is summarized.

Instrumental Issues: For the Tsukuba data, a potential timing error could be identified: Compared to the TS, the TCCON XAIR data shows a high airmass dependency which is decreasing over the course of the day, indicating a timing error. For the TK-LR data, the airmass dependency could be mitigated almost completely by a time correction of -44 s.

Both, the TK and WG data-sets show a large noise level. The reason for this could be traced back to the shape of the spectra which has a significant intensity drop towards higher wavenumbers. Hence in the O₂ window, the SNR is low for both spectrometers.

As two spectrometers are affected by the same problem, it is suspected that other TCCON sites may face the same issue. By an analysis of the signal-to-noise ratio in the O₂ window of the spectra of various other sites, it could be shown that several instruments across the network are facing this issue. A realignment of the TK TCCON spectrometer improved the SNR significantly.

To simplify this task, a method to correlate the noise and the SNR in the O₂ window and in spectral windows of another species is developed using the private GGG2020 engineering files. This method allowed to show that for most of the sites a large noise level is correlated with a high SNR in the spectra.

The WG data shows an unusual large difference in the noise level between the low- and high-resolution data. For investigating this more closely, a method which compares the natively and

truncated low-resolution spectra was developed. Even though this method could not reveal the reason for the difference, it confirms an unknown issue with the WG data.

In ETL, the laser of the TCCON site broke shortly before the arrival of the TS. Therefore, no side-by-side measurements were possible. However, several days of HR and LR measurements could still be collected before it broke down. This data was used for consistency checks which did not reveal any instrumental problems.

Pressure Records: For all three sites, the pressure comparison revealed a good agreement with the reference sensor. The largest deviation is found at the ETL site with a deviation of 0.135 80 hPa.

The analysis of the pressure data of the WG site was very important, as it revealed two important issues. First, it turned out, that the wrong pressure data was used for the evaluation of the pressure data so far: The pressure sensor is located 5 m below the TCCON tracker and hence, it is necessary to correct for this altitude difference. The altitude correction changes the pressure of about 0.58 hPa which is a significant value. Furthermore, an error in the assumed altitude of a new TCCON spectrometer currently being installed in Wollongong could be detected which is also very important as it prevents a systematic error at a new TCCON site.

XGas Comparison: Finally, the XGas values measured by the TCCON sites are compared to the Karlsruhe reference spectrometer. For XCO₂, all datasets except the TK-LR are within the estimated TCCON site-to-site bias.

For XCH₄, all data are within the estimated TCCON site-to-site bias. However considering the error, there is a probability that the TK-HR data is outside of this range.

For XCO, there are large deviations from the estimated TCCON site-to-site bias. However for XCO, there is a known issue with the a priori which probably causes the problems.

For the TK data, the impact of the timing error is investigated for the TK-LR data: The correction increases the relative deviation to the Karlsruhe reference for XCO₂ and XCO but decreases the deviation for XCH₄.

These examples of three visited sites show impressively how valuable the EM27/SUN Travel Standard is for the consistency of the TCCON as it successfully demonstrated the use of the data to quantitatively compare the TCCON sites to a common reference. Furthermore, a timing error in Tsukuba and pressure issues in Wollongong could be detected. Moreover, with the spectra analysis and the GGG2020 engineering data analysis across the network and the analysis of low-resolution and truncated high-resolution spectra three small tools to analyze the quality of the spectrometers could be developed. They can be applied without the need of additional hardware. Therefore, these might be additional tools for the TCCON QA/QC checks in the future.

Chapter 6

Summary and Outlook

This work successfully demonstrated the deployment of an EM27/SUN spectrometer as a Travel Standard (TS) within the TCCON. The main idea of the TS is to serve as a common reference for visited TCCON sites. Three campaigns, each on a different continent, were conducted. The TS is based in Karlsruhe where it is compared to the COCCON reference unit before and after each campaign in order to detect misalignment.

In the first part of this thesis the prerequisites for the TS are created. The first prerequisite is the operation and the retrieval of the data of the Karlsruhe TCCON site which serves as a reference for the COCCON network as a whole but in particular also for the TS. In 2020, the retrieval software of the TCCON was updated to a new version called GGG2020. As the Karlsruhe TCCON site is measuring continuously since 2014, the whole dataset was reprocessed. During the operation of the Karlsruhe TCCON site, a few errors were detected and could be solved.

The second prerequisite is the ability to process the data of the TS. In 2021/2022, PROFFAST2, a new version of the retrieval software of the COCCON, was developed at IMK-ASF. To simplify the usage of this, the PROFFASTPYLOT, an easy-to-use interface for PROFFAST2, was developed by the author in cooperation with Feld, L. Moreover, the new PROFFAST2 was calibrated to agree with the GGG2020 results. The comparison to the TCCON data revealed a so far undetected dependency of the XGas difference of PROFFAST2 and GGG2020 values on XH₂O. For XCO₂, the difference between GGG2020 and PROFFAST2 for a low and a high water vapor amount (500 ppm and 6500 ppm) is up to 3 ppm (0.7%), 0.01 ppm (0.55%) for XCH₄ and 0.56 ppb (0.56%) for XCO. The origin of this bias is still unknown. Furthermore, it is not clear which of the retrieval software is closer to the truth. Hence, this requires further investigations. However, as an intermediate solution, the GGG2020 values are considered as a reference. An empirical XH₂O correction was introduced for the PROFFAST2 to be in agreement with GGG2020. A comparison of the so calibrated COCCON data with the TCCON data yielded relative deviations of $(0.002840 \pm 0.11337) \%$ for XCO₂, $(-0.01310 \pm 0.19023) \%$ for XCH₄ and $(-0.27420 \pm 1.60327) \%$ for XCO. The first number is the relative average deviation of the data binned in 10 minute intervals. The second number gives the relative standard deviation of the differences of the 10 minute intervals.

The third prerequisite is the monitoring of the TS between the campaigns to ensure the stability of the TS. For this, laboratory measurements to retrieve the ILS as well as solar side-by-side measurements with the COCCON reference unit were conducted. All ILS measurements were within the normal range expected for an EM27/SUN spectrometer. The maximum change found between the campaigns is 0.31 ppm for XCO₂, 0.0019 ppm for XCH₄ and -0.51 ppb for XCO. For

all gases, this is below the estimated TCCON site-to-site bias. For XCO, a SZA dependent difference of the TS spectrometer relative to the reference unit was found and corrected by an empirical linear correction. The reason for this difference is still unknown.

The TS is deployed in an enclosure developed by the TUM. To enable campaigns worldwide, the hardware was adapted such, that it can be operated in any power grid available. Furthermore, a reliable and accurate pressure sensors as well as transport loggers to monitor potential mechanical impacts at the shipments were installed.

The second part of the thesis covers the deployment and the evaluation of the TS campaigns in Tsukuba (Japan), East Trout Lake (ETL) (Canada), and Wollongong (Australia). Each visited TCCON site was checked for 1) instrumental errors, 2) pressure consistency, and 3) the deviation of the XGas values relative to the Karlsruhe reference. At each site, the TS performed several days of side-by-side measurements with the TCCON spectrometer. For the campaigns, the TCCON spectrometers collected standard TCCON measurements as well as low-resolution spectra with the same resolution as the EM27/SUN (0.5 cm^{-1}) in an alternating manner. This ensures that resolution-based effects were excluded and allowed to process the spectra with the PROFFAST retrieval software. By this, systematic biases can be excluded. The standard TCCON measurements were retrieved by the PI of the site with GGG2020 and therefore are similar to the official TCCON data except that they are not reviewed by the TCCON QA/QC management.

The following instrumental issues were found: For both, Tsukuba and Wollongong, high-noise levels were revealed. The reason for both could be traced back to an intensity drop in the spectra towards higher wavenumbers. This causes a low SNR in the O₂ spectral window which influences all XGas values. The intensity drop is caused by bad alignment and most likely a characteristic of the used beam-splitter. In addition, for the Tsukuba data, a timing error was found. For the low-resolution data, an offset of -44 s was found empirically. For the high-resolution data, the issue is still under investigation.

The comparison of the raw pressure data did not encounter significant deviations. However in Wollongong, the pressure analysis helped to detect that the altitudes used so far for the evaluation were wrong: the tracker was assumed to be at 30 masl but actually it is at 35 masl. Furthermore, the pressure sensor is mounted 5 m below the tracker. In both, the GGG2014 and the GGG2020 evaluations this is not considered. Luckily, the GGG2020 data analysis is not released, yet. Hence, a correction was still possible.

In ETL, the reference laser in the TCCON-spectrometer broke down shortly before the arrival of the TS. Hence, no side-by-side measurements could be performed. However, several days of alternating low-, and high-resolution measurements were collected already which were used to check for any instrumental issues like timing errors, misalignment or similar errors. However, none were found.

A quantitative comparison of the XGas values relative to the COCCON reference unit which is tied to the Karlsruhe TCCON site was made. For XCO₂ and XCH₄, deviations for the low- and high-resolution measurements are within the estimated TCCON site-to-site bias ($\pm 0.1 \%$ for XCO₂ and $\pm 0.215 \%$ for XCH₄). The only exception was the Tsukuba low-resolution XCO₂ data with a deviation of 0.113%. For XCO, the TK-LR and the WG-HR are within the estimated TCCON site-to-site bias ($\pm 2.7 \%$). The TK-HR data showed large deviations of more than 7%. This deviation probably is caused by a known issue with the a priori. For WG-LR, a deviation

of -5.6% is found. As the WG-LR is measured with a low sampling rate, some sharp peaks measured in XCO could not be resolved correctly.

For all species, a random error and a calibration error have been calculated. The errors of all species are dominated by the calibration uncertainty, which is derived from a potential drift of the TS device relative to the COCCON reference unit.

The high noise level in both, Tsukuba and Wollongong originated in the same reason. Therefore, an evaluation of this issue in the whole network is performed. For this, the SNR ratio in the O₂ window is examined for several other stations by analyzing spectra recorded at a bright day at local noon. The results varied across the network. However, some sites with exceptional low SNR could be identified. In addition to this, a systematic method to evaluate the correlation of the SNR in the spectra and the noise in the different species was developed. This method is based on the data which is provided by the TCCON-internal engineering files. The systematic analysis revealed a correlation between the SNR and the noise level in the XGas retrievals. But also cases where the high noise level is higher than indicated by the SNR. Hence, for those sites further investigation are needed.

Furthermore, a new consistency test of data using the noise is developed: In theory, the noise in a low-resolution spectrum and in a spectrum which is downsampled from a high resolution measurement should be the same (assuming the same scan speed and number of scans). A large deviation from this ideal behavior indicates an issue with the instrument. For none of the visited sites large deviations were found.

In summary, this thesis successfully improved the consistency and the accuracy of ground-based remote sensing FTIR measurements by various contributions.

The first is the successful application of an EM27/SUN as an international operating Travel Standard. The analysis of its data showed that for the two major products XCO₂ and XCH₄ the site-to-site estimations are mainly within the expected range. Second, site specific issues (timing error and altitude error) could be revealed and partly corrected. Third, the network-wide noise analysis helped to find an issue which occurs at several sites, hence contributing to improve the accuracy within the TCCON. This is especially valuable since the SNR analysis and the low-resolution consistency test can be evaluated without further hardware and therefore, might be used for the regular QA/QC of the TCCON data. The fourth is the detection of the dependency of GGG and PROFFAST on the XH₂O value. It is of great importance to pin down this dependency, which is up to 0.7% , in order to continue to provide precise reference data. The fifth is the development of the PROFFASTPYLOT. This is a very important tool as it significantly simplifies the usage of the PROFFAST2 software and is used as a standard interface for PROFFAST2 by groups worldwide. It is a valuable contribution to the COCCON community because due to its simplicity helps to reduce errors when operating PROFFAST. Furthermore, it allows the processing of the spectra by people less experienced with FTIR-spectroscopy and hence, helps to further extend the measurement network.

For further testing and improving the consistency of the TCCON, a continuation of the TS activities is planned. The next scheduled campaigns are in Izaña (Spain) and in Paris (France). In the data collected so far, there are still some open issues: In Tsukuba, the timing error needs to be corrected for the high-resolution TCCON data and the deviation compared to Karlsruhe needs to be recalculated. In Wollongong, the reason of the significant larger noise for the HR compared to the LR data is still unclear. It would be interesting to test, if an realignment of the instrument solves this issue.

The comparison of the low-resolution and high-resolution data gives different values. Especially

for XCH_4 , for both sites the LR data is lower. There, a larger data-set is needed to find systematics in the comparison and to better assess the evaluation when comparing different resolutions.

For the data measured in ETL, there are the following possibilities to evaluate them. At ETL, the TS collected side-by-side measurements with other EM27/SUN which are stationed in Canada. When the broken laser is replaced, one of the Canadian EM27/SUN could serve as a proxy for the TS linked by the aforementioned side-by-side measurements. Else, simulation data like CAMS could be used to extrapolate the ETL-TCCON measurements to the period of the TS collected measurements.

A further very important point for future research is to validate the retrieval software of both the TCCON and the COCCON in order to find the reason for the observed XH_2O dependency. The most direct and promising approach is to use column-averaged DMFs derived from air-cores collected at days with a different water vapor amount in the atmosphere.

Appendix A

Appendix to the Technical Details of the Travel Standard

In summer 2021 a long-term side-by-side measurement of the Travel Standard instrument (SN39) with the COCCON reference instrument (SN37) was collected. The results, including the side-by-side measurements used for calibrating the TS, are plotted in Figure A.1 There, the

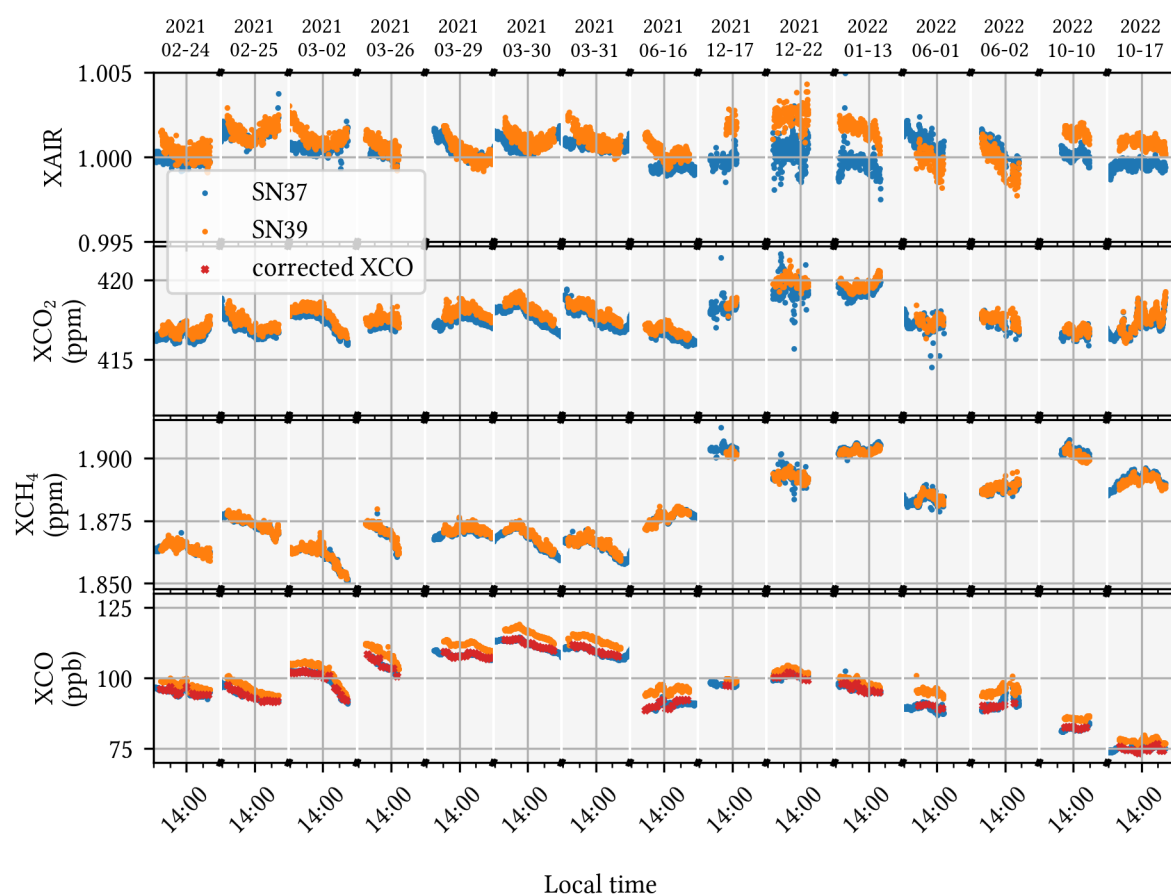


Figure A.1: Long term side-by-side measurement of the Travel Standard (SN39) in orange and the COCCON reference (SN37) in blue. For all gases except for XCO the differences between the two instruments over time keeps constant. For XCO, however, the difference varies in the course of the year. The reason for this is found in a SZA dependency of XCO. The origin of this dependency is not known. However, an empirical correction is used to correct for this. The corrected XCO data is plotted using red crosses.

Table A.1.: Records of the transport data-logger mounted inside of the enclosure.

Site	Temperature	Humidity	Shock thresholds	Shock records
Tsukuba	$T_{\max} = 42.4\text{ }^{\circ}\text{C}$ $T_{\min} = 7\text{ }^{\circ}\text{C}$	$H_{\max} = 66\text{ }%$	$a_{\min;\max} = [-4.0; 4.0]\text{g}$ $T_{\text{dur}} = 40\text{ ms}$ $f_{\text{rate}} = 400\text{ Hz}$	No events recorded
ETL	$T_{\max} = 62.9\text{ }^{\circ}\text{C}$ $T_{\min} = 23.5\text{ }^{\circ}\text{C}$	$H_{\max} = 58.3\text{ }%$	$a_{\min;\max} = [-4; 4]\text{g}$ $T_{\text{dur}} = 25\text{ ms}$ $f_{\text{rate}} = 400\text{ Hz}$	No events recorded
Wollongong	$T_{\max} = 30.3\text{ }^{\circ}\text{C}$ $T_{\min} = 13.1\text{ }^{\circ}\text{C}$	$H_{\max} = 61.2\text{ }%$	$a_{\min;\max} = [-4.0; 4.0]\text{g}$ $T_{\text{dur}} = 15\text{ ms}$ $f_{\text{rate}} = 400\text{ Hz}$	5 events $a_{\max} = 16\text{ g}$ $T_{\text{dur}}^{\max} = 40\text{ ms}$

all gases except XCO are in good agreement. For XCO a dependency on the SZA is found and discussed in Section 4.2.3. Using the XCO data shown in Figure A.1 an empirical correction is derived. Compare with Figure 4.7.

In Table A.1 a overview of the data recorded by the transport logger mounted inside the enclosure is given. Compare with Section 4.1. For all three campaigns the temperatures and the humidity are in a non-critical range. The shocks recorded when doing the transportation for the Wollongong campaigns are quite large. However, no misalignment in the instruments could be detected.

Appendix B

Results of the Calibration of the PROFFAST2 Algorithm

To calibrate the PROFFAST 2 retrieval algorithm, the data measured by several instruments (SN037, SN039 and SN122) are evaluated. The calibration procedure is described in detail in Section 3.2.2. There, only plots of XCO_2 measured by the SN037 instrument are shown. Here, the remaining plots of the other gases and instruments are shown.

B.1. Airmass Dependent Correction Factors

The Figure B.1 and B.2 show the same data as Figure 3.8 but measured with the instruments SN39 and SN122 respectively.

B.2. Airmass Independent Calibration

The figures B.1 to B.16 show the same data as given in Figure 3.10 in the main part but for the gases XCO_2 , XCH_4 , XCH_4^{SP} , XCO , XH_2O for the instruments SN037, SN039, SN122. The order of the plots is the same as the order of the gases and the instruments given above. For all plots, no time series of are given (missing panel a)). This is because, no relevant information can be read derived from it.

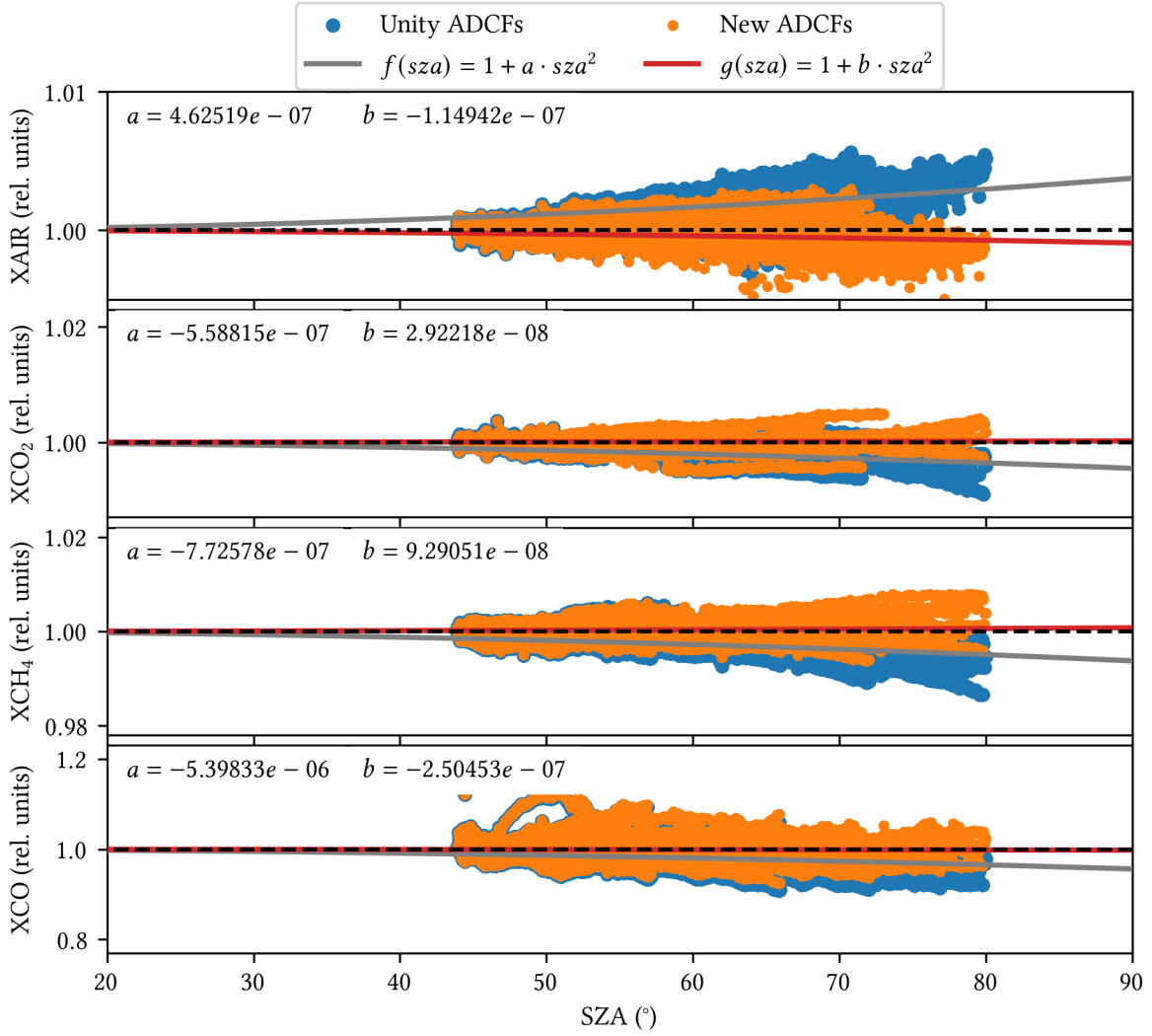


Figure B.1.: Results of the air mas dependent correction for the data measured by the instrument SN039.

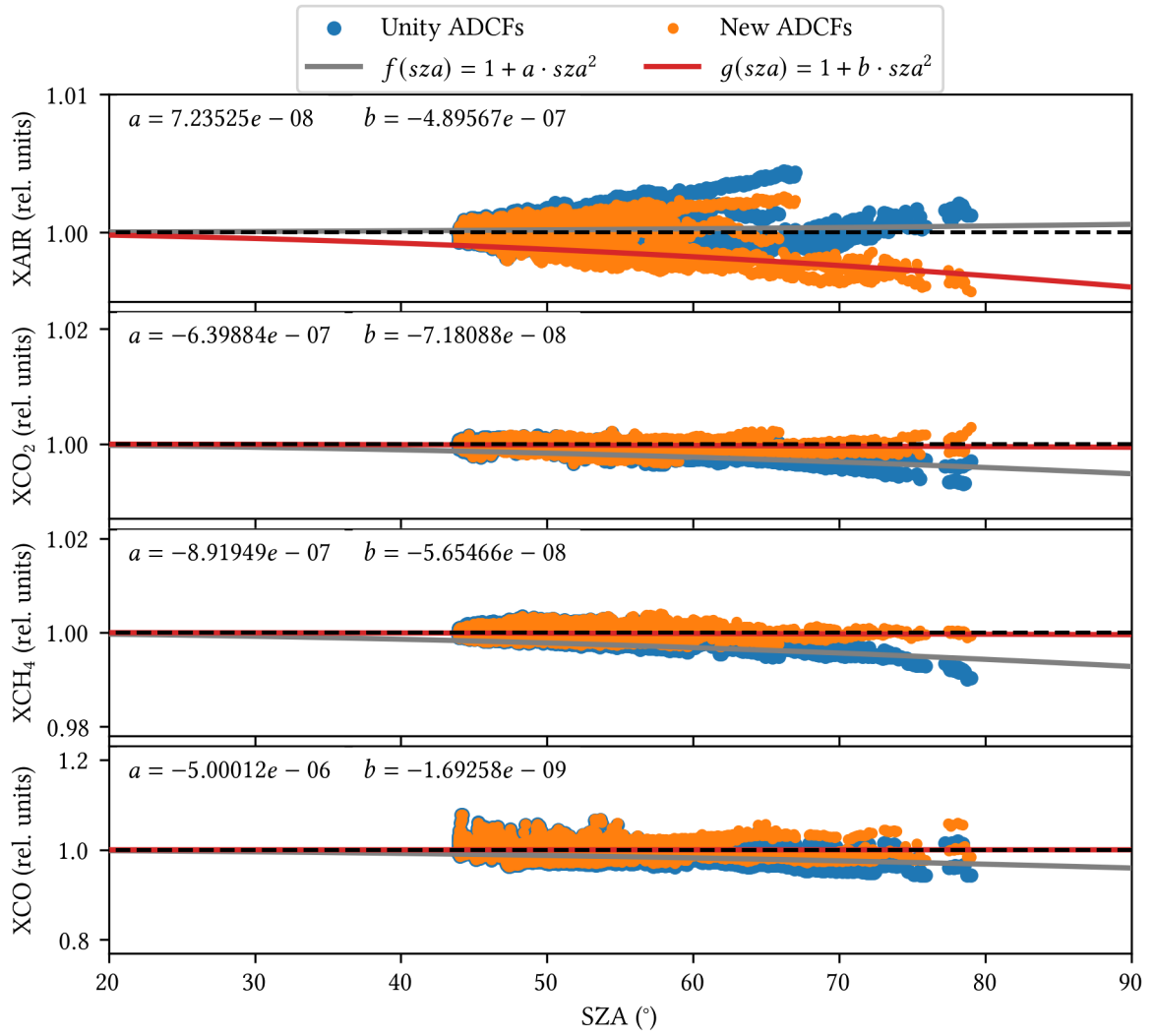


Figure B.2.: Results of the air mas dependent correction for the data measured by the instrument SN122.

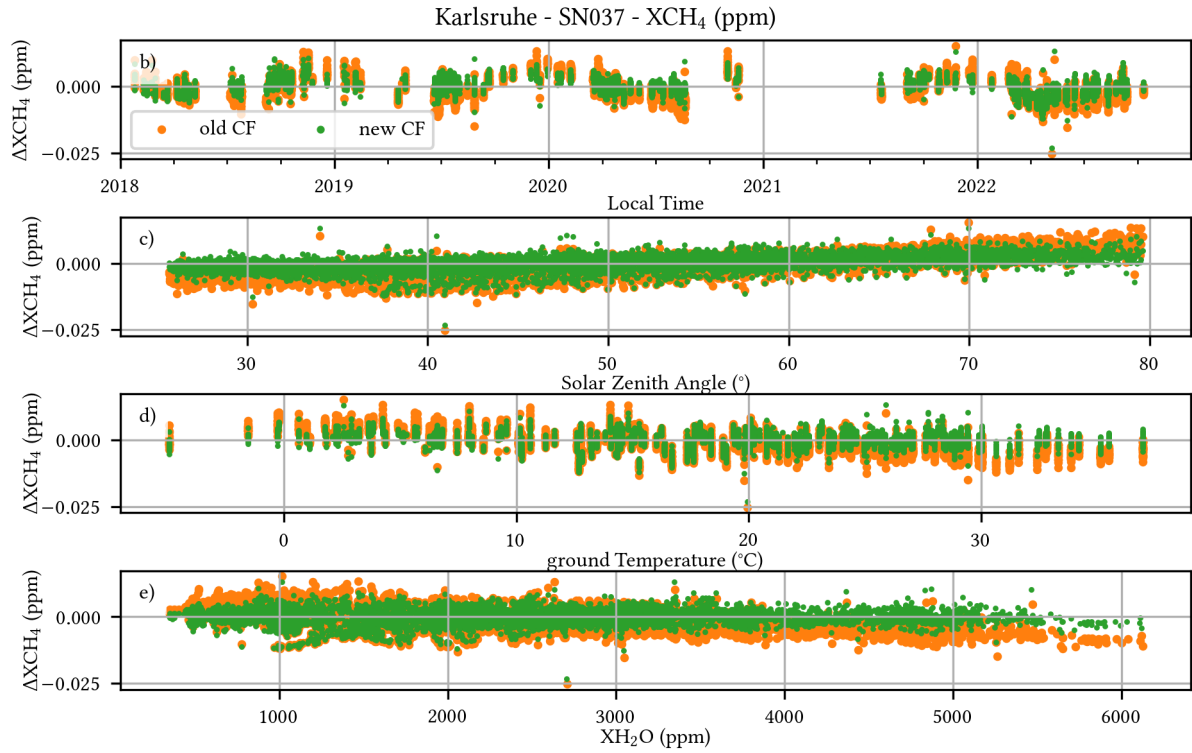


Figure B.3.: Results of the new calibration including the XH_2O correction for XCH_4 and instrument SN037.

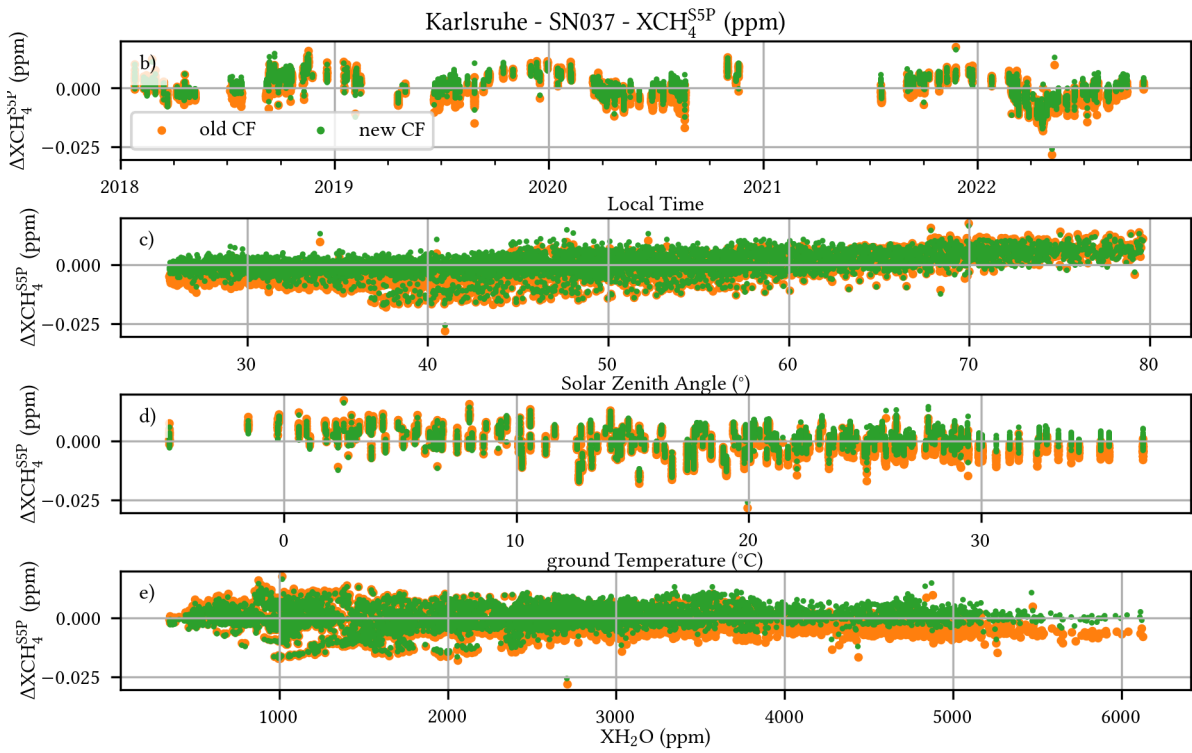


Figure B.4.: Results of the new calibration including the XH_2O correction for $\text{XCH}_4^{\text{S5P}}$ and instrument SN037.

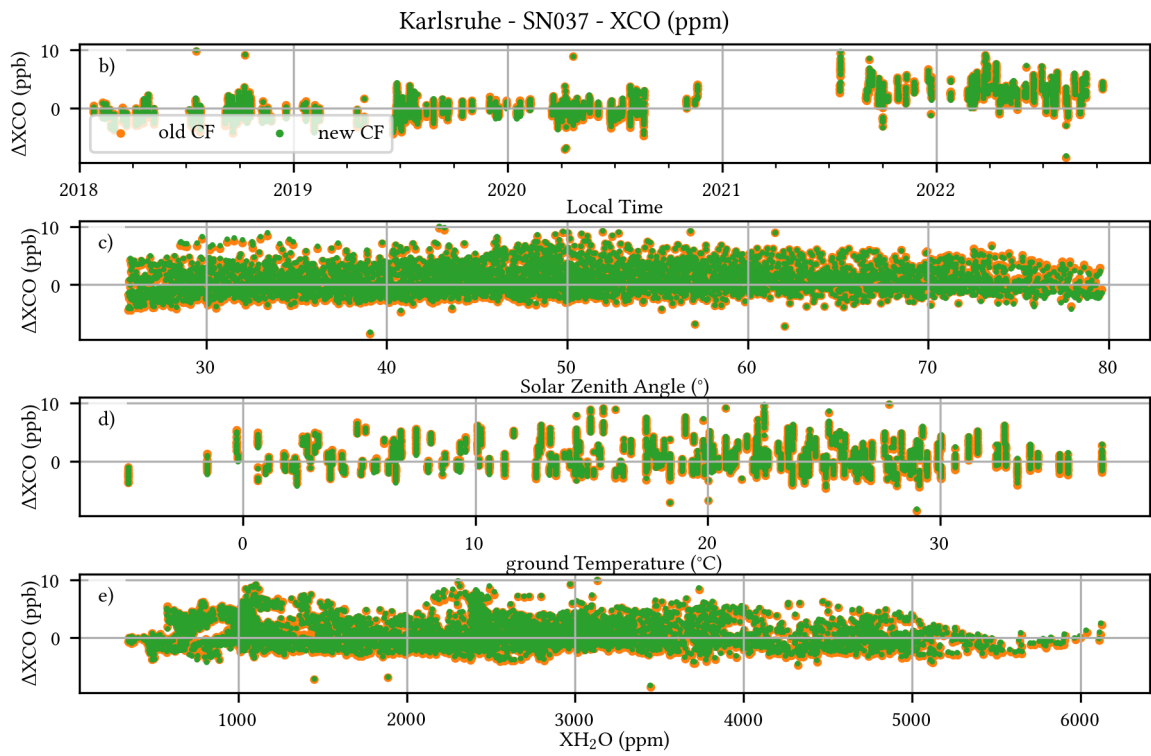


Figure B.5.: Results of the new calibration including the XH_2O correction for XCO and instrument SN037.

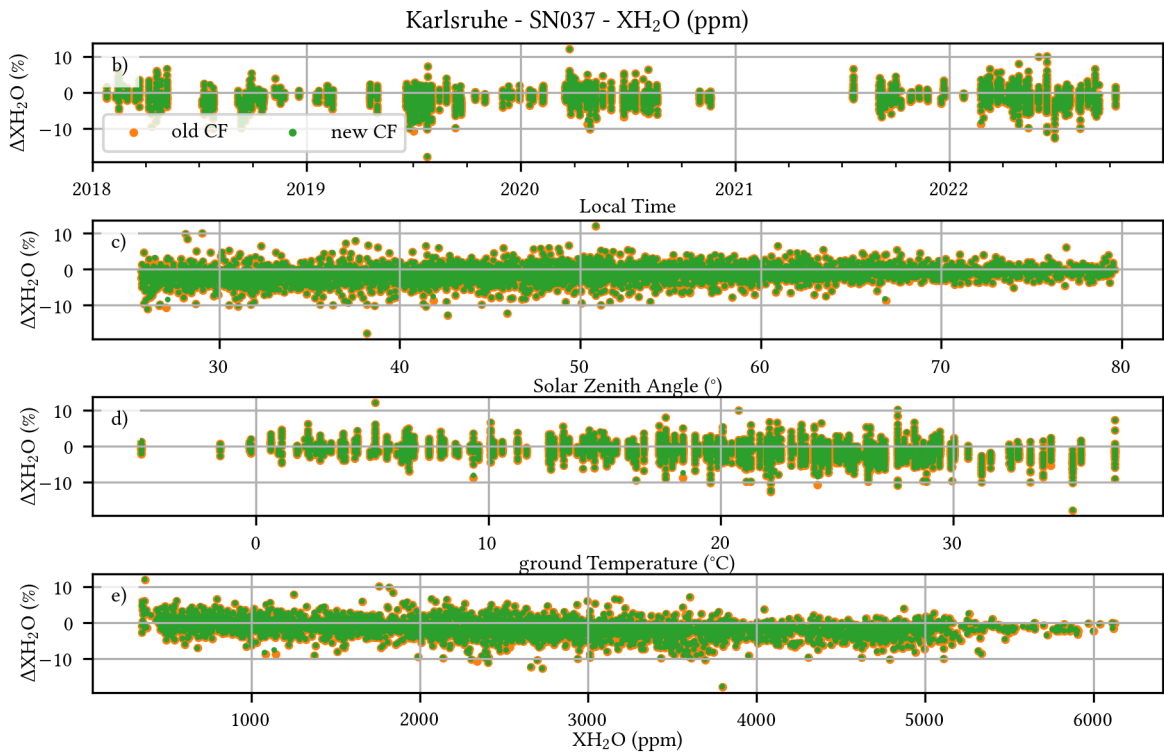


Figure B.6.: Results of the new calibration including the XH_2O correction for XH_2O and instrument SN037.

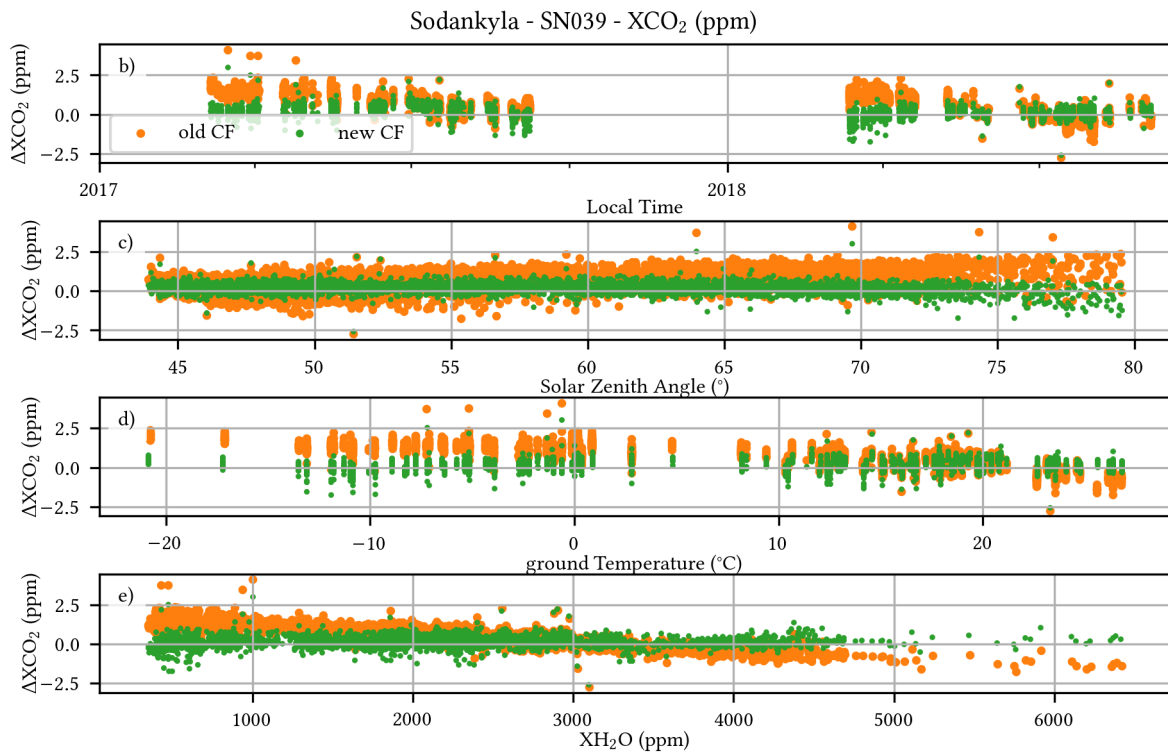


Figure B.7.: Results of the new calibration including the XH₂O correction for XCO₂ and instrument SN039.

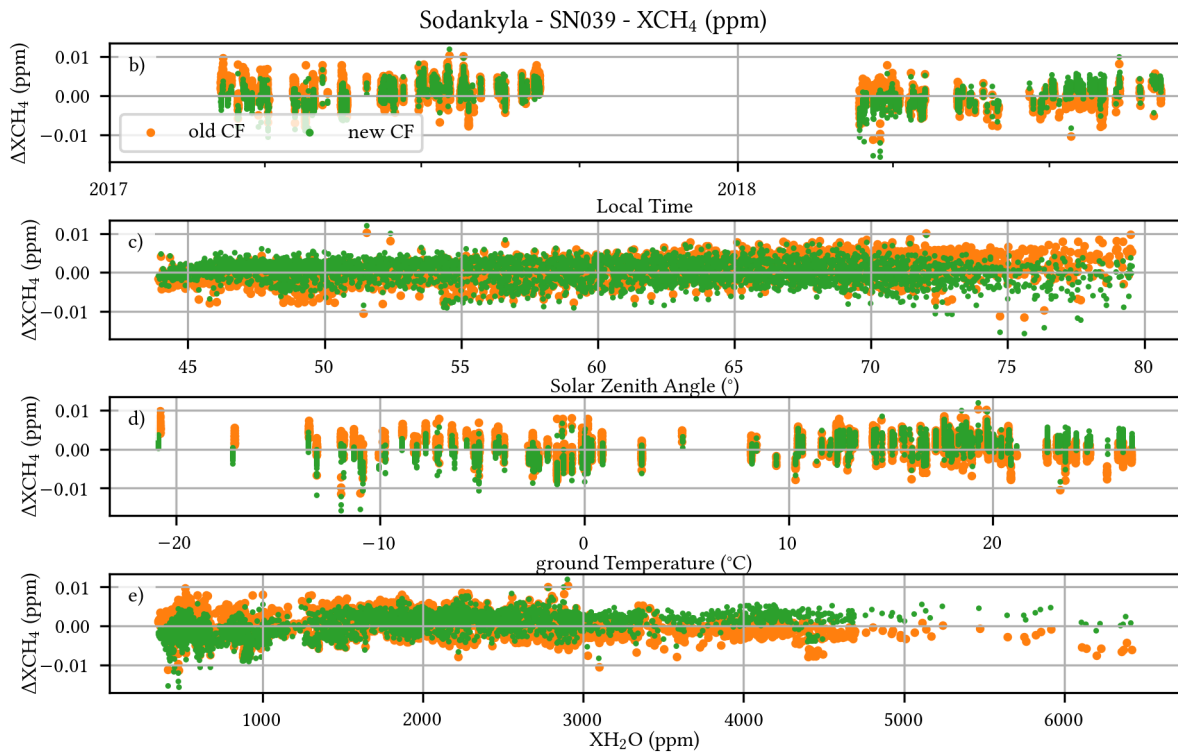


Figure B.8.: Results of the new calibration including the XH₂O correction for XCH₄ and instrument SN039.

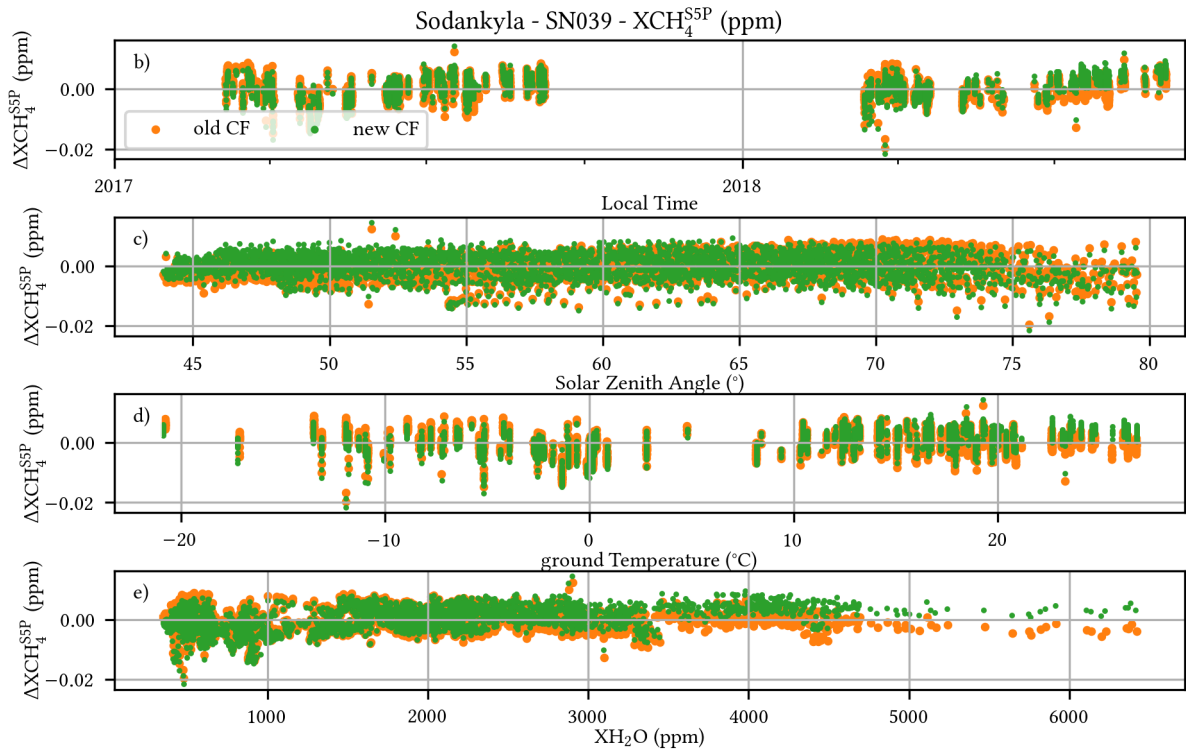


Figure B.9.: Results of the new calibration including the XH_2O correction for XCH_4^{S5P} and instrument SN039.

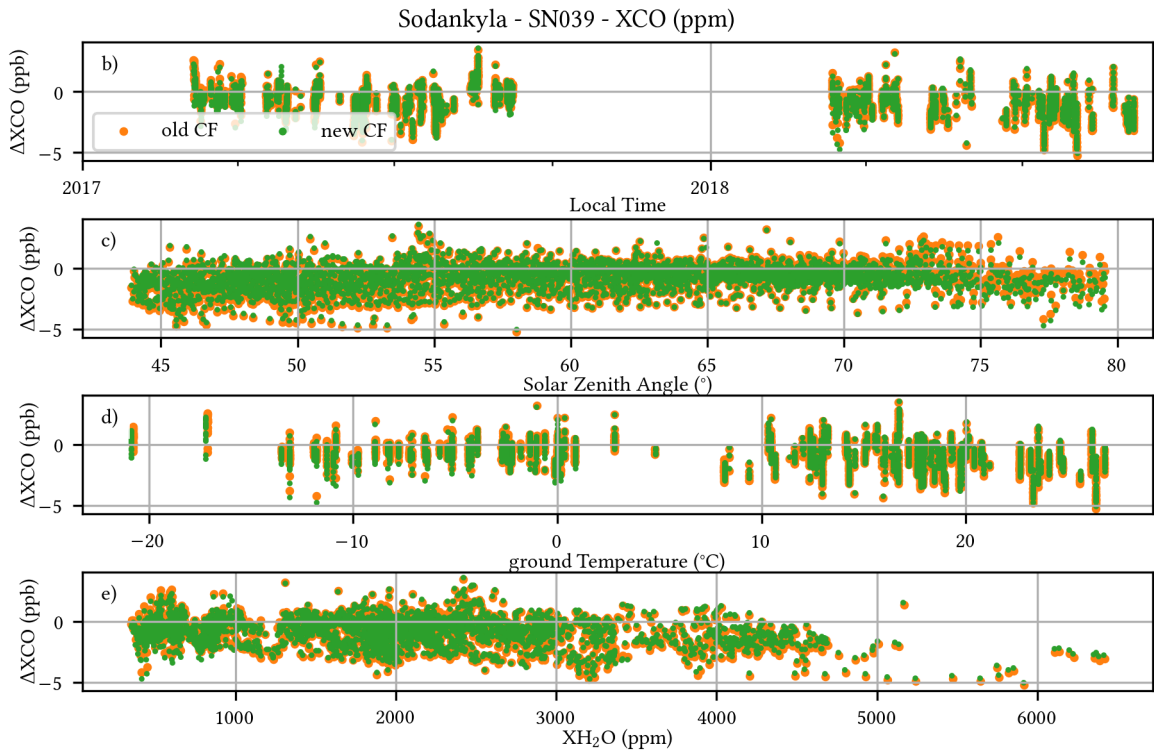


Figure B.10.: Results of the new calibration including the XH_2O correction for XCO and instrument SN039.

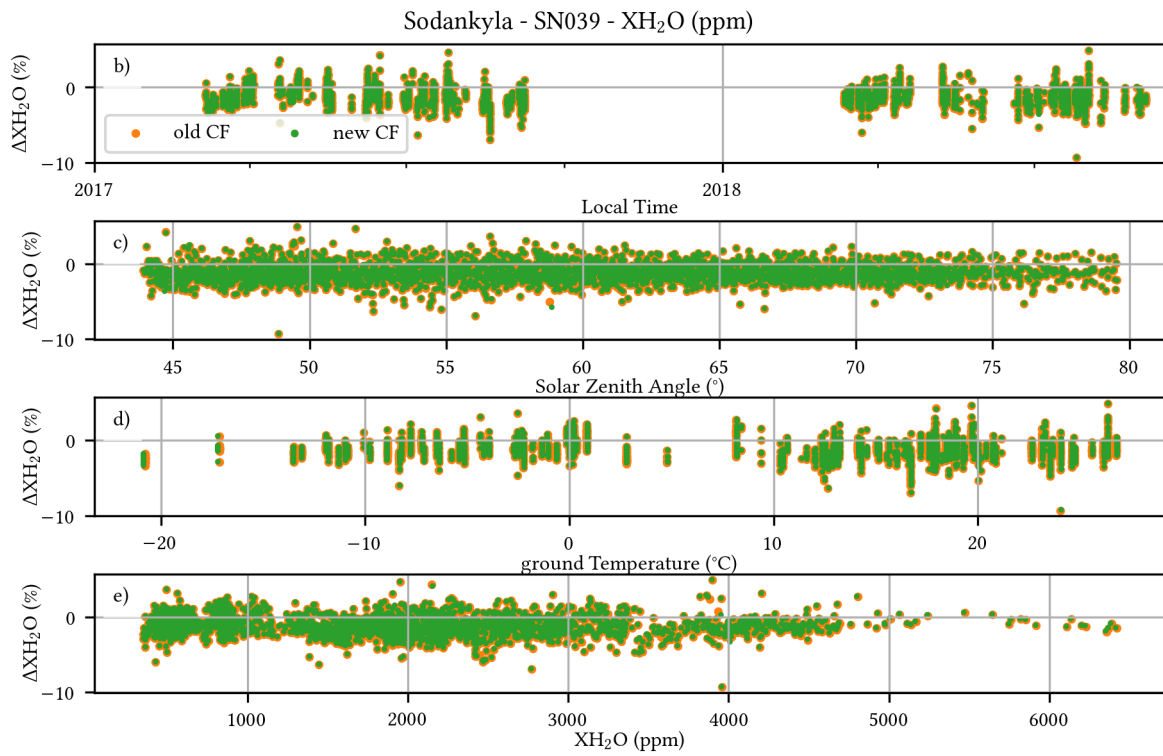


Figure B.11.: Results of the new calibration including the XH₂O correction for XH₂O and instrument SN039.

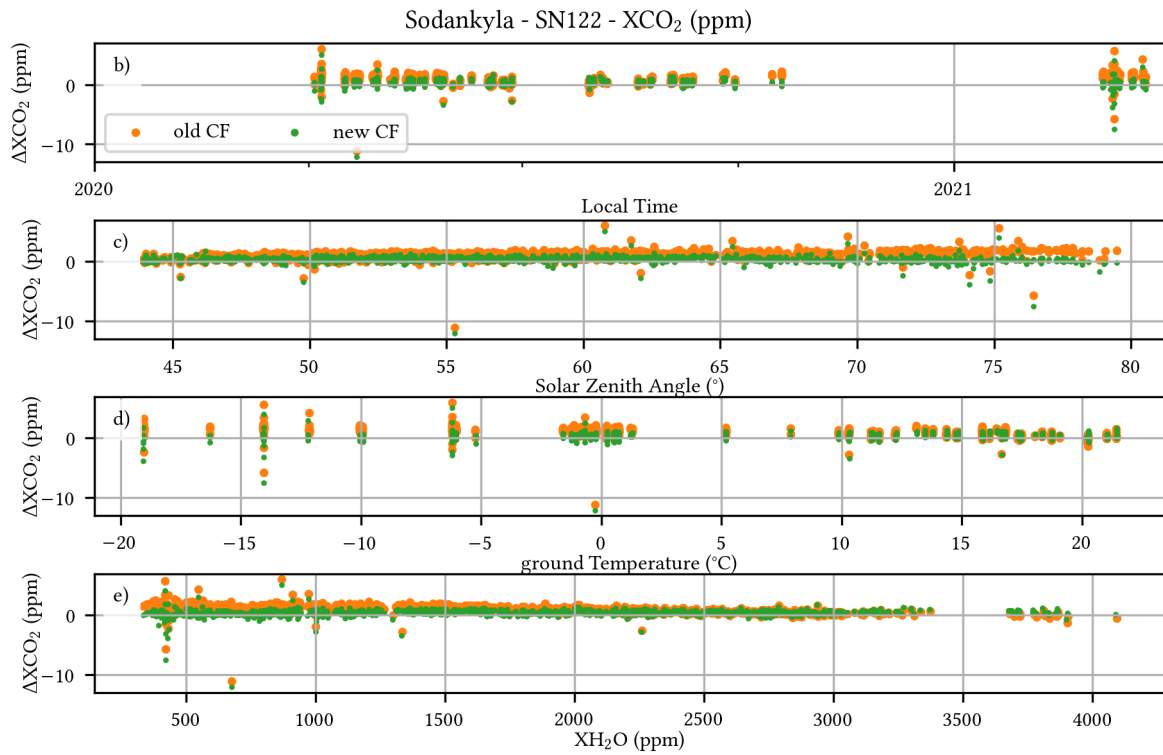


Figure B.12.: Results of the new calibration including the XH₂O correction for XCO₂ and instrument SN122.

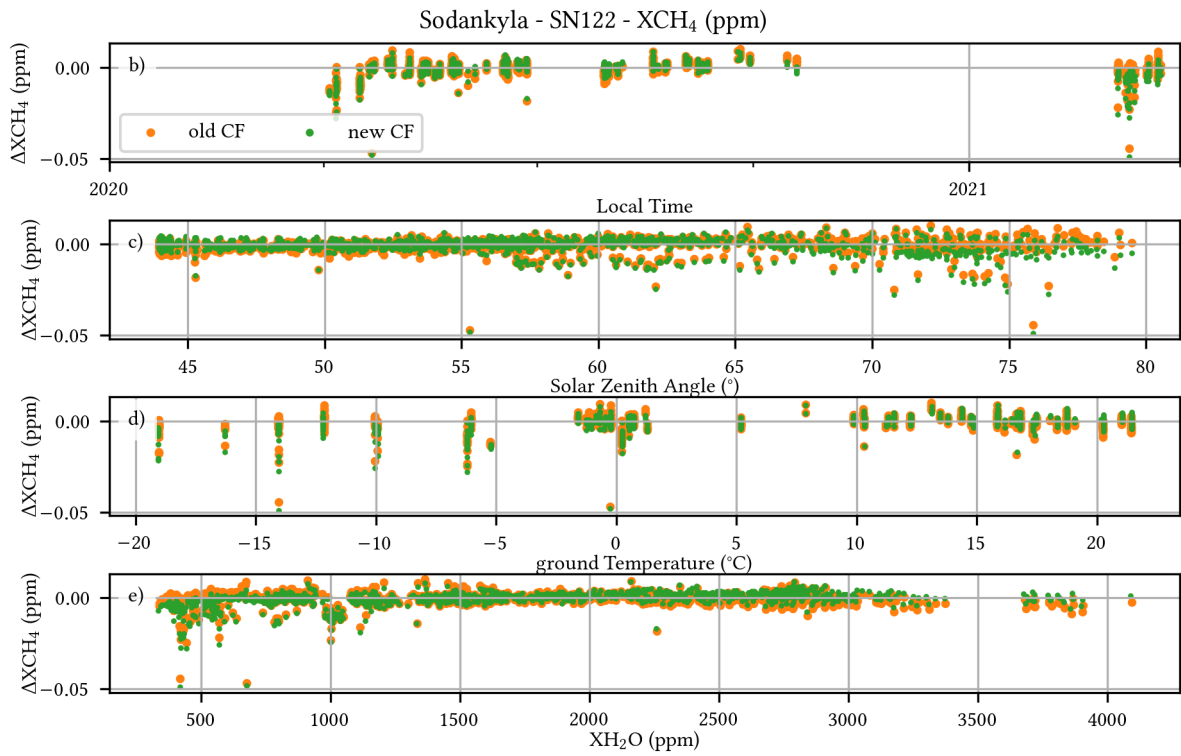


Figure B.13.: Results of the new calibration including the XH_2O correction for XCH_4 and instrument SN122.

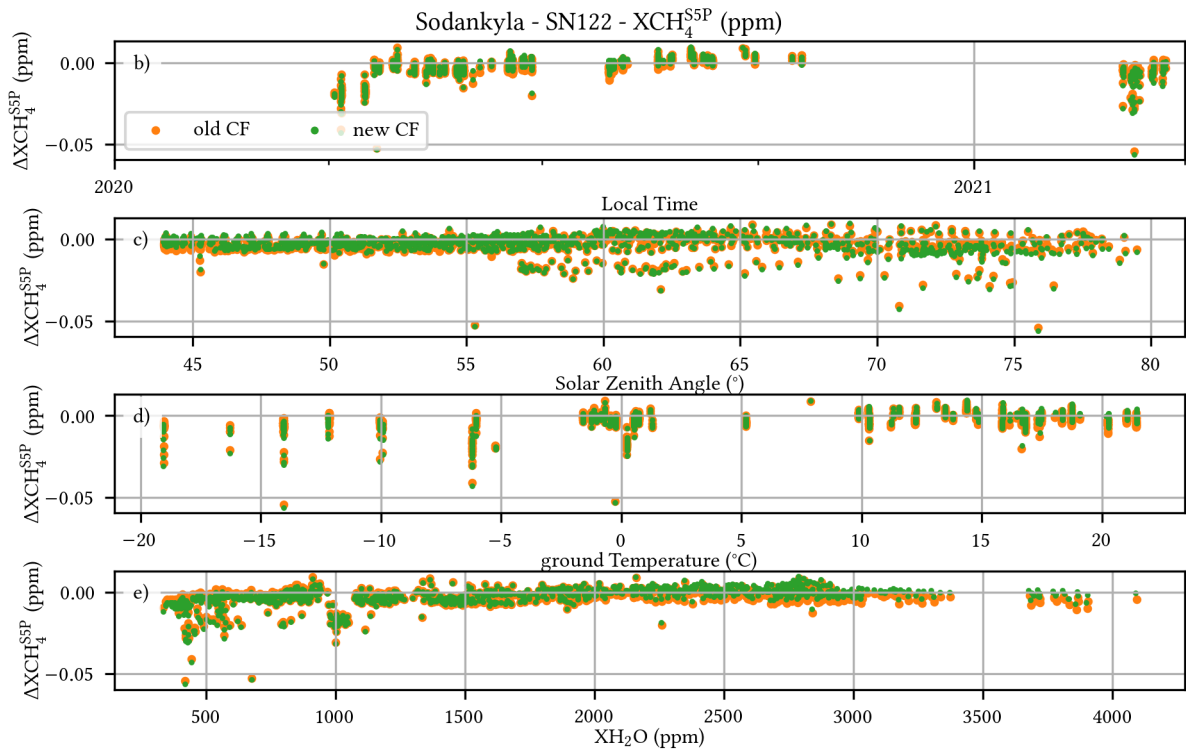


Figure B.14.: Results of the new calibration including the XH_2O correction for XCH_4^{SP} and instrument SN122.

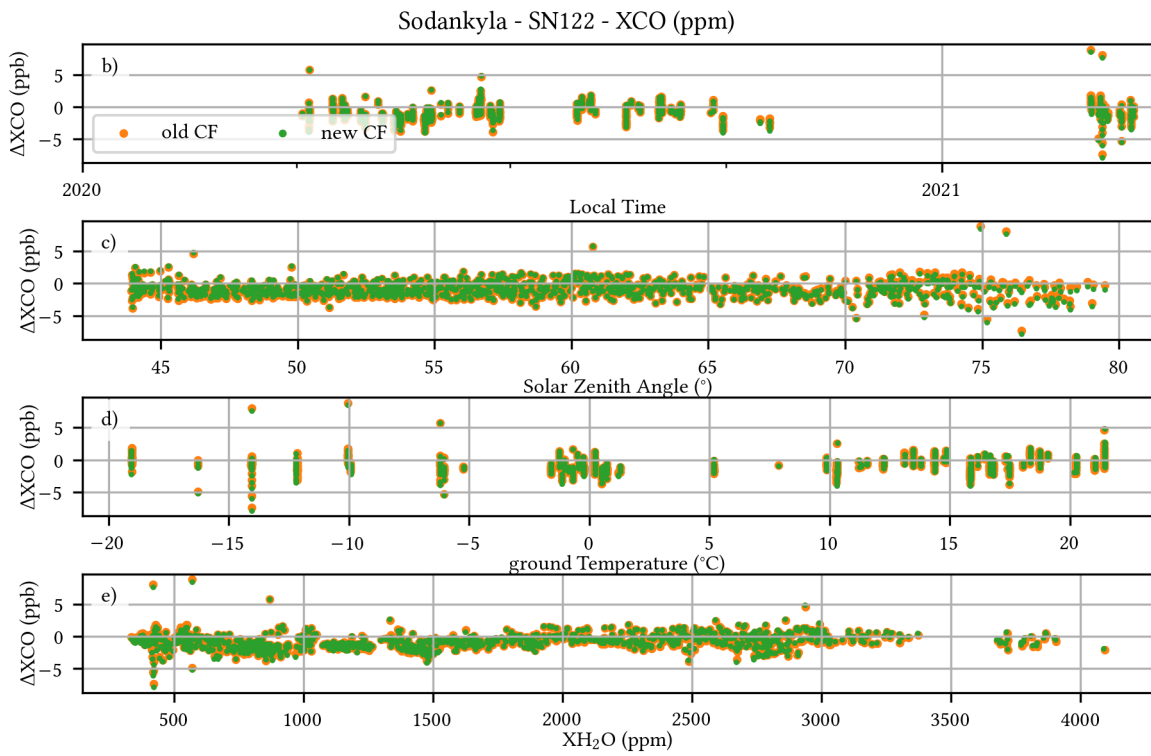


Figure B.15.: Results of the new calibration including the XH_2O correction for XCO and instrument SN122.

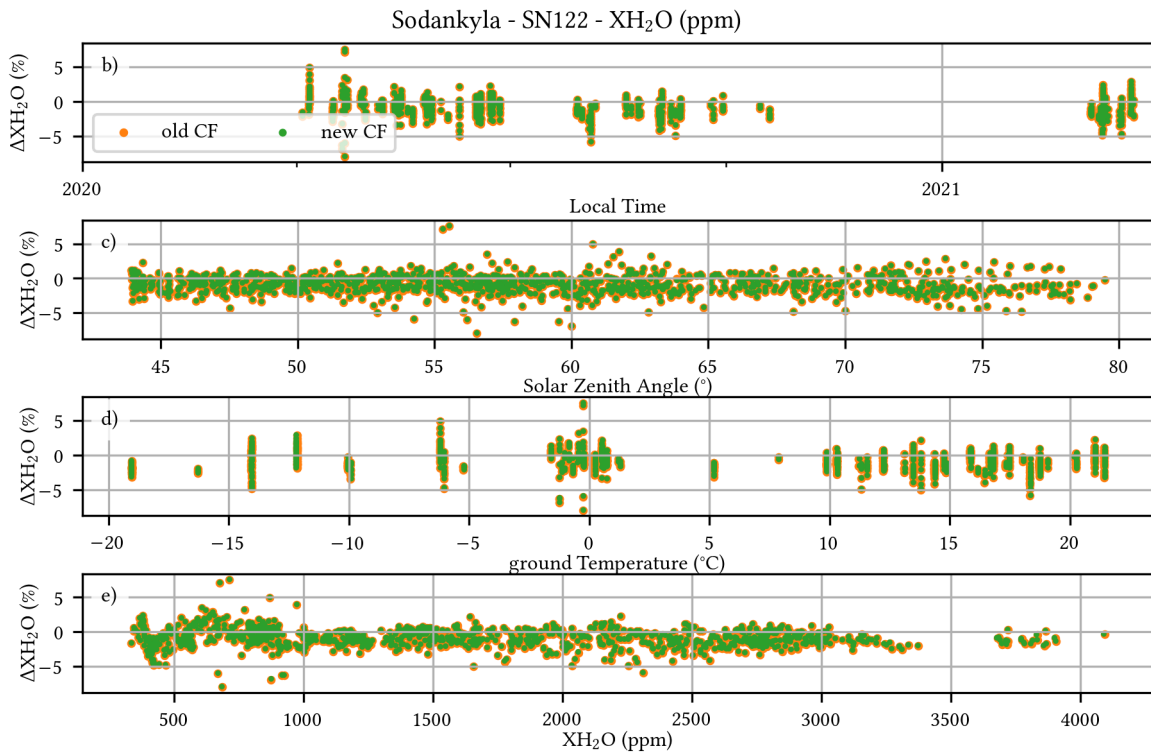


Figure B.16.: Results of the new calibration including the XH_2O correction for XH_2O and instrument SN0122.

Appendix C

Systematic Noise Analysis for XCH₄

In this section the network-wide noise analysis for CH₄ is carried out using the method presented in Section 5.5.3.2. Furthermore, Table C.1 gives the mapping of the two letter TCCON site IDs to the location of the sites.

Figure C.1 shows the correlation of the σ_{XCH_4} values and the quadratically added SSQ values. Similar as for CO₂ in the main part, the data shows clearly that the XCH₄ noise levels are related to the SSQs.

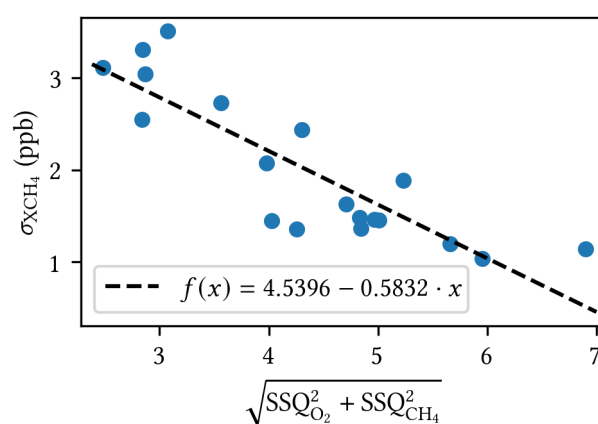


Figure C.1.: The figure shows the correlation between the quadratically added SSQs and the XCH₄ noise level σ_{XCH_4} . The calculated values are based on the internal TCCON-engineering files starting from 2021-01-01. As for XCO₂ in the main part, a correlation between both quantities is visible.

To assign the data-points in Figure C.1 to the sites, a bar chart is given in Figure C.2. The result is qualitatively the same as for CO₂ in the main part. The same six sites as for CO₂ (“js”, “rj”, “xh”, “ni”, “ci”, “pr”) have the highest noise values in the XGas time series. However, they are ordered differently. Equally as for CO₂, the sites with low noise levels in the XCH₄ time series (below 1.4 ppb) show high SSQs.

Hence, the conclusion derived in Section 5.5.3.2 for CO₂ are also valid for CH₄.

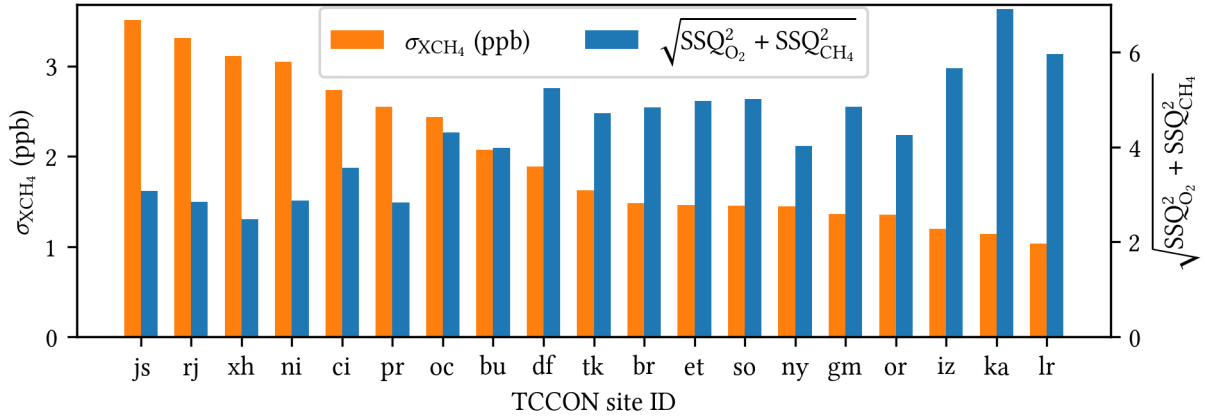


Figure C.2.: A bar chart of the noise levels of the XCH₄ time series (σ_{XCH_4}) and the SSQs for various TCCON sites. The data is the same as given in Figure C.1. The σ_{XCO_2} values refers to the scale on the left ordinate, the quadratically summed SSQs to the scale at the right ordinate. Similar as for XCO₂ in the main part it can be seen that in general a higher SNR gives a lower noise level. However, there are also some exceptions as e.g. “df”. The sites are sorted in descending order of the σ_{XCH_4} values from left to right. A list of the TCCON site abbreviations (ID) is given in Table C.1.

Table C.1.: The two letter site ID of a various TCCON sites used in this work.

ID	City	country
br	Bremen	Germany
bu	Burgos	Philippines
ci	Pasadena;California	USA
df	AFRC; Edwards	USA
et	East Trout Lake	Canada
fc	Four Corners;NM	USA
gm	Garmisch	Germany
if	Indianapolis; Indiana	USA
iz	Izana; Tenerife	Spain
js	Saga	Japan
ka	Karlsruhe	Germany
lr	Lauder	New Zealand
ni	Nicosia	Cyprus
ny	Ny-Alesund;Svalbard	Norway
oc	Lamont; Oklahoma	USA
or	Orleans	France
pr	Sorbonne Universite	Paris
so	Sodankyä	Finland
tk	Tsukuba; Ibaraki	Japan
wg	Wollongong	Australia
xh	Xianghe	China

Bibliography

- Alberti, C., Hase, F., Frey, M., Dubravica, D., Blumenstock, T., Dehn, A., Castracane, P., Surawicz, G., Harig, R., Baier, B. C., Bès, C., Bi, J., Boesch, H., Butz, A., Cai, Z., Chen, J., Crowell, S. M., Deutscher, N. M., Ene, D., Franklin, J. E., García, O., Griffith, D., Grouiez, B., Grutter, M., Hamdouni, A., Houweling, S., Humpage, N., Jacobs, N., Jeong, S., Joly, L., Jones, N. B., Jouglet, D., Kivi, R., Kleinschek, R., Lopez, M., Medeiros, D. J., Morino, I., Mostafavipak, N., Müller, A., Ohyama, H., Palmer, P. L., Pathakoti, M., Pollard, D. F., Raffalski, U., Ramonet, M., Ramsay, R., Sha, M. K., Shiomi, K., Simpson, W., Stremme, W., Sun, Y., Tanimoto, H., Té, Y., Tsidu, G. M., Velazco, V. A., Vogel, F., Watanabe, M., Wei, C., Wunch, D., Yamasoe, M., Zhang, L., and Orphal, J. (2022a). “Improved calibration procedures for the EM27/SUN spectrometers of the COllaborative Carbon Column Observing Network (COCCON)”. In: *Atmospheric Measurement Techniques* 15.8, pp. 2433–2463. DOI: [10.5194/amt-15-2433-2022](https://doi.org/10.5194/amt-15-2433-2022) (cit. on pp. 2, 46–47, 64, 69).
- Alberti, C., Tu, Q., Hase, F., Makarova, M. V., Griбанov, K., Foka, S. C., Zakharov, V., Blumenstock, T., Buchwitz, M., Diekmann, C., Ertl, B., Frey, M. M., Imhasin, H. K., Ionov, D. V., Khosrawi, F., Osipov, S. I., Reuter, M., Schneider, M., and Warneke, T. (2022b). “Investigation of spaceborne trace gas products over St Petersburg and Yekaterinburg, Russia, by using COllaborative Column Carbon Observing Network (COCCON) observations”. In: *Atmospheric Measurement Techniques* 15.7, pp. 2199–2229. DOI: [10.5194/amt-15-2199-2022](https://doi.org/10.5194/amt-15-2199-2022) (cit. on p. 46).
- Arias, P. et al. (2021). “Technical Summary”. In: *Climate Change 2021: The Physical Science Basis. Contribution of Working Group I to the Sixth Assessment Report of the Intergovernmental Panel on Climate Change*. Cambridge, United Kingdom and New York, NY, USA: Cambridge University Press, pp. 33–144. DOI: [10.1017/9781009157896.002](https://doi.org/10.1017/9781009157896.002) (cit. on pp. 1, 13).
- Artsang, P., Pongchalee, P., Palawong, K., Buisset, C., and Meemon, P. (2018). “A technique for phase correction in Fourier transform spectroscopy”. In: *International Society for Optics and Photonics* 10714. Ed. by T. Mayteevarunyoo, 107140U. DOI: [10.1117/12.2300966](https://doi.org/10.1117/12.2300966) (cit. on p. 29).
- Asimellis, G. (Aug. 2020). “Introduction to Optics: Lectures in Optics, Vol. 1”. In: SPIE, pp. 2-53–2-54. ISBN: 978-1-5106-1944-9. DOI: [10.1117/3.2318475](https://doi.org/10.1117/3.2318475) (cit. on p. 10).
- Baek, C.-Y., Lee, K.-M., and Park, K.-H. (2014). “Quantification and control of the greenhouse gas emissions from a dairy cow system”. In: *Journal of Cleaner Production* 70, pp. 50–60. ISSN: 0959-6526. DOI: [10.1016/j.jclepro.2014.02.010](https://doi.org/10.1016/j.jclepro.2014.02.010) (cit. on p. 1).
- Bergamaschi, P., Colomb, A., De Mazière, M., Emmenegger, L., Kubistin, D., Lehner, I., Lehtinen, K., Leuenberger, M., Lund Myhre, C., Marek, M., Platt, S. M., Plaß-Dülmer, C., Ramonet, M., Schmidt, M., Apadula, F., Arnold, S., Chen, H., Conil, S., Couret, C., Cristofanelli, P., Forster, G., Hatakka, J., Heliasz, M., Hermansen, O., Hoheisel, A., Kneuer, T., Laurila, T., Leskinen, A., Levula, J., Lindauer, M., Lopez, M., Mammarella, I., Manca, G., Meinhardt, F., Müller-Williams, J., Ottosson-Löfvenius, M., Piacentino, S., Pitt, J., Scheeren, B., Schumacher, M., Sha, M. K., Smith, P., Steinbacher, M., Sørensen, L. L., Vítková, G.,

- Yver-Kwok, C., Sarra, A. di, Conen, F., Kazan, V., Roulet, Y.-A., Biermann, T., Delmotte, M., Heltai, D., Komínková, K., Laurent, O., Lunder, C., Marklund, P., Pichon, J.-M., Trisolino, P., ICOS Atmosphere Thematic Centre, ICOS ERIC - Carbon Portal, ICOS Flask And Calibration Laboratory (FCL), ICOS Flask And Calibration Laboratory (FCL), and ICOS Central Radiocarbon Laboratory (CRL) (2022). *ICOS Atmosphere Release 2022-1 of Level 2 Greenhouse Gas Mole Fractions of CO₂, CH₄, N₂O, CO, meteorology and 14CO₂*. DOI: [10.18160/KCYX-HA35](https://doi.org/10.18160/KCYX-HA35) (cit. on p. 2).
- Burrows, J. P., Platt, U., and Borrell, P. (2011). “Tropospheric Remote Sensing from Space”. In: *The Remote Sensing of Tropospheric Composition from Space*. Berlin, Heidelberg: Springer Berlin Heidelberg, pp. 1–65. ISBN: 978-3-642-14791-3. DOI: [10.1007/978-3-642-14791-3_1](https://doi.org/10.1007/978-3-642-14791-3_1) (cit. on pp. 32–33).
- Butz, A., Dinger, A. S., Bobrowski, N., Kostinek, J., Fieber, L., Fischerkeller, C., Giuffrida, G. B., Hase, F., Klappenbach, F., Kuhn, J., Lübcke, P., Tirpitz, L., and Tu, Q. (2017). “Remote sensing of volcanic CO₂, HF, HCl, SO₂, and BrO in the downwind plume of Mt. Etna”. In: *Atmospheric Measurement Techniques* 10.1, pp. 1–14. DOI: [10.5194/amt-10-1-2017](https://doi.org/10.5194/amt-10-1-2017) (cit. on p. 46).
- Butz, A., Hanft, V., Kleinschek, R., Frey, M., Müller, A., Knapp, M., Morino, I., Agustí-Panareda, A., Hase, F., Landgraf, J., Vardag, S., and Tanimoto, H. (2022). “Versatile and Targeted Validation of Space-Borne XCO₂, XCH₄ and XCO Observations by Mobile Ground-Based Direct-Sun Spectrometers”. In: *Frontiers in Remote Sensing* 2. ISSN: 2673-6187. DOI: [10.3389/frsen.2021.775805](https://doi.org/10.3389/frsen.2021.775805) (cit. on p. 46).
- Byrne, B., Baker, D. F., Basu, S., Bertolacci, M., Bowman, K. W., Carroll, D., Chatterjee, A., Chevallier, F., Ciais, P., Cressie, N., Crisp, D., Crowell, S., Deng, F., Deng, Z., Deutscher, N. M., Dubey, M. K., Feng, S., Garcia, O. E., Griffith, D. W. T., **Herkommer, B.**, Hu, L., Jacobson, A. R., Janardanan, R., Jeong, S., Johnson, M. S., Jones, D. B. A., Kivi, R., Liu, J., Liu, Z., Maksyutov, S., Miller, J. B., Miller, S. M., Morino, I., Notholt, J., Oda, T., O’Dell, C. W., Oh, Y.-S., Ohyama, H., Patra, P. K., Peiro, H., Petri, C., Philip, S., Pollard, D. F., Poulter, B., Remaud, M., Schuh, A., Sha, M. K., Shiomi, K., Strong, K., Sweeney, C., Te, Y., Tian, H., Velasco, V. A., Vrekoussis, M., Warneke, T., Worden, J. R., Wunch, D., Yao, Y., Yun, J., Zammit-Mangion, A., and Zeng, N. (2023). “National CO₂ budgets (2015–2020) inferred from atmospheric CO₂ observations in support of the global stocktake”. In: *Earth System Science Data* 15.2, pp. 963–1004. DOI: [10.5194/essd-15-963-2023](https://doi.org/10.5194/essd-15-963-2023) (cit. on pp. v, 38).
- Codding, E. G. and Horlick, G. (1973). “Apodization and Phase Information in Fourier Transform Spectroscopy”. In: *Applied Spectroscopy* 27.2, pp. 85–92. DOI: [10.1366/000370273774333731](https://doi.org/10.1366/000370273774333731) (cit. on p. 29).
- Cooley, J. W. and Tukey, J. W. (1965). “An Algorithm for the Machine Calculation of Complex Fourier Series”. In: *Mathematics of Computation* 19.90, pp. 297–301. ISSN: 00255718 (cit. on p. 23).
- Cox, A. et al. (2022). *Multi-laboratory compilation of atmospheric carbon dioxide data for the period 1957-2021; obspack_co2_1_GLOBALVIEWplus_v8.0_2022-08-27*. DOI: [10.25925/20220808](https://doi.org/10.25925/20220808) (cit. on p. 2).
- Crippa, M., Guizzardi, D., Banja, M., Solazzo, E., Muntean, M., Schaaf, E., F. P., Monforti-Ferrario, F., Olivier, J. G. J., Quadrelli, R., Riquez Martin, A., Taghavi-Moharamli, P., Grassi, G., Rossi, S., Oom, D., Branco, A., San-Miguel, J., Vignati, E., and Commission), J. R. C. (2022). *CO₂ emissions of all world countries: JRC/IEA/PBL 2022 report*. eng. LU: Publications Office of the European Union. ISBN: 978-92-76-55802-6 (cit. on p. 2).
- Crisp, D. (2015). “Measuring atmospheric carbon dioxide from space with the Orbiting Carbon Observatory-2 (OCO-2)”. In: *Earth Observing Systems XX*. Ed. by J. J. Butler, X. (Xiong,

- and X. Gu. Vol. 9607. International Society for Optics and Photonics. SPIE, p. 960702. DOI: [10.1117/12.2187291](https://doi.org/10.1117/12.2187291) (cit. on p. 2).
- Crommelynck, D., Fichot, A., Domingo, V., and Lee III, R. (1996). “SOLCON Solar Constant Observations from the ATLAS Missions”. In: *Geophysical Research Letters* 23.17, pp. 2293–2295. DOI: [10.1029/96GL01878](https://doi.org/10.1029/96GL01878) (cit. on p. 10).
- Cusworth, D. H., Duren, R. M., Thorpe, A. K., Eastwood, M. L., Green, R. O., Dennison, P. E., Frankenberg, C., Heckler, J. W., Asner, G. P., and Miller, C. E. (2021). “Quantifying Global Power Plant Carbon Dioxide Emissions With Imaging Spectroscopy”. In: *AGU Advances* 2.2. e2020AV000350 2020AV000350, e2020AV000350. DOI: [10.1029/2020AV000350](https://doi.org/10.1029/2020AV000350) (cit. on p. 2).
- Daniel, J. S. and Solomon, S. (1998). “On the climate forcing of carbon monoxide”. en. In: *Journal of Geophysical Research: Atmospheres* 103.D11, pp. 13249–13260. ISSN: 2156-2202. DOI: [10.1029/98JD00822](https://doi.org/10.1029/98JD00822) (cit. on p. 13).
- Davis, S. P., Abrams, M. C., and Brault, J. W. (May 2001). *Fourier Transform Spectrometry*. en. Academic Press. ISBN: 978-0-12-042510-5 (cit. on pp. 20, 25, 30, 91).
- Demtröder, W. (2018). *Atoms, Molecules and Photons: An Introduction to Atomic-, Molecular- and Quantum Physics*. en. Graduate Texts in Physics. Berlin, Heidelberg: Springer. ISBN: 978-3-662-55521-7. DOI: [10.1007/978-3-662-55523-1](https://doi.org/10.1007/978-3-662-55523-1) (cit. on pp. 13–14, 17–18).
- Deutscher, N. M., Sherlock, V., Mikaloff Fletcher, S. E., Griffith, D. W. T., Notholt, J., Macatangay, R., Connor, B. J., Robinson, J., Shiona, H., Velazco, V. A., Wang, Y., Wennberg, P. O., and Wunch, D. (2014). “Drivers of column-average CO₂ variability at Southern Hemispheric Total Carbon Column Observing Network sites”. In: *Atmospheric Chemistry and Physics* 14.18, pp. 9883–9901. DOI: [10.5194/acp-14-9883-2014](https://doi.org/10.5194/acp-14-9883-2014) (cit. on p. 38).
- Dietrich, F., Chen, J., Voggenreiter, B., Aigner, P., Nachtigall, N., and Reger, B. (2021). “MUC-Cnet: Munich Urban Carbon Column network”. In: *Atmospheric Measurement Techniques* 14.2, pp. 1111–1126. DOI: [10.5194/amt-14-1111-2021](https://doi.org/10.5194/amt-14-1111-2021) (cit. on pp. 46, 60).
- Dils, B., Buchwitz, M., Reuter, M., Schneising, O., Boesch, H., Parker, R., Guerlet, S., Aben, I., Blumenstock, T., Burrows, J. P., Butz, A., Deutscher, N. M., Frankenberg, C., Hase, F., Hasekamp, O. P., Heymann, J., De Mazière, M., Notholt, J., Sussmann, R., Warneke, T., Griffith, D., Sherlock, V., and Wunch, D. (2014). “The Greenhouse Gas Climate Change Initiative (GHG-CCI): comparative validation of GHG-CCI SCIAMACHY/ENVISAT and TANSO-FTS/GOSAT CO₂ and CH₄ retrieval algorithm products with measurements from the TCCON”. In: *Atmospheric Measurement Techniques* 7.6, pp. 1723–1744. DOI: [10.5194/amt-7-1723-2014](https://doi.org/10.5194/amt-7-1723-2014) (cit. on pp. 2, 37).
- Douville, H., Raghavan, K., Renwick, J., Allan, R., Arias, P., Barlow, M., Cerezo-Mota, R., Cherchi, A., Gan, T., Gergis, J., Jiang, D., Khan, A., Pokam Mba, W., Rosenfeld, D., Tierney, J., and Zolina, O. (2021). “Water Cycle Changes”. In: *Climate Change 2021: The Physical Science Basis. Contribution of Working Group I to the Sixth Assessment Report of the Intergovernmental Panel on Climate Change*. Ed. by V. Masson-Delmotte, P. Zhai, A. Pirani, S. Connors, C. Péan, S. Berger, N. Caud, Y. Chen, L. Goldfarb, M. Gomis, M. Huang, K. Leitzell, E. Lonnoy, J. Matthews, T. Maycock, T. Waterfield, O. Yelekçi, R. Yu, and B. Zhou. Cambridge, United Kingdom and New York, NY, USA: Cambridge University Press, pp. 1055–1210. DOI: [10.1017/9781009157896.010](https://doi.org/10.1017/9781009157896.010) (cit. on p. 1).
- Dutton, G. and Hall, B. (2022). *Global Atmospheric Nitrous Oxide Dry Air Mole Fractions from the NOAA GML Halocarbons in situ Network*. Version Version 2022-10-03. DOI: [10.7289/V5X0659V](https://doi.org/10.7289/V5X0659V) (cit. on p. 6).
- Efremenko, D. and Kokhanovsky, A. (2021). *Foundations of Atmospheric Remote Sensing*. en. Cham: Springer International Publishing. ISBN: 978-3-030-66744-3. DOI: [10.1007/978-3-030-66745-0](https://doi.org/10.1007/978-3-030-66745-0) (cit. on pp. 8, 11, 32).

- Feld, L., Herkommer, B., and Dubravica, D. (May 1, 2023a). *PROFFASTpylot on GitLab*. URL: <https://gitlab.eudat.eu/coccon-kit/proffastpylot> (cit. on p. 50).
- Feld, L., **Herkommer, B.**, Dubravica, D., Alberti, C., and Hase, F. (2023b). *PROFFASTpylot: Running PROFFAST with Python*. JOSS: The Journal of Open Source Software. Submitted (cit. on pp. v, 47).
- Fox-Kemper, B., Hewitt, H., Xiao, C., Adalgeirsdóttir, G., Drijfhout, S., Edwards, T., Golledge, N., Hemer, M., Kopp, R., Krinner, G., Mix, A., Notz, D., Nowicki, S., Nurhati, I., Ruiz, L., Sallée, J.-B., Slangen, A., and Yu, Y. (2021). “Ocean, Cryosphere and Sea Level Change”. In: *Climate Change 2021: The Physical Science Basis. Contribution of Working Group I to the Sixth Assessment Report of the Intergovernmental Panel on Climate Change*. Ed. by V. Masson-Delmotte, P. Zhai, A. Pirani, S. Connors, C. Péan, S. Berger, N. Caud, Y. Chen, L. Goldfarb, M. Gomis, M. Huang, K. Leitzell, E. Lonnoy, J. Matthews, T. Maycock, T. Waterfield, O. Yelekçi, R. Yu, and B. Zhou. Cambridge, United Kingdom and New York, NY, USA: Cambridge University Press, pp. 1211–1362. DOI: [10.1017/9781009157896.011](https://doi.org/10.1017/9781009157896.011) (cit. on p. 1).
- Frey, M., Hase, F., Blumenstock, T., Groß, J., Kiel, M., Mengistu Tsidu, G., Schäfer, K., Sha, M. K., and Orphal, J. (2015). “Calibration and instrumental line shape characterization of a set of portable FTIR spectrometers for detecting greenhouse gas emissions”. In: *Atmospheric Measurement Techniques* 8.7, pp. 3047–3057. DOI: [10.5194/amt-8-3047-2015](https://doi.org/10.5194/amt-8-3047-2015) (cit. on pp. 47, 64).
- Frey, M., Sha, M. K., Hase, F., Kiel, M., Blumenstock, T., Harig, R., Surawicz, G., Deutscher, N. M., Shiomi, K., Franklin, J. E., Bösch, H., Chen, J., Grutter, M., Ohyama, H., Sun, Y., Butz, A., Mengistu Tsidu, G., Ene, D., Wunch, D., Cao, Z., Garcia, O., Ramonet, M., Vogel, F., and Orphal, J. (2019). “Building the COllaborative Carbon Column Observing Network (COCCON): long-term stability and ensemble performance of the EM27/SUN Fourier transform spectrometer”. In: *Atmospheric Measurement Techniques* 12.3, pp. 1513–1530. DOI: [10.5194/amt-12-1513-2019](https://doi.org/10.5194/amt-12-1513-2019) (cit. on pp. 2, 46–47).
- Frey, M. (2018). “Characterisation and application of portable solar absorption spectrometers for the detection of greenhouse gas emissions from regional anthropogenic sources”. 12.03.01; LK 01. Doktorarbeit. Karlsruher Institut für Technologie (KIT). 117 pp. DOI: [10.5445/IR/1000088312](https://doi.org/10.5445/IR/1000088312) (cit. on pp. 29, 69).
- Fröhlich, C. and Lean, J. (Dec. 2004). “Solar radiative output and its variability: evidence and mechanisms”. In: *The Astronomy and Astrophysics Review* 12.4, pp. 273–320. ISSN: 1432-0754. DOI: [10.1007/s00159-004-0024-1](https://doi.org/10.1007/s00159-004-0024-1) (cit. on p. 10).
- Gisi, M., Hase, F., Dohe, S., and Blumenstock, T. (2011). “Camtracker: a new camera controlled high precision solar tracker system for FTIR-spectrometers”. In: *Atmospheric Measurement Techniques* 4.1, pp. 47–54. DOI: [10.5194/amt-4-47-2011](https://doi.org/10.5194/amt-4-47-2011) (cit. on p. 42).
- Gisi, M., Hase, F., Dohe, S., Blumenstock, T., Simon, A., and Keens, A. (2012). “XCO₂-measurements with a tabletop FTS using solar absorption spectroscopy”. In: *Atmospheric Measurement Techniques* 5.11, pp. 2969–2980. DOI: [10.5194/amt-5-2969-2012](https://doi.org/10.5194/amt-5-2969-2012) (cit. on pp. 3, 46).
- Gordon, I. et al. (2022). “The HITRAN2020 molecular spectroscopic database”. In: *Journal of Quantitative Spectroscopy and Radiative Transfer* 277, p. 107949. ISSN: 0022-4073. DOI: <https://doi.org/10.1016/j.jqsrt.2021.107949> (cit. on p. 33).
- Gordon, I. E., Rothman, L. S., and Toon, G. C. (2011). “Revision of spectral parameters for the B- and γ -bands of oxygen and their validation against atmospheric spectra”. In: *Journal of Quantitative Spectroscopy and Radiative Transfer* 112.14, pp. 2310–2322. ISSN: 0022-4073. DOI: <https://doi.org/10.1016/j.jqsrt.2011.05.007> (cit. on p. 38).

- Griffiths, P., De Haseth, J., and Winefordner, J. (2007). *Fourier Transform Infrared Spectrometry*. Chemical Analysis: A Series of Monographs on Analytical Chemistry and Its Applications. Wiley. ISBN: 9780470106297 (cit. on pp. 20, 25).
- Haken, H. and Wolf, H. C. (1987). “Allgemeine Gesetzmäßigkeiten optischer Übergänge”. In: *Atom- und Quantenphysik: Eine Einführung in die experimentellen und theoretischen Grundlagen*. Berlin, Heidelberg: Springer Berlin Heidelberg, pp. 285–301. ISBN: 978-3-642-97025-2. DOI: [10.1007/978-3-642-97025-2_16](https://doi.org/10.1007/978-3-642-97025-2_16) (cit. on p. 19).
- Hall, B. D., Crotwell, A. M., Kitzis, D. R., Mefford, T., Miller, B. R., Schibig, M. F., and Tans, P. P. (2021). “Revision of the World Meteorological Organization Global Atmosphere Watch (WMO/GAW) CO₂ calibration scale”. In: *Atmospheric Measurement Techniques* 14.4, pp. 3015–3032. DOI: [10.5194/amt-14-3015-2021](https://doi.org/10.5194/amt-14-3015-2021) (cit. on pp. 3, 40, 47).
- Hase, F., Blumenstock, T., and Paton-Walsh, C. (May 1999). “Analysis of the instrumental line shape of high-resolution Fourier transform IR spectrometers with gas cell measurements and new retrieval software”. In: *Appl. Opt.* 38.15, pp. 3417–3422. DOI: [10.1364/AO.38.003417](https://doi.org/10.1364/AO.38.003417) (cit. on pp. 3, 30, 41).
- Hase, F., Drouin, B. J., Roehl, C. M., Toon, G. C., Wennberg, P. O., Wunch, D., Blumenstock, T., Desmet, F., Feist, D. G., Heikkinen, P., De Mazière, M., Rettinger, M., Robinson, J., Schneider, M., Sherlock, V., Sussmann, R., Té, Y., Warneke, T., and Weinzierl, C. (2013). “Calibration of sealed HCl cells used for TCCON instrumental line shape monitoring”. In: *Atmospheric Measurement Techniques* 6.12, pp. 3527–3537. DOI: [10.5194/amt-6-3527-2013](https://doi.org/10.5194/amt-6-3527-2013) (cit. on p. 41).
- Hase, F., Frey, M., Blumenstock, T., Groß, J., Kiel, M., Kohlhepp, R., Mengistu Tsidu, G., Schäfer, K., Sha, M. K., and Orphal, J. (2015). “Application of portable FTIR spectrometers for detecting greenhouse gas emissions of the major city Berlin”. In: *Atmospheric Measurement Techniques* 8.7, pp. 3059–3068. DOI: [10.5194/amt-8-3059-2015](https://doi.org/10.5194/amt-8-3059-2015) (cit. on p. 46).
- Hase, F., Frey, M., Kiel, M., Blumenstock, T., Harig, R., Keens, A., and Orphal, J. (2016). “Addition of a channel for XCO observations to a portable FTIR spectrometer for greenhouse gas measurements”. In: *Atmospheric Measurement Techniques* 9.5, pp. 2303–2313. DOI: [10.5194/amt-9-2303-2016](https://doi.org/10.5194/amt-9-2303-2016) (cit. on pp. 46, 69).
- Hase, F. (2000). “Inversion von Spurengasen aus hochaufgelösten bodengebundenen FTIR-Messungen in Absorption”. de. PhD thesis. Institut für Meteorologie und Klimaforschung (cit. on pp. 19, 27).
- Hedelius, J. K., Viatte, C., Wunch, D., Roehl, C. M., Toon, G. C., Chen, J., Jones, T., Wofsy, S. C., Franklin, J. E., Parker, H., Dubey, M. K., and Wennberg, P. O. (2016). “Assessment of errors and biases in retrievals of X_{CO₂}, X_{CH₄}, X_{CO}, and X_{N₂O} from a 0.5 cm⁻¹ resolution solar-viewing spectrometer”. In: *Atmospheric Measurement Techniques* 9.8, pp. 3527–3546. DOI: [10.5194/amt-9-3527-2016](https://doi.org/10.5194/amt-9-3527-2016) (cit. on pp. 3, 47).
- Heinle, L. and Chen, J. (2018). “Automated enclosure and protection system for compact solar-tracking spectrometers”. In: *Atmospheric Measurement Techniques* 11.4, pp. 2173–2185. DOI: [10.5194/amt-11-2173-2018](https://doi.org/10.5194/amt-11-2173-2018) (cit. on pp. 60–61).
- Herkommer, B.**, Alberti, C., Castracane, P., Chen, J., Dehn, A., Dietrich, F., Deutscher, N. M., Frey, M. M., Groß, J., Gillespie, L., Hase, F., Morino, I., Pak, N. M., Walker, B., and Wunch, D. (2024). “Using a portable FTIR spectrometer to evaluate the consistency of TCCON measurements on a global scale: The COCCON Travel Standard”. In: *EGUsphere* 2024, pp. 1–46. DOI: [10.5194/egusphere-2023-3089](https://doi.org/10.5194/egusphere-2023-3089) (cit. on pp. v, 59, 73).
- Hodson, E. L., Poulter, B., Zimmermann, N. E., Prigent, C., and Kaplan, J. O. (2011). “The El Niño–Southern Oscillation and wetland methane interannual variability”. In: *Geophysical Research Letters* 38.8. DOI: [10.1029/2011GL046861](https://doi.org/10.1029/2011GL046861) (cit. on p. 2).

- Hong, X., Zhang, P., Bi, Y., Liu, C., Sun, Y., Wang, W., Chen, Z., Yin, H., Zhang, C., Tian, Y., and Liu, J. (2022). “Retrieval of Global Carbon Dioxide From TanSat Satellite and Comprehensive Validation With TCCON Measurements and Satellite Observations”. In: *IEEE Transactions on Geoscience and Remote Sensing* 60, pp. 1–16. DOI: [10.1109/TGRS.2021.3066623](https://doi.org/10.1109/TGRS.2021.3066623) (cit. on p. 37).
- Inoue, M., Morino, I., Uchino, O., Nakatsuru, T., Yoshida, Y., Yokota, T., Wunch, D., Wennberg, P. O., Roehl, C. M., Griffith, D. W. T., Velazco, V. A., Deutscher, N. M., Warneke, T., Notholt, J., Robinson, J., Sherlock, V., Hase, F., Blumenstock, T., Rettinger, M., Sussmann, R., Kyrö, E., Kivi, R., Shiomi, K., Kawakami, S., De Mazière, M., Arnold, S. G., Feist, D. G., Barrow, E. A., Barney, J., Dubey, M., Schneider, M., Iraci, L. T., Podolske, J. R., Hillyard, P. W., Machida, T., Sawa, Y., Tsuboi, K., Matsueda, H., Sweeney, C., Tans, P. P., Andrews, A. E., Biraud, S. C., Fukuyama, Y., Pittman, J. V., Kort, E. A., and Tanaka, T. (Aug. 2016). “Bias corrections of GOSAT SWIR XCO₂ and XCH₄ with TCCON data and their evaluation using aircraft measurement data”. English. In: *Atmospheric Measurement Techniques* 9.8. Publisher: Copernicus GmbH, pp. 3491–3512. ISSN: 1867-1381. DOI: [10.5194/amt-9-3491-2016](https://doi.org/10.5194/amt-9-3491-2016) (cit. on pp. 40, 49).
- Jones, C. D., Fraise, C. W., and Ozores-Hampton, M. (2012). “Quantification of greenhouse gas emissions from open field-grown Florida tomato production”. In: *Agricultural Systems* 113, pp. 64–72. ISSN: 0308-521X. DOI: [10.1016/j.agsy.2012.07.007](https://doi.org/10.1016/j.agsy.2012.07.007) (cit. on p. 1).
- Jones, P. D., New, M., Parker, D. E., Martin, S., and Rigor, I. G. (1999). “Surface air temperature and its changes over the past 150 years”. In: *Reviews of Geophysics* 37.2, pp. 173–199. DOI: [10.1029/1999RG900002](https://doi.org/10.1029/1999RG900002) (cit. on p. 12).
- K.W., T., A.M., C., and J.W., M. (2022). *Atmospheric Carbon Dioxide Dry Air Mole Fractions from continuous measurements at Mauna Loa, Hawaii, Barrow, Alaska, American Samoa and South Pole*. Version Version 2022-05. National Oceanic and Atmospheric Administration (NOAA), Global Monitoring Laboratory (GML), Boulder, Colorado, USA. DOI: [10.15138/yaf1-bk21](https://doi.org/10.15138/yaf1-bk21) (cit. on pp. 1, 6, 12).
- Kaloyerou, P. N. (2018). “Error Analysis”. In: *Basic Concepts of Data and Error Analysis: With Introductions to Probability and Statistics and to Computer Methods*. Cham: Springer International Publishing, pp. 27–59. ISBN: 978-3-319-95876-7. DOI: [10.1007/978-3-319-95876-7_3](https://doi.org/10.1007/978-3-319-95876-7_3) (cit. on p. 65).
- Karimipour, H., Tam, V. W. Y., Burnie, H., and Le, K. N. (2019). “Quantifying the effects of general waste reduction on greenhouse-gas emissions at public facilities”. In: *Journal of the Air & Waste Management Association* 69.10, pp. 1247–1257. DOI: [10.1080/10962247.2019.1642967](https://doi.org/10.1080/10962247.2019.1642967) (cit. on p. 1).
- Karion, A., Sweeney, C., Tans, P., and Newberger, T. (2010). “AirCore: An Innovative Atmospheric Sampling System”. In: *Journal of Atmospheric and Oceanic Technology* 27.11, pp. 1839–1853. DOI: [10.1175/2010JTECHA1448.1](https://doi.org/10.1175/2010JTECHA1448.1) (cit. on pp. 3, 40, 49).
- Kern, C. and Jess, A. (2021). “Reducing Global Greenhouse Gas Emissions to Meet Climate Targets—A Comprehensive Quantification and Reasonable Options”. In: *Energies* 14.17. ISSN: 1996-1073. DOI: [10.3390/en14175260](https://doi.org/10.3390/en14175260) (cit. on p. 1).
- Kerner, H. and Wahl, W. von (2013). “Funktionentheorie”. In: *Mathematik für Physiker*. Berlin, Heidelberg: Springer Berlin Heidelberg, pp. 399–465. ISBN: 978-3-642-37654-2. DOI: [10.1007/978-3-642-37654-2_14](https://doi.org/10.1007/978-3-642-37654-2_14) (cit. on p. 10).
- Kiel, M. [(2016). “Trace gas measurements from different spectral regions using FTIR spectroscopy”. aa. Karlsruhe: Karlsruher Institut für Technologie (KIT). DOI: [10.5445/IR/1000056859](https://doi.org/10.5445/IR/1000056859) (cit. on p. 42).
- Klappenbach, F., Bertleff, M., Kostinek, J., Hase, F., Blumenstock, T., Agustí-Panareda, A., Razinger, M., and Butz, A. (2015). “Accurate mobile remote sensing of XCO₂ and XCH₄

- latitudinal transects from aboard a research vessel”. In: *Atmospheric Measurement Techniques* 8.12, pp. 5023–5038. DOI: [10.5194/amt-8-5023-2015](https://doi.org/10.5194/amt-8-5023-2015) (cit. on p. 46).
- Kleber, A. and Richter-Krautz, J. (2022). “Forschungsgeschichte des Klimawandels”. In: *Klimawandel FAQs - Fake News erkennen, Argumente verstehen, qualitativ antworten*. Berlin, Heidelberg: Springer Berlin Heidelberg, pp. 87–98. ISBN: 978-3-662-64548-2. DOI: [10.1007/978-3-662-64548-2_2](https://doi.org/10.1007/978-3-662-64548-2_2) (cit. on p. 1).
- Klose, B. and Klose, H. (2016). “Die Erdatmosphäre: Ihre chemische Zusammensetzung, vertikale Struktur und Physik”. In: *Meteorologie: Eine interdisziplinäre Einführung in die Physik der Atmosphäre*. Berlin, Heidelberg: Springer Berlin Heidelberg, pp. 15–81. ISBN: 978-3-662-43622-6. DOI: [10.1007/978-3-662-43622-6_2](https://doi.org/10.1007/978-3-662-43622-6_2) (cit. on pp. 6, 8).
- Knapp, M., Kleinschek, R., Hase, F., Agusti-Panareda, A., Inness, A., Barre, J., Landgraf, J., Borsdorff, T., Kinne, S., and Butz, A. (2021). “Shipborne measurements of XCO₂, XCH₄, and XCO above the Pacific Ocean and comparison to CAMS atmospheric analyses and S5P/TROPOMI”. In: *Earth System Science Data* 13.1, pp. 199–211. DOI: [10.5194/essd-13-199-2021](https://doi.org/10.5194/essd-13-199-2021) (cit. on p. 46).
- Kramm, G. and Mölders, N. (Jan. 2009). “Planck’s blackbody radiation law: Presentation in different domains and determination of the related dimensional constants”. In: *arXiv e-prints*, arXiv:0901.1863. Provided by the SAO/NASA Astrophysics Data System, arXiv:0901.1863. DOI: [10.48550/arXiv.0901.1863](https://doi.org/10.48550/arXiv.0901.1863) (cit. on p. 9).
- Kurylo, M. J. (1991). “Network for the detection of stratospheric change”. In: *Remote Sensing of Atmospheric Chemistry*. Ed. by J. L. McElroy and R. J. McNeal. Vol. 1491. International Society for Optics and Photonics. SPIE, pp. 168–174. DOI: [10.1117/12.46658](https://doi.org/10.1117/12.46658) (cit. on p. 2).
- L., F. M., H., S. W., and Vanasse, G. A. (Jan. 1966). “Correction of Asymmetric Interferograms Obtained in Fourier Spectroscopy*”. In: *J. Opt. Soc. Am.* 56.1, pp. 59–63. DOI: [10.1364/JOSA.56.000059](https://doi.org/10.1364/JOSA.56.000059) (cit. on p. 29).
- Lan, X., Dlugokencky, E., A.M., C., K.W., T., and J.W., M. (2022). *Atmospheric Methane from quasi-continuous measurements at Barrow, Alaska and Mauna Loa, Hawaii*. Version Version: 2022-03. DOI: [10.15138/ve0c-be70](https://doi.org/10.15138/ve0c-be70) (cit. on pp. 6, 12).
- Laughner, J. L. (May 12, 2023). private communication (cit. on pp. 40, 78).
- Laughner, J. L., Roche, S., Kiel, M., Toon, G. C., Wunch, D., Baier, B. C., Biraud, S., Chen, H., Kivi, R., Laemmle, T., McKain, K., Quéhé, P.-Y., Rousogonous, C., Stephens, B. B., Walker, K., and Wennberg, P. O. (2023). “A new algorithm to generate a priori trace gas profiles for the GGG2020 retrieval algorithm”. In: *Atmospheric Measurement Techniques* 16.5, pp. 1121–1146. DOI: [10.5194/amt-16-1121-2023](https://doi.org/10.5194/amt-16-1121-2023) (cit. on p. 78).
- Lisboa, C., Butterbach-Bahl, K., Mauder, M., and Kiese, R. (2011). “Bioethanol production from sugarcane and emissions of greenhouse gases – known and unknowns”. In: *GCB Bioenergy* 3.4, pp. 277–292. DOI: [10.1111/j.1757-1707.2011.01095.x](https://doi.org/10.1111/j.1757-1707.2011.01095.x) (cit. on p. 1).
- Liu, Y., Lin, J., Huang, G., Guo, Y., and Duan, C. (May 2001). “Simple empirical analytical approximation to the Voigt profile”. In: *J. Opt. Soc. Am. B* 18.5, pp. 666–672. DOI: [10.1364/JOSAB.18.000666](https://doi.org/10.1364/JOSAB.18.000666) (cit. on p. 20).
- Luther, A., Kleinschek, R., Scheidweiler, L., Defratyka, S., Stanisavljevic, M., Forstmaier, A., Dandocsi, A., Wolff, S., Dubravica, D., Wildmann, N., Kostinek, J., Jöckel, P., Nickl, A.-L., Klausner, T., Hase, F., Frey, M., Chen, J., Dietrich, F., Necki, J., Swolkien, J., Fix, A., Roiger, A., and Butz, A. (2019). “Quantifying CH₄ emissions from hard coal mines using mobile sun-viewing Fourier transform spectrometry”. In: *Atmospheric Measurement Techniques* 12.10, pp. 5217–5230. DOI: [10.5194/amt-12-5217-2019](https://doi.org/10.5194/amt-12-5217-2019) (cit. on p. 46).
- Meinshausen, M., Vogel, E., Nauels, A., Lorbacher, K., Meinshausen, N., Etheridge, D. M., Fraser, P. J., Montzka, S. A., Rayner, P. J., Trudinger, C. M., Krummel, P. B., Beyerle, U., Canadell, J. G., Daniel, J. S., Enting, I. G., Law, R. M., Lunder, C. R., O’Doherty, S., Prinn,

- R. G., Reimann, S., Rubino, M., Velders, G. J. M., Vollmer, M. K., Wang, R. H. J., and Weiss, R. (2017). “Historical greenhouse gas concentrations for climate modelling (CMIP6)”. In: *Geoscientific Model Development* 10.5, pp. 2057–2116. DOI: [10.5194/gmd-10-2057-2017](https://doi.org/10.5194/gmd-10-2057-2017) (cit. on pp. 1, 12–13).
- Mertz, L. (1965). *Transformations in Optics*. Wiley. ISBN: 9780471596400 (cit. on p. 29).
- (1967). “Auxiliary computation for Fourier spectrometry”. In: *Infrared Physics* 7.1, pp. 17–23. ISSN: 0020-0891. DOI: [10.1016/0020-0891\(67\)90026-7](https://doi.org/10.1016/0020-0891(67)90026-7) (cit. on p. 29).
- Messerschmidt, J., Geibel, M. C., Blumenstock, T., Chen, H., Deutscher, N. M., Engel, A., Feist, D. G., Gerbig, C., Gisi, M., Hase, F., Katrynski, K., Kolle, O., Lavrić, J. V., Notholt, J., Palm, M., Ramonet, M., Rettinger, M., Schmidt, M., Sussmann, R., Toon, G. C., Truong, F., Warneke, T., Wennberg, P. O., Wunch, D., and Xueref-Remy, I. (2011). “Calibration of TCCON column-averaged CO₂: the first aircraft campaign over European TCCON sites”. In: *Atmospheric Chemistry and Physics* 11.21, pp. 10765–10777. DOI: [10.5194/acp-11-10765-2011](https://doi.org/10.5194/acp-11-10765-2011) (cit. on pp. 3, 40–41, 47, 49).
- Messerschmidt, J., Parazoo, N., Wunch, D., Deutscher, N. M., Roehl, C., Warneke, T., and Wennberg, P. O. (2013). “Evaluation of seasonal atmosphere–biosphere exchange estimations with TCCON measurements”. In: *Atmospheric Chemistry and Physics* 13.10, pp. 5103–5115. DOI: [10.5194/acp-13-5103-2013](https://doi.org/10.5194/acp-13-5103-2013) (cit. on pp. 1, 37).
- Messerschmidt, J., Macatangay, R., Nothold, J., Petri, C., Warneke, T., and Weinzierl, C. (2010). *Side by side measurements of CO₂ by ground-based Fourier transform spectrometry (FTS)*. DOI: [10.1111/j.1600-0889.2010.00491.x](https://doi.org/10.1111/j.1600-0889.2010.00491.x) (cit. on p. 27).
- Möller, D. (Feb. 2019). *Volume 1 Fundamentals and Processes*. en. Publication Title: Volume 1 Fundamentals and Processes. De Gruyter. ISBN: 978-3-11-056126-5. DOI: [10.1515/9783110561265](https://doi.org/10.1515/9783110561265) (cit. on p. 6).
- Morice, C. P., Kennedy, J. J., Rayner, N. A., Winn, J. P., Hogan, E., Killick, R. E., Dunn, R. J. H., Osborn, T. J., Jones, P. D., and Simpson, I. R. (2021). “An Updated Assessment of Near-Surface Temperature Change From 1850: The HadCRUT5 Data Set”. In: *Journal of Geophysical Research: Atmospheres* 126.3, e2019JD032361. DOI: [10.1029/2019JD032361](https://doi.org/10.1029/2019JD032361) (cit. on p. 12).
- Mostafavi Pak, N., Hedelius, J. K., Roche, S., Cunningham, L., Baier, B., Sweeney, C., Roehl, C., Laughner, J., Toon, G., Wennberg, P., Parker, H., Arrowsmith, C., Mendonca, J., Fogal, P., Wizenberg, T., Herrera, B., Strong, K., Walker, K. A., Vogel, F., and Wunch, D. (2023). “Using portable low-resolution spectrometers to evaluate Total Carbon Column Observing Network (TCCON) biases in North America”. In: *Atmospheric Measurement Techniques* 16.5, pp. 1239–1261. DOI: [10.5194/amt-16-1239-2023](https://doi.org/10.5194/amt-16-1239-2023) (cit. on pp. 3, 40, 47, 49, 101).
- Petri, C., Warneke, T., Jones, N., Ridder, T., Messerschmidt, J., Weinzierl, T., Geibel, M., and Notholt, J. (2012). “Remote sensing of CO₂ and CH₄ using solar absorption spectrometry with a low resolution spectrometer”. In: *Atmospheric Measurement Techniques* 5.7, pp. 1627–1635. DOI: [10.5194/amt-5-1627-2012](https://doi.org/10.5194/amt-5-1627-2012) (cit. on p. 74).
- Pörtner, H.-O. et al. (2022). “Technical Summary”. In: *Climate Change 2022: Impacts, Adaptation and Vulnerability. Contribution of Working Group II to the Sixth Assessment Report of the Intergovernmental Panel on Climate Change*. Cambridge, UK and New York, USA: Cambridge University Press, pp. 37–118. DOI: [10.1017/9781009325844.002](https://doi.org/10.1017/9781009325844.002) (cit. on p. 13).
- Riddick, S. N., Mauzerall, D. L., Celia, M., Harris, N. R. P., Allen, G., Pitt, J., Staunton-Sykes, J., Forster, G. L., Kang, M., Lowry, D., Nisbet, E. G., and Manning, A. J. (2019). “Methane emissions from oil and gas platforms in the North Sea”. In: *Atmospheric Chemistry and Physics* 19.15, pp. 9787–9796. DOI: [10.5194/acp-19-9787-2019](https://doi.org/10.5194/acp-19-9787-2019) (cit. on p. 1).

- Rodgers, C. (2000). *Inverse Methods For Atmospheric Sounding: Theory And Practice*. Series On Atmospheric, Oceanic And Planetary Physics. World Scientific Publishing Company. ISBN: 9789814498685 (cit. on p. 32).
- Roedel, W. and Wagner, T. (2017). *Physik unserer Umwelt: Die Atmosphäre*. de. Berlin, Heidelberg: Springer Berlin Heidelberg. ISBN: 978-3-662-54257-6. DOI: [10.1007/978-3-662-54258-3](https://doi.org/10.1007/978-3-662-54258-3) (cit. on pp. 6–8).
- Schulze, E.-D. (2006). “Biological control of the terrestrial carbon sink”. In: *Biogeosciences* 3.2, pp. 147–166. DOI: [10.5194/bg-3-147-2006](https://doi.org/10.5194/bg-3-147-2006) (cit. on p. 2).
- Seneviratne, S., Zhang, X., Adnan, M., Badi, W., Dereczynski, C., Di Luca, A., Ghosh, S., Iskandar, I., Kossin, J., Lewis, S., Otto, F., Pinto, I., Satoh, M., Vicente-Serrano, S., Wehner, M., and Zhou, B. (2021). “Weather and Climate Extreme Events in a Changing Climate”. In: *Climate Change 2021: The Physical Science Basis. Contribution of Working Group I to the Sixth Assessment Report of the Intergovernmental Panel on Climate Change*. Ed. by V. Masson-Delmotte, P. Zhai, A. Pirani, S. Connors, C. Péan, S. Berger, N. Caud, Y. Chen, L. Goldfarb, M. Gomis, M. Huang, K. Leitzell, E. Lonnoy, J. Matthews, T. Maycock, T. Waterfield, O. Yelekçi, R. Yu, and B. Zhou. Cambridge, United Kingdom and New York, NY, USA: Cambridge University Press, pp. 1513–1766. DOI: [10.1017/9781009157896.013](https://doi.org/10.1017/9781009157896.013) (cit. on p. 1).
- Sha, M. K., De Mazière, M., Notholt, J., Blumenstock, T., Chen, H., Dehn, A., Griffith, D. W. T., Hase, F., Heikkinen, P., Hermans, C., Hoffmann, A., Huebner, M., Jones, N., Kivi, R., Langerock, B., Petri, C., Scolas, F., Tu, Q., and Weidmann, D. (2020). “Intercomparison of low- and high-resolution infrared spectrometers for ground-based solar remote sensing measurements of total column concentrations of CO₂, CH₄, and CO”. In: *Atmospheric Measurement Techniques* 13.9, pp. 4791–4839. DOI: [10.5194/amt-13-4791-2020](https://doi.org/10.5194/amt-13-4791-2020) (cit. on pp. 3, 40, 45, 49).
- Sha, M. K., Langerock, B., Blavier, J.-F. L., Blumenstock, T., Borsdorff, T., Buschmann, M., Dehn, A., De Mazière, M., Deutscher, N. M., Feist, D. G., García, O. E., Griffith, D. W. T., Grutter, M., Hannigan, J. W., Hase, F., Heikkinen, P., Hermans, C., Iraci, L. T., Jeseck, P., Jones, N., Kivi, R., Kumps, N., Landgraf, J., Lorente, A., Mahieu, E., Makarova, M. V., Mellqvist, J., Metzger, J.-M., Morino, I., Nagahama, T., Notholt, J., Ohyama, H., Ortega, I., Palm, M., Petri, C., Pollard, D. F., Rettinger, M., Robinson, J., Roche, S., Roehl, C. M., Röhling, A. N., Rousogonous, C., Schneider, M., Shiomi, K., Smale, D., Stremme, W., Strong, K., Sussmann, R., Té, Y., Uchino, O., Velazco, V. A., Vigouroux, C., Vrekoussis, M., Wang, P., Warneke, T., Wizenberg, T., Wunch, D., Yamanouchi, S., Yang, Y., and Zhou, M. (2021). “Validation of methane and carbon monoxide from Sentinel-5 Precursor using TCCON and NDACC-IRWG stations”. In: *Atmospheric Measurement Techniques* 14.9, pp. 6249–6304. DOI: [10.5194/amt-14-6249-2021](https://doi.org/10.5194/amt-14-6249-2021) (cit. on p. 37).
- Solazzo, E., Crippa, M., Guizzardi, D., Muntean, M., Choulga, M., and Janssens-Maenhout, G. (2021). “Uncertainties in the Emissions Database for Global Atmospheric Research (EDGAR) emission inventory of greenhouse gases”. In: *Atmospheric Chemistry and Physics* 21.7, pp. 5655–5683. DOI: [10.5194/acp-21-5655-2021](https://doi.org/10.5194/acp-21-5655-2021) (cit. on p. 2).
- Someya, Y., Yoshida, Y., Ohyama, H., Nomura, S., Kamei, A., Morino, I., Mukai, H., Matsunaga, T., Laughner, J. L., Velazco, V. A., **Herkommer, B.**, Te, Y., Sha, M. K., Kivi, R., Zhou, M., Oh, Y. S., Deutscher, N. M., and Griffith, D. W. T. (2023). “Update on the GOSAT TANSO-FTS SWIR Level 2 retrieval algorithm”. In: *Atmospheric Measurement Techniques* 16.6, pp. 1477–1501. DOI: [10.5194/amt-16-1477-2023](https://doi.org/10.5194/amt-16-1477-2023) (cit. on pp. v, 37).
- Spivakovsky, C. M., Logan, J. A., Montzka, S. A., Balkanski, Y. J., Foreman-Fowler, M., Jones, D. B. A., Horowitz, L. W., Fusco, A. C., Brenninkmeijer, C. A. M., Prather, M. J., Wofsy, S. C., and McElroy, M. B. (2000). “Three-dimensional climatological distribution of tropospheric

- OH: Update and evaluation”. In: *Journal of Geophysical Research: Atmospheres* 105.D7, pp. 8931–8980. DOI: [10.1029/1999JD901006](https://doi.org/10.1029/1999JD901006) (cit. on p. 13).
- Stocker, B. D., Roth, R., Joos, F., Spahni, R., Steinacher, M., Zaehle, S., Bouwman, L., Xu-Ri, and Prentice, I. C. (July 2013). “Multiple greenhouse-gas feedbacks from the land biosphere under future climate change scenarios”. In: *Nature Climate Change* 3.7, pp. 666–672. ISSN: 1758-6798. DOI: [10.1038/nclimate1864](https://doi.org/10.1038/nclimate1864) (cit. on p. 1).
- Supran, G., Rahmstorf, S., and Oreskes, N. (2023). “Assessing ExxonMobil’s global warming projections”. In: *Science* 379.6628, eabk0063. DOI: [10.1126/science.abk0063](https://doi.org/10.1126/science.abk0063) (cit. on p. 1).
- Sussmann, R., Forster, F., Rettinger, M., and Bousquet, P. (2012). “Renewed methane increase for five years (2007–2011) observed by solar FTIR spectrometry”. In: *Atmospheric Chemistry and Physics* 12.11, pp. 4885–4891. DOI: [10.5194/acp-12-4885-2012](https://doi.org/10.5194/acp-12-4885-2012) (cit. on p. 38).
- Tran, H., Hartmann, J.-M., Toon, G., Brown, L., Frankenberg, C., Warneke, T., Spietz, P., and Hase, F. (2010). “The 2ν₃ band of CH₄ revisited with line mixing: Consequences for spectroscopy and atmospheric retrievals at 1.67μm”. In: *Journal of Quantitative Spectroscopy and Radiative Transfer* 111.10, pp. 1344–1356. ISSN: 0022-4073. DOI: <https://doi.org/10.1016/j.jqsrt.2010.02.015> (cit. on p. 38).
- Tsuruta, A., Kivimäki, E., Lindqvist, H., Karppinen, T., Backman, L., Hakkarainen, J., Schneising, O., Buchwitz, M., Lan, X., Kivi, R., Chen, H., Buschmann, M., **Herkommer, B.**, Notholt, J., Roehl, C., Té, Y., Wunch, D., Tamminen, J., and Aalto, T. (2023). “CH₄ Fluxes Derived from Assimilation of TROPOMI XCH₄ in CarbonTracker Europe-CH₄: Evaluation of Seasonality and Spatial Distribution in the Northern High Latitudes”. In: *Remote Sensing* 15.6. ISSN: 2072-4292. DOI: [10.3390/rs15061620](https://doi.org/10.3390/rs15061620) (cit. on pp. v, 38).
- Tu, Q. (2019). “Observation of atmospheric greenhouse gas abundances on regional scales in boreal areas using portable FTIR Spectrometers”. Doktorarbeit. Karlsruher Institut für Technologie (KIT). 163 pp. DOI: [10.5445/IR/1000095901](https://doi.org/10.5445/IR/1000095901) (cit. on pp. 61, 102).
- Tu, Q., Hase, F., Schneider, M., Garcia, O., Blumenstock, T., Borsdorff, T., Frey, M., Khosrawi, F., Lorente, A., Alberti, C., Bustos, J. J., Butz, A., Carreno, V., Cuevas, E., Curcoll, R., Diekmann, C. J., Dubravica, D., Ertl, B., Estruch, C., Leon-Luis, S. F., Marrero, C., Morgui, J.-A., Ramos, R., Scharun, C., Schneider, C., Sepulveda, E., Toledano, C., and Torres, C. (2022a). “Quantification of CH₄ emissions from waste disposal sites near the city of Madrid using ground- and space-based observations of COCCON, IASI”. In: *Atmospheric Chemistry and Physics* 22.1, pp. 295–317. DOI: [10.5194/acp-22-295-2022](https://doi.org/10.5194/acp-22-295-2022) (cit. on pp. 1–2).
- Tu, Q., Hase, F., Schneider, M., Garcia, O., Blumenstock, T., Borsdorff, T., Frey, M., Khosrawi, F., Lorente, A., Alberti, C., Bustos, J. J., Butz, A., Carreño, V., Cuevas, E., Curcoll, R., Diekmann, C. J., Dubravica, D., Ertl, B., Estruch, C., León-Luis, S. F., Marrero, C., Morgui, J.-A., Ramos, R., Scharun, C., Schneider, C., Sepúlveda, E., Toledano, C., and Torres, C. (2022b). “Quantification of CH₄ emissions from waste disposal sites near the city of Madrid using ground- and space-based observations of COCCON, IASI”. In: *Atmospheric Chemistry and Physics* 22.1, pp. 295–317. DOI: [10.5194/acp-22-295-2022](https://doi.org/10.5194/acp-22-295-2022) (cit. on p. 46).
- United-Nations (2015). *The Paris Agreement*. URL: <https://unfccc.int/process-and-meetings/the-paris-agreement> (cit. on p. 1).
- Veeffkind, J., Aben, I., McMullan, K., Förster, H., de Vries, J., Otter, G., Claas, J., Eskes, H., de Haan, J., Kleipool, Q., van Weele, M., Hasekamp, O., Hoogeveen, R., Landgraf, J., Snel, R., Tol, P., Ingmann, P., Voors, R., Kruizinga, B., Vink, R., Visser, H., and Levelt, P. (2012). “TROPOMI on the ESA Sentinel-5 Precursor: A GMES mission for global observations of the atmospheric composition for climate, air quality and ozone layer applications”. In: *Remote Sensing of Environment* 120. The Sentinel Missions - New Opportunities for Science, pp. 70–83. ISSN: 0034-4257. DOI: [10.1016/j.rse.2011.09.027](https://doi.org/10.1016/j.rse.2011.09.027) (cit. on p. 2).

- Wolf, H. C. and Haken, H. (2006). *Molekülphysik und Quantenchemie*. de. Springer-Lehrbuch. Berlin/Heidelberg: Springer-Verlag. ISBN: 978-3-540-30314-5. DOI: [10.1007/3-540-30315-4](https://doi.org/10.1007/3-540-30315-4) (cit. on pp. 13–14, 17–18).
- Wu, L., Hasekamp, O., Hu, H., Landgraf, J., Butz, A., Brugh, J. aan de, Aben, I., Pollard, D. F., Griffith, D. W. T., Feist, D. G., Koshelev, D., Hase, F., Toon, G. C., Ohyama, H., Morino, I., Notholt, J., Shiomi, K., Iraci, L., Schneider, M., Mazière, M. de, Sussmann, R., Kivi, R., Warneke, T., Goo, T.-Y., and Té, Y. (2018). “Carbon dioxide retrieval from OCO-2 satellite observations using the RemoTeC algorithm and validation with TCCON measurements”. In: *Atmospheric Measurement Techniques* 11.5, pp. 3111–3130. DOI: [10.5194/amt-11-3111-2018](https://doi.org/10.5194/amt-11-3111-2018) (cit. on pp. 2, 37).
- Wunch, D., Toon, G., Sherlock, V., Deutscher, N., Liu, C., Feist, D., and Wennberg, P. (2015). *The Total Carbon Column Observing Network’s GGG2014 Data Version*. DOI: [10.14291/TCCON.GGG2014.DOCUMENTATION.RO/1221662](https://doi.org/10.14291/TCCON.GGG2014.DOCUMENTATION.RO/1221662) (cit. on pp. 40–41).
- Wunch, D., Toon, G. C., Wennberg, P. O., Wofsy, S. C., Stephens, B. B., Fischer, M. L., Uchino, O., Abshire, J. B., Bernath, P., Biraud, S. C., Blavier, J.-F. L., Boone, C., Bowman, K. P., Browell, E. V., Campos, T., Connor, B. J., Daube, B. C., Deutscher, N. M., Diao, M., Elkins, J. W., Gerbig, C., Gottlieb, E., Griffith, D. W. T., Hurst, D. F., Jiménez, R., Keppel-Aleks, G., Kort, E. A., Macatangay, R., Machida, T., Matsueda, H., Moore, F., Morino, I., Park, S., Robinson, J., Roehl, C. M., Sawa, Y., Sherlock, V., Sweeney, C., Tanaka, T., and Zondlo, M. A. (2010). “Calibration of the Total Carbon Column Observing Network using aircraft profile data”. In: *Atmospheric Measurement Techniques* 3.5, pp. 1351–1362. DOI: [10.5194/amt-3-1351-2010](https://doi.org/10.5194/amt-3-1351-2010) (cit. on pp. 3, 40, 49).
- Wunch, D., Wennberg, P. O., Messerschmidt, J., Parazoo, N. C., Toon, G. C., Deutscher, N. M., Keppel-Aleks, G., Roehl, C. M., Randerson, J. T., Warneke, T., and Notholt, J. (2013). “The covariation of Northern Hemisphere summertime CO₂ with surface temperature in boreal regions”. In: *Atmospheric Chemistry and Physics* 13.18, pp. 9447–9459. DOI: [10.5194/acp-13-9447-2013](https://doi.org/10.5194/acp-13-9447-2013) (cit. on p. 37).
- Wunch, D., Wennberg, P. O., Osterman, G., Fisher, B., Naylor, B., Roehl, C. M., O’Dell, C., Mandrake, L., Viatte, C., Kiel, M., Griffith, D. W. T., Deutscher, N. M., Velazco, V. A., Notholt, J., Warneke, T., Petri, C., De Mazière, M., Sha, M. K., Sussmann, R., Rettinger, M., Pollard, D., Robinson, J., Morino, I., Uchino, O., Hase, F., Blumenstock, T., Feist, D. G., Arnold, S. G., Strong, K., Mendonca, J., Kivi, R., Heikkinen, P., Iraci, L., Podolske, J., Hillyard, P. W., Kawakami, S., Dubey, M. K., Parker, H. A., Sepulveda, E., García, O. E., Te, Y., Jeseck, P., Gunson, M. R., Crisp, D., and Eldering, A. (2017). “Comparisons of the Orbiting Carbon Observatory-2 (OCO-2) X_{CO₂} measurements with TCCON”. In: *Atmospheric Measurement Techniques* 10.6, pp. 2209–2238. DOI: [10.5194/amt-10-2209-2017](https://doi.org/10.5194/amt-10-2209-2017) (cit. on p. 37).
- Wunch, D., Wennberg, P. O., Toon, G. C., Connor, B. J., Fisher, B., Osterman, G. B., Frankenberg, C., Mandrake, L., O’Dell, C., Ahonen, P., Biraud, S. C., Castano, R., Cressie, N., Crisp, D., Deutscher, N. M., Eldering, A., Fisher, M. L., Griffith, D. W. T., Gunson, M., Heikkinen, P., Keppel-Aleks, G., Kyrö, E., Lindenmaier, R., Macatangay, R., Mendonca, J., Messerschmidt, J., Miller, C. E., Morino, I., Notholt, J., Oyafuso, F. A., Rettinger, M., Robinson, J., Roehl, C. M., Salawitch, R. J., Sherlock, V., Strong, K., Sussmann, R., Tanaka, T., Thompson, D. R., Uchino, O., Warneke, T., and Wofsy, S. C. (2011a). “A method for evaluating bias in global measurements of CO₂ total columns from space”. In: *Atmospheric Chemistry and Physics* 11.23, pp. 12317–12337. DOI: [10.5194/acp-11-12317-2011](https://doi.org/10.5194/acp-11-12317-2011) (cit. on p. 37).
- Wunch, D., Toon, G. C., Blavier, J.-F. L., Washenfelder, R. A., Notholt, J., Connor, B. J., Griffith, D. W. T., Sherlock, V., and Wennberg, P. O. (2011b). “The Total Carbon Column

- Observing Network”. In: *Philosophical Transactions of the Royal Society A: Mathematical, Physical and Engineering Sciences* 369.1943, pp. 2087–2112. DOI: [10.1098/rsta.2010.0240](https://doi.org/10.1098/rsta.2010.0240) (cit. on pp. 2, 39).
- Yokota, T., Yoshida, Y., Eguchi, N., Ota, Y., Tanaka, T., Watanabe, H., and Maksyutov, S. (2009). “Global Concentrations of CO₂ and CH₄ Retrieved from GOSAT: First Preliminary Results”. In: *SOLA* 5, pp. 160–163. DOI: [10.2151/sola.2009-041](https://doi.org/10.2151/sola.2009-041) (cit. on p. 2).
- Yoshida, Y., Kikuchi, N., Morino, I., Uchino, O., Oshchepkov, S., Bril, A., Saeki, T., Schutgens, N., Toon, G. C., Wunch, D., Roehl, C. M., Wennberg, P. O., Griffith, D. W. T., Deutscher, N. M., Warneke, T., Notholt, J., Robinson, J., Sherlock, V., Connor, B., Rettinger, M., Sussmann, R., Ahonen, P., Heikkinen, P., Kyrö, E., Mendonca, J., Strong, K., Hase, F., Dohe, S., and Yokota, T. (2013). “Improvement of the retrieval algorithm for GOSAT SWIR XCO₂ and XCH₄ and their validation using TCCON data”. In: *Atmospheric Measurement Techniques* 6.6, pp. 1533–1547. DOI: [10.5194/amt-6-1533-2013](https://doi.org/10.5194/amt-6-1533-2013) (cit. on pp. 2, 37).
- Zhang, Y., Gautam, R., Pandey, S., Omara, M., Maasackers, J. D., Sadavarte, P., Lyon, D., Nesser, H., Sulprizio, M. P., Varon, D. J., Zhang, R., Houweling, S., Zavala-Araiza, D., Alvarez, R. A., Lorente, A., Hamburg, S. P., Aben, I., and Jacob, D. J. (2020). “Quantifying methane emissions from the largest oil-producing basin in the United States from space”. In: *Science Advances* 6.17, eaaz5120. DOI: [10.1126/sciadv.aaz5120](https://doi.org/10.1126/sciadv.aaz5120) (cit. on p. 2).

List of Figures

2.1.	Illustration of an air parcel in an hydrostatic atmosphere.	7
2.2.	The PLANCK spectrum of two black bodies	9
2.3.	A simplified model of the Earth's energy balance.	11
2.4.	The Earth's surface anomaly and GHG concentrations from 1850 until now	12
2.5.	Schematic plot of the MORSE-potential and the harmonic potential.	15
2.6.	A schematic drawing of a rovibrational spectrum and the corresponding level scheme	18
2.7.	A schematic drawing of the MICHELSON-interferometer	23
2.8.	Simulated pairs of spectra and interferograms	26
2.9.	The sinc function	28
3.1.	A map of the TCCON-network	38
3.2.	An photograph of the Karlsruhe TCCON instrument	39
3.3.	The time series of the Karlsruhe TCCON site.	43
3.4.	Visualization and assessment of the timing error at the Karlsruhe TCCON site . . .	44
3.5.	Bifurcation in XAIR with respect to the SZA	45
3.6.	The COCCON and the EM27/SUN	46
3.7.	Flowchart of the PROFFAST and the PROFFASTPYLOT	48
3.8.	The ai mass dependency of XGas values using unity and new ADCFs	51
3.9.	Comparing the "old" PROFFAST2 calibration with the Karlsruhe TCCON site . . .	53
3.10.	The result of the XH ₂ O correction for XCO ₂ in the Karlsruhe data	54
3.11.	Difference of the retrievals using the H ₂ O line list of PROFFAST1 and PROFFAST2	55
3.12.	Comparison of the XH ₂ O dependency of GGG2020 and PROFFAST1	56
3.13.	Comparison of the XH ₂ O dependency of GGG2020 and GGG2014	57
4.1.	Enclosure of the Travel Standard	60
4.2.	Temperature records inside and outside of the enclosure	61
4.3.	Example of dynamic pressure create by fan in the enclosure.	62
4.4.	Pressure sensor inside the enclosure.	62
4.5.	Side-by-side measurements with the COCCON reference unit in Karlsruhe	67
4.6.	ILS parameter of the TS spectrometer.	69
4.7.	The SZA dependency of XCH ₄ , XCH ₄ ^{S5P} and XCO	70
4.8.	Pressure comparisons of the sensor deployed with the TS, a reference in Karlsruhe .	71
4.9.	Comparison of the Vaisala PTB330 sensor at the rooftop of the IMK-ASF with the DWD sensor in Rheinstetten.	72
5.1.	Pressure comparison in Tsukuba, Japan	75
5.2.	The time series of the measurements collected in Tsukuba, Japan	76
5.3.	XGas results of the Tsukuba data with -44 s time correction	79
5.4.	Side-by-side comparison of pressure data in ETL	79
5.5.	XGas measurements in ETL, Canada	80
5.6.	Pressure comparison in WG.	81

5.7. XGas measurements in Wollongong	82
5.8. Noise analysis of the TCCON sites visited with the TS	84
5.9. Total columns of O ₂ and CO ₂ measured in Tsukuba.	85
5.10. Comparison of spectra from Tsukuba and Karlsruhe	85
5.11. Comparison of the HR and LR spectra of the Karlsruhe TCCON spectrometer	86
5.12. Calculation of the SNR for the O ₂ window	89
5.13. Comparison of the SSQ and the SNR.	93
5.14. Correlations between the SSQs and the XCO ₂ noise level σ_{XCO_2}	94
5.15. A bar chart of the XCO ₂ noise levels and the SSQs for various TCCON sites	94
5.16. A bar chart of the XCO ₂ noise levels and the SSQs including the TCCON data of the TS campaigns	95
5.17. A graphical illustration of the calculation of the bias compensation factors	97
5.18. Deviation of the TCCON sites to Karlsruhe in percentage.	100
5.19. Comparison of the time corrected and uncorrected TK data.	100
A.1. Long term side-by-side measurement of the Travel Standard and the COCCON reference unit	109
B.1. Air mas dependent correction for Instrument SN039	112
B.2. Air mas dependent correction for Instrument SN122	113
B.3. Results of the new PROFFAST calibration for XCH ₄ and instrument SN037	114
B.4. Results of the new PROFFAST calibration for XCH ₄ ^{S5P} and instrument SN037	114
B.5. Results of the new PROFFAST calibration for XCO and instrument SN037	115
B.6. Results of the new PROFFAST calibration for XH ₂ O and instrument SN037	115
B.7. Results of the new PROFFAST calibration for XCO ₂ and instrument SN039	116
B.8. Results of the new PROFFAST calibration for XCH ₄ and instrument SN039	116
B.9. Results of the new PROFFAST calibration for XCH ₄ ^{S5P} and instrument SN039	117
B.10. Results of the new PROFFAST calibration for XCO and instrument SN039	117
B.11. Results of the new PROFFAST calibration for XH ₂ O and instrument SN039	118
B.12. Results of the new PROFFAST calibration for XCO ₂ and instrument SN122	118
B.13. Results of the new PROFFAST calibration for XCH ₄ and instrument SN122	119
B.14. Results of the new PROFFAST calibration for XCH ₄ ^{S5P} and instrument SN122	119
B.15. Results of the new calibration including the XH ₂ O correction for XCO and instrument SN122.	120
B.16. Results of the new PROFFAST calibration for XCH ₂ O and instrument SN122	120
C.1. Correlations between the SSQs and the XCH ₄ noise level σ_{XCO_2}	121
C.2. A bar chart of the XCO ₂ noise levels and the SSQs for various TCCON sites	122

List of Tables

2.1. Composition of the Earth's atmosphere	6
3.2. Performance of the COCCON compared to the TCCON	58
4.1. Records of the transport data-logger attached to the EM27/SUN.	63
4.2. Bias compensation factors of the TS relative to the COCCON reference unit	66
5.1. Average bias of the TS to the TK data	77
5.2. Average bias of the TS to the TK data	83
5.3. Noise analysis of the TCCON sites visited with the TS	84
5.4. The number of fwd (n_{fwd}) and bwd (n_{bwd}) scans averaged for the HR and LR measurements at different sites as well as the scan speed. The scan speed are the number of iterferogram points sampled per seconds.	87
5.5. Comparison of the NR of LR and truncated HR spectra.	88
5.6. Comparison of different methods to calculate the SNR	90
5.7. SNR analysis of various TCCON sites.	91
5.8. The bias compensation factors of the TCCON site relative to the TS	96
5.9. Bias compensation factors between TCCON-ID and the Karlsruhe reference	97
5.10. Deviation of the TCCON sites to the Karlsruhe reference in percentage	97
5.11. Bias compensation factors for the time-corrected Tsukuba data.	99
5.12. Deviation of the pressure values to the DWD Rheinstetten station	102
A.1. Records of the transport data-logger mounted inside of the enclosure.	110
C.1. The two letter site ID of a selection of TCCON sites	122

Acronyms

masl meters above sea level. 74

ppb parts per billion. 6

ppm parts per million. 6

ADCF Airmass Dependend Correction Factor. 49–51, 53, 131

AICF Airmass Independend Correction Factor. 49, 51, 53, 58

bwd backward. 42–45

Caltech CALIFORNIA INSTITUTE OF TECHNOLOGY. 39, 40

COCCON Collaborative Carbon Column Observing Network. i, 2–4, 13, 37, 38, 45–47, 49–52, 57–60, 63, 66–70, 73, 93–95, 97, 101–105, 131, 133

DFT discrete FOURIER transformation. 22, 23

DMF dry-air mole fractions. 2, 3, 38, 42, 44, 52, 66, 104

DOF degrees of freedom. 18

DWD Deutscher Wetterdienst. 64, 70–72, 99, 131, 133

ESA European Space Agency. 45, 49

ETL East Trout Lake. i, 63, 69, 70, 73, 79, 80, 83, 84, 100, 102, 104, 131

ETL-HR East Trout Lake high-resolution. 79, 80, 84

ETL-LR East Trout Lake low-resolution. 79, 80, 84

FFT Fast FOURIER transformation. 23

FRM4GHG Fiducial Reference Measurements for Ground-Based Infrared Greenhouse Gas Observations. 45, 49

FTIR FOURIER Transform Infrared. i, 2–5, 20, 22–24, 26, 28, 31–33, 35, 37, 39, 41, 43, 45, 46, 49, 68, 74, 90, 103

fwd forward. 42–45

FWHM full width at half maximum. 19

- GEOS-FPIT** Goddard Earth Observing System - Forward Processing for Instrument Teams. 77, 78
- GHG** greenhouse gas. i, 1, 2, 5, 12, 13, 20, 31, 37, 41, 45, 46, 131
- GOSAT** Greenhouse Gases Observing Satellite. 2
- HITRAN** High-resolution Transmission Molecular Absorption Database. 33
- HR** high-resolution. i, 84, 87, 93, 100, 103, 132
- I2S** INTERFEROGRAMS TO SPECTRA. 39, 43
- ILS** instrumental line shape. i, 3, 29, 41, 46, 63, 64, 66, 68, 69, 87, 101
- IMK-ASF** Institute for Meteorology and Climate Research - Atmospheric Trace Gases and Remote Sensing. 3, 60, 71, 72, 101, 131
- InGaAs** Indium Gallium Arsenide. 42
- InSb** Indium Antimonide. 39, 42
- IPCC** Intergovernmental Panel for Climate Change. 13
- IR** infrared. 14, 32
- IRWG** infrared working group. 2
- KA** Karlsruhe. 42, 44, 84, 85, 87, 94
- KA-HR** Karlsruhe high-resolution. 87
- KIT** KARLSRUHE INSTITUTE OF TECHNOLOGY. 37, 42, 45, 70
- LR** low-resolution. i, 84, 87, 93, 98, 100, 103, 132
- ME** modulation efficiency. 29, 30, 68, 69
- MIR** mid-infrared. 2, 42
- NASA** National Aeronautic and Space Administration. 37
- NDACC** Network for Detection of Atmospheric Composition Change. 2, 42
- NIR** near-infrared. 2, 42, 86, 87
- NOAA** National Oceanic and Atmospheric Administration. 2
- OCO-2** Orbiting Carbon Observatory - 2. 2
- OPD** optical path difference. 23, 26–30, 87
- OPD_{max}** maximum optical path difference. 30, 39, 43, 74, 86, 87
- PE** phase error. 29, 30, 68, 69

- PI** principal investigator. 75, 78, 82, 88, 90, 96
- PLC** programmable logic controller. 60
- QC** quality control. 44
- rmsocl** “root-mean-square-over-continuum-level”. 90
- RTE** radiative transfer equation. 32, 33
- SNR** signal-to-noise ratio. i, 30, 31, 86–93, 99, 100, 102, 103, 118, 132, 133
- SSQ** “spectral signal quality”. 90–93, 117, 118, 132
- SZA** Solar Zenith Angle. 42, 44, 45, 49–54, 57, 64, 66, 69, 70, 101, 105, 106, 131
- TCCON** Total Carbon Columns Observing Network. i, 2–4, 13, 37–45, 47, 49, 51–53, 56–59, 61, 67, 68, 70, 73–75, 77–104, 117, 118, 131–133
- TK** Tsukuba. i, ii, 73, 77, 83–85, 87, 88, 92, 96–100, 132, 133
- TK-HR** Tsukuba high-resolution. 74–78, 84, 85, 96–98, 100, 102
- TK-LR** Tsukuba low-resolution. i, 74–78, 84, 85, 96–100, 102
- TROPOMI** TROPOspheric Monitoring Instrument. 2, 46
- TS** Travel Standard. i, 3, 4, 44, 59–63, 65–71, 73–75, 77, 79–85, 87–89, 93–95, 97, 99–105, 131–133
- TUM** Technical University Munich. 60, 102
- UPS** uninterruptible power supply. 60
- UV** ultraviolet. 5, 6, 8, 14
- WG** Wollongong. i, 73, 81, 82, 87, 88, 98–100, 131
- WG-HR** Wollongong high-resolution. i, 81–84, 86, 102
- WG-LR** Wollongong low-resolution. i, 81–84, 86, 97, 102
- WMO** World Meteorological Organization. 3, 40, 47, 49
- ZPD** zero path difference. 25

Acknowledgment

Zunächst möchte ich mich bei Prof. Dr. Peter Braesike für die kurzfristige Übernahme des Referats herzlich bedanken.

Ein weiterer Dank geht an Dr. Thomas Blumenstock und PD Dr. Frank Hase für die Aufnahme in die Boden-Gruppe und damit die Möglichkeit, diese Arbeit dort zu schreiben. Dr. Thomas Blumenstock sei an dieser Stelle nochmals für die Durchsicht dieser Arbeit und die wertvollen Kommentare dazu gedankt.

Ein besonderer Dank geht an PD Dr. Frank Hase für die Übernahme des Koreferats und die direkte wissenschaftliche Betreuung. Damit verbunden ist die Bereitschaft, jederzeit Fragen zu beantworten, Ergebnisse zu diskutieren und Zweifel auszuräumen. Bedanken möchte ich mich auch für die Freiheit und das Vertrauen, die Richtung meiner Arbeit, so fern es durch äußere Vorgaben möglich war, selbständig wählen zu können, was unter anderem zur Entwicklung des PROFFASTpylots geführt hat.

Ein weiterer Dank geht an Jochen Groß für die vielen pragmatischen Hilfen und Tipps im Hard- und Softwarebereich, ohne die der Travel Standard nicht so flexibel und robust einsetzbar gewesen wäre. Dies hat meinen Wissensschatz außerhalb der wissenschaftlichen Arbeit sehr bereichert.

I would also like to thank Dr. Carlos Alberti for his willingness to help me with many questions, especially at the beginning of my Ph.D., providing me with measurement data, and helping me with the ILS measurements.

Danke auch an Lena Feld für die entspannte und produktive Zusammenarbeit bei der Entwicklung des PROFFASTpylot, die fachlichen Diskussionen, das Korrekturlesen von Teilen der Arbeit, die vielen interessanten Gespräche und das gemeinsame Klettern (wenn auch viel zu selten ;-)).

Ein weiterer Dank geht an Valentin Hanft, Clemens Herkommer, Leo Krause, Magdalena Lindner und Kilian Marten für das Korrekturlesen von Teilen oder der gesamten Arbeit.

Bedanken möchte ich mich auch bei der gesamten Boden-Arbeitsgruppe für die freundliche Aufnahme in die Gruppe und - trotz Corona-Maßnahmen - schöne Gruppenausflüge zum Baggersee: Carlos Alberti, Thomas Blumenstock, Christopher Diekmann, Darko Dubravica, Benjamin Ertl, Lena Feld, Jochen Groß, Frank Hase, Farah Khosrawi, Nga Ying Lo, Amelie Röhling und Matthias Schneider.

Mein größter Dank, den man eigentlich nicht in Worte fassen kann, gilt meiner Frau Kerstin. Vielen Dank für deine immerwährende und vielfältige Unterstützung und für deine Geduld und deinen Verzicht, vor allem in der Schlussphase der Arbeit. Danke, dass du mir den Rücken gestärkt und freigehalten hast.